Imperial College London
Department of Bioengineering

Wired, wireless and wearable bioinstrumentation for high-precision recording of bioelectrical signals in bidirectional neural interfaces

Konstantinos Petkos

September 2019

Supervised by Prof. Emmanuel M. Drakakis,
Prof. P. Brown and Prof. T. Denison

Submitted in partial fulfilment of the requirements for the degree of
Doctor of Philosophy of Imperial College London and
the Diploma of Imperial College London

Declaration of originality

I hereby declare that all material provided in this thesis is a product of my own work and, if not, it has been appropriately referenced. Any contribution made to this research by others is explicitly acknowledged in the text.

Konstantinos Petkos

30th September 2019, London

Copyright declaration

The copyright of this thesis rests with the author and is made available under a Creative Commons Attribution Non-Commercial No Derivatives licence.

Researchers are free to copy, distribute or transmit the thesis on the condition that they attribute it, that they do not use it for commercial purposes and that they do not alter, transform or build upon it. For any reuse or redistribution, researchers must make clear to others the licence terms of this work.

Abstract

It is widely accepted by the scientific community that bioelectrical signals, which can be used for the identification of neurophysiological biomarkers indicative of a diseased or pathological state, could direct patient treatment towards more effective therapeutic strategies. However, the design and realisation of an instrument that can precisely record weak bioelectrical signals in the presence of strong interference stemming from a noisy clinical environment is one of the most difficult challenges associated with the strategy of monitoring bioelectrical signals for diagnostic purposes. Moreover, since patients often have to cope with the problem of limited mobility being connected to bulky and mains-powered instruments, there is a growing demand for small-sized, high-performance and ambulatory biopotential acquisition systems in the Intensive Care Unit (ICU) and in High-dependency wards.

Furthermore, electrical stimulation of specific target brain regions has been shown to alleviate symptoms of neurological disorders, such as Parkinson's disease, essential tremor, dystonia, epilepsy etc. In recent years, the traditional practice of continuously stimulating the brain using static stimulation parameters has shifted to the use of disease biomarkers to determine the intensity and timing of stimulation. The main motivation behind closed-loop stimulation is minimization of treatment side effects by providing only the necessary stimulation required within a certain period of time, as determined from a guiding biomarker. Hence, it is clear that high-quality recording of local field potentials (LFPs) or electrocorticographic (ECoG) signals during deep brain stimulation (DBS) is necessary to investigate the instantaneous brain response to stimulation, minimize time delays for closed-loop neurostimulation and maximise the available neural data.

To our knowledge, there are no commercial, small, battery-powered, wearable and wireless recording-only instruments that claim the capability of recording ECoG signals, which are of particular importance in closed-loop DBS and epilepsy DBS. In addition, existing recording systems lack the ability to provide artefact-free high-

frequency (> 100 Hz) LFP recordings during DBS in real time primarily because of the contamination of the neural signals of interest by the stimulation artefacts.

To address the problem of limited mobility often encountered by patients in the clinic and to provide a wide variety of high-precision sensor data to a closed-loop neurostimulation platform, a low-noise (8 nV/√Hz), eight-channel, battery-powered, wearable and wireless multi-instrument (55 × 80 mm^2) was designed and developed. The performance of the realised instrument was assessed by conducting both *ex vivo* and *in vivo* experiments. The combination of desirable features and capabilities of this instrument, namely its small size (~one business card), its enhanced recording capabilities, its increased processing capabilities, its manufacturability (since it was designed using discrete off-the-shelf components), the wide bandwidth it offers (0.5 – 500 Hz) and the plurality of bioelectrical signals it can precisely record, render it a versatile tool to be utilized in a wide range of applications and environments.

Moreover, in order to offer the capability of sensing and stimulating via the same electrode, novel real-time artefact suppression methods that could be used in bidirectional (recording and stimulation) system architectures are proposed and validated. More specifically, a novel, low-noise and versatile analog front-end (AFE), which uses a high-order (8th) analog Chebyshev notch filter to suppress the artefacts originating from the stimulation frequency, is presented. After defining the system requirements for concurrent LFP recording and DBS artefact suppression, the performance of the realised AFE is assessed by conducting both *in vitro* and *in vivo* experiments using unipolar and bipolar DBS (monophasic pulses, amplitude ranging from 3 to 6 V peak-to-peak, frequency 140 Hz and pulse width 100 μs). Under both *in vitro* and *in vivo* experimental conditions, the proposed AFE provided real-time, low-noise and artefact-free LFP recordings (in the frequency range 0.5 – 250 Hz) during stimulation. Finally, a family of tunable hardware filter designs and a novel method for real-time artefact suppression that enables wide-bandwidth biosignal recordings during stimulation are also presented. This work paves the way for the development of miniaturized research tools for closed-loop neuromodulation that use a wide variety of bioelectrical signals as control signals.

Acknowledgements

First and foremost, I would like to thank my supervisor **Professor E.M. Drakakis** for the support, advice and guidance he gave me throughout my PhD, despite his busy schedule. I would also like to thank my project supervisors **Professor Tim Denison** and **Professor Peter Brown** who along with Professor E.M. Drakakis gave me the opportunity to work on this challenging project.

Moreover, I would like to express my appreciation to my colleagues **Dr George Zafeiropoulos** and **Mr Simos Koutsoftidis** who spent time with me exchanging views and approaches on this project. Furthermore, I would like to express my gratitude to **Dr Graham Peyton** who was always an easy-to-reach person for me, willing to discuss any questions I had and to give me advice on how to solve problems in my circuits. Many thanks to **Dr Hamid Soleimani** whose opinion and advice helped me to reconsider strategies for achieving my project goals. I would also like to thank my friends who made my stay in London much better: **Oscar, Mireia, Aimilios and Marina.**

Last but not least, I would like to express my gratitude to **Medtronic** for fully funding my project and **the Centre for Doctoral Training (CDT) in Neurotechnology** for the studentship I was offered and the support I was given throughout my PhD.

Contents

Declaration of originality ..... **II**

Copyright declaration ..... **III**

Abstract ..... **IV**

Acknowledgements ..... **VI**

List of Tables **6**

List of Figures **8**

Abbreviations **35**

Chapter 1. Introduction **38**

1.1 Motivation **38**

1.2 Research objectives **39**

1.3. Thesis Outline **40**

Chapter 2. Introduction to bioelectrical signal acquisition and closed-loop deep brain stimulation **42**

2.1 Clinical value of bioelectrical signals **42**

2.2 Biopotential electrodes **47**

2.2.1 Introduction to biopotential electrodes 47

2.2.2 Perfectly polarizable electrodes 48

2.2.3 Perfectly non-polarizable electrodes 50

2.2.4 Equivalent circuit model of a biopotential electrode 51

2.2.5 Types of biopotential electrodes for ExG signal acquisition 52

2.3 Analog front-end design for biopotential acquisition **53**

2.3.1 Introduction to biopotential recording systems 53

2.3.2 Challenges in the design of the front-end electronics 55
2.3.2.1 Interference theory 55
2.3.2.2 Spectral location of the noise/interference sources 57
2.4 Deep brain stimulation 58
2.4.1 Introduction to deep brain stimulation 58
2.4.2 Deep brain stimulation electrodes 61
2.4.3 Biomarkers for closing the loop 64
2.5 Artefact suppression in bidirectional neural interfaces 67
2.5.1 Introduction to artefact suppression techniques 67
2.5.2 Artefact prevention techniques 70
2.5.3 Front-end artefact suppression techniques 71
2.5.4 Back-end artefact suppression techniques 73
2.6 The approach in this work 76
Chapter 3. Design of a wearable and wireless multi-instrument for real-time monitoring of bioelectrical signals 78
3.1 Introduction 78
3.2 System overview 79
3.2.1 Design requirements and implementation of the AFE 79
3.2.2 Architecture of the overall system 84
3.2.3 Design considerations for low-noise biosignal recordings in a noisy clinical environment 88
3.3 Measured results 89
3.3.1 Transfer function and input referred noise 92
3.3.2 Total harmonic and intermodulation distortion 93

3.3.3 Step and impulse response 95
3.3.4 *Ex vivo* recordings of ExG (EEG, EMG and ECG) signals and fasciculations 97
3.3.5 *In vivo* recordings of LFPs 102
3.3.6 Recording of resonant neural response 103
3.3.7 Recording of PV ectopic activity 105
3.3.8 Recording of acceleration signals 106
3.3.9 Comparison with other biosignal acquisition systems 108
3.4 Discussion/Conclusion 118
Chapter 4. Design of a low-noise analog front-end for recording of field potentials during deep brain stimulation 123
4.1 Introduction 123
4.2 System overview 126
4.2.1 System requirements, design and implementation of the AFE 126
4.2.2 *In vitro* experimental setup for artefact suppression testing 132
4.3 Measured results 135
4.3.1 AFE characterization – Measured results 135
4.3.1.1 Impulse/Step response 135
4.3.1.2 Bode magnitude plot/Noise 136
4.3.1.3 Measured results versus specifications 138
4.3.1.4 Total harmonic distortion and intermodulation distortion 138
4.3.1.5 Key properties of the Chebyshev notch AFE 140
4.3.2 Performance evaluation of the AFE based on recordings of physiological signals 141

4.3.3 Performance evaluation of the AFE based on comparisons with commercial biopotential acquisition devices 143

4.3.4 Evaluation of the artefact suppression capabilities of the AFE by *in vitro* DBS tests 149

4.3.5 Evaluation of the artefact suppression capabilities of the AFE by *in vivo* DBS tests 157

4.4 Discussion/Conclusion 159

4.4.1 Methodological significance 159

4.4.2 Limitations and further improvements 165

4.4.3 Pathophysiological significance 166

4.4.4 Conclusion 168

Chapter 5. Purely analog and mixed mode (analog & digital) approaches for artefact suppression during electrical stimulation 169

5.1 Introduction 169

5.2 Tunable analog filters 170

5.3 A novel mixed mode (analog & digital) artefact suppression method 178

5.3.1 Design methodology 178

5.3.2 Measured results 185

5.3.2.1 Proof of concept using test signals 185

5.3.2.2 Application of the proposed method in cardiac sensing & stimulation 190

5.4 Discussion/Conclusion 192

Chapter 6. Conclusions – Future work 195

6.1 Summary 195

6.2. Future work 199

THESIS CONTRIBUTIONS **201**

LIST OF PUBLICATIONS & PATENTS **203**

APPENDICES **204**

A. Permissions **204**

BIBLIOGRAPHY **212**

List of Tables

Table 2.1: Biosignal characteristics [14]. 44

Table 2.2: Tradeoffs of different sensing modalities. *Reproduced from ref. [15].* 45

Table 2.3: List of established and experimental DBS targets. *Adapted from ref.* [44].....59

Table 2.4: Techniques for artefact prevention. *Reproduced from ref.* [54]. 70

Table 2.5: Front-end artefact suppression techniques. *Reproduced from ref.* [54].....74

Table 2.6: Back-end artefact suppression techniques. *Reproduced from ref.* [54].....75

Table 3.1: Summary of key performance specifications related to the AFE of the proposed instrument. 79

Table 3.2: Comparison of the proposed instrument with the Warner amplifier and the bioamplifier included in Powerlab 26T.....113

Table 3.3: Comparison of the proposed instrument with commercial (portable and implantable) wireless biopotential acquisition systems.115

Table 3.4: Comparison of the proposed instrument with other state-of-the-art wearable and wireless biopotential acquisition systems existing in the literature.....117

Table 3.5: Comparison of the proposed instrument's AFE with state-of-the-art ASICs for biopotential signal acquisition (note that, as anticipated, a tradeoff exists between ultra-low power consumption (state-of-the-art

ASICs) and superior noise performance (proposed instrument's AFE)). 118

Table 4.1: Key AFE requirements for reliable acquisition of LFPs during deep brain stimulation. 127

Table 4.2: Key properties of the Chebyshev notch AFE. 140

Table 6.1: Provided bandwidth and parameters of the stimulation pulses that can be rejected by the artefact suppression methods proposed in this thesis. 198

List of Figures

Figure 2.1: Frequency bands of abnormal phase synchrony characterizing serious neurological disorders [4, 5]. The last decade of LFP analysis also revealed that the power of ultra-weak, high-frequency oscillations detected in the 300 Hz (270 − 330 Hz) frequency band [18] also correlates with PD motor symptoms and clinical conditions. The aim of this Thesis is to provide ultra low-noise and wide-bandwidth biomedical instruments that are capable of accurately recording those weak, high-frequency oscillations. 43

Figure 2.2: Recording sites of various neural sensing modalities. *Adapted from ref. [15].* 44

Figure 2.3: Double layer model when anions are specifically absorbed. 49

Figure 2.4: Equivalent circuit model of a biopotential electrode. *Adapted from ref.* [37]. 51

Figure 2.5: Block diagram describing a generic biopotential recording system. BPA, amplifier with band-pass characteristics; VGA, variable gain amplifier; MUX, multiplexer; ADC, analog-to-digital converter; TX, transmitter. *Adapted from ref.* [42]. 54

Figure 2.6: Electrostatic interference to the human body. *Adapted from ref.* [37]. 56

Figure 2.7: Amplitude and frequency characteristics of ExG (EEG, ECG, and EMG) signals and contaminating signals. *Reproduced from ref.* [43] *© 2007 IEEE.* 58

Figure 2.8: (a) The electrodes and pulse generators are permanently implanted, self-contained systems. Electrodes can be implanted in one or both hemispheres of the brain, depending on the laterality of the symptoms. The pulse generator implanted in the chest is connected to the electrodes implanted in the brain. (b) Basal ganglia and cortex are structures that are coupled into loops. Hence, wide-scale network modulation of the basal ganglia and cortex is enabled by DBS. Many overlapping loops exist, however only a loop controlling the arm is presented here for illustrative purposes. GPe, globus pallidus externa; GPi, globus pallidus interna. *Adapted from ref.* [44]. 60

Figure 2.9: Comparison of emerging DBS electrode lead technology. BSN, Boston Scientific Neuromodulation; STJ, St. Jude Medical; MDT, Medtronic. *Adapted from ref.* [51]. 62

Figure 2.10: (a) Magnetic resonance imaging scan showing a DBS electrode that targets the subthalamic nucleus. Perioperative imaging is necessary and intraoperative imaging desirable in the accurate placement of electrodes. (b) Prototype research electrodes have been fabricated with higher densities of smaller contacts. (c) These have been designed with the intention of offering finer control of the electric field (blue volume). The top panel depicts the spherical field predominating when a complete ring of contacts is activated to mimic the field generated by conventional DBS (where 4-contact DBS leads are typically used). On the right, the electrode and electric field are superimposed on a brain atlas. In conventional DBS, the electrode is in the target, which is the subthalamic nucleus, but the electric field extends outside of this, risking side effects. On the contrary, as the lower panel shows, when a subset of contacts of a segmented DBS electrode is simultaneously activated, a

different shaping of the electrical field can be achieved. In this case, the field is limited to the subthalamic nucleus. *Adapted from ref.* [44].....63

Figure 2.11: Comparison of different stimulation strategies. (a) Stimulation timing and parameters are fine-tuned by a clinician during follow-up visits (usually twice a year). No automatic adjustment of stimulation parameters, guided by a disease biomarker, exists in this case. (b) LFPs are continuously recorded (using depth electrodes) and used to automatically adjust stimulation timing or intensity. Stimulation is delivered via the same depth electrodes. (c) Cortical signals are continuously recorded (using an electrocorticography array) and used to automatically adjust stimulation timing or intensity. Since stimulation is delivered across the depth electrodes, a spatial separation between sensing and stimulation sites is created. (d) Peripheral signals, such as electromyographic and/or acceleration signals, obtained from noninvasive measurement devices (e.g. accelerometers and wearable EMG recording systems), are used to automatically adjust stimulation timing or intensity. As in c, a separation between sensing and stimulation sites exists, which minimizes the effect of stimulation artefacts on the recorded signals. The gray box represents a computing device (e.g. an implantable pulse generator, a personal computer or a cloud-based computing system). The computing device processes the recorded biosignals in the digital domain and extracts features, such as the intensity of neural activity in a specific frequency band or phase–amplitude coupling, to determine stimulation parameters and timing. *Adapted from ref.* [44]. 66

Figure 2.12: Architecture of a bidirectional neural interface where local field potentials are used as feedback signals. Stimulation artefacts contaminate the recorded signals and impede robust extraction of

biomarkers. To enable concurrent sensing and stimulation, neuromodulation systems can attenuate stimulation artefacts by applying either frontend or backend cancellation methods. AMP, amplifier; STIM, stimulator; ADC, analog-to-digital converter. *Adapted from ref.* [54].....68

Figure 2.13: Linear circuit model of an electrode in a setup where electrical stimulation is applied. The electrodes are represented as parallel RC circuits. A time dependent resistor models the stimulation switch. *Adapted from ref.* [57]. 69

Figure 2.14: Description of different front-end (left) and back-end (right) artefact mitigation techniques. Front-end artefact cancellation techniques improve linearity and duration of recorded artefacts, and back-end methods remove them. Recorded analog signals (solid blue line) contain artefacts that distort the underlying neural activity (dotted green line). Back-end cancellation methods attempt to recover the neural signal of interest (solid green line). (a) Typical AFE architectures face saturation issues during the artefact and the front-end amplifier recovers slowly. (b) By increasing the dynamic range of the AFE, saturation can be prevented and signal distortion can be reduced. Hence, back-end artefact subtraction methods can be used to remove the artefacts. (c) AFEs that quickly recover from a saturating signal can minimize the amount of distorted signals. (d) Saturation prevention and rapid recovery can both be applied to increase the quality of the recorded biosignals. (e) Some back-end methods identify the artefact segments and reconstruct the underlying neural activity using interpolation. (f) Subtractive methods cancel artefact by subtracting estimated artefact waveforms. Artefact estimation is accomplished using adaptive filtering or template building. (g) Recorded waveforms can be separated into artefactual and neural

components. Clean neural components are used to reconstruct the underlying neural activity. *Adapted from ref.* [54]. 72

Figure 2.15: Block diagram of the high-performance analog front-end presented in [80]. This front-end has been designed to record local field potentials from the human brain. MUX, multiplexer; OCMFB, output common mode feedback; LPF, low-pass filter; ADC, analog-to-digital converter. *Adapted from ref.* [80]. 77

Figure 3.1: Block diagram showing the overall AFE and the ADC section of the proposed instrument. The overall AFE consists of eight channels (five channels on the PCB of the instrument and another three channels on a stacked PCB that is adjusted on two headers located on the main PCB). The biopotential recording AFE consists of three stages: (i) a differential pre-amplification stage with high-pass characteristics, (ii) an active, 1st order high-pass filter that enhances the dc offset rejection capabilities of the AFE, and (iii) a passive, 2nd order low-pass filter that defines the passband of the AFE and also serves as an anti-alias filter for the ADC stage, which follows in the signal chain. The inputs of the first five channels are differential, whereas the inputs of channels 6, 7 and 8 can either be differential or single-ended depending on the type of biosignals (either amperometric or potentiometric or biopotential signals or a combination of them) the stacked PCB is intended to record. INA, instrumentation amplifier; AFE, analog front-end; PCB, printed circuit board; MUX, multiplexer; ADC, analog-to-digital converter. 80

Figure 3.2: Block diagram showing the overall architecture of the proposed instrument. The data received by the receiver module can either be directed i) to a PC through the USB 2.0 interface, or ii) to a commercially available data acquisition system (e.g. Powerlab) that

digitizes and depicts the data on a PC. Path (ii) ensures that the proposed instrument can functionally integrate with existing medical biosignal acquisition systems, if required. AFE, analog front-end; ADC, analog-to-digital converter; FPGA, field programmable gate array; Tx, transmitter; Rx, receiver; DAC, digital-to-analog converter; USB, universal serial bus; PC, personal computer. 84

Figure 3.3: Structure of the proposed wearable/wireless instrument. The instrument's architecture includes: (a) a high-performance, eight-channel (five channels on the main board and another three channels on a stacked PCB that is adjusted on the two headers shown in the picture) AFE, (b) an analog, low-power 3-axis accelerometer, (c) an eight-channel, 24-bit ADC, (d) an FPGA module, (e) a 2 MBps Zigbee transceiver, and (f) a 2.4 GHz antenna.....86

Figure 3.4: Final version of the proposed wearable/wireless instrument. 87

Figure 3.5: Experimental setup for measuring the input referred noise of the instrument in an operating theatre. The system was not protected from EMI sources in order to assess its noise performance under the worst possible conditions. 91

Figure 3.6: Input-referred noise measurements conducted in: (a) a university laboratory, and (b) an operating theatre. (c) The amplitude spectrums of the two noise recordings approximate each other and do not include any peak at 50 Hz. (d) The boxplot shows that the noise recordings conducted in the two different settings (operating theatre and university laboratory) exhibit approximately the same behaviour.....91

Figure 3.7: Measured Bode magnitude plot (a) and input-referred noise (b) of the proposed instrument's biopotential recording AFE. (a) The

biopotential recording AFE provides a passband between 0.5 and 500 Hz. The roll-off of the analog high- and low-pass filters equals +10 dB/Oct and -40 dB/decade, respectively. (b) Noise power spectral density estimate in the passband for the biopotential recording AFE is 8 nV/$\sqrt{Hz}$, with the residual 1/f corner estimated at roughly 5 Hz. 92

Figure 3.8: THD (a) and IMD_3 (b) of the proposed instrument's AFE (gain=60 dB). (a) Taking into consideration that the available dynamic range of the AFE is from 1 μV peak to 2.3 mV peak, it is clear that the achieved THD is less than 0.3%. (b) The two tones applied to the AFE of the proposed instrument were f_1 = 4.9 Hz and f_2 = 5.1 Hz. The output power of a single fundamental tone (in dBm - red line in the graph) and the relative power of the IMD_3 products referenced to a single tone (blue circles) are plotted against the applied input power. The third-order intercept line (dashed blue line) is extended to intersect the extension of the fundamental output signal line (dashed red line). This intersection is termed the third order intercept point IP_3. The calculated IP_3 exhibits a relatively high value, which is desired, since the higher the IP_3 value the better the linearity of the amplifier and the weaker the output intermodulation products that will be generated at the amplifier's output. THD, total harmonic distortion; IP_3, third order intercept point; IMD_3, third order intermodulation distortion. 94

Figure 3.9: (a) Step response, (b) impulse response and (c) response to a biphasic pulse, which characterize the proposed instrument's AFE. (d) The step response of the AFE, which initially exhibits an undershoot of 250 μV, is free of ringing (there is no decaying oscillatory activity after the undershoot). (e) The impulse response of the AFE exhibits a relatively fast settling. (f) The response of the AFE to a biphasic pulse exhibits a significantly faster settling in comparison to its corresponding impulse

response (shown in (e)). In all cases, the output voltage (black line) is presented after removing the gain of 60 dB that is applied by the biopotential recording AFE. 96

Figure 3.10: Measurement setup for comparing the quality of biosignals recorded using two different methods. In the first method (wired transmission), the signals are recorded by the AFE of the proposed instrument and are directly digitized and depicted on the computer by a commercial instrument (Powerlab 16/35). In the second method (wireless transmission), the signals are recorded by the proposed instrument, are wirelessly transmitted to a receiver module and are depicted on the computer by the Powerlab 16/35 hardware. 98

Figure 3.11: Biosignal acquisition using the setup presented in Figure 3.10. The applied gain was 60 dB and the sampling frequency was equal to 1 kSPS. (a) Wired vs wireless EEG acquisition. (b) Wired vs wireless EMG acquisition from the palmaris longus muscle. (c) Wired vs wireless ECG acquisition. (d) Detailed view of the wireless and wired time-domain EEG recordings. (e) Detailed view of the wireless and wired time-domain EMG recordings. (f) Detailed view of the wireless and wired time-domain ECG recordings. (g) The SNR of the EEG signals was measured and found to be continuously higher than 25 dB. (h) The SNR of the EMG signals was measured and found to be continuously higher than 25 dB. (i) The SNR of the ECG signals was measured and found to be continuously higher than 30 dB. SNR, signal-to-noise ratio. 99

Figure 3.12: (a) Amplitude spectrum (the reference level of amplitudes equals 1 V) of EEG signals recorded by the proposed instrument when the subject's eyes are open and when they are closed. A high-performance commercial bioamplifier (Powerlab 26T, ADInstruments)

was also used as a reference instrument in this series of experiments. It is clear that in the 7.5 – 12.5 Hz band the amplitude spectrum of the EEG signals recorded when eyes are closed is significantly higher than the amplitude spectrum of the signals recorded when eyes are open. Furthermore, the results acquired using the wireless transmission method: 1) are in full agreement with the results acquired using the wired transmission method, and 2) are in full agreement with the results acquired using the commercial bioamplifier. (b) EEG spectrogram calculated from the EEG data wirelessly recorded by the proposed instrument. Alpha waves in the 7.5 – 12.5 Hz band during the eyes closed period are clearly visible. 101

Figure 3.13: Wireless recording of benign fasciculations. 101

Figure 3.14: Experimental setup for evaluating the recording capabilities of the proposed instrument *in vivo*. A DBS electrode (electrode A, model DB-2201, Boston Scientific Neuromodulation) was implanted into the thalamus of an anaesthetised non-human primate. LFP signals were differentially recorded through contacts 1 and 3 of electrode A. The non-human primate was under anaesthesia with the head held in a primate stereotactic frame, which was connected to the ground of the recording system. The LFP signals were digitized by the wearable/wireless instrument at a sampling frequency of 1 kSPS and were wirelessly transmitted to the receiver module (wireless transmission method – described in Figure 3.10). 103

Figure 3.15: (a) Differential LFP recordings acquired from the thalamus of an anaesthetised non-human primate with the experimental setup illustrated in Figure 3.14. (b) A detailed view of the recorded LFPs reveals their small amplitudes (< 20 μV peak). (c) Amplitude spectrum of the

recorded LFPs. Clearly, the proposed instrument can wirelessly provide low-noise recordings of weak LFP signals in a noisy clinical environment. 104

Figure 3.16: (a) Temporal response of the proposed instrument's AFE when a signal segment containing ERNA, recorded by a dc-coupled commercial instrument from the STN at 2048 SPS, is injected to the instrument's AFE. The signal was recorded by the instrument's AFE and was then digitized by the Powerlab hardware at 4 kSPS (wired transmission method). (b) Temporal response recorded by the proposed instrument with and without the application of a real-time digital high-pass filter at 30 Hz when a signal that contains high-frequency stimulation (HFS) pulses and ectopic activity was injected to the biopotential recording AFE's input by a waveform generator (Agilent 33220A). The signal was sampled by means of the wearable/wireless instrument at 1 kSPS, was wirelessly transmitted to the receiver module and was depicted on the computer using the Powerlab 16/35 hardware (wireless transmission method). (c) Detailed view of the successfully recorded ERNA of interest. (d) Detailed view of the successfully recorded ectopic activity. It is clear that the application of a digital high-pass filter enables real-time recording of a high-quality signal, which approximates the signal recorded by the dc-coupled commercial medical device. 105

Figure 3.17: Time-domain profiles of acceleration signals recorded during three separate sessions. (a) during the first session, movements of the proposed instrument's PCB, where the accelerometer is located, were produced along the x-axis for a duration of approximately 9 seconds (b) during the second session, movements of the proposed instrument's PCB were produced along the y-axis for a duration of approximately 9 seconds (c) during the third session, movements of the proposed

instrument's PCB were produced along the z-axis for a duration of approximately 9 seconds. In all recording sessions, the instrument started from immobility and at the end of the produced movements it returned back to immobility. Clearly, under all examined circumstances (tremor movements in X, Y and Z axes), the accelerometer was able to successfully discriminate the state of immobility from the state where tremor occurs.....107

Figure 3.18: Recording of LFPs injected by a waveform generator (Agilent 33220A) to the inputs of: a) the proposed instrument's AFE, b) a commercial high-gain differential amplifier (model DP-301, Warner instruments), and c) a very high-performance commercial bioamplifier (Powerlab 26T, ADInstruments).....109

Figure 3.19: (a) Recording of LFPs. The original LFP signal, which was previously recorded from the STN in a patient with PD withdrawn from levodopa, was injected by a waveform generator (Agilent 33220A) to the inputs of the proposed instrument's AFE, the DP-301 differential amplifier and the bioamplifier included in the Powerlab 26T data acquisition system. (b) Amplitude spectrum of the signals presented in Figure 3.19 (a). (c) The output of the proposed instrument's AFE better tracks the changes occurring in the original LFP signal in comparison to the other two instruments. This is verified by the fact that the RMSE between the original LFP signal and the signal recorded by the proposed instrument's AFE is less than the errors characterizing the other two instruments. (d) The detailed amplitude spectrum shows that the AFE of the proposed instrument provides accurate recording of the LFP signal, whereas the other two instruments cannot accurately record the frequencies of the LFP signal that are higher than 120 Hz. 110

Figure 3.20: (a) Recording of ECoG signals (original signal is shown in blue) injected by a waveform generator (Agilent 33220A) to the inputs of the proposed instrument's AFE (black line), the DP-301 differential amplifier (red line) and the very high-performance bioamplifier included in the Powerlab 26T data acquisition system (pink line). (b) Amplitude spectrum of the signals presented in Figure 3.20 (a). (c) It is clear that the three instruments are able to accurately record the injected ECoG signal. (d) The detailed amplitude spectrum verifies the conclusion that the recorded ECoG signals are of high quality. ECoG, electrocorticography. 111

Figure 3.21: (a) Amplitude spectrum of the output voltage recorded from the AFE of the proposed instrument, the DP-301 Warner differential amplifier and the bioamplifier included in the Powerlab 26T data acquisition system when two sinusoidal single tones (5 Hz and 25 Hz, amplitude 100 nV peak) were injected sequentially to the inputs of the instruments. The outputs of the three instruments were sampled at 1 kSPS. (b) Amplitude spectrum of the output voltage recorded from the thee instruments when two sinusoidal single tones (5 Hz and 25 Hz, amplitude 30 nV peak) were injected sequentially to the inputs of the instruments. The outputs of the three instruments were sampled at 1 kSPS. (c) It is clear that the AFE of the proposed instrument and the bioamplifier can accurately record the weak sinusoidal tone, whereas the DP-301 differential amplifier detects the tone but it cannot provide an accurate recording. (d) As in the case of the 100 nV peak sinusoidal tone, only the AFE of the proposed instrument and the bioamplifier can precisely record the 30 nV peak sinusoidal tone. It is important to note here that the noise floor of the proposed instrument is lower than the noise floors of the other two instruments. 112

Figure 4.1: Architecture of Analog Front-End (AFE) design for artefact-free local field potential (LFP) recording during deep brain stimulation (DBS). The AFE consists of (a) a differential pre-amplification stage with high-pass characteristics, which suppresses the common mode artefact voltage (CMAV), (b) an 8th order analog notch filter that suppresses the main frequency of the differential mode artefact voltage (DMAV), (c) a 2nd order analog low-pass filter that suppresses the high-frequency harmonics of the DMAV and (d) a final amplification stage that uses a programmable gain instrumentation amplifier to achieve the required gain. Two AFEs, based on the architecture presented above, have been designed. They only differ in their second stage, where the first AFE (Chebyshev notch channel) employs an 8th order Chebyshev notch filter, whereas the second AFE (Bessel notch channel) employs an 8th order Bessel notch filter.....128

Figure 4.2: Graphical representation of the four blocks constituting the AFE architecture. The resistors and capacitors included in these blocks are characterized by a tolerance of 0.1% and 10%, respectively. (a) The signals coming from two contacts of the DBS electrode are subtracted and amplified with a gain of 40 dB by an INA with high-pass characteristics (the high-pass knee frequency was set at 0.5 Hz). (b) An eight-pole Bainter 140 Hz notch filter is used to suppress the main frequency of the stimulation artefacts. (c) A two-pole 500 Hz Sallen-Key low-pass filter is used to suppress the high-frequency harmonics of the stimulation artefacts and define the passband of the system. (d) An INA provides either 20 dB or 40 dB amplification, which is digitally determined via a multiplexer.....131

Figure 4.3: The *in vitro* experimental setup for unipolar (a) and bipolar (b) stimulation. A DBS electrode (electrode A in (a) and (b), model DB-2201,

Boston Scientific Neuromodulation) was placed in a glass container filled with tyrode solution at room temperature. The monophasic stimulation pulses (3 V peak-to-peak amplitude, 140 Hz frequency and 100 μs pulse width) were delivered by means of a commercial stimulator (Grass, Astromed, Inc., USA) and the LFP signals (representing the LPF signals recorded from the human neural tissue in a typical post-operative LFP recording session) were injected to the solution by an Agilent 33220A waveform generator. The LFP signals were injected to the solution as a differential signal through a second electrode (electrode B in (a) and (b), model 401261, St. Jude Medical). One of the four contacts of electrode B was connected to the ground of the recording system. In both unipolar and bipolar settings the stimulation ground was electrically isolated from the mains by using a commercial isolator (SIU5 stimulus isolation point, Grass, Astromed, Inc., USA). The LFP signals recorded by the proposed AFE were digitized at a sampling frequency of 20 kSPS (samples per second) and depicted on a computer by the Powerlab data acquisition system (ADInstruments). (a) In the unipolar stimulation setting, we sense differentially and symmetrically in space about the unipolar stimulation contact 1a of electrode A by sensing across the two nearest, equi-distant to contact 1a, neighbour contacts (contacts 0 and 2a). However, since the surface areas of contacts 0 and 2a differ, the sensing is not completely symmetrical and thus some differential-mode interference from stimulation is expected to appear and be suppressed by the analog notch filter of the proposed AFE. The anode (ground) of the stimulator was connected to one of the contacts of a third electrode (electrode C), which is the 8-contact Vercise DBS lead (Boston Scientific). Electrode C was placed approximately 4 cm away from the stimulation site and represents the case of the implantable pulse generator, which acts as an anode in

the unipolar stimulation setting. (b) In the bipolar stimulation setting, two contacts of electrode A (0 and 1a) were used for stimulation (anode and cathode of the stimulator) and another two for recording (2a and 3). ..133

Figure 4.4: (a) Impulse response, (b) response to a biphasic pulse and (c) step response of the Chebyshev (red line) and Bessel (blue line) notch channels. (d) Chebyshev and Bessel notch channels exhibit approximately the same settling time. (e) The response of both channels to a biphasic pulse exhibits a faster settling in comparison to their corresponding impulse responses. (f) The step response of the Chebyshev notch channel shows a slightly bigger overshoot and ringing in comparison to the Bessel notch channel. As in the case of the impulse response, the differences are not significant. 136

Figure 4.5: Measured Bode magnitude plot with the gain of both channels set at 60 dB (a) and input-referred noise (b) of the Chebyshev notch channel (red line) and the Bessel notch channel (blue line). (a) Both channels provide a passband between 0.5 and 500 Hz. The roll-off of the high- and the low-pass filters equals + 20 dB/decade and -40 dB/decade, respectively, for both topologies. However, the Chebyshev notch channel provides a sharper transition between the passband and the stopband and stronger attenuation at the central frequency of the notch (= 140 Hz), compared to the Bessel notch channel. Besides, the Chebyshev notch channel exhibits a flat magnitude response in the passband and approximates the magnitude response of the Bessel notch channel. (b) Based on the input-referred noise graph, it is concluded that both channels are low-noise with the Chebyshev notch channel presenting a slightly better noise performance. Noise power spectral density estimates in the passband for the Chebyshev and the Bessel notch channels are 4 nV/ 137

Figure 4.6: THD (a) and IMD_3 (the reference impedance equals 50 Ω) (b) measured with the gain of the Chebyshev notch channel set at 60 dB. (a) After examining the available dynamic range of the channel (from 1 μV peak to 2.3 mV peak), it is clear that the achieved THD is less than 0.2%. (b) The two tones applied to the Chebyshev notch channel were f_1 = 4.9 Hz and f_2 = 5.1 Hz. The output power of a single fundamental tone (in dBm - red line in the graph) and the relative amplitude of the third order IMD_3 products referenced to a single tone (blue circles in Figure 4.6b) are plotted as a function of the applied input power. The third order intercept line (dashed blue line) is extended to intersect the extension of the fundamental output signal line (dashed red line). The calculated IP_3 is characterized by a relatively high value, which is a positive result since the higher the IP_3 values the better the linearity of the amplifier and the weaker the output intermodulation products that will be generated at the amplifier's output.....139

Figure 4.7: Biosignal acquisition using the Chebyshev notch channel. The applied gain was 60 dB and the sampling frequency was equal to 1 kSPS. (a) EMG signal acquisition. The signal inside the dotted rectangle was recorded while the subject was producing tremor movements. (b) The SNR of the EMG signals was measured and found to be continuously higher than 30 dB. (c) EEG signal acquisition. Since the frequency range of interest for EEG analysis in studies on PD is between 0.5 and 30 Hz, a digital low-pass filter at 40 Hz was applied on the recorded EEG signals. (d) The SNR of the EEG signals was measured and found to be continuously higher than 30 dB. (e) ECG signal acquisition. (f) The SNR of the ECG signals was measured and found to be continuously higher than 34 dB. 142

Figure 4.8: (a) Amplitude spectrum (the reference level of amplitudes equals 1 V) of the EEG signals recorded when the subject's eyes are open (blue line) and when they are closed (red line). It is clear that in the 7.5 – 12.5 Hz band the amplitude spectrum of the EEG signals recorded when eyes are closed is significantly higher than the amplitude spectrum of the signals recorded when eyes are open. (b) EEG spectrogram. Alpha waves in the 7.5 – 12.5 Hz band during the eyes closed period are clearly visible. 143

Figure 4.9: (a) Output voltage (after removing the gain of 80 dB) recorded from the Chebyshev notch channel when a sinusoidal single tone (25 Hz, amplitude 100 nV peak) was injected to the input of the channel. (b) Output voltage recorded from the Powerlab 26T bioamplifier when a sinusoidal single tone (25 Hz, amplitude 100 nV peak) was injected to the input of the system. (c) Amplitude spectrum calculated when two sinusoidal tones, one low-frequency (= 5 Hz) and one higher-frequency (= 25 Hz) are sequentially injected to the inputs of the two AFEs. The amplitude spectrums of both systems present two spectral peaks at 5 and 25 Hz, which are characterized by the same amplitude. (d) Output voltage (after removing the gain of 80 dB) recorded from the Chebyshev notch channel when a sinusoidal single tone (25 Hz, amplitude 30 nV peak) was injected to the input of the channel. (e) Output voltage recorded from the Powerlab 26T bioamplifier when a sinusoidal single tone (25 Hz, amplitude 30 nV peak) was injected to the input of the system. (f) Amplitude spectrum calculated when two sinusoidal tones, one low-frequency (= 5 Hz) and one higher-frequency (= 25 Hz), are sequentially injected to the inputs of the two AFEs. The amplitude spectrums of both systems present two spectral peaks at 5 and 25 Hz, which are characterized by the same amplitude. 145

Figure 4.10: A weak LFP signal is injected into the inputs of the Chebyshev notch channel and the DP-301 commercial differential amplifier (ADInstruments). (a) Comparison of the Chebyshev notch channel's output (red line – after removing the gain of 80 dB) with the DP-301 amplifier's output (blue line – after removing the gain of 80 dB) in the time domain. (b) The amplitude spectrum of the Chebyshev notch channel's output (red line) approximates the amplitude spectrum of the original LFP signal (pink line). (c) The LFP recordings acquired by the Chebyshev notch channel and the DP-301 amplifier approximate each other. This shows that the proposed AFE architecture is capable of recording weak LFP signals without introducing any phase distortion or ringing oscillations. (d) The proposed AFE architecture provides more accurate recording of the high frequencies (f>350 Hz) included in the original LFP signal in comparison to the DP-301 amplifier. 148

Figure 4.11: Time and frequency responses of the Chebyshev notch channel, in and without the presence of bipolar stimulation (140 Hz, 3 V peak, 100 μs). The test signal was a sinusoidal single tone with an amplitude of approximately 1 μV peak and a frequency of 15 Hz. (a) Time-domain recording without the presence of stimulation for a passband set from 0.5 to 140 Hz. (b) Time-domain recording in the presence of stimulation for a passband set from 0.5 to 140 Hz. (c) Time-domain recording without the presence of stimulation for a passband ranging from 0.5 to 250 Hz. (d) Time-domain recording in the presence of stimulation for a passband ranging from 0.5 to 250 Hz. (e) Amplitude spectrum of the signals presented in Figure 4.11a. (f) Amplitude spectrum of the signals presented in Figure 4.11b. (g) Amplitude spectrum of the signals presented in Figure 4.11c. (h) Amplitude spectrum of the signals presented in Figure 4.11d. 150

Figure 4.12: Temporal response and spectral profile of the Chebyshev (blue – corresponding to the left y-axis) and Bessel (red – corresponding to the right y-axis) notch channels, in and without the presence of bipolar and unipolar stimulation. (a) Time-domain LFP recording without the presence of bipolar stimulation for a passband of (0.5-140 Hz). (b) Time-domain LFP recording in the presence of bipolar stimulation for a passband of (0.5-140 Hz). (c) Time-domain LFP recording without the presence of bipolar stimulation for a passband of (0.5-250 Hz). (d) Time-domain LFP recording in the presence of bipolar stimulation for a passband of (0.5-250 Hz). (e) Amplitude spectrum of the signals presented in Figure 4.12a. (f) Amplitude spectrum of the signals presented in Figure 4.12b. (g) Amplitude spectrum of the signals presented in Figure 4.12c. (h) Amplitude spectrum of the signals presented in Figure 4.12d. (i) Time-domain LFP recording without the presence of unipolar stimulation for a passband of (0.5-140 Hz). (j) Time-domain LFP recording in the presence of unipolar stimulation for a passband of (0.5-140 Hz). (k) Time-domain LFP recording without the presence of unipolar stimulation for a passband of (0.5-250 Hz). (l) Time-domain LFP recording in the presence of unipolar stimulation for a passband of (0.5-250 Hz). (m) Amplitude spectrum of the signals presented in Figure 4.12i. (n) Amplitude spectrum of the signals presented in Figure 4.12j. (o) Amplitude spectrum of the signals presented in Figure 4.12k. (p) Amplitude spectrum of the signals presented in Figure 4.12l. 152

Figure 4.13: Detailed view of the time-domain LFP recordings taken from the Chebyshev (blue line corresponding to the left y-axis) and the Bessel (red line corresponding to the right y-axis) notch channels, with (solid line) and without (dash-dot line) unipolar stimulation. (a) The passband

of both channels is between 0.5 Hz and 140 Hz. (b) The passband of both channels is between 0.5 Hz and 250 Hz. 153

Figure 4.14: Detailed view of the time-domain LFP recordings taken from the Chebyshev (blue line corresponding to the left y-axis) and the Bessel (red line corresponding to the right y-axis) notch channels, with (solid line) and without (dash-dot line) bipolar stimulation. (a) The passband of both channels is between 0.5 Hz and 140 Hz. (b) The passband of both channels is between 0.5 Hz and 250 Hz. 153

Figure 4.15: Amplitude spectrum (recorded from the Chebyshev notch channel) of the 1) signals entering the negative (green) and positive (red) inputs of the front-end INA during stimulation, 2) the AFE output voltage during stimulation (black), and 3) the AFE output voltage without the presence of stimulation (pink). a) Unipolar stimulation setting, and b) Bipolar stimulation setting. INA, instrumentation amplifier; AFE, analog front-end. 155

Figure 4.16: Normalised RMSE values between the signals recorded in and without the presence of unipolar (a) and bipolar (b) stimulation. The green vectors show the main stimulation frequency component (=140 Hz) and the stimulation harmonic that is closer to the available passband (=280 Hz). The red lines (correspond to the right y-axis) show the available bandwidth (BW) for each recording trial and the blue lines (correspond to the left y-axis) depict the calculated RMSE values. RMSE, root mean square error; BW, bandwidth. 156

Figure 4.17: Experimental setup for evaluating the artefact suppression capabilities of the proposed Chebyshev AFE channel architecture *in vivo*. A deep brain stimulation electrode (electrode A, model DB-2201, Boston Scientific Neuromodulation) was implanted into the thalamus of an

anaesthetised non-human primate. The monophasic stimulation pulses (6 V peak-to-peak amplitude, 142 Hz frequency and 100 µs pulse width) were delivered by means of a commercial stimulator (Grass, Astromed, Inc., USA). Unipolar stimulation was applied to contact A2 and LFP signals were differentially recorded through contacts A1 and A3. The stimulation ground was introduced into the brain tissue through a second electrode (contact B1, model 401261, St. Jude Medical) that was placed over the frontal cortex. The stimulation ground was electrically isolated from the mains using a commercial isolator (SIU5 stimulus isolation point, Grass, Astromed, Inc., USA).The non-human primate was under anaesthesia with the head held in a primate stereotactic frame, which was connected to the ground of the recording system. The LFP signals recorded by the proposed AFE were digitized at a sampling frequency of 20 kSPS (samples per second) and depicted on a computer by the Powerlab data acquisition system (ADInstruments). AFE, analog front-end. 158

Figure 4.18: The proposed Chebyshev AFE architecture for artefact-free local field potential (LFP) recordings during unipolar deep brain stimulation (DBS) *in vivo*. LFP signals were recorded from the thalamus of an anaesthetised non-human primate in and without the presence of DBS with the experimental setup illustrated in Figure 4.17. (a) Bipolar (differential) LFP recordings without DBS. (b) Bipolar (differential) LFP recordings during DBS. (c) Detailed view of the LFP recordings acquired without DBS. (d) Detailed view of the LFP recordings acquired during DBS. (e) Amplitude spectrum of the LFP signal recorded without DBS. (f) Amplitude spectrum of: 1) the LFP signal recorded during DBS (blue line), and 2) the stimulation pulses presented at the positive (red line) and negative (black line) inputs of the front-end instrumentation amplifier. It

is clear that the proposed artefact suppression strategy (analog notch filtering at 140 Hz and digital low-pass filtering at 250 Hz) allows for artefact-free LFP recordings during DBS (observe the 142 Hz stimulation fundamental frequency, which has been strongly attenuated by the high-order notch filtering action). 159

Figure 5.1: Block diagram of a tunable analog notch filter that is implemented by cascading a tunable 2nd order low-pass filter and a tunable 2nd order high-pass filter. An analog amplification block is also added to ensure that the same gain is applied on the signals entering the two inputs of the instrumentation amplifier. LPF, low-pass filter; HPF, high-pass filter; MUX, multiplexer; INA, instrumentation amplifier..... 171

Figure 5.2: Block diagram showing the implementation of a tunable analog notch filter that is based on a single-operational amplifier 2nd order tunable band-pass filter. An analog amplification/signal inversion block is also added to ensure that the signals entering the two inputs of the instrumentation amplifier do not face any gain/phase mismatch. BPF, band-pass filter; MUX, multiplexer; INA, instrumentation amplifier..... 171

Figure 5.3: Block diagram of a tunable 2nd order (low- or high-pass) filter that is based on the Sallen-Key filter architecture. MUX, multiplexer; FFC, filter forming circuitry. 172

Figure 5.4: Block diagram of a tunable 2nd order (low-, high- or band-pass) filter that is based on the multiple feedback filter architecture. MUX, multiplexer; FFC, filter forming circuitry. 173

Figure 5.5: Measured system response of a tunable 2nd order low-pass filter that is based on the SK architecture and provides 4 different corner frequencies (50 Hz, 600 Hz, 1 kHz, 10 kHz). 174

Figure 5.6: Measured system response of a tunable 2nd order high-pass filter that is based on the SK architecture and provides 4 different corner frequencies (0.1 Hz, 10 Hz, 100 Hz, 1 kHz). 175

Figure 5.7: Measured system response of a tunable 2nd order band-pass filter that is formed by cascading the tunable low-pass and high-pass filter blocks presented in Figures 5.5 and 5.6, respectively. In order to assess the selectivity of the filter, four different system passbands were selected using the system multiplexers. 175

Figure 5.8: Measured system response of a tunable 2nd order notch filter that is based on the architecture shown in Figure 5.1. The passband of the band-pass filter block included in the notch filter architecture was tuned to be between 10 Hz and 50 Hz. Thus, this range of frequencies is anticipated to be cut by the notch filter. The centre frequency of the notch filter is equal to the centre frequency of the band-pass filter, which is fC = $fL \times fH$, where fL and fH are the low- and high- cut-off frequencies of the band-pass filter, respectively. By substituting the values of fL = 10 Hz and fH = 50 Hz, the theoretical centre frequency of the notch filter is found to be equal to 22.36 Hz. It is clear that the measured centre frequency (24 Hz) approximates the theoretical one (22.36 Hz), while the measured low- and high- cut-off frequencies are equal to 11 and 50 Hz, respectively. The observed overshoot stays within acceptable levels since it is lower than 1.5 dB. 176

Figure 5.9: Simulated system response of a tunable 2nd order MFB notch filter (solid red line), which is based on the architecture shown in Figure 5.2, and a fixed 2nd order Bainter notch filter (solid blue line). It is clear that the reponse of the MFB notch filter does not exhibit any undesired overshoot. 177

Figure 5.10: Block diagram of a high-order MFB notch filter. In this topology, the multiplexer included in every tunable BPF block shares the same control lines (A0, A1,…, Ap) with the multiplexer of the corresponding inverting amplifier. This approach ensures that the signals at the two paths culminating in the two inputs of the instrumentation amplifier are characterized by the same amplitude and phase. 177

Figure 5.11: Block diagram of the proposed artefact suppression strategy. MCU, microcontroller unit.....178

Figure 5.12: Block diagram of the proposed artefact suppression strategy where an RMS-to-DC converter block is used as a pulse amplitude estimator. MCU, microcontroller unit; INA, instrumentation amplifier. 179

Figure 5.13: Block diagram of an AFE architecture where the proposed artefact suppression block is placed at the first stage of the signal chain. DSP, digital signal processing; MCU, microcontroller unit; INA, instrumentation amplifier.....180

Figure 5.14: Block diagram of an AFE architecture where a front-end differential amplifier block is placed before the proposed artefact suppression block. DSP, digital signal processing; MCU, microcontroller unit; INA, instrumentation amplifier.....180

Figure 5.15: Detailed block diagram of the proposed artefact suppression strategy in the case where monophasic pulses have to be suppressed. Regarding the structure of the RMS-to-DC converter block, a gain stage is added before the RMS-to-DC converter to convert the RMS estimate into amplitude estimate and compensate for small errors that may exist in the estimation of the pulse RMS value given by the RMS-to-DC

converter. DSP, digital signal processing; MCU, microcontroller unit; INA, instrumentation amplifier.....182

Figure 5.16: Detailed block diagram of the proposed artefact suppression strategy in the case where monophasic pulses have to be suppressed. Regarding the structure of the RMS-to-DC converter block, a gain stage is added after the RMS-to-DC converter to convert the RMS estimate into amplitude estimate and compensate for small errors that may exist in the estimation of the pulse RMS value given by the RMS-to-DC converter. DSP, digital signal processing; MCU, microcontroller unit; INA, instrumentation amplifier.....182

Figure 5.17: Detailed block diagram of the proposed artefact suppression strategy in the case where biphasic pulses have to be suppressed. Regarding the structure of the RMS-to-DC converter block, an inverting stage is added in the signal path (after the RMS-to-DC converter, in parallel to the non-inverting stage) to reject the negative phase of the biphasic pulses. A gain is added in both inverting and non-inverting stages (the same gain value should be used in the case of balanced biphasic pulses, whereas different gain values should be used in the case of non-balanced biphasic pulses) to convert the RMS value returned by the RMS-to-DC converter into amplitude and compensate for small errors that may exist in the estimation of the pulse RMS value given by the RMS-to-DC converter. DSP, digital signal processing; MCU, microcontroller unit; INA, instrumentation amplifier.....184

Figure 5.18: Detailed block diagram of the proposed digital artefact suppression implementation. MCU, microcontroller unit. 185

Figure 5.19: Application of stimulation pulses (making use of a commercial waveform generator), which contain a sudden dc offset

voltage change, on the designed analog front-end implementing the proposed method. The aim was to examine the real-time capabilities of the proposed artefact suppression method. It is clear that a sudden change in the offset of the pulses does not affect the estimation returned by the RMS-to-DC converter. As a result, the system (after a short transient response) is able to continue providing reliable recording (please see "AFE output") of the biosignal of interest during stimulation. AFE, analog front-end. 186

Figure 5.20: Application of stimulation pulses (making use of a commercial waveform generator), which contain a sudden decrease in their amplitude (frequency and pulse width of the pulses are kept the same), on the designed analog front-end (AFE) implementing the proposed method. The aim was to examine the real-time capabilities of the proposed artefact suppression method. It is clear that a sudden change in the amplitude of the pulses is immediately detected by the RMS-to-DC converter and the new amplitude estimate is calculated (an analog gain stage which multiplies the RMS estimation with the crest factor of the monophasic pulses follows the RMS-to-DC converter in this experiment) and subtracted from the contaminated signal in the analog domain. As a result, the system (after a short transient response) is able to continue providing reliable recording (see "AFE output") of the biosignal of interest during stimulation. AFE, analog front-end. 187

Figure 5.21: Time-domain recording and amplitude spectrum of local field potentials recorded in a saline tank during voltage-mode DBS (monophasic pulses, amplitude 7 V_{pp}, frequency 140 Hz and pulse width 200 μsec). The stimulation artefacts (solid pink line), which pass through the front-end instrumentation amplifier (designed with a gain of 20 V/V), are characterized by an amplitude of approximately 30 mV_{pp} (after

removing the gain of 20 V/V). The application of the proposed method in combination with a real-time digital low-pass filter at 500 Hz (to remove weak switching voltage spikes) allows for the successful retrieval of the neural activity of interest. As shown in the amplitude spectrums, the stimulation harmonics are significantly attenuated at such an extent that allows the (time-domain) neural recording to be artefact-free. In addition, the spectrum of the signal recorded during stimulation contains both the peak in the beta frequency band (13-30 Hz) and the peak at 80 Hz, which correspond to physiological activity. As shown in the bottom graph, the contaminating 142 Hz harmonic and all the other harmonics within the passband are successfully suppressed by at least 37 dB. Finally, it is clear that the suppression of the stimulation pulses achieved by the proposed method also leads to the suppression of the strong 50 Hz harmonics. DBS, deep brain stimulation. 189

Figure 5.22: Time-domain recording and amplitude spectrum of cardiac signals recorded in a saline tank during current-mode stimulation (monophasic pulses, amplitude 15 mA, frequency 20 Hz and pulse width 10 msec). A comparison, in terms of signal quality, is drawn between the proposed method and the biosignal blanking during stimulation technique. In contrast to the biosignal blanking during stimulation technique, which eliminates information during the artefact, the proposed method successfully retrieves the signal of interest without corrupting it. 191

Abbreviations

ADC: Analog-to-digital converter

AF: Atrial fibrillation

AFE: Analog front-end

ALS: Amyotrophic lateral sclerosis

ASICs: Application-specific integrated circuits

BER: Bit error rate

BMIs: Brain-machine interfaces

CMRR: Common mode rejection ratio

CPU: Central processing unit

DAC: Digital-to-analog converter

DBS: Deep brain stimulation

DSP: Digital signal processing

DSSS: Direct sequence spread spectrum

ECG: Electrocardiographic

ECoG: Electrocorticographic

EEG: Electroencephalographic

EMG: Electromyographic

EMI: Electromagnetic interference

ERNA: Evoked resonant neural activity

FFC: Filter forming circuitry

FIR: Finite impulse response

FPGA: Field-programmable gate array

GP: Ganglionated plexi

GPe: Globus pallidus externa

GPi: Globus pallidus interna

GSM: Global system for mobile communications

HFS: High frequency stimulation

ICU: Intensive care unit

IMD: Intermodulation distortion

IMD_3: Third-order intermodulation distortion

INA: Instrumentation amplifier

IP_3: Third-order intercept point

IPG: Implantable pulse generator

ISM: Industrial, scientific and medical radio band

LAN: Local-area network

LFPs: Local field potentials

MCU: Microcontroller unit

MFB: Multiple feedback

MSK: Minimum Shift Keying (modulation scheme)

PC: Personal computer

PCB: Printed circuit board

PD: Parkinson's disease

PGA: Programmable gain amplifier

PV: Pulmonary vein

RMSE: Root mean square error

SK: Sallen-Key

SMA: Sub-miniature version A

SNR: Signal-to-noise ratio

SoC: System-on-chip

SPI: Serial peripheral interface

STN: Subthalamic nucleus

TBI: Traumatic brain injury

THD: Total harmonic distortion

Tx: Transmitter

USB: Universal serial bus

UWB: Ultra-wideband radio transmission scheme

VIM: Ventralis intermedius thalamus

VTA: Volume of tissue activated

Chapter 1. Introduction

1.1 Motivation

Clinical monitoring is an effective strategy that allows the clinicians to monitor disease progression, assess the effects of therapy and direct patient treatment towards more effective therapeutical strategies. Hence, research on monitoring systems, which are low-power and provide portability to the patient, is of paramount importance for a wide portion of people and not just the scientific community.

Furthermore, electrical stimulation of specific target brain regions, which is called deep brain stimulation (DBS), has been shown to alleviate symptoms of neurological disorders, such as Parkinson's disease (PD), essential tremor, dystonia, and epilepsy. However, current neuromodulation systems operate in an open-loop mode and thus they deliver continuous stimulation without sensing or interpreting a patient's state. In the absence of this sensing capability, the adjustment of stimulation parameters (amplitude, frequency and pulse width) is essentially performed through either direct observation and programming by a clinician or by limited patient intervention.

On the contrary, since a closed-loop system of neuromodulation uses sensors that detect and record various symptom-related biosignals, it can ensure that the electrode will provide a stimulus that adjusts to the momentary symptoms. This closed-loop strategy could reduce some side effects which occur in conventional DBS treatment, such as gait imbalance or speech impairment. In addition, it could improve longevity of the neurostimulator device.

It is clear that the closed-loop stimulation strategy requires continuous visibility into potentially useful neurological information derived from the electrodes. However, to our knowledge, existing recording systems lack the ability to provide artefact-free high-frequency (> 100 Hz) LFP recordings (in real time) during DBS in bidirectional setups where concurrent sensing and stimulation take place at the same site. This is mainly explained by the fact that the neural signals of interest are contaminated by the stimulation artefacts. This restricted access to high-quality biopotential recordings

during stimulation limits the observation of biomarkers that might be useful for therapy optimization. Moreover, there are no commercial, small, battery-powered, wearable and wireless recording-only instruments that claim the capability of recording ECoG signals, which are of particular importance in closed-loop DBS and epilepsy DBS.

All in all, continuous monitoring of bioelectrical signals using small-sized and ambulatory biopotential readout circuits might help address these unmet needs and create new clinical applications in the future. The ability to chronically sense, process and telemeter signals from the nervous system could lead to: a) improved monitoring of disease progression, b) increased therapy efficacy, c) a decrease in the burden required from the clinician and patient to optimize the therapy, and d) improved longevity of implantable biomedical devices.

1.2 Research objectives

This research focuses on the design of high-performance bioinstrumentation that can be used in a clinical setting to provide accurate and real-time biopotential measurements in bidirectional neural interfaces. Since the portability of medical devices is a very significant advantage that often relaxes the requirement for hospitalization of a patient, extra care was taken to enhance the wearable character and the wireless capabilities of the designed bioinstrumentation. Apart from the requirement for the design of small-sized recording devices, the research of this thesis is tackling a number of challenges associated with the problem of isolating the biosignal activity of interest from artefacts stemming from various noise sources (stimulation artefacts, inherent noise of the instrument, ambient noise from the clinical environment etc). These are listed below:

- Since biomarkers of various neurological disorders may exist in weak neural oscillations, previously hidden by the inherent noise of older biopotential acquisition systems, could it be possible to employ techniques that would enable portable/wearable instruments to reliably record nV-scale biosignals?

- Since observations during electrical stimulation could reveal novel neural activity patterns that are not present in neural tissue in the absence of stimulation, could it be possible to employ techniques that would enable portable/wearable instruments to reliably record weak neural activity during electrical stimulation?

1.3. Thesis Outline

This thesis is outlined as follows:

- **Chapter 2:** This chapter introduces the reader to the field of bioelectrical engineering, describes the origin and characteristics of the biopotential signals and highlights the pivotal contribution of bioelectrical signal monitoring towards the improvement of diagnosis and therapy of chronic diseases. Moreover, this chapter analyses the concept and merits of closed-loop neurostimulation and provides information about the advances in the field of neuromodulation. Furthermore, this introduction describes the challenges associated with the design of ambulatory biopotential readout circuits which are intended to record extremely weak biosignals from the human body in the presence of various noise sources (ambient noise, inherent noise of the apparatus used, artefacts stemming from the electrical stimulation of the neural tissue in bidirectional neural interfaces etc). Finally, this chapter elaborates on techniques that have been proposed so far for achieving artefact suppression in bidirectional neural interfaces and emphasizes the scope of this work.
- **Chapter 3:** This chapter introduces a low-noise (8 nV/√Hz), eight-channel, battery-powered, wearable and wireless multi-instrument (55 × 80 mm^2) which can be used as a portable/wearable recording-only device in the clinic or as a recording modality that provides a wide variety of clinical data to a closed-loop neurostimulation platform. Although it has been primarily designed for being used in bidirectional setups which provide spatial separation between sensing and stimulation sites, it can also precisely record LFP signals from the

stimulation site when no DBS is applied, and evoked resonant neural response, which appears 4 msec after the last DBS pulse. A number of *ex vivo* and *in vivo* experiments, which were conducted in order to assess the instrument's performance in terms of signal quality under different experimental conditions, are presented. Finally, this chapter summarizes the instrument's merits and presents possible avenues of research that could be further explored using this low-noise device.

- **Chapter 4:** This chapter introduces a high-performance (4 nV/√Hz) application specific analog front-end architecture (70 × 20 mm^2) that provides artefact-free LFP recordings in bidirectional setups where concurrent sensing and stimulation take place at the same site. A number of *in vitro* and *in vivo* experiments, which were conducted in order to assess the instrument's performance in terms of signal quality in and without the presence of DBS, are presented. Finally, this chapter summarizes the merits and limitations of the designed AFE architecture and exhibits possible avenues of research that could be explored using the proposed artefact suppression method.
- **Chapter 5:** This chapter presents a family of tunable hardware filter designs that could be used in bidirectional setups where simultaneous sensing and stimulation at the same site are required. In contrast to the artefact suppression approach presented in Chapter 4, which allows for the suppression of artefacts originating from a specific stimulation frequency, these novel filters can provide flexibility on the stimulation frequency that can be suppressed. Finally, a novel and versatile method for real-time artefact suppression that enables wide-bandwidth biosignal recordings during electrical stimulation is demonstrated.
- **Chapter 6:** This chapter presents the conclusions, contributions and achievements of this work and compares the three different artefact suppression strategies proposed in this thesis. In addition, this chapter elaborates on future work and the potential paths that could be followed in order to expand and get advantage of the accomplishments of this thesis.

Chapter 2. Introduction to bioelectrical signal acquisition and closed-loop deep brain stimulation

2.1 Clinical value of bioelectrical signals

Neuroelectrical activity in the brain generates oscillatory bioelectrical signals, occurring in multiple frequency bands, such as alpha (8–12 Hz), beta (13–30 Hz) and gamma (40–80 Hz) [1]. These oscillations result from the coordination or synchronization of neural activity and have been linked to a wide range of cognitive and perceptual processes [2]. However, they may also reflect abnormal function and present as key biomarkers of many serious neurological disorders, such as PD, epilepsy, traumatic brain injury (TBI), schizophrenia and autism [3]. Such biomarkers could enhance the accuracy of diagnosis of the disease state and facilitate the correct therapy. Hence, their identification is becoming more and more crucial.

Figure 2.1 lists the frequency bands where abnormal phase synchrony linked to serious neurological disorders exists, and the percentage of the population affected by each disease [1, 4, 5]. Significant biomarkers that reveal the onset of severe diseases can be extracted from bioelectrical signals (Table 2.1). In practice, a number of system limitations, such as the measurement electrode's spatial resolution, the spectral content of the bioelectrical signals of interest, and the power requirements for recording, processing, and wirelessly transmitting the desired information determine the choice of a specific measurement approach [6].

Recording of neurophysiological activity is an accepted medical strategy for applications ranging from seizure monitoring to neuroprosthesis [6]. Various techniques (Figure 2.2), each with a different set of tradeoffs in terms of invasiveness, spatial resolution and long-term quality and stability of chronic recording (Table 2.2), can be used to measure neuronal activity. Single-cell recording [6–9] provides high spatial resolution, but at the expense of challenging requirements for chronic electrode–tissue interface stability, the need for preprocessing of information prior to

its wireless transmission and increased amplifier power [6, 8–10]. Electroencephalography offers minimally invasive recording, but at the cost of limited spatial resolution, and the acquisition of weak signals, vulnerable to environmental noise and motion/muscle artefacts [6, 10].

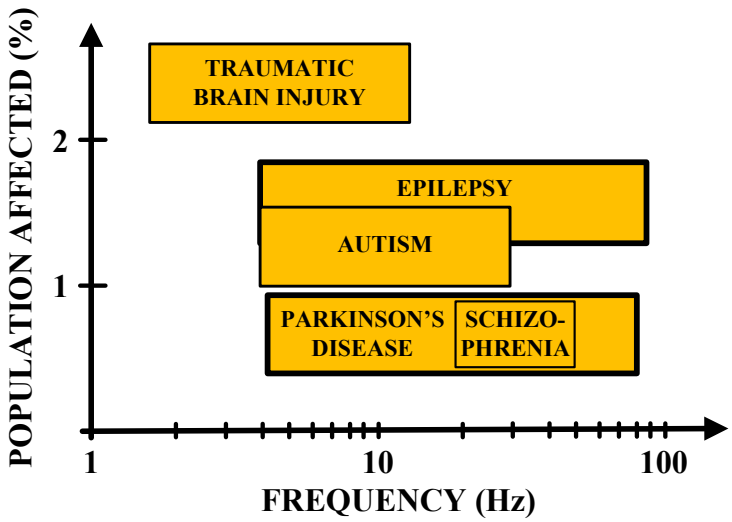

Figure 2.1: Frequency bands of abnormal phase synchrony characterizing serious neurological disorders [4, 5]. The last decade of LFP analysis also revealed that the power of ultra-weak, high-frequency oscillations detected in the 300 Hz (270 − 330 Hz) frequency band [18] also correlates with PD motor symptoms and clinical conditions. The aim of this Thesis is to provide ultra low-noise and wide-bandwidth biomedical instruments that are capable of accurately recording those weak, high-frequency oscillations.

In other invasive biopotential acquisition techniques, neural measurements are obtained, both on the surface of the cortex (electrocorticographic/ECoG signals) [11] and from a region around an implanted electrode (LFPs). The merit of these techniques is that they are less susceptible to chronic measurement issues compared to single-unit measurements, and can thus provide more robust measurement of biomarkers [6, 9, 10]. This is attributed to the fact that ECoG and LFP signals represent the ensemble activity of thousands to millions of neurons and thus their recording is significantly less susceptible to issues such as tissue encapsulation and micromotion encountered in single-cell recording [6, 9, 10, 12]. They are also less vulnerable to artefacts encountered in externalized surface EEG recording setups [6, 10].

Furthermore, ECoG and LFP signals encode biomarkers related to epileptic seizures [13] and the spectral decomposition of these signals can encode the necessary information for implementing an effective neuroprosthetic interface [10, 12, 13].

Table 2.1: Biosignal characteristics [14].

Signal	Bandwidth	Amplitude	Invasiveness
Spikes	100 Hz–10 kHz	50–500 μV	Invasive
LFP	0.5–200 Hz	10 μV–1 mV	Invasive
EEG	0.5–100 Hz	1–20 μV	Non-invasive
ECoG	0.5–200 Hz	5–100 μV	Moderately invasive
EMG	7–500 Hz	50 μV–2 mV	Minimally or non-invasive
ECG	0.5–40 Hz (monitoring)	0.1–5 mV	Non-invasive

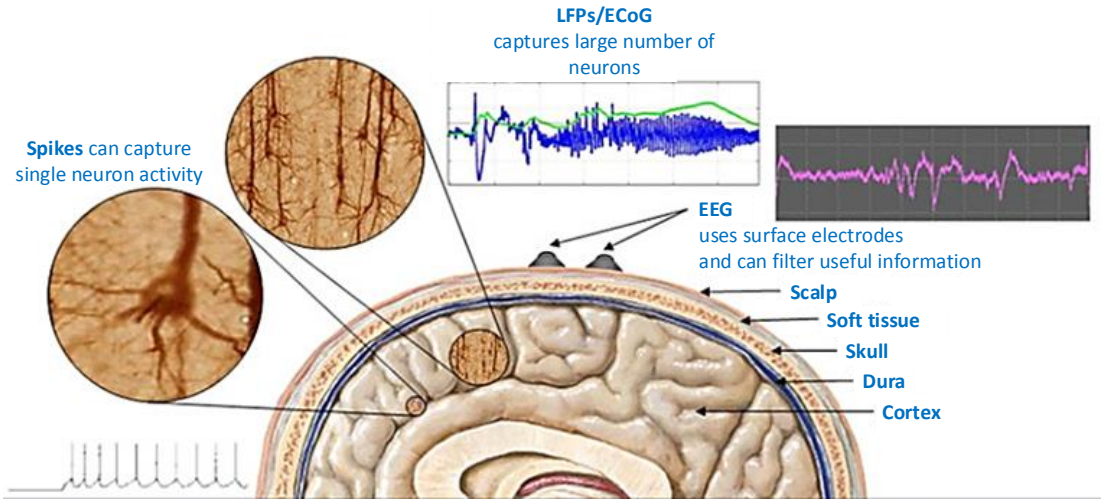

Figure 2.2: Recording sites of various neural sensing modalities. *Adapted from ref. [15].*

Increasing evidence suggests that the strength of LFP oscillations in the beta frequency band (13–30 Hz), which can be consistently picked up in the subthalamic nucleus (STN) of patients with PD, correlates with the severity of the disease and the

efficacy of therapy [16, 17]. However, the last decade of LFP analysis also focused on spectral power extraction from higher frequency bands, such as high gamma (60 − 80 Hz) and 300 Hz (270 − 330 Hz) [18]. The power of these oscillations also correlates with PD motor symptoms and clinical conditions, thus being eligible as a biomarker [19].

Table 2.2: Tradeoffs of different sensing modalities. *Reproduced from ref. [15].*

Sensing Methodology	Chronic Recording	Information Coding	System Power
Spike Recording	Challenging Interface Stability	High Fidelity, Need Ensemble Averages for Disease State	High Bandwidth/Power & Data Processing Req.
Field Potentials	Less sensitive to Interface Stability, Reuse Existing Technology	Medium Fidelity, Direct Relation to Disease State	Less Bandwidth/ Power & Data Processing Req.
Surface EEG	Irritation High Interference	Lower Fidelity, Less Spatial, Temporal & Spectral Resolution	External Power Source Can Be Used

Resonant neural response evoked by DBS, which is a rapidly expanding treatment for neurological and psychiatric diseases, is a large-amplitude neural signal that focally appears in the STN. This response is greatest in the dorsal region, which is the clinically optimal stimulation target for PD, coincides with improved clinical performance, is chronically recordable, and is present under general anesthesia [20]. These features render it as a readily utilizable electrophysiological signal and a target-specific biomarker that could potentially be used for guiding electrode implantation surgery and optimizing DBS therapy to improve patient outcomes [20].

Fasciculations, which are random muscle twitches that can be observed clinically, are associated with electrical events recorded by a needle electrode as fasciculation potentials [21]. A fasciculation potential represents the spontaneous discharge of a motor unit or part of it [21]. Although fasciculation potentials are seen in many conditions, such as peripheral neuropathy [22], radiculopathy [23] and peripheral

nerve hyper-excitability syndromes [24], they are of paramount importance in the diagnosis of motor neuron diseases [21]. In the benign fasciculation syndrome, fasciculation potentials occur predominantly, but not exclusively, in the distal leg muscles [21]. The exact origin of these fasciculation potentials is unknown [21].

Aside from recording neuronal electrophysiological signals, acquisition of non-neuronal biological signals is also of paramount importance, especially in closed-loop neurostimulation systems [25]. Taking into account the dopaminergic-related origins of PD and biochemical basis of other neuropsychiatric diseases, the concept of integrating real-time biochemical assessments could be useful for managing dynamic fluctuations in medication effects [25]. Other non-neuronal biosignals which indicate patient movement and clinical status in real-time are peripheral physiological signals recorded using electromyographic techniques and signals recorded by non-invasive accelerometers or gyroscopes [25]. It has been shown that EMG signals of patients with PD contain more tonic background activity and rhythmic burst activations than healthy controls [26]. Moreover, the signal morphology of EMG recorded from patients suffering from PD has been analyzed and it has been successfully used to differentiate patients with PD from healthy subjects [27]. Accelerometers attached to patients' wrists have been used for determining effective stimulation sites within the STN for treatment of tremor, bradykinesia and gait disturbance [28].

Furthermore, electrocardiography examines changes in cardiac electrical activity, e.g. rhythm disturbances, and is thus considered to be a crucial diagnostic modality [29, 30]. Finally, pulmonary veins (PV) play a major role in triggering atrial fibrillation (AF) in humans but the mechanisms underlying PV ectopy remain unclear [31]. In animal studies, direct application of acetylcholine to PV preparations shortens refractory periods and promotes stable, reentrant PV tachycardias [32]. Schauerte showed that it was possible to identify areas in the atria that were richly innervated with autonomic nerves, termed ganglionated plexi (GP), using high frequency stimulation (HFS) through an endovascular approach [33]. Ablation of these GPs abolished these effects [34–36]. Spontaneous PV ectopy, which is known to trigger clinical AF, may be reduced by adjunctive atrial autonomic ablation [31].

Taking into account that the identification of new biomarkers related to serious diseases is of paramount importance, bioelectrical signal monitoring is a crucial part of both medical diagnosis systems and implantable systems that provide a stimulus which adjusts to the momentary symptoms. Nowadays, these signals are recorded routinely in the clinic. However, patients have to cope with the problem of limited mobility because they are connected to bulky and mains-powered instruments. This prevents the continuous monitoring of patients, restricts the signal acquisition time and deteriorates the diagnostics of serious diseases. Hence, there is a growing demand for small-sized, low-power and ambulatory biosignal acquisition devices [37].

2.2 Biopotential electrodes

2.2.1 Introduction to biopotential electrodes

Although the input impedance of the biopotential acquisition circuits implemented in complementary metal oxide semiconductor (CMOS) technology is very high, a non-zero current should flow from the body to the input of the biopotential acquisition system [37]. In the human body, this current is carried by ions, whereas outside the body is carried by electrons on the wires that are connected to the readout circuit. Hence, the existence of a transducer interface between the body and the biopotential acquisition circuit is essential in order to convert the ionic current into electronic current, or vice versa. This transducer is called a biopotential electrode [37].

Biopotential electrodes can be split into the following two categories [37]:

- **Perfectly polarizable electrodes:** In the case of perfectly polarizable electrodes there is no actual charge transfer across the electrode-electrolyte interface. Of course, there has to be current across the interface, but this current is a displacement current, and the electrode behaves as a capacitor.

- **Perfectly non-polarizable electrodes:** In this case, the current passes freely across the electrode-electrolyte interface. Therefore, these electrodes behave as resistors.

In fact, neither of these two types can be fabricated. As a result, all practical electrodes are somewhere in between these two types [37].

2.2.2 Perfectly polarizable electrodes

Since charge cannot cross the perfectly polarizable electrode's interface when the potential across it is changed, the behavior of the electrode-solution interface is analogous to that of a capacitor. Since the materials of those electrodes are relatively inert, it is difficult for them to oxidize and dissolve. At a given potential, a charge q^M will exist on the metal electrode and a charge q^S in the solution. Equation $q^M = -q^S$ holds at all times. The potential across the interface and the composition of the solution determine whether the charge on the metal is negative or positive with respect to solution [38]. However, in an actual experiment, at least two electrodes and thus two interfaces must be considered.

The charge on the metal q^M represents an excess or deficiency of electrons and resides in an extremely thin layer (<0.1 Å) on the metal surface. The charge in solution q^S consists of an excess of either cations or anions that exist in the area surrounding the electrode surface [38]. The charges q^M and q^S are often expressed as charge densities (in $\mu C/cm^2$) by dividing their value by the electrode area:

$$\sigma^M = q^M/A \qquad (2.1)$$

The whole array of charged species and oriented dipoles that exist at the metal-solution interface is called the electrical double layer. At a given potential, the electrode-solution interface is characterized by a double-layer capacitance, C_d, which typically ranges from 10 to 40 $\mu F/cm^2$. However, unlike real capacitors, whose capacitance is independent of the voltage across them, C_d is often a function of potential [38].

The solution side of the double layer is considered to consist of several "layers". The inner layer, which is the closest to the electrode, contains solvent molecules and ions that are said to be specifically adsorbed. This inner layer (Figure 2.3) is called the compact, Helmholtz, or Stern layer [38]. The locus of the centres of the specifically adsorbed ions is called the inner Helmholtz plane (IHP), which is located at a distance d_1 from the electrode surface. The specifically adsorbed ions which are located in this plane are characterized by a total charge density σ^i ($\mu C/cm^2$).

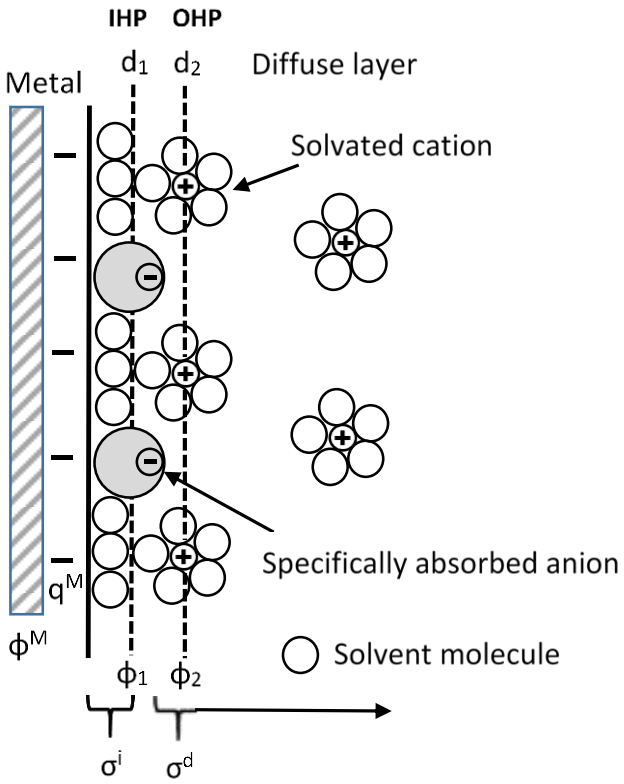

Figure 2.3: Double layer model when anions are specifically absorbed.

The locus of the centres of the solvated ions, which can approach the metal only to a distance d_2, constitutes the outer Helmholtz plane (OHP). The interaction of the solvated ions with the charged metal includes only long-range electrostatic forces, so that their interaction is independent of the chemical properties of the ions. These ions are called nonspecifically absorbed [38]. The thermal agitation in the solution urges the nonspecifically adsorbed to be distributed in a three-dimensional region, called the

diffuse layer, which extends from the OHP into the bulk of the solution. As the excess charge density in the diffuse layer is σ^d, the total excess charge density on the solution side of the double layer, σ^s, is provided by

$$\sigma^s = \sigma^i + \sigma^d = -\sigma^M \qquad (2.2)$$

Finally, the thickness of the diffuse layer, which depends on the total ionic concentration in the solution, is less than ~100 Å for ionic concentrations greater than 10^{-2} M [38].

2.2.3 Perfectly non-polarizable electrodes

When electrons are transferred across the metal-solution interface, oxidation or reduction processes occur. Since such reactions are governed by Faraday's law (i.e., the amount of chemical reaction caused by the flow of current is proportional to the amount of electricity passed), they are called faradaic processes. Electrodes at which faradaic processes take place are often called charge transfer electrodes [38].

In electrochemical cells, the electrode at which reductions occur is called cathode, whereas the electrode at which oxidations occur is called anode. A current in which electrons cross the interface from the electrode to a species in solution is a cathodic current, while electron flow from a solution species into the electrode is an anodic current.

Information about an electrode reaction is often gained by determining current as a function of potential (by extracting i-E curves). Certain terms are sometimes associated with features of the curves [38]. If a cell has a defined equilibrium potential, that potential is a significant reference point of the system. The departure of the electrode potential (or cell potential) from the equilibrium value upon passage of faradaic current is called polarization. It is important to emphasize here that an ideal non-polarizable electrode (or ideal depolarized electrode) is an electrode whose potential does not change upon passage of current. In other words, it is an electrode of fixed potential.

The silver/silver chloride (Ag/AgCl) electrode is a practical electrode that approaches the behaviour of a perfectly non-polarizable electrode. Regarding the structure of this electrode, a silver metal base with attached insulated lead wire is coated with a layer of the ionic compound AgCl [39]. The half-cell potential of this electrode is quite stable when it is placed in an electrolyte containing Cl^- as the principal anion, given that the activity of the Cl^- remains stable. Since this is the case in the human body, the Ag/AgCl electrode is relatively stable in biological applications [39].

2.2.4 Equivalent circuit model of a biopotential electrode

Figure 2.4 exhibits the equivalent circuit of a biopotential electrode. In this schematic, C_A and R_A represent the impedance of the electrode-electrolyte interface and R_s is the resistance of the electrolyte solution. The voltage source V_{hc} represents the half-cell potential of the interface [37].

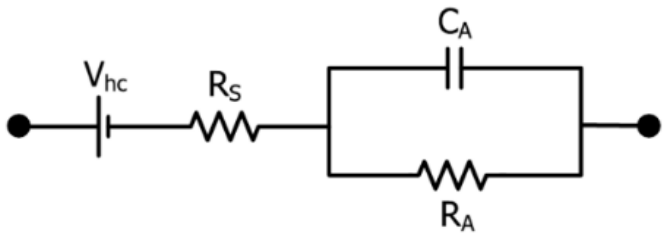

Figure 2.4: Equivalent circuit model of a biopotential electrode. *Adapted from ref.* [37].

Electrodes made of noble metals, such as platinum, approach the behaviour of perfectly polarizable electrodes and thus their characteristics show a strong capacitive effect [39]. In conventional electrodes, the electrolyte represents the gel that is placed in between the tissue and the electrode. However, since the biosignals are mainly extracted differentially from two electrodes, a mismatch is always observed between the half-cell potentials that is attributed to the difference in the gel-tissue interface [37]. This is explained by the fact that different epidermis and sweat glands affect the half-cell potentials of the two electrodes [37].

Similarly, in applications where differential biosignal recording from implantable biopotential electrodes is required, an electrode/tissue impedance mismatch is

observed, which is hard to control within a biological environment [16]. The aforementioned mismatch gives rise to a dc potential between the two electrodes which is much larger (in mV scale) than the μV level biopotential signals. This dc potential will be referred as differential dc electrode offset voltage in the rest of this thesis. It is thus clear that the biopotential acquisition systems should exhibit high-pass filter characteristics in order to prevent the saturation of their front-end electronics.

2.2.5 Types of biopotential electrodes for ExG signal acquisition

Biopotential electrodes for ExG signal acquisition can be separated into the following three categories [37]:

- **Wet electrodes:** In this type of electrodes a gel-type electrolyte is used between the electrode and the surface of the skin. The most widely used type of wet electrode is the Ag/AgCl electrode which approaches the behaviour of a perfectly non-polarizable electrode. The metal electrode material is silver (Ag), which is coated with an AgCl layer. The electrical contact between the electrode and the skin is established by using an electrolyte gel. The low impedance and the low production of artefacts constitute the most significant merits of Ag/AgCl electrodes. On the contrary, the necessity of using a gel in the measurement setup increases the preparation time of the whole biosignal acquisition procedure [37].
- **Dry electrodes:** In this type of electrodes there is no need for any kind of gel to make contact between the electrode and the body. Hence, the preparation time diminishes in this case. However, since there is no electrolyte in the measurement setup, their behaviour approaches that of a perfectly polarizable electrode which can be represented as a leaky capacitor. In order to tackle this problem, the biopotential acquisition system has to provide very high input impedance (>> 1GΩ). Due to this extremely high impedance, the circuit must be placed very close to the electrode in order to prevent the electromagnetic interference [37]. This can be accomplished by making use of active electrodes

[40]. However, these electrodes require matched components to achieve high common mode rejection ration (CMRR), which is difficult to be achieved in CMOS process. Alternatively, MEMS processing technology has introduced dry electrodes with micromachined spikes [41]. These spikes are able to penetrate the stratum corneum of the skin and bring the electrode directly in contact with the electrically conductive epidermis.

- **Non-contact electrodes:** These electrodes can be viewed as a pure capacitor between the human body and the biosignal acquisition electronics. Thus, they permit remote sensing of the bioelectric potential signals. They are biocompatible and per se safe because no DC current is drawn from the body. However, they require a readout circuit with an extremely high input impedance. Besides that, they are very sensitive to artefacts that are produced by motions of the electrode with respect to the body due to the change of capacitance [37].

2.3 Analog front-end design for biopotential acquisition

2.3.1 Introduction to biopotential recording systems

Biopotential recording systems have to face various problems while extracting the biopotential signals from the human body. These problems are associated to the noisy environment, the device used for the signal recording and the extremely low amplitudes that characterize this type of signals. Before diving deeper into the challenges and their causes, it would be useful to present the general structure that characterize this type of circuits.

A generic biopotential recording system is illustrated in Figure 2.5. A crucial and power consuming building block is the AFE, which defines the quality of the extracted signals [37]. Its role is to amplify weak bioelectrical signals and then condition (incorporating band-pass characteristics) and digitize them using an analog-to-digital converter

(ADC). After the AFE, digital signal processing (DSP) building blocks usually follow. The final part is the transmitter (TX), which sends the recorded information wirelessly to a personal computer (PC) [14].

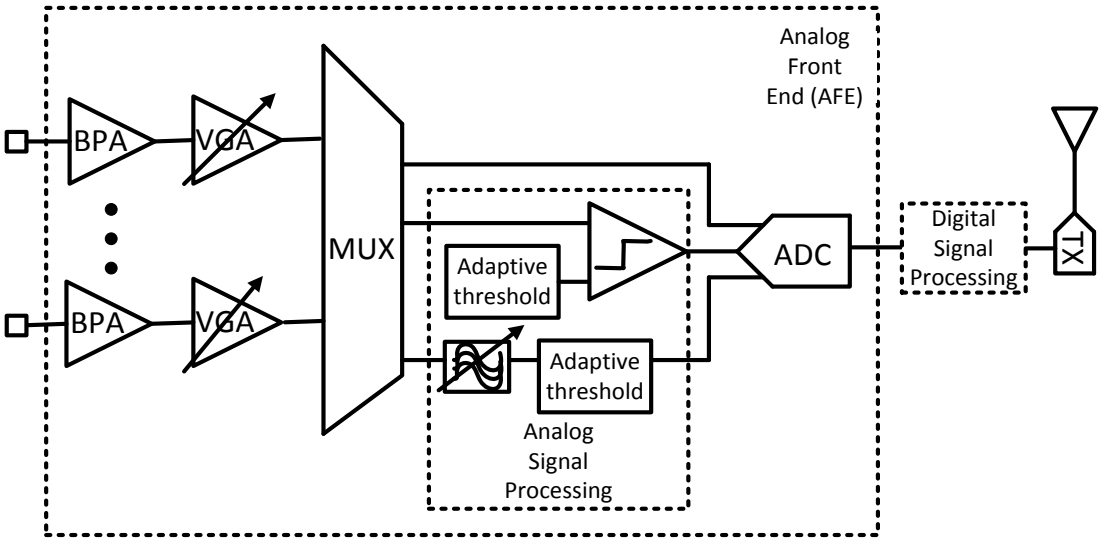

Figure 2.5: Block diagram describing a generic biopotential recording system. BPA, amplifier with band-pass characteristics; VGA, variable gain amplifier; MUX, multiplexer; ADC, analog-to-digital converter; TX, transmitter. *Adapted from ref.* [42].

Analog multiplexing could theoretically reduce the number of front-end amplifiers. However, analog multiplexing requires switching times much shorter than the time constants associated with the amplifier in order to capture details of constantly changing neural activity across multiple channels [14]. Therefore, typical multi-channel systems use one separate low-noise amplifier per channel [14]. This design decision ensures high signal quality but severely restricts the available power for each amplifier. This is the reason why specific circuit techniques have been developed to reduce power consumption of a biopotential amplifier.

Referring to Figure 2.5, one possible implementation of a biopotential acquisition system would be to fully digitize the signals and then wirelessly transmit them to an external computer for processing (thus skipping the analog and DSP blocks shown in Figure 2.5). In this way, the raw data are directly available. Furthermore, this strategy benefits from the flexibility and processing power of general-purpose computers.

Circuits based on this design usually have several channels multiplexed to share an ADC. This channel multiplexing approach can reduce the area required for ADCs, but: a) it is not efficient in circuits that contain a large number of channels, and b) it increases power dissipation because additional buffering is required [14].

A second strategy would be to acquire the signals and digitally process them locally [14]. In this case, the analog signal processing block presented in Figure 2.5 is skipped. A local central processing unit (CPU) or DSP unit could be used to extract features, perform classification and implement a specific strategy (e.g. a certain stimulation policy in DBS). It could also detect action potentials (or spikes), perform spike sorting and record the time and channel for each spike that it detects. The resulting data (e.g. spike descriptors, spectral estimation etc.) can be transmitted wirelessly to an external computer. A methodology of this type requires the same area of digitization and power as the first methodology [14]. However, it does not send full waveforms, thus it decreases the demands on the wireless transmitter. The drawback is that substantial local processing power is required.

Another approach would be to do the processing locally using dedicated analog circuits. Similarly to the approach that applies DSP locally, the burden on the communication link is relatively light because only a few data (e.g. spike descriptors, spectral estimation etc.) are transmitted [14]. Unlike either of the other two architectures, there is no need for a continuously-running ADC since the clinical information is extracted and processed in the analog domain (in the analog signal processing block shown in Figure 2.5). In fact, the ADC could be omitted entirely, although it may be desirable to include one in the system design in order to occasionally send some raw waveforms for verification purposes [14].

2.3.2 Challenges in the design of the front-end electronics

2.3.2.1 Interference theory

Interference from the mains is a common disturbance for biopotential acquisition systems. The two main types of interference are the electromagnetic and the

electrostatic interference [37]. In the former case, the alternating mains current creates a magnetic field which cuts the loop enclosed by the human body, the leads of the circuit and the biopotential amplifier. This produces an electromotive force, which gives rise to an AC potential at the input of the circuit [37]. One way to reduce electromagnetic interference is to twist the cables in order to decrease the area of the loop. Another way would be to place miniaturized portable bio-signal recording devices much closer to the electrodes in order to reduce the cable length [37].

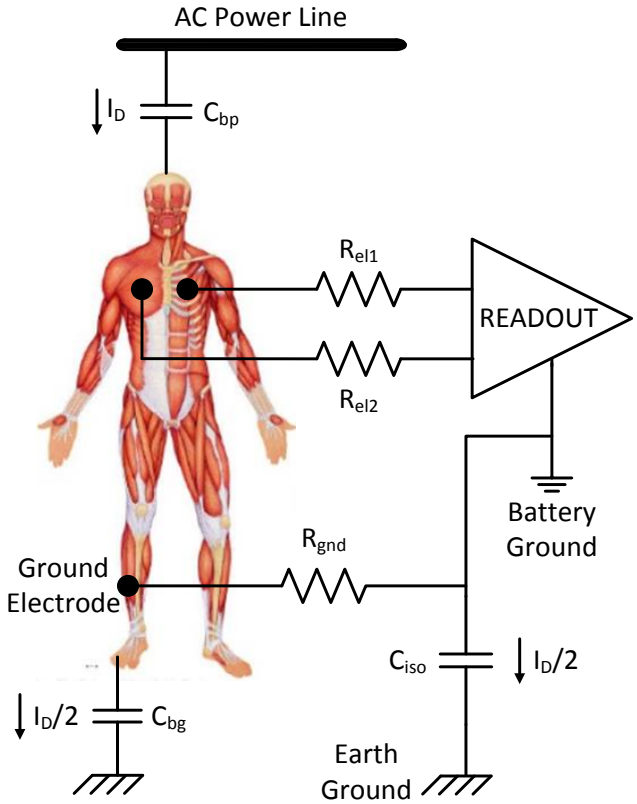

Figure 2.6: Electrostatic interference to the human body. *Adapted from ref.* [37].

Electrostatic interference can be better understood from the equivalent circuit of Figure 2.6. The human body is capacitively coupled to the mains via C_{bp} and to the ground via C_{bg}. Except for these two capacitances, there is also an isolation capacitance C_{iso} between the earth and the ground of the amplifier battery. Therefore, a displacement

current I_D is created by the path through the coupling capacitors. This current is split equally between the C_{bg} and C_{iso} ($C_{bg} \approx C_{iso}$ and R_{gnd} is much smaller than the impedance of C_{bg} and C_{iso} at 50/60 Hz) [37].

Thus, an AC voltage with the following magnitude appears on the human body [37]:

$$V_{CM} = \left(\frac{I_D}{2}\right) R_{gnd} \qquad (2.3)$$

If there is no mismatch between R_{el1} and R_{el2}, this AC voltage appears as a common-mode input to the amplifier and can be rejected by the amplifiers that are characterized by high CMRR. However, as there is always a mismatch between the electrode impedances, a differential error signal is created which has the following amplitude [37]:

$$\Delta V_{IN} = \left(\frac{|R_{el1} - R_{el2}|}{Z_{in}}\right) V_{CM} \qquad (2.4)$$

where Z_{in} is the input impedance of the amplifier. From equation (2.3) it is clear that except for CMRR, the instrumentation amplifier (INA) should also exhibit high input impedance in order to completely reject electrostatic interference.

2.3.2.2 Spectral location of the noise/interference sources

The design of a robust biopotential readout AFE circuit requires careful consideration of all the challenges and limitations that characterize this type of circuits. First and foremost, the low frequency behaviour of the biosignals makes the in-band noise of the AFE to be dominated by flicker (1/f) noise. Another noise source that designers of biomedical devices have to take into account when designing low-noise AFEs is the electromagnetic (EMI) interference stemming from the noisy clinical environment. Furthermore, the common-mode interference from the mains to the human body also contaminates the signals. The DC electrode offset that is generated at the skin-electrode interface must also be taken into consideration. The bandwidth of most of the above-mentioned contaminating signals along with the frequency range of various biosignals (EEG, EMG, ECG) are shown in Figure 2.7 [43].

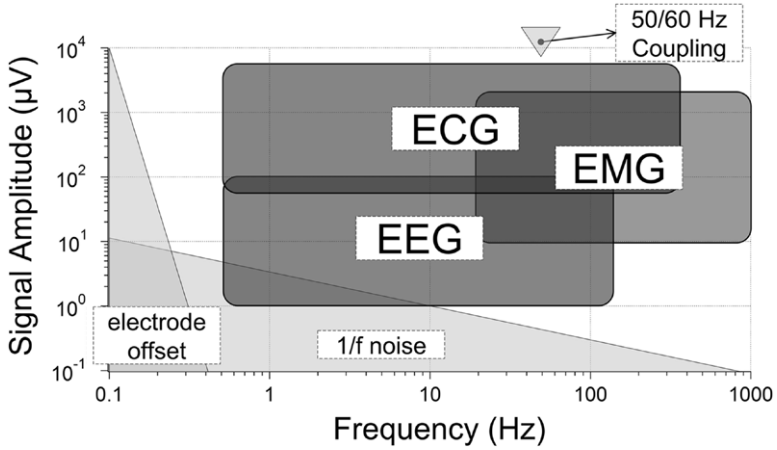

Figure 2.7: Amplitude and frequency characteristics of ExG (EEG, ECG, and EMG) signals and contaminating signals. *Reproduced from ref.* [43] © *2007 IEEE.*

2.4 Deep brain stimulation

2.4.1 Introduction to deep brain stimulation

Deep brain stimulation is an effective treatment for common movement disorders and has been used to modulate neural activity through delivery of electrical stimulation to key brain regions [44]. The long-term efficacy of this approach in treating PD and essential tremor has encouraged its application to a wide range of neurological and psychiatric disorders (Table 2.3). Empirically chosen stimulation parameters (e.g. 130–180 Hz stimulation frequency, 60–200 μs pulse width, and 1–3.5 V stimulation pulse amplitude) induce similar clinical outcomes to those observed with surgical ablation [44, 45]. Some of the important merits of high-frequency DBS are [44]: a) the long-term efficacy it achieves when applied to key brain structures, b) its reversible nature, and c) the offered prospect of reducing the amount of drugs administered to patients with PD. All these advantages have helped adoption of this electroceutical treatment, which can reduce symptoms by an average of ~40% 3–4 years after surgery [46]. However, even in PD, as few as 2% of patients undergo DBS [47], potentially reflecting the invasive nature of this treatment, the high cost and limited access to, or fear of, surgery [44].

Table 2.3: List of established and experimental DBS targets. *Adapted from ref.* [44].

Disorder	Target brain region	DBS approach
Parkinson's Disease	Subthalamic nucleus Globus pallidus (internal) Ventrolateral thalamus Pedunculopontine nucleus	Continuous high-frequency stimulation Closed-loop DBS
Essential tremor	Ventrolateral thalamus	Continuous high-frequency stimulation Closed-loop DBS
Dystonia	Globus pallidus (internal)	Continuous high-frequency stimulation
Epilepsy	Centromedian thalamus Anterior thalamic nucleus Seizure foci	Intermittent 20-Hz stimulation High-frequency stimulation (continuous or cyclic mode)
Pain	Spinal cord Periventricular or periaqueductal gray matter Sensory thalamus Internal capsule	Continuous low- or high-frequency stimulation Closed-loop stimulation
Obsessive compulsive disorder	Subthalamic nucleus Nucleus accumbens Anterior limb of the internal capsule Ventral capsule or ventral striatum Inferior thalamic peduncle	Continuous high-frequency stimulation
Major depression	Subcallosal cingulate Ventral capsule or ventral striatum	Continuous high-frequency stimulation
Tourette syndrome	Globus pallidus (internal) Centromedian–parafascicular	Continuous high-frequency stimulation Closed-loop DBS
Alzheimer's disease	Fornix	Continuous high-frequency stimulation

The current consensus in respect to the mechanism of DBS is that high-frequency DBS modulates neural activity (Figure 2.8) at key brain regions to restore function [44]. For oscillopathies, such as PD, essential tremor and dystonia, where the severity of patients' symptoms is correlated with excessive rhythmic neural activity at the DBS target structure and projection targets, high-frequency electrical stimulation has been proven to suppress rhythmic neural activity and simultaneously alleviate patients' symptoms [44]. A similar mechanism has been recently observed during stimulation of the anterior nucleus of the thalamus for the treatment of refractory focal seizures: stimulation led to the desynchronization of downstream hippocampal activity only when it was applied at high frequencies [48].

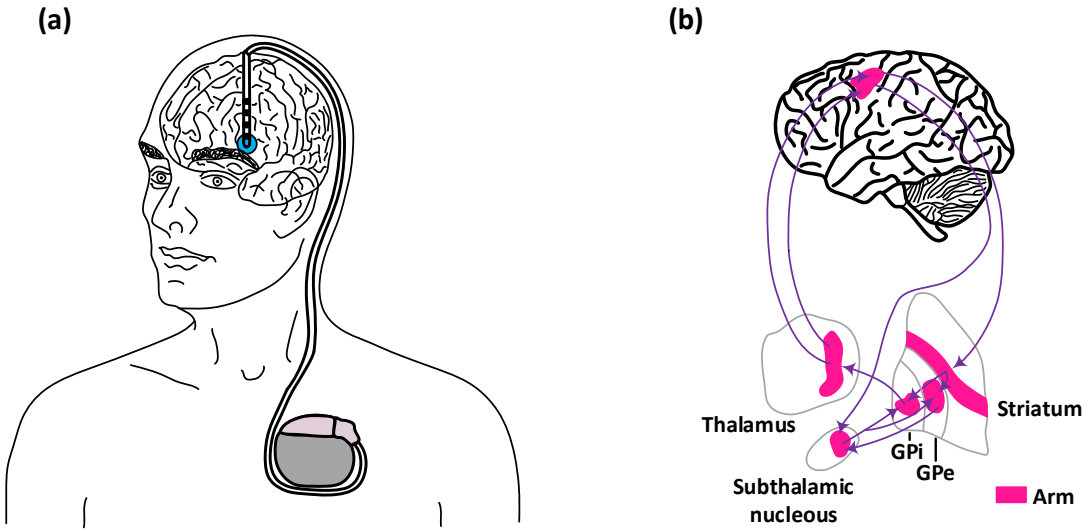

Figure 2.8: (a) The electrodes and pulse generators are permanently implanted, self-contained systems. Electrodes can be implanted in one or both hemispheres of the brain, depending on the laterality of the symptoms. The pulse generator implanted in the chest is connected to the electrodes implanted in the brain. (b) Basal ganglia and cortex are structures that are coupled into loops. Hence, wide-scale network modulation of the basal ganglia and cortex is enabled by DBS. Many overlapping loops exist, however only a loop controlling the arm is presented here for illustrative purposes. GPe, globus pallidus externa; GPi, globus pallidus interna. *Adapted from ref.* [44].

This stimulation mechanism, which accomplished an increased stimulation efficacy, has been associated to a suppression of epileptic activity [44]. In addition, new evidence suggests that oscillatory activity may also play a significant role in psychiatric

disorders, such as obsessive-compulsive disorder and Tourette's syndrome [44]. However, DBS does not exclusively overwrite pathological oscillatory activities; it may also overwrite abnormal, arrhythmic circuit motifs underlying symptoms.

2.4.2 Deep brain stimulation electrodes

Deep brain stimulation procedures consist of implanting DBS electrodes in specific brain regions (e.g. subthalamic nucleus – STN, globus pallidus interna – GPi), where electrical current is delivered to treat disease-specific motor symptoms in patients with PD. The anatomical convergence of information into small strategic regions allows influencing entire systems by DBS of spatially very circumscribed areas. The spatial selectivity of DBS is of upmost importance for the clinical result; first to optimally reach the target area with the therapeutic stimulation, and second to avoid unwanted stimulation of neighbouring structures resulting in adverse effects.

The most commonly used DBS electrode is a quadripolar electrode with 4 circular contacts along its length, therefore 4 levels with one contact per level (model MDT 3389 in Figure 2.9). Postoperatively all these contacts have to be tested manually to first identify the contacts that are best located in the target. Next, the best configuration for symptom relieve must be identified among the myriad of possible different stimulation parameters. The choice of the best located stimulation contacts is the pivotal first step of DBS programming in every individual patient. This manual screening procedure is very time consuming for medical staff, fatiguing for the patient and results are often suboptimal. Consequently, this procedure has to be repeated several times until the best contact configuration of stimulation has been identified. Moreover, in many patients this best stimulation setting is never attained due to lack of expertise or availability of a clinical expert [49, 50].

Since November 2015 new directional DBS electrodes have been implemented in clinical practice (Figure 2.9). Segmented electrodes allow for greater control over the volume of tissue activated (VTA) through independent control of electrode contacts and field steering [44]. Current commercial variants (e.g. the Boston Scientific DB-

2201 lead, denoted as “BSN” at the top panel of Figure 2.9, which is the electrode used to record LFPs in this thesis) accomplish directionality by replacing the middle two cylindrical contacts of traditional quadripolar electrodes with three segmented electrodes, thus increasing the total number of programmable contacts from four to eight and allowing three radial directions of stimulation separated by 120 degrees.

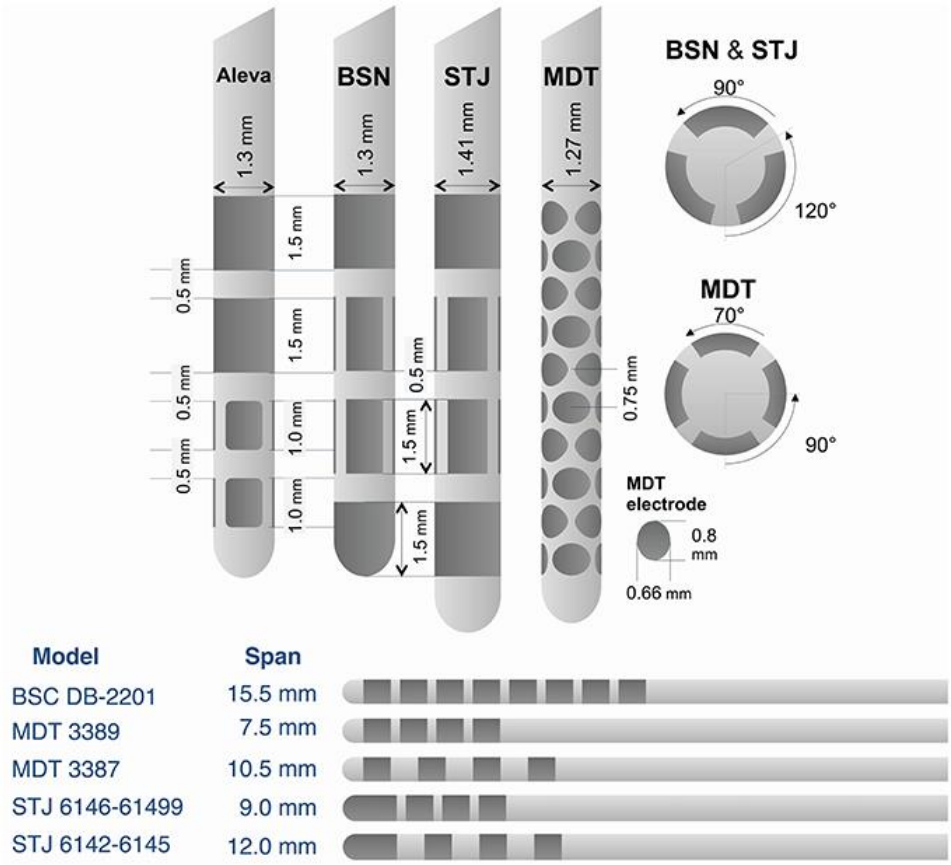

Figure 2.9: Comparison of emerging DBS electrode lead technology. BSN, Boston Scientific Neuromodulation; STJ, St. Jude Medical; MDT, Medtronic. *Adapted from ref.* [51].

The advantage of this directional electrode is the possibility of shaping the stimulation field to the direction within the target that provides the best clinical effect and to leave out the directions that may induce stimulation-related side effects (Figure 2.10). This new segmented lead presents a considerable advantage because the target structures of DBS are not necessarily spherical and the implanted electrode may not

be perfectly in the middle of the structure to be stimulated (Figure 2.10). These segmented electrodes enable clinicians to modify side-effect thresholds and provide a greater margin (known as therapeutic window) between symptom suppression and side-effect induction [44].

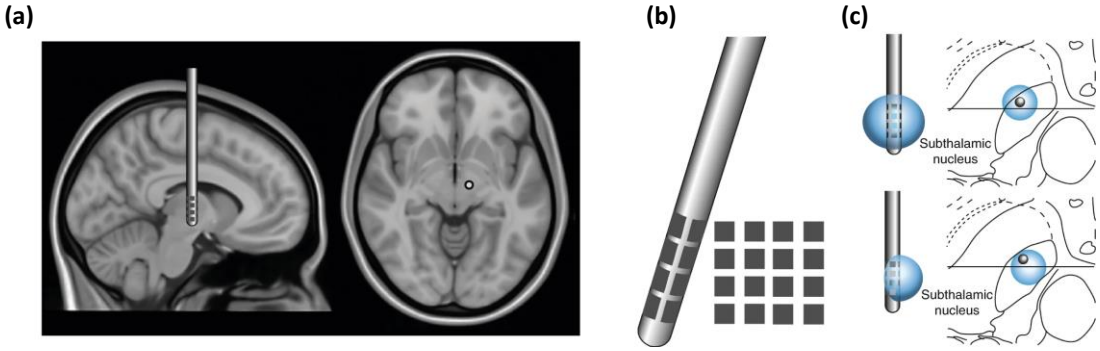

Figure 2.10: (a) Magnetic resonance imaging scan showing a DBS electrode that targets the subthalamic nucleus. Perioperative imaging is necessary and intraoperative imaging desirable in the accurate placement of electrodes. (b) Prototype research electrodes have been fabricated with higher densities of smaller contacts. (c) These have been designed with the intention of offering finer control of the electric field (blue volume). The top panel depicts the spherical field predominating when a complete ring of contacts is activated to mimic the field generated by conventional DBS (where 4-contact DBS leads are typically used). On the right, the electrode and electric field are superimposed on a brain atlas. In conventional DBS, the electrode is in the target, which is the subthalamic nucleus, but the electric field extends outside of this, risking side effects. On the contrary, as the lower panel shows, when a subset of contacts of a segmented DBS electrode is simultaneously activated, a different shaping of the electrical field can be achieved. In this case, the field is limited to the subthalamic nucleus. *Adapted from ref.* [44].

Another lead (Medtronic-Sapiens, denoted as “MDT” at the top panel of Figure 2.9) possesses an advanced multiplexer unit that supports a total of 40 electrodes and a span of 7.41 mm. With 10 rows of 4 electrodes per row, and alternating rows offset by 45 degrees, 8 radial electrode directions are available. Stimulation can be further shaped by selecting a wide range of combinations of active electrodes and splitting the current between them [51]. Furthermore, since recording of LFPs is possible from each of the 40 electrodes, spatiotemporal information on pathologic neuronal activity could potentially be offered. Preliminary intraoperative testing of this lead suggests that it may be possible to make use of intraoperative LFP recordings to assess the

effect of stimulation in different electrode combinations and current settings on pathological subthalamic neural activity [51]. This field shaping capability may possibly avoid stimulation of unwanted regions and support engagement of target areas [51].

Another recently tested lead (Aleva – Figure 2.9) possesses eight electrodes and a span of 5.5 mm. Out of four rings, two are the traditional ring electrodes and the remaining two are divided into three segments each, allowing for directional current delivery through each segment. Clinical data suggest that this directional lead, when tested in either the STN or the ventralis intermedius (VIM) thalamus, can enlarge the window between therapeutic effect and adverse effects, and may possibly make use of less current to accomplish the same therapeutic benefits [51].

2.4.3 Biomarkers for closing the loop

Implantable devices for electrical stimulation of the brain have been in routine clinical use since 1997, when the first commercial DBS system was approved for the treatment of tremor [25]. The fundamental feature of these devices is that they function in an “open-loop” mode, which means that they provide a unidirectional signal, generated from the device and delivered to the brain. This signal is an invariant train of stimulatory pulses at a fixed frequency.

However, open-loop DBS operates without sensing or interpreting a patient’s state and thus cannot determine when and how the disease is affecting the patient. In the absence of embedded sensing and titration algorithms, the sensing process is essentially performed through either direct observation and programming by a clinician or by limited patient intervention [15] and the stimulation is provided in a continuous mode. However, the symptoms of PD are not constant [52]. As a result, the researchers argue that constantly stimulating the brain with the same signal is not the most efficient treatment.

On the contrary, a closed-loop operation of the neurostimulator device can ensure that the electrode will provide a stimulus that adjusts to the momentary symptoms. This closed-loop strategy could reduce some side effects [53] which occur in conventional

DBS treatment, such as gait imbalance or speech impairment. Finally, it could improve longevity of the neurostimulator device [53].

Pathological neural activity and peripheral signals are some of the biosignals that have been used so far in order to extract useful biomarkers for neurological disorders [44]. Biomarkers do not have to be directly related to disease mechanisms, but should correlate with the severity of disease symptoms and track the response to therapeutic strategies. The relevant signals may be relatively unprocessed or subject to a number of processing stages to extract the information of interest, with or without the application of machine learning approaches [44]. Processing typically involves spectral analysis, thus allowing for focusing on a particular pathological oscillation. However, in future implementations, control is more likely to involve combinations of spectral and other features, some with different temporal resolutions, such as phase – amplitude coupling and coherence between brain sites [44].

Specific signal features, such as neural activity in the beta or gamma frequency bands, have been used so far in applications of closed-loop DBS to control stimulation timing for a range of movement disorders [44]. However, since the exact mapping between neural activity and symptom severity remains unknown for most neuropsychiatric disorders, the employment of alternative methodologies is required. Subthalamic LFPs from patients with PD have been successfully used to determine the amount of muscular force exerted, while features extracted from thalamic LFPs have been used to decode onset of tremor in a group of patients with essential tremor [44]. Fast Fourier transforms and wavelet transforms could be used to enrich the feature space by examining different frequency bands obtained from electrophysiological recordings. However, processing cost of decoding algorithms and power consumption should be taken into consideration to ensure real-time implementation of such strategies.

Regarding the closed-loop stimulation control strategies implemented so far, two types of neural control signal have been used to determine the timing and intensity of stimulation. First, the instantaneous power of rhythmic neural activity in the beta band (~20 Hz) can be tracked in LFP recordings at the site of stimulation [44]. This strategy

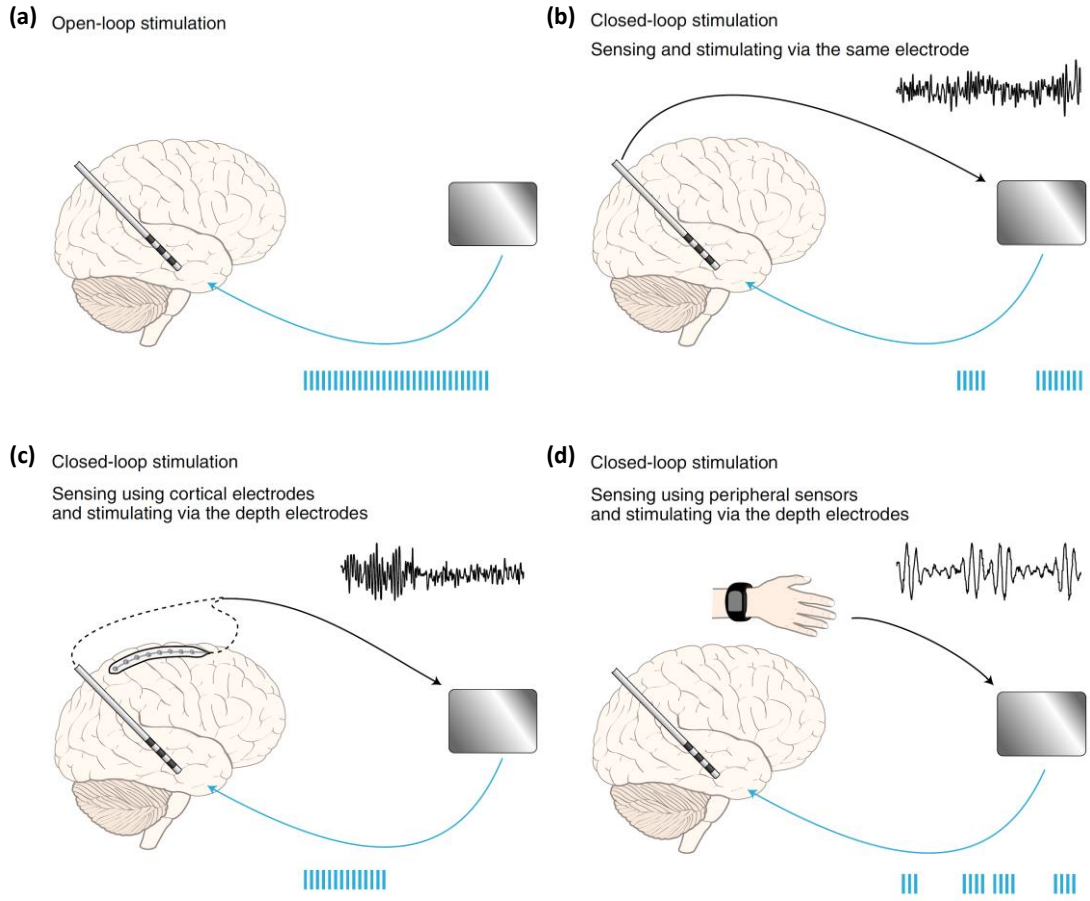

Figure 2.11: Comparison of different stimulation strategies. (a) Stimulation timing and parameters are fine-tuned by a clinician during follow-up visits (usually twice a year). No automatic adjustment of stimulation parameters, guided by a disease biomarker, exists in this case. (b) LFPs are continuously recorded (using depth electrodes) and used to automatically adjust stimulation timing or intensity. Stimulation is delivered via the same depth electrodes. (c) Cortical signals are continuously recorded (using an electrocorticography array) and used to automatically adjust stimulation timing or intensity. Since stimulation is delivered across the depth electrodes, a spatial separation between sensing and stimulation sites is created. (d) Peripheral signals, such as electromyographic and/or acceleration signals, obtained from noninvasive measurement devices (e.g. accelerometers and wearable EMG recording systems), are used to automatically adjust stimulation timing or intensity. As in c, a separation between sensing and stimulation sites exists, which minimizes the effect of stimulation artefacts on the recorded signals. The gray box represents a computing device (e.g. an implantable pulse generator, a personal computer or a cloud-based computing system). The computing device processes the recorded biosignals in the digital domain and extracts features, such as the intensity of neural activity in a specific frequency band or phase–amplitude coupling, to determine stimulation parameters and timing. *Adapted from ref.* [44].

has the advantage of sensing and stimulating via the same electrode (Figure 2.11b) and hence minimizing surgical instrumentation required to build an implantable closed-loop neurostimulation modality. Directly recording from the stimulation electrode may also allow feedback through evoked resonant neural activity (ERNA) [20]. Second, the instantaneous power of rhythmic neural activity can be tracked in the motor cortex [44]. In this case (Figure 2.11c), studies have focused on gamma activity (~75 Hz) in the control of dyskinesias or on movement-related modulation of beta activity in the control of tremor [44]. This technique leverages the enhanced signal-to-noise ratio (SNR) of cortical recordings and prevents contamination of the feedback signal by stimulation artefacts.

An alternative approach, which also prevents the stimulation artefacts from being coupled into the signal of interest, is to use peripheral sensors for feedback (Figure 2.11d). This technique may prove useful for gait disturbance and tremor [44]. However, various challenges associated with this approach, such as the amount of power required for the wireless communication between the peripheral sensor and the implanted stimulator, the security of wireless communication and the fact that information from peripheral sensors follows the development of symptoms and is thus not predictive [44]. Finally, patient compliance in the wearing of peripheral sensors is another significant factor that has to be taken into consideration.

2.5 Artefact suppression in bidirectional neural interfaces

2.5.1 Introduction to artefact suppression techniques

As already described in Section 2.4.3, closed-loop therapies can treat complex disorders whose symptoms are not always present, necessitating concurrent sensing, biomarker extraction, and targeted therapeutic stimulation in the brain. Today, despite the advances in simultaneous sensing and stimulation, there are still major limitations in applying therapeutic stimulation in a closed-loop, on-demand manner [54]. Stimulation pulses create interference with biopotential readout circuits, which appear as artefacts masking the underlying neural signal and making simultaneous sensing

and stimulation a challenge [54]. To provide continuous recordings of LFPs during stimulation and real-time biomarker extraction, closed-loop neurostimulation systems must be able to tolerate and reject large stimulation artefacts (Figure 2.12).

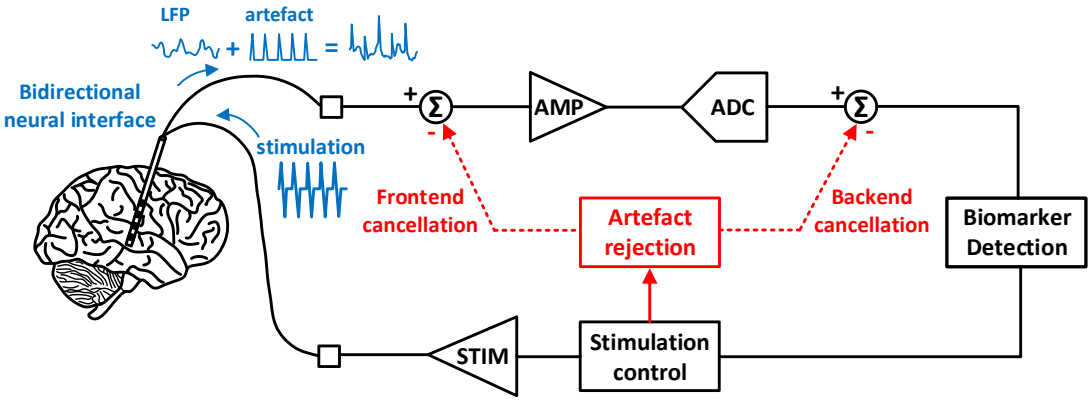

Figure 2.12: Architecture of a bidirectional neural interface where local field potentials are used as feedback signals. Stimulation artefacts contaminate the recorded signals and impede robust extraction of biomarkers. To enable concurrent sensing and stimulation, neuromodulation systems can attenuate stimulation artefacts by applying either frontend or backend cancellation methods. AMP, amplifier; STIM, stimulator; ADC, analog-to-digital converter. *Adapted from ref.* [54].

Stimulation artefacts typically appear as large voltage transients coinciding with the delivery of stimulation pulses. More specifically, a stimulation artefact is generally defined as a short, high-amplitude peak (direct artefact) followed by a slow, exponential decay (residual artefact) superimposed on the underlying neural activity [54]. To analyse the origin of stimulation artefacts, the linear circuit model of an electrode in a setup where stimulation is applied is shown in Figure 2.13. The electrode double-layer capacitance (C_{DL}), charge-transfer resistance (R_{CT}), and spread resistance (R_S) are functions of the electrode's area, geometry, material, and surface roughness [55]. Artefacts arise from voltage drops across stimulating electrodes and tissue as current passes through them [54].

It is clear that all the remaining recording electrodes in the array are affected since the artefact propagates to them through the spread resistance. Precise modeling of the artefact is difficult because: a) electrode impedance is nonlinear and varies with voltage [54], and b) electrode impedance can change over time with chronic

implantation [56]. However, the linear model is effective for estimating the duration of an artefact and the peak voltage induced by stimulation [54].

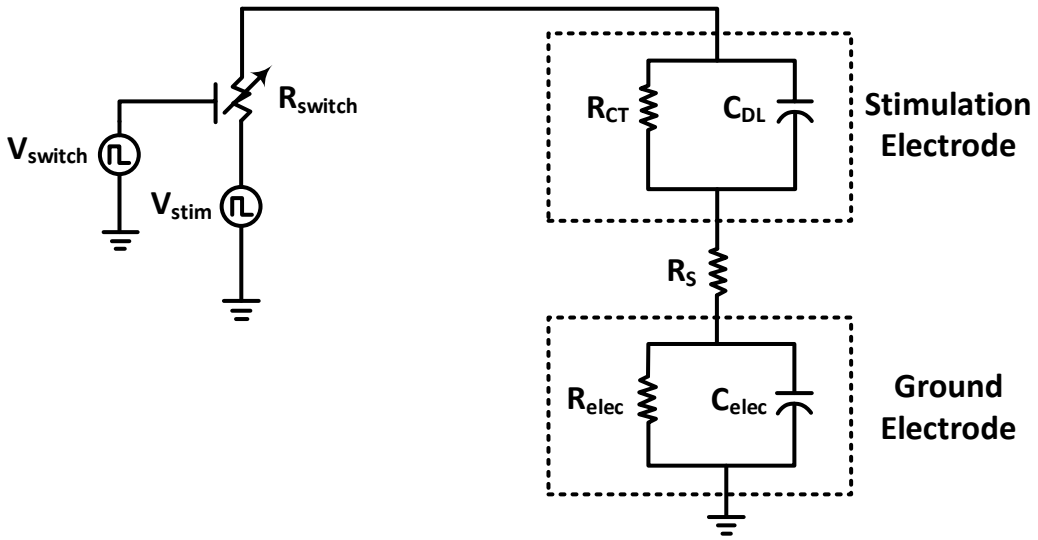

Figure 2.13: Linear circuit model of an electrode in a setup where electrical stimulation is applied. The electrodes are represented as parallel RC circuits. A time dependent resistor models the stimulation switch. *Adapted from ref.* [57].

Artefacts are often misclassified as action potentials by some detection algorithms, and subsequent action potentials cannot be recorded until the front-end amplifier has recovered from saturation. The combination of artefact peaks and resulting decay creates strong distortion in the power spectrum at the stimulation frequency and also spreading into frequency bands of interest for LFP and ECoG recording applications [54]. It is thus clear that rejection of those artefacts is necessary in order to provide accurate recordings of action potentials, as well as LFPs and ECoG signals. This chapter presents artefact mitigation techniques that have been proposed so far. These techniques are divided into the following categories: a) artefact prevention techniques, b) front-end artefact suppression techniques, and c) back-end artefact suppression techniques.

2.5.2 Artefact prevention techniques

To prevent stimulation artefacts from affecting the biosignals of interest, specific factors, such as stimulator architecture and performance, stimulation waveform, and electrode configuration are important factors that the circuit designers have to take into account when designing closed-loop neuromodulation systems (Table 2.4). A typical source of significant artefacts is the amplitude mismatch (usually equal to 1%) that characterizes the two current sources that produce the anodic and cathodic stimulation phases included in a neurostimulator [58]. Some systems monitor offset voltage at the electrode from accumulated charge and calibrate the second phase current to minimize this offset [59]. In other systems calibration takes place prior to stimulation via current-copying using the cathodic current source as a reference for the anodic current [60, 61]. Another proposed methodology is to use an H-bridge circuit, which is a stimulator topology that makes use of a single current source and a set of switches that allows the same current source to be used in both stimulation phases [62]. This technique has been shown to accomplish a mismatch between pulses of less than 0.02% [62].

Table 2.4: Techniques for artefact prevention. *Reproduced from ref.* [54].

Methods	Variants	Toward closed-loop
Stimulation pulse charge-balance	Voltage offset correction Current copying Current source reuse	Improving charge balance reduces artefact size and duration, relaxing requirements on signal acquisition chain
Stimulation waveform design	Tri-phasic stimulation Zero-forcing equalization of waveform	Compensates for artefact-inducing properties of stimulator, neural tissue and recording circuitry
Electrode and reference configuration	Symmetric stim and sense electrode geometry Artefact-tracking voltage supply	Keeps artefact common-mode, which can be tracked by the supply and also cancelled through differential amplification

Stimulation setups where tri-phasic stimulation waveforms are delivered were also used in order to minimize artefact duration [63]. Chu *et al.* [64] designed a waveform shape that inverts the transfer function, thus diminishing the artefact duration by 73%. Deliberate placement of recording, stimulation, and reference electrodes has also been proved to attenuate the stimulation artefacts. For instance, a symmetric configuration between stimulation and recording electrodes achieves successful rejection of stimulation artefacts by presenting them as common-mode signals to the two inputs of differential recording amplifiers [65]. Peterson *et al.* [66] eliminated a common ground between the recording and stimulation subsystems, allowing the recording reference to track common-mode artefacts. It is important to clarify here that the prevention techniques proposed so far do not completely eliminate artefacts, but do ease requirements on front-end acquisition [54].

2.5.3 Front-end artefact suppression techniques

Even stimulation pulses that are perfectly balanced with equal charge in each phase can produce large and long artefacts if recorded by inadequate circuits. High fidelity recording of weak neural activity necessitates the design of low-noise bioinstrumentation that is able to detect biosignals down to microvolt amplitudes. Since power consumption trades off with noise performance, the AFE architectures consisting of biosignal amplification and digitization circuit blocks, typically dominate the overall power of a biopotential recording system. So far, AFE designs have primarily focused on optimizing power efficiency to extend battery life and minimize heat dissipation [54]. Power-efficient AFE design is further exacerbated as biopotential readout circuits scale to higher channel counts (>1000), due to tight area constraints and high communication data rates [54].

Due to these constraints, most existing biopotential recording devices have not been designed to achieve concurrent sensing and stimulation and are thus vulnerable to artefacts. For instance, power-efficient AFEs typically apply a large gain on the recorded signals to maximize their sensitivity. Hence, the power requirements of subsequent processing stages, such as the ADC, are relaxed. However, a high front-

end gain increases the risk of amplifier saturation. In addition, conventional AFEs use an analog high-pass filter with a low corner frequency to block DC offsets. This design decision results in a slow recovery from saturation due to the large, rapid transient voltage of a stimulation artefact (Figure 2.14a).

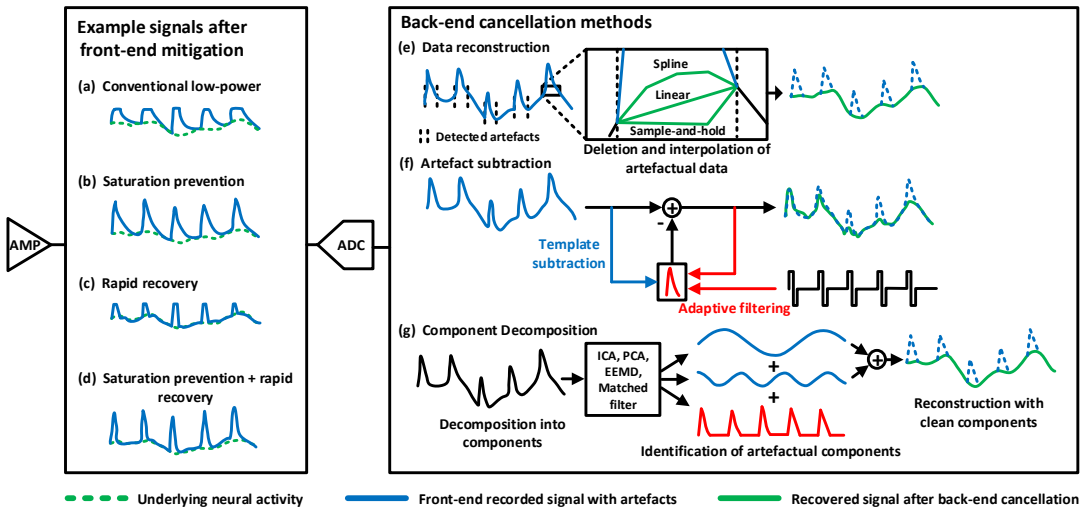

Figure 2.14: Description of different front-end (left) and back-end (right) artefact mitigation techniques. Front-end artefact cancellation techniques improve linearity and duration of recorded artefacts, and back-end methods remove them. Recorded analog signals (solid blue line) contain artefacts that distort the underlying neural activity (dotted green line). Back-end cancellation methods attempt to recover the neural signal of interest (solid green line). (a) Typical AFE architectures face saturation issues during the artefact and the front-end amplifier recovers slowly. (b) By increasing the dynamic range of the AFE, saturation can be prevented and signal distortion can be reduced. Hence, back-end artefact subtraction methods can be used to remove the artefacts. (c) AFEs that quickly recover from a saturating signal can minimize the amount of distorted signals. (d) Saturation prevention and rapid recovery can both be applied to increase the quality of the recorded biosignals. (e) Some back-end methods identify the artefact segments and reconstruct the underlying neural activity using interpolation. (f) Subtractive methods cancel artefact by subtracting estimated artefact waveforms. Artefact estimation is accomplished using adaptive filtering or template building. (g) Recorded waveforms can be separated into artefactual and neural components. Clean neural components are used to reconstruct the underlying neural activity. *Adapted from ref.* [54].

Some front-end techniques attempt to mitigate the effects of stimulation artefacts by preventing saturation [54]. One such technique is to increase the dynamic range of the recording circuits by decreasing the amount of signal amplification. In this case, the AFE is able to tolerate and record larger voltages. Moreover, a smaller artefact can remain in the linear range of the amplifier, so signal linearity is maintained and

stimulation artefact can, in theory, be rejected using back-end artefact subtraction techniques (Figure 2.14b). However, this approach sacrifices power efficiency since a higher supply voltage and a higher-resolution ADC for biosignal digitization are required.

Alternatively, by using a series switch at the input to disconnect the front-end when stimulation is applied, artefacts are prevented from reaching the recording electronics [67]. However, this technique can suffer from slow transient settling once reconnected. While spikes may be detected and analyzed even when superimposed on the long decays following amplifier saturation, these settling responses severely degrade LFP and ECoG signals [54]. It is thus clear that this approach necessitates the design of a robust recording front-end that is able to rapidly recover from saturation (Figure 2.14c). Resetting the recording circuits at every sample can clear the saturating charge and eliminate the long transient responses that result. Since stimulation often causes charge to accumulate on the recording electrode, some circuit designs actively discharge the electrode itself to an averaged pre-stimulus voltage [54]. Finally, a combination of saturation prevention and rapid recovery techniques was proposed in [62]. In this architecture, the recording circuits are reset at every sample and the front-end dynamic range is increased (Figure 2.14d). All the aforementioned front-end artefact suppression techniques are summarized in Table 2.5.

2.5.4 Back-end artefact suppression techniques

Back-end artefact suppression techniques (Table 2.6) are applied to the digitized signals at the ADC output to reject remaining stimulation artefacts. These techniques are generally divided into three main categories: a) data reconstruction (Figure 2.14e), b) artefact subtraction (Figure 2.14f), and c) component decomposition (Figure 2.14g). Closed-loop neurostimulation systems require fast, low-power, and low-complexity online implementations. Although the first implementations of these techniques were mostly offline, some have been implemented online in order to offer real-time artefact cancellation [54].

Table 2.5: Front-end artefact suppression techniques. *Reproduced from ref.* [54].

Methods	Variants	Toward closed-loop
Saturation prevention	High Dynamic Range Front-end subtraction Electrode disconnection	Keeps recorded artefact linear, improving the performance of back-end techniques
Rapid recovery	Amplifier charge reset High-pass pole shifting Active electrode discharge	Recovers from saturation quickly, reduces data loss, and lowers requirements on front-end dynamic range

Reconstruction methods remove samples contaminated with artefacts and replace them with interpolated values. More specifically, sample-and-hold methods hold over the last known good sample for the duration of each artefact [68, 69]. This procedure requires only a single sample of memory, but may cause significant distortion [54]. To reduce distortion, samples may be replaced by linear interpolation between the nearest clean samples [70, 71], an estimation from a learned Gaussian probability density [72] for data segments, or a reconstruction using cubic spline interpolation [73]. Although simple to implement, reconstruction methods require artefact detection. This can be done using blind detection algorithms [68, 70, 72], or using timing indicators from the stimulator [71]. These methods lose information during the artefact, degrading the achieved SNR [54]. High dynamic range is less critical since saturated data are discarded anyway.

However, high dynamic range front-ends are essential for subtraction and component decomposition techniques, since the artefact waveform has to be recorded without being distorted. In template subtraction techniques, templates are typically formed from averaging artefacts or fitting artefacts to a predefined function type [54]. These techniques suffer from varying artefact morphology originating from undersampling the artefact shape and misalignment between stimulation and sample timing [54, 74]. Similarly, adaptive filtering methods filter the stimulation pulse [75] or the artefact recorded on a neighbouring channel [76] in order to estimate and subtract the artefact

while filter coefficients are adapted. According to [54], these subtraction methods can be implemented with low latency, but require artefact detection, template building and on-board memory for template storage. To prevent signal distortion, templates must be regularly updated to track any changes in artefact shape or stimulation waveform. Besides that, estimated templates often take time to converge, resulting in varying levels of cancellation over time [54].

Table 2.6: Back-end artefact suppression techniques. *Reproduced from ref.* [54].

Methods	Variants	Toward closed-loop
Data reconstruction	Sample and hold interpolation (offline) Linear interpolation (online) Linear interpolation (offline) Gaussian interpolation (offline) Cubic spline interpolation (offline)	Simplest to implement and is effective with relaxed SNR requirements
Artefact subtraction	Averaged template subtraction (online) Averaged template subtraction (offline) Averaged template resampling and subtraction (offline) Function fitting template subtraction (offline) Adaptive filter (online)	Can theoretically remove artefact without distortion to underlying signal if paired with high-dynamic-range front-end
Component decomposition	Ensemble empirical mode decomposition (offline) Independent component analysis (offline)	Can remove stimulation artefact while providing other information and removing other types of artefact

Component decomposition techniques (Figure 2.14g) separate recorded channels into artefact and non-artefact components and reconstruct a clean neural signal with only the non-artefact components [54]. The most commonly used approaches for blindly separating artefacts from neural signals are ensemble empirical mode decomposition [77, 78] and independent component analysis [77, 79]. These methods offer great accuracy in reconstruction, however, they involve very intensive computation,

requiring iterative processing steps. Hence, according to [54], they have to date not been implemented for online use. All the aforementioned back-end artefact suppression methods are summarized in Table 2.6.

2.6 The approach in this work

The main aspiration of this work is to design and deliver high-performance wired and wireless bioinstrumentation that can be used either to solve the problem of limited mobility often encountered by patients in the clinic, or to support closed-loop neurostimulation systems. More specifically, the instrumentation presented in this thesis aims at providing real-time and high-quality bioelectrical signal recordings which can be used as control signals. The ultimate intent is to exploit the high performance and versatility of the designed instruments in order to cover the unmet need for high-precision biosignal recording in demanding DBS setups, such as the ones presented in Figure 2.11.

Hence, the initial focus of this work was to design and assess a state-of-the-art AFE that is able to: a) offer an adequate passband and dynamic range for recording a wide variety of biosignals, b) successfully combine low power consumption with high performance, c) interface with both low-impedance and high-impedance electrodes, and d) provide accurate biosignal recordings in order to investigate the existence of possible biomarkers that are associated with serious neurological disorders. This versatile and high-performance AFE would then be used as the fundamental building block for producing a wearable and wireless device that could act independently or in conjunction with a neurostimulator unit to form a closed-loop neurostimulation modality.

The next step towards achieving the aims of this work was to propose alternative methods for artefact suppression in bidirectional neural interfaces and assess their artefact suppression capabilities. Since most of the front-end artefact cancellation techniques make use of passive band-pass filters (Figure 2.15) in order to prevent the front-end amplifier from being saturated, the aim of this work was to propose

alternative front-end architectures that can provide better artefact suppression capabilities, higher sensitivity to weak biosignals and more bandwidth for bioelectrical signal recording.

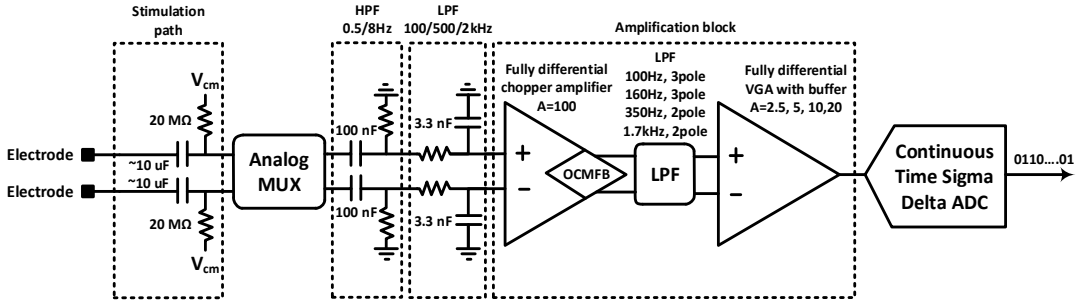

Figure 2.15: Block diagram of the high-performance analog front-end presented in [80]. This front-end has been designed to record local field potentials from the human brain. MUX, multiplexer; OCMFB, output common mode feedback; LPF, low-pass filter; ADC, analog-to-digital converter. *Adapted from ref.* [80].

Chapter 3. Design of a wearable and wireless multi-instrument for real-time monitoring of bioelectrical signals

3.1 Introduction

The need to create a system that:

- offers an adequate passband and dynamic range for recording a plethora of bioelectrical signals
- successfully combines small size with low power consumption and high performance
- is able to effectively interface with both low-impedance (e.g. electrodes used in electroencephalography) and high-impedance electrodes (e.g. segmented electrodes used in DBS [51, 81, 82])
- provides accurate biosignal recordings that can be used to investigate the existence of possible biomarkers that characterize various diseases
- can either be used as a portable/wearable recording-only device in the clinic for providing real-time monitoring of various types of biosignals (e.g. ExG/ECoG/LFP signals, accelerometer data, PV ectopic activity etc) or as a recording modality that provides high-quality symptom-related biosignals (acceleration signals, neurochemical signals, EMG signals, wide-frequency-range LFPs/ECoG) to a closed-loop neuromodulation system,

led into the design of a low-noise (8 nV/√Hz), eight-channel, battery-powered, wearable and wireless multi-instrument (55 × 80 mm^2) that can be used in a plethora of applications and scenarios. Previous experience on analog front-end design for high-precision biopotential recording, as presented in Section 2.3, provided insight on the potential challenges that could be encountered due to the nature of the

bioelectrical signal collection setups. This chapter[1] describes the methodology followed for the design of the proposed multi-instrument. The employed circuit topologies are exhibited and discussed in detail.

3.2 System overview

3.2.1 Design requirements and implementation of the AFE

To achieve the goals specified in the Introduction, a number of strict specifications for signal acquisition were imposed. These specifications are summarized in Table 3.1:

Table 3.1: Summary of key performance specifications related to the AFE of the proposed instrument.

Property	Value	Units/Comments
Gain	≥ 40	dB
Integrated noise	≤ 300	nVrms (0.5 to 500 Hz)
CMRR	≥ 100	dB
DC tolerance	≥ 50	mV
Current consumption	≤ 5	mA
Input dynamic range	≥ ± 2	mV
Input impedance	≥ 1	GΩ
High-pass knee frequency	0.5	Hz
Low-pass knee frequency	500	Hz

[1] Sections 3.2 to 3.3 were excerpted from the author's open access publication with title "A high-performance 8 nV/$\sqrt{Hz}$ wearable and wireless system for real-time monitoring of bioelectrical signals" published in Journal of Neuroengineering and Rehabilitation, 2019 [129]. However, some additional information was added in these Sections in order to fully cover the requirements of this Thesis. The contributions of the co-authors are explicitly described in the "Authors' Contributions" Section of this research article and are acknowledged here. At this point, it should be highlighted that the author of this Thesis designed and developed the wireless/wearable biosignal recording device presented in this Chapter, performed the data collections and processing and wrote the manuscript of the (published) open access research article under the supervision of Professors Drakakis, Brown and Denison.

Clearly, a high gain and CMRR along with low noise levels are required in order to ensure precise recordings of weak bioelectrical signals. Moreover, a relatively wide dynamic range in combination with adequate dc offset rejection capabilities are required in order to prevent the output of the instrument's AFE from saturation caused by the dc offsets stemming from the recording electrodes.

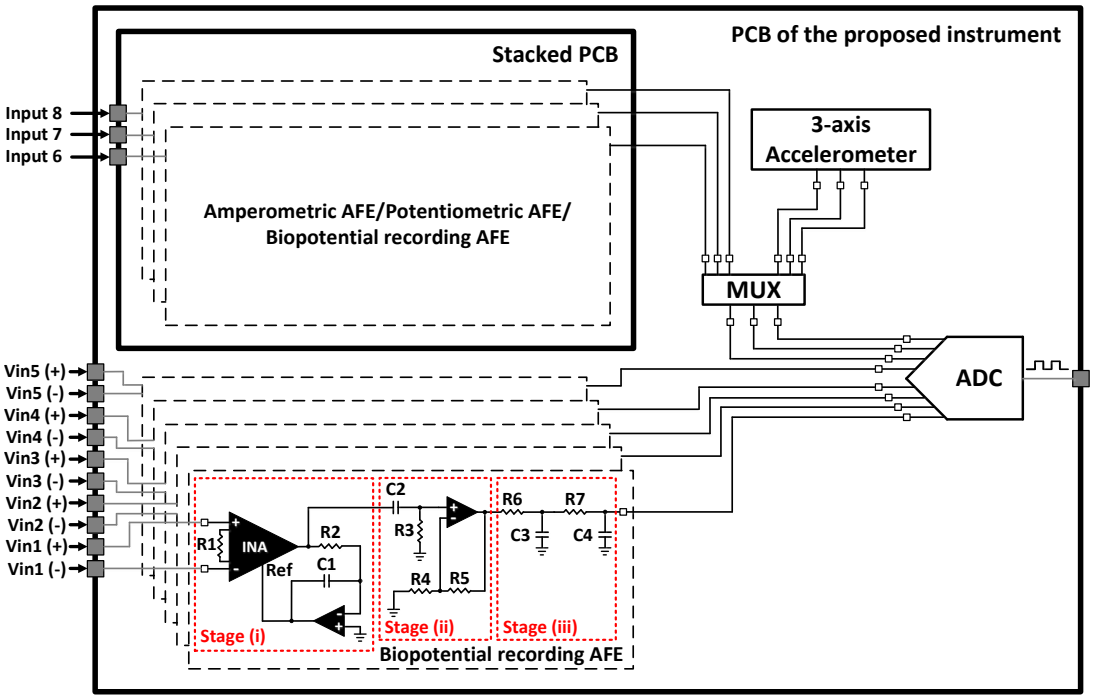

Figure 3.1: Block diagram showing the overall AFE and the ADC section of the proposed instrument. The overall AFE consists of eight channels (five channels on the PCB of the instrument and another three channels on a stacked PCB that is adjusted on two headers located on the main PCB). The biopotential recording AFE consists of three stages: (i) a differential pre-amplification stage with high-pass characteristics, (ii) an active, 1st order high-pass filter that enhances the dc offset rejection capabilities of the AFE, and (iii) a passive, 2nd order low-pass filter that defines the passband of the AFE and also serves as an anti-alias filter for the ADC stage, which follows in the signal chain. The inputs of the first five channels are differential, whereas the inputs of channels 6, 7 and 8 can either be differential or single-ended depending on the type of biosignals (either amperometric or potentiometric or biopotential signals or a combination of them) the stacked PCB is intended to record. INA, instrumentation amplifier; AFE, analog front-end; PCB, printed circuit board; MUX, multiplexer; ADC, analog-to-digital converter.

To meet the requirements for data acquisition, a biopotential recording AFE consisting of three main stages was designed and implemented (Figure 3.1): (i) a differential pre-

amplification stage with high-pass characteristics; (ii) an active, 1st order high-pass filter that enhances the dc offset rejection capabilities of the AFE; and (iii) a passive, 2nd order low-pass filter that defines the passband of the AFE and also serves as an anti-alias filter for the ADC stage, which follows in the signal chain.

The pre-amplification stage consists of a low-noise INA (model AD8422, Analog Devices, USA). Taking into consideration that neural signals, such as EEG signals and LFPs, are characterized by very low amplitudes (typical range: 1–50 μV [16]), a high CMRR in the front-end amplifier is required in order to increase the SNR of the recording instrument.

Another challenge that has to be taken into account in the design of the AFE is that the placement of a metallic electrode in tissue results, in general, in charge redistribution, creating a capacitive double layer that can lead to polarization voltages [55]. These offsets may easily saturate the high-gain front-end INA and must be adequately rejected [6, 83]. The strategy of using passive high-pass filters before the front-end amplifier to remove those dc offsets was rejected because such an approach would increase the input-referred noise and degrade the CMRR of the system [84].

The strategy followed in this design was to introduce an active feedback integrator [85], implemented with a single operational amplifier (model ADA4522, Analog Devices, USA). The resulting topology functions as a 1st order high-pass filter; its knee frequency was set at 0.5 Hz. Crucially, this engineering design decision along with the choice of introducing a high gain (= 40 dB) on the front-end INA chip, allows us to fully exploit the high CMRR offered by the AD8422 INA chip (134 dB for a gain of 40 dB). Moreover, since there is no passive filtering network before the front-end amplifier and the gain of the first stage is sufficiently high (equal to 40 dB) - thus allowing the effective noise factor to be the noise factor of the first stage without an impact on the subsequent stages [86, 87] - the input-referred noise of the designed AFE is expected to approximate the measured input-referred noise reported in the datasheet of the AD8422 chip (≈ 8 nV/√Hz).

The second stage (see Figure 3.1) includes an active 1st order high-pass filter, which provides an amplification of 20 dB. The role of this filter is to enhance the dc offset

rejection capabilities of the overall AFE and offer the additional gain required to better exploit the full scale voltage range of the ADC (± 2.5 V). Finally, the strict area and power consumption requirements imposed on the AFE design led to the introduction of a passive 2nd order low-pass filter as the third stage of the AFE, because it can be implemented with fewer components in comparison with an active low-pass filter of the same order.

Referring to Figure 3.1, resistor R_1 determines the gain of the front-end INA, while resistor R_2 and capacitor C_1 determine the cut-off frequency of the 1st order high-pass filter introduced in the first stage of the AFE. Next, resistor R_3 and capacitor C_2 define the cut-off frequency, while the ratio of resistors R_4 and R_5 define the gain ($1+R_5/R_4$) of the 1st order high-pass filter located in the second stage of the AFE. Finally, resistors R_6, R_7 and capacitors C_3, C_4 determine the cut-off frequency of the 2nd order low-pass filter existing in the third (final) stage of the AFE architecture.

The first stage (differential pre-amplification) is supplied with ± 5 V to ensure that an adequate headroom is provided and eliminate the risk of saturation originating from electrode dc offsets. However, the second stage (active high-pass filter) is supplied with ± 2.5 V to be able to interface with the high-performance and low-power commercial ADC chip (model ADS1298, Texas Instruments, USA) that follows in the signal chain. The fundamental building block for the design of the filtering stages is the operational amplifier ADA4522 by Analog Devices. Finally, it should be noted that the resistors and capacitors included in this three-stage AFE architecture are characterized by a tolerance of 0.1% and 10% respectively. Due to these tolerances, the high-pass knee frequency could range from 0.42 Hz to 0.59 Hz, and the low-pass knee frequency could range from 455 Hz to 555 Hz.

As shown in Figure 3.1, five recording channels of the proposed instrument have been designed according to the above-described AFE architecture (entitled “biopotential recording AFE” in Figure 3.1). These five channels culminate in five out of eight channels of the ADC chip and can record a wide variety of bioelectrical signals, such as EEG, EMG, ECG, ECoG, LFP signals, PV ectopic activity and ERNA. Furthermore, the proposed instrument has been designed to record some additional biosignals,

such as acceleration signals, which are recorded by an analog three-axis accelerometer (ADXL335, Analog Devices, USA) located on the instrument's main PCB, or signals stemming from amperometric and potentiometric biosensors, which can be recorded by three auxiliary AFEs located on a stacked PCB that is adjusted on the main PCB of the instrument. In other words, many types of stacked PCBs could be designed, each one of them providing the ability to record different types of biosignals (amperometric/potentiometric/biopotential). The nature of the biosignals of interest would determine the type of the stacked PCB to be placed on top of the main PCB. The user can determine through software the type of biosignals (either acceleration signals or analog signals stemming from the three auxiliary AFEs located on the stacked PCB) to be digitized by the last three channels of the ADC chip.

At this point, it is important to clarify that in normal operation: 1) all 8 channels of the ADC can be used (if required) to simultaneously sample bioelectrical signals, 2) the addition of three low-power auxiliary AFEs (on the stacked PCB) will not significantly affect the power consumption of the overall system, and 3) the digital bit stream, which is generated after the analog to digital conversion of the biosignals sampled by all 8 channels of the ADC, is provided to the processing unit (FPGA) of the system. It is thus clear that the proposed instrument is an 8-channel system that offers flexibility on the type of biosignals that can be recorded by the last three channels of the ADC chip.

Finally, the above-described low-power three-axis accelerometer, which is mainly intended to be used in applications where tremor activity of patients with PD or essential tremor needs to be monitored, is characterized by an output sensitivity of 250 mV/g and a noise of approximately 840 μgRMS (X, Y axis) and 1.7 mgRMS (Z axis) for an available bandwidth of 10 Hz. The reason behind the selection of a limited bandwidth (= 10 Hz) for the acceleration measurements lies in the fact that: a) tremor frequency of patients with PD ranges from 3 to 8 Hz [45], and b) the lower the available bandwidth the better the resolution of the accelerometer.

3.2.2 Architecture of the overall system

As shown in Figure 3.2, the overall system consists of an 8-channel AFE – illustrated in Figure 3.1 - followed by the 8-channel, simultaneous sampling, 24-bit, delta-sigma ADS1298 chip that digitizes the analog outputs of the biosignal recording channels. Next, a field-programmable gate array (FPGA) module (Spartan 3e – 48 MHz) controls the communication between the ADS1298 chip and the radio transceiver, which is the final stage of the system design. It is important to note here that the ADS1298 chip includes a built-in programmable gain amplifier (PGA) that can further amplify the analog outputs of the biosignal recording channels before being digitized. More specifically, the gain settings of this PGA are 1, 2, 3, 4, 6, 8, and 12 V/V.

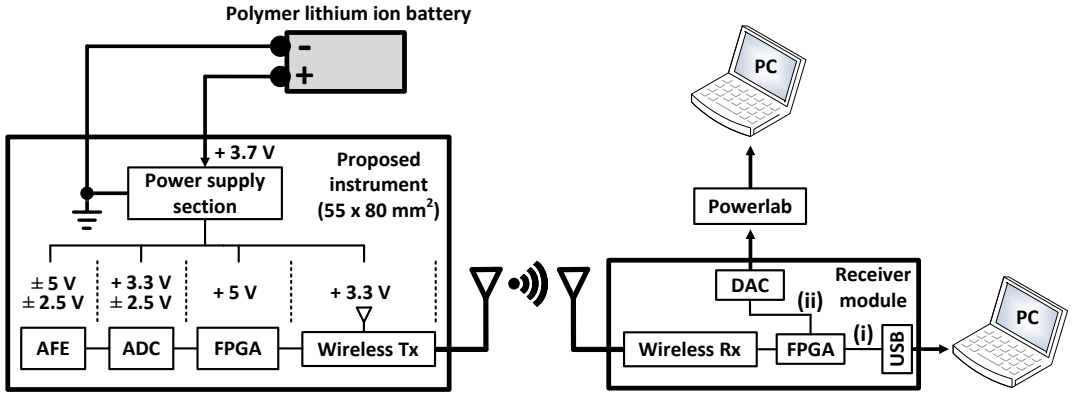

Figure 3.2: Block diagram showing the overall architecture of the proposed instrument. The data received by the receiver module can either be directed i) to a PC through the USB 2.0 interface, or ii) to a commercially available data acquisition system (e.g. Powerlab) that digitizes and depicts the data on a PC. Path (ii) ensures that the proposed instrument can functionally integrate with existing medical biosignal acquisition systems, if required. AFE, analog front-end; ADC, analog-to-digital converter; FPGA, field programmable gate array; Tx, transmitter; Rx, receiver; DAC, digital-to-analog converter; USB, universal serial bus; PC, personal computer.

Regarding wireless transmission, the most popular communication protocol standards are Bluetooth (IEEE 802.15.1), ZigBee (IEEE 802.15.4), Wi-Fi (IEEE 802.11) and ultra-wideband radio transmission scheme (UWB). Bluetooth and Zigbee are suitable for low data rate applications with limited battery power (such as portable devices and battery-operated sensor networks), due to their low power consumption leading to a long lifetime [88]. In contrast, UWB and Wi-Fi are better solutions for high data rate

implementations (such as audio/video surveillance systems), because of their low normalized energy consumption [88].

Since the aim of this work was to deliver a battery-powered instrument, UWB and Wi-Fi protocols were rejected. The radio transceiver used for the wireless transmission of the recorded data is the AT86RF231 chip (Microchip Technology, USA), which is based on the IEEE 802.15.4 protocol. The reason behind the choice of IEEE 802.15.4 protocol over Bluetooth lies in the fact that the 802.15.4 protocol offers extremely good bit error rate (BER) performance at low SNRs [89]. More specifically, the BER performance of the 802.15.4 transmission is between 7 and 18 dB better than that of Bluetooth and Wi-Fi. This can be directly translated to a range increase from 2 to 8 times the distance for the same energy per bit, or an exponential increase in reliability at any given range [89].

Clearly, the enhanced robustness to interference that the 802.15.4 protocol exhibits along with many other inherent merits that characterize it, such as large operating distance, low static noise, reduced cross-talk interference and inherent security [90], were crucial factors that influenced the final engineering design decision since several radio services (e.g. 2.4 GHz industrial, scientific and medical radio band/ISM, 5.3 GHz local-area network/LAN, global system for mobile communications/GSM900, GSM1800, TV bands, etc.) exist in a typical clinical setting, where the proposed instrument is intended to be used. Moreover, the λ/4 monopole, 2.4 GHz antenna, which is characterized by a length of 21 mm, a nominal gain of 0 dBi, an omni-directional design and sub-miniature version A (SMA)-plug fixing, was chosen since it combines small size, low cost and high performance.

The power supply section of the instrument includes a high-efficiency, step-up DC-DC switching regulator (LM2623, Texas Instruments, USA), which is suitable for battery-powered and low input voltage systems. This regulator converts the + 3.7 V supplied by the battery to + 5 V, which is required for the operation of the AFE and the FPGA. Furthermore, the voltage regulator chip TPS7A8001 (Texas Instruments, USA), the low-noise regulated switched-capacitor voltage inverter LM27761 (Texas Instruments, USA) and the voltage converter LM2662 (Texas Instruments, USA) provide all the

voltage levels (± 2.5 V, + 3.3 V and - 5 V) required for proper operation of the remaining parts of the device. The proposed instrument is powered by a 1 Ah lithium battery and can provide more than eight hours of continuous wireless biosignal transmission. Finally, its size approximates the size of a business card (55×80 mm^2), as shown in Figure 3.3.

By carrying out the circuit design using discrete components the barrier to manufacturing and replication is lowered. Since these components are recommended by their manufacturers for being used in medical instrumentation, their incorporation in the designs of medical devices that are intended to be used in the clinic: 1) maximizes the possibilities of successfully completing the relevant clinical tests, and 2) enables a faster acquisition of the appropriate medical approvals, and thus a faster launch into the market.

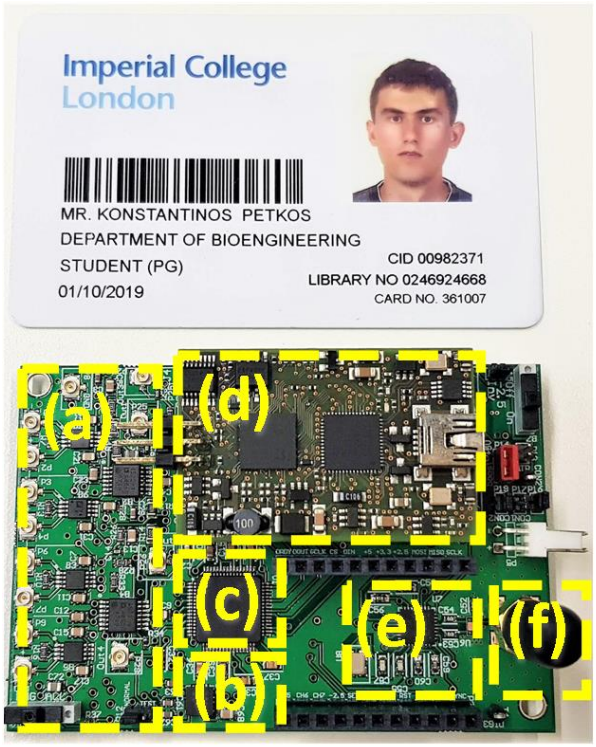

Figure 3.3: Structure of the proposed wearable/wireless instrument. The instrument's architecture includes: (a) a high-performance, eight-channel (five channels on the main board and another three channels on a stacked PCB that is adjusted on the two headers shown in the picture) AFE, (b) an analog, low-power 3-axis accelerometer, (c) an eight-channel, 24-bit ADC, (d) an FPGA module, (e) a 2 MBps Zigbee transceiver, and (f) a 2.4 GHz antenna.

Regarding the research outcomes of this work, the strategy of using (very high-performance) discrete components in the system architecture instead of designing an application specific integrated circuit (ASIC), aims at providing a low-noise instrument (with a noise performance that is better than the noise performance provided by existing devices, such as ASICs existing in the literature, commercial devices and academic works based on discrete off-the-shelf components) that can achieve a more complete sampling of the physiomarker space. Next, based on what is discovered, we can define a bespoke ASIC that would provide the resolution required within the power constraints of a miniaturized wireless device (either implantable or just wearable).

The investigational character of the proposed device also led to the design decision to maintain the provided number of channels at a relatively moderate level (=8). Since the IEEE 802.15.4 wireless protocol can support much larger data payloads than the one produced and transmitted with the 8-channel architecture, the best approach for increasing the channel count of the wireless device (if required) is to redesign the proposed instrument with more channels (≥16) and maintain the single transmitter-single receiver system architecture. In this way, challenges in the real-time character of the system or data synchronization issues that may emerge in architectures where multiple transmitters (with one or more receivers) exist can be avoided.

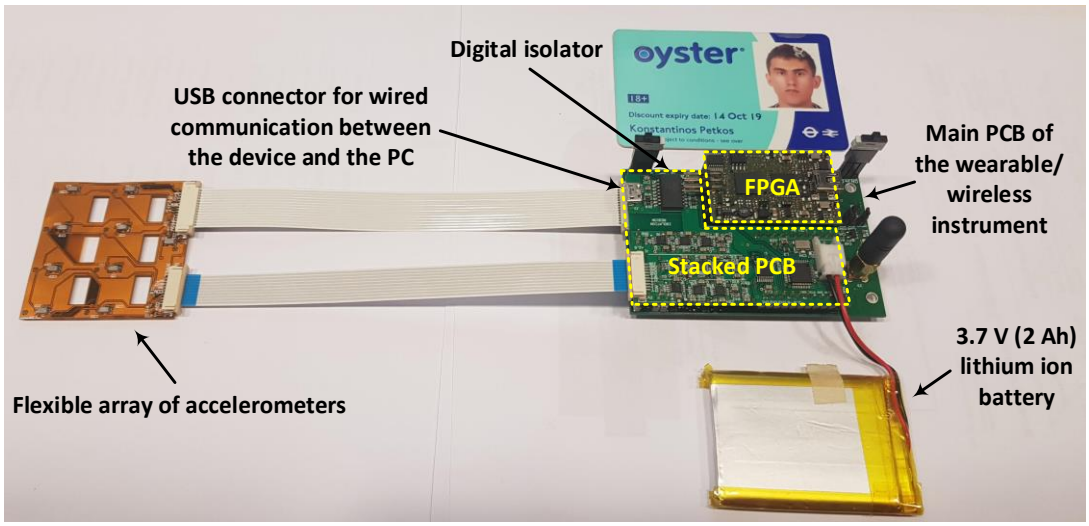

Figure 3.4: Final version of the proposed wearable/wireless instrument.

The final version of the proposed wearable/wireless device is presented in Figure 3.4. In this design, the stacked PCB described in Section 3.2.1 was incorporated into the overall system. As shown in Figure 3.4, a flexible array of accelerometers was connected to the system for testing purposes. Finally, a USB connector was introduced in the system design to add a wired communication capability to the device.

Regarding the architecture of the receiver module (see Figure 3.2), it consists of: a) the AT86RF231 chip that receives the data transmitted by the proposed instrument, b) an FPGA that can direct the data either to a PC through the USB 2.0 interface that is provided by the FPGA module (path (i) in Figure 3.2), or to a commercially available 16-bit digital-to-analog converter (DAC) chip (AD5362, Analog Devices, USA - path (ii) in Figure 3.2). The analog output of the DAC chip can then be digitized and depicted on the PC by a commercial data acquisition system (e.g. Powerlab 16/35 that is used in this study). The second path (FPGA-DAC-Powerlab) was added in the system architecture to ensure that the wireless instrument can functionally integrate with existing commercial devices (e.g. Powerlab 16/35) and be used in medical studies.

3.2.3 Design considerations for low-noise biosignal recordings in a noisy clinical environment

As far as the noise sources at low frequencies are concerned, it is well-accepted that the most important source of electromagnetic interference (EMI) at low frequencies is the 50 Hz noise from the mains. In order to protect the designed system from the 50 Hz interference, the following strategy was cumulatively implemented: a) the device was always battery-powered during the experiments to prevent the recorded biosignals from being contaminated by the strong 50 Hz interference (and its harmonics) stemming from the mains, b) an INA with a high CMRR value (>130 dB) and a high input impedance (200 GΩ, 2 pF) was chosen to be the first stage of the designed biopotential recording AFE. These two features of the INA (high CMRR and input impedance values) suppress interference originating from the mains, c) the front-end INA further attenuates the 50 Hz noise due to the inherent cancellation of even-order harmonics it offers (since it's a differential system).

As far as the noise sources at high frequencies are concerned, in order to protect the designed system from high-frequency EMI (e.g. radio frequencies, operating frequencies of medical devices used in the clinic, such as ultrasound, MRI devices etc) existing in the clinical setting, the following strategy was cumulatively implemented: a) a passive, 2nd order low-pass filter at 500 Hz was placed in the AFE of the wearable/wireless instrument. This filter significantly attenuates high-frequency (>tens of kHz) noise components, b) a passive, 1st order EMI (low-pass) filter at 3 MHz is included in the ADS1298 chip, which is the ADC of the overall system. This filter further attenuates high-frequency (>tens of MHz) noise components, c) a high-performance INA with high CMRR values was placed at the first stage of the designed AFE. As a result, high-frequency noise components (present in the ambient environment) that appear as common-mode signals at both inputs of this front-end INA are adequately suppressed by its high CMRR (>80 dB at 100 kHz), and d) during the biosignal (ExG) acquisition experiments, the cables that were used to connect the ExG electrodes to the wireless/wearable device were twisted (whenever practically possible) and wrapped in foil to minimize the effects of noise on the recorded bioelectrical signals.

It should be clarified here that during all the experiments (both *ex vivo* and *in vivo*) presented in this Chapter, the PCB of the wireless/wearable device was not placed in any enclosure that could function as a Faraday cage (it was thus completely exposed to external noise/EMI) in order to assess the worst case scenario. Of course, in a real clinical setting a proper plastic enclosure with EMI/RFI copper conductive coating (that functions as a Faraday cage) has to be used to host the designed PCB and protect the electronics from external noise/interference sources (coating manufacturers often specify an attenuation of more than 75 dB from 1 MHz to 1 GHz).

3.3 Measured results

In this section, a number of strict tests, which are performed on the biopotential recording AFE to assess its performance in terms of noise, linearity and temporal response, are presented and analyzed. Furthermore, indicative *ex vivo* recordings of

EEG, ECG, EMG, acceleration signals and fasciculations, which were acquired from two healthy male subjects, aged 30 and 48 years old, using the proposed instrument, are reported. These experiments took place in a university laboratory, where the subjects were comfortably seated in an upright chair and were asked to perform the required actions. Moreover, *in vivo* recordings of weak LFPs, which were wirelessly acquired in real time using DBS electrodes implanted in the thalamus of a non-human primate, are also presented. Finally, raw anonymized data including extremely weak LFP signals, ERNA and PV ectopy, which were previously recorded by approved wired instruments during invasive experimental sessions are used to evaluate the performance of the proposed instrument against high-performance commercial biopotential acquisition systems. In this study, the above-described raw anonymized data are presented to the input of the instruments that are examined in each series of experiments by means of a commercial waveform generator (Agilent 33220A).

The results shown in this section were derived from signal recordings that took place in a university laboratory, which is vulnerable to noise/EMI originating from a wide variety of devices that are in operation (e.g. servers, ultrasonic cleaners, air fume hoods, laboratory pumps for fluid or gas transfer, a variety of automatic heating/cooling elements and systems, several other electric appliances such as fridges etc). Similar comments hold for the *in vivo* experiments reported here which took place at Newcastle University in a high-tech space which can be characterized as an ICU for non-human primates that contains a plethora of sized monitoring devices.

Additional experiments (Figure 3.5) conducted in an active operating theatre (Hammersmith Hospital, London, UK), which is primarily used for cardiac interventions and procedures, show that the instrument's input-referred noise levels remain unaffected when the instrument is placed (again without making use of any enclosure that could function as a Faraday cage) in a noisy clinical environment (Figure 3.6). Hence, it is clear that the high CMRR of the designed AFE in conjunction with the analog (low- pass) filtering strategy followed in the AFE design of the wearable/wireless device successfully suppress external EMI and thus prevent noise from being coupled into the physiological measurements. Finally, no 50 Hz

interference was present in the amplitude spectrum of the acquired noise recordings (Figure 3.6c).

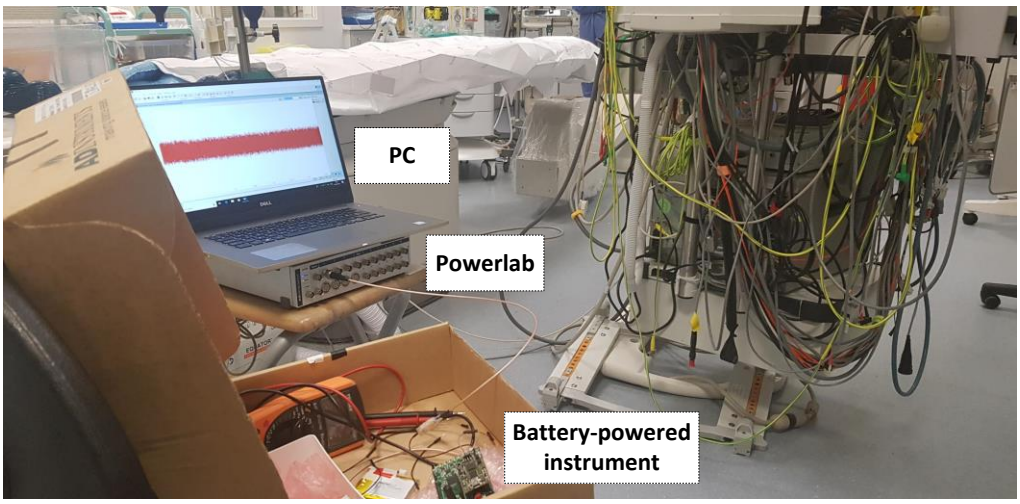

Figure 3.5: Experimental setup for measuring the input referred noise of the instrument in an operating theatre. The system was not protected from EMI sources in order to assess its noise performance under the worst possible conditions.

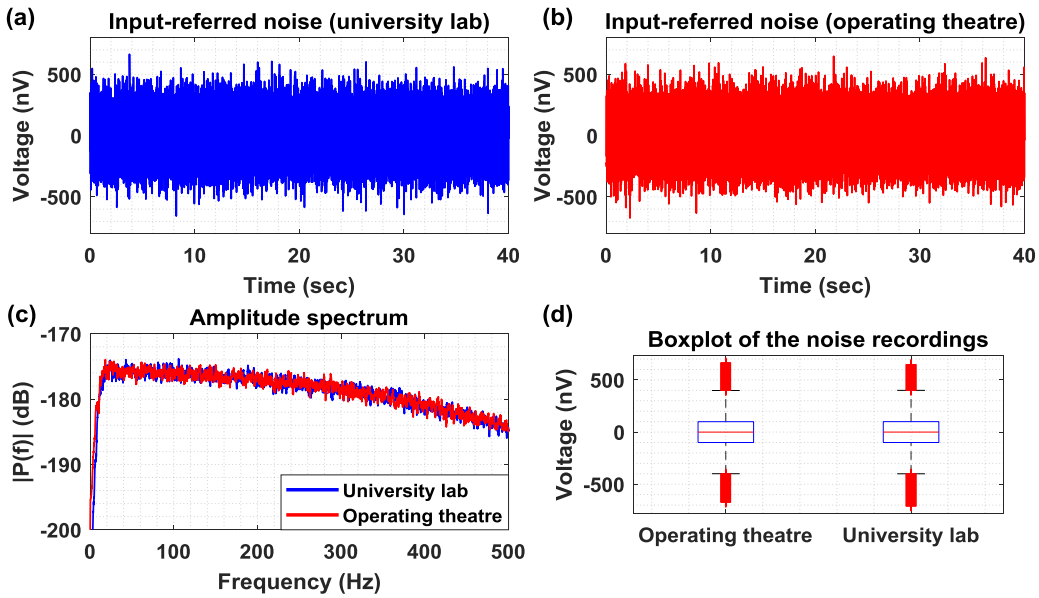

Figure 3.6: Input-referred noise measurements conducted in: (a) a university laboratory, and (b) an operating theatre. (c) The amplitude spectrums of the two noise recordings approximate each other and do not include any peak at 50 Hz. (d) The boxplot shows that the noise recordings conducted in the two different settings (operating theatre and university laboratory) exhibit approximately the same behaviour.

3.3.1 Transfer function and input referred noise

From the measured Bode magnitude plot shown in Figure 3.7a, it is clear that the proposed instrument's AFE provides a passband between 0.5 and 500 Hz and achieves the desired gain of 60 dB. The roll-off of the high- and the low-pass filters equals +10 dB/Oct and -40 dB/decade, respectively.

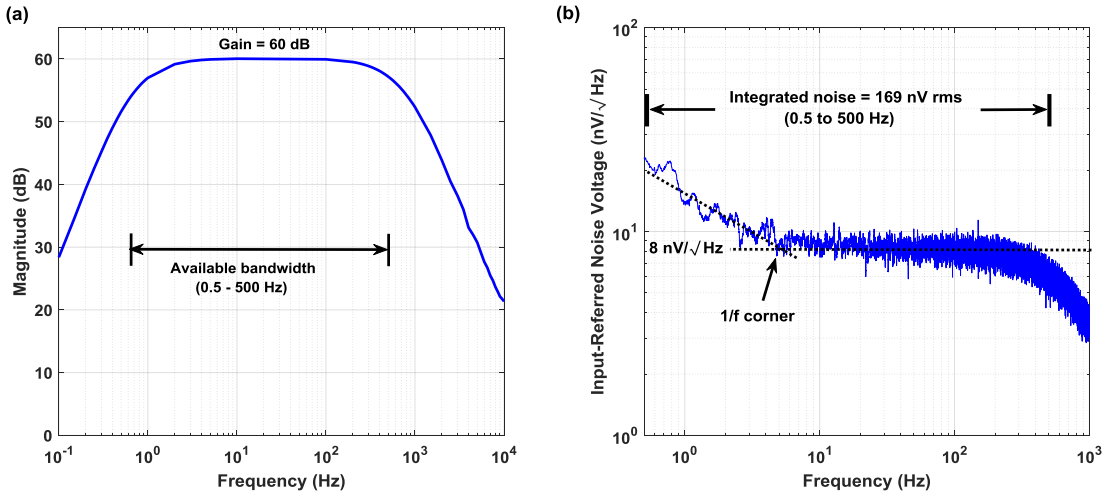

Figure 3.7: Measured Bode magnitude plot (a) and input-referred noise (b) of the proposed instrument's biopotential recording AFE. (a) The biopotential recording AFE provides a passband between 0.5 and 500 Hz. The roll-off of the analog high- and low-pass filters equals +10 dB/Oct and -40 dB/decade, respectively. (b) Noise power spectral density estimate in the passband for the biopotential recording AFE is 8 nV/$\sqrt{Hz}$, with the residual 1/f corner estimated at roughly 5 Hz.

An input-referred noise voltage graph presents the input noise voltage of a system versus frequency. It is widely used to assess the flicker (or 1/f) and the thermal noise of a system, as well as the noise corner frequency, which is the point in the frequency spectrum where the flicker noise and thermal (or white) noise are equal to each other [91]. The input-referred noise was measured by connecting both inputs of the front-end INA to the ground of the PCB, recording the output voltage of the AFE and then dividing it by the gain, which is equal to 60 dB.

Since there is no passive filtering network before the front-end AD8422 INA chip and the gain of the first stage is sufficiently high (equal to 40 dB), the input-referred noise

of the designed AFE should approximate the measured input-referred noise reported in the datasheet of the AD8422 chip. The integrated noise of the proposed instrument's AFE over the frequency range 0.5 – 500 Hz was measured and found to be equal to 169 nV rms. According to Figure 3.7b, the noise power spectral density estimate in the passband for the designed AFE is 8 nV/$\sqrt{Hz}$, with the residual 1/f corner estimated roughly at 5 Hz. Indeed, these measured results are in agreement with the noise measurements reported in the datasheet of the front-end AD8422 INA chip.

3.3.2 Total harmonic and intermodulation distortion

In general, the appearance of distortion is attributed to nonlinearities of electronic components. Two of the most common methods to assess the linearity of an amplifying system is to specify its total harmonic distortion (THD) and its intermodulation distortion (IMD) levels.

THD is the ratio of the root-sum-square value of all the harmonics (2×, 3×, 4×, etc.) to the rms signal level [92]. In principle, only the first five or six harmonics are significant in the THD measurement [92]. In other words, THD measures the nonlinearity of a system, while applying a single sinusoidal signal as its input. The measured THD of the proposed instrument's AFE (gain = 60 dB) is presented in Figure 3.8a. Taking into consideration that the available dynamic range of the AFE is from 1 μV peak to 2.3 mV peak, it is clear that the achieved THD is less than 0.3%.

Generally speaking, when a spectrally pure sinusoidal signal passes through an amplifier, various harmonic distortion products are produced depending on the nature and the strength of the nonlinearities [92]. However, simply measuring harmonic distortion levels produced by single tone sinusoidal signals of various frequencies does not always convey all the information required to evaluate the amplifier's potential performance in a clinical setting, where reliable recording of weak bioelectrical signals is required. As a result, it is often required that an amplifier be evaluated in terms of its IMD product levels produced when two or more specified tones are applied at its inputs [92].

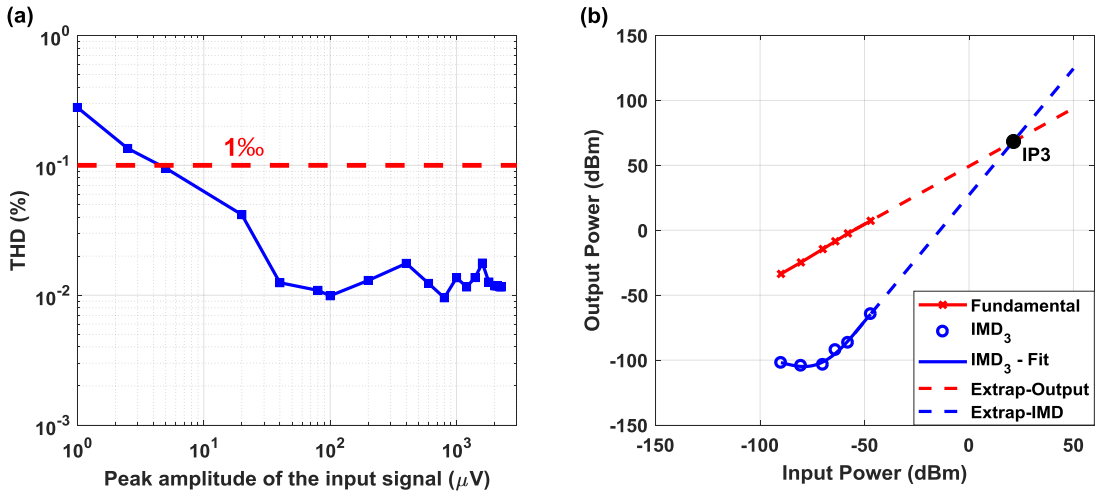

Figure 3.8: THD (a) and IMD_3 (b) of the proposed instrument's AFE (gain=60 dB). (a) Taking into consideration that the available dynamic range of the AFE is from 1 μV peak to 2.3 mV peak, it is clear that the achieved THD is less than 0.3%. (b) The two tones applied to the AFE of the proposed instrument were f_1 = 4.9 Hz and f_2 = 5.1 Hz. The output power of a single fundamental tone (in dBm - red line in the graph) and the relative power of the IMD_3 products referenced to a single tone (blue circles) are plotted against the applied input power. The third-order intercept line (dashed blue line) is extended to intersect the extension of the fundamental output signal line (dashed red line). This intersection is termed the third order intercept point IP_3. The calculated IP_3 exhibits a relatively high value, which is desired, since the higher the IP_3 value the better the linearity of the amplifier and the weaker the output intermodulation products that will be generated at the amplifier's output. THD, total harmonic distortion; IP_3, third order intercept point; IMD_3, third order intermodulation distortion.

Hence, it is of importance to not only examine the THD of the proposed instrument's AFE but also to investigate its IMD performance. When two tones of frequencies f_1 and f_2 are applied to the input of a nonlinear system, they produce second and third order products. The second order products are located at frequencies $f_2 + f_1$ and $f_2 – f_1$. The third order products, which are located at frequencies $2f_1 + f_2$ and $2f_2 + f_1$, can often be filtered out. However, the third order products located at $2f_1 – f_2$ and $2f_2 – f_1$ are situated close to the main tones f_1 and f_2 and thus it is difficult to be rejected by filtering and can be used for the assessment of linearity of even a narrowband amplifying system [92].

Two spectrally pure tones are applied to the AFE of the instrument. The two tones were f_1 = 4.9 Hz and f_2 = 5.1 Hz. In Figure 3.8b, the output power of a single fundamental tone (in dBm - red line in the graph) and the relative power of the third-

order products referenced to a single tone (blue circles in Figure 3.8b, defined as IMD_3) are plotted against input power. Clearly, the fundamental line is characterized by a slope that is equal to 1 dB/dB.

The third-order intercept line (dashed blue line) is extended to intersect the extension of the fundamental output signal line (dashed red line). This intersection is termed the third order intercept point (IP_3), describes third order IMD performance, and is a figure of merit for comparing amplifiers. The higher the IP_3 values the more linear the amplifier and the weaker the distortion products at its output. As shown in Figure 3.8b, the IP_3 of the proposed instrument's AFE is characterized by a desirable relatively high value.

3.3.3 Step and impulse response

The impulse function is defined as an infinitely high, infinitely narrow pulse, with an area of unity [93]. In practice, when the applied impulse width is much less than the rise time of the filter, the resulting response of the filter will give a reasonable approximation of the actual impulse response of the filter [93]. Rise time is typically defined as the time between 10% response to 90% response of the final or steady state value [94].

The step response of a filter, which is the integral of the impulse response, is useful in determining the envelope distortion of a modulated signal [93]. The two most important characteristics of a filter's step response are the overshoot and the ringing. Overshoot must be minimal for good pulse response and ringing must decay as fast as possible, so that interference with subsequent pulses is avoided. Transient response curves cannot provide a completely accurate estimation of the output since, in practice, signals typically are not made up of impulse pulses or steps. However, these curves constitute a convenient figure of merit so that transient responses of various filter types can be compared on an equal footing [93].

In Figure 3.9a, an undershoot phenomenon, which is equal to 250 μV (this is the difference between the negative peak value (≈ - 250 μV) and the final value of the step

response (0 μV)), appears due to the existence of a 2nd order high-pass filter (in other words a double zero exists in the transfer function of the system) in the AFE of the wireless device. However, this undershoot can be considered tolerable taking into account the enhancement this 2nd order high-pass filter offers in the recording capabilities of the overall system. As shown in Figure 3.9a, this undershoot is not followed by any decaying oscillatory activity, hence the response of the designed AFE is free of ringing. Furthermore, the impulse response of the AFE (see Figure 3.9b) exhibits a relatively fast settling.

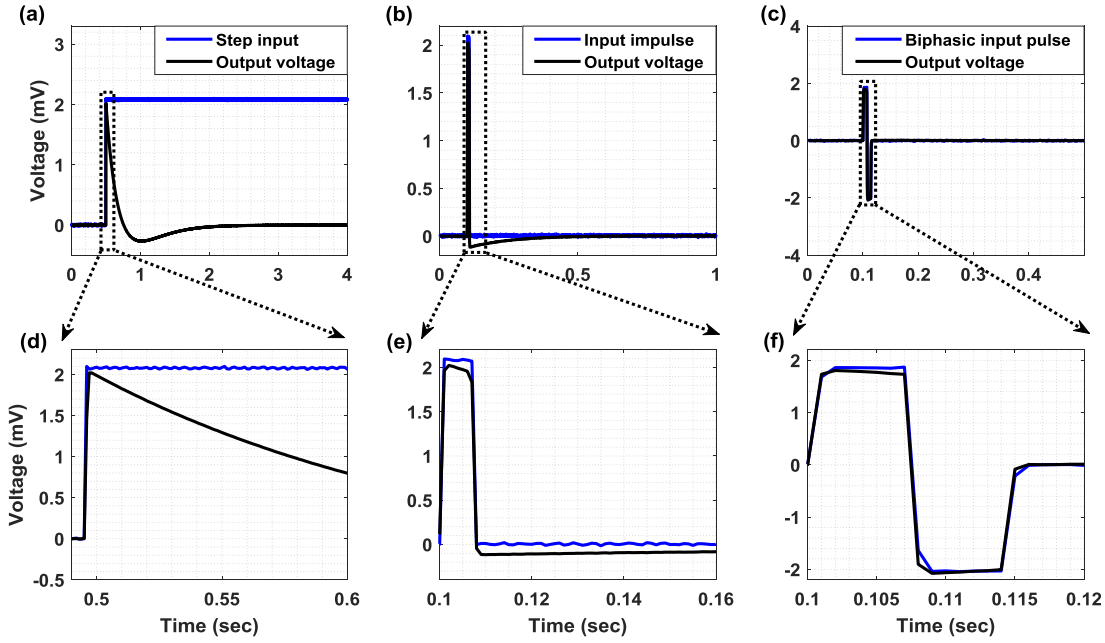

Figure 3.9: (a) Step response, (b) impulse response and (c) response to a biphasic pulse, which characterize the proposed instrument's AFE. (d) The step response of the AFE, which initially exhibits an undershoot of 250 μV, is free of ringing (there is no decaying oscillatory activity after the undershoot). (e) The impulse response of the AFE exhibits a relatively fast settling. (f) The response of the AFE to a biphasic pulse exhibits a significantly faster settling in comparison to its corresponding impulse response (shown in (e)). In all cases, the output voltage (black line) is presented after removing the gain of 60 dB that is applied by the biopotential recording AFE.

Another important test for evaluating the temporal response of the designed AFE is to inject a biphasic pulse to its input. As anticipated, the response of the proposed AFE to a biphasic pulse (Figure 3.9c) exhibits a significantly faster settling in comparison

to its impulse response. Finally, it is important to note here that the minimum slew rate achieved by the front-end amplifiers of the wireless instrument is 0.8 V/μs.

3.3.4 *Ex vivo* recordings of ExG (EEG, EMG and ECG) signals and fasciculations

In order to assess the low-noise recording capabilities of the designed instrument, physiological signal recordings that do not require invasive measurement techniques along with SNR measurements were obtained. Another objective of these biosignal recordings was to show that in spite of the high gain (60 dB minimum) and the relatively small dynamic range (± 2.3 mV) that characterize the biopotential recording AFE, it is capable of rejecting the dc offsets originating from the electrodes and thus avoiding saturation.

The measurement setup (Figure 3.10) used in this series of experiments allows for the comparison of the quality of signals recorded using two different methods. In the first method (wired transmission), the signals are recorded by the AFE of the proposed instrument and are directly digitized and depicted on the computer by a commercial instrument (Powerlab 16/35) bypassing all the stages of the proposed instrument located after its AFE (Figure 3.10). In the second method (wireless transmission), the signals are recorded and digitized by the proposed instrument, are wirelessly transmitted to the receiver module and are depicted on the computer by the Powerlab 16/35 hardware. This setup aims at confirming that the proposed instrument can functionally integrate with existing commercial devices used in clinical studies and provide faithful wireless transception. It is clear that this setup can be perceived as the worst case scenario, since, in the wireless communication method, the recorded biosignals have to be digitized by the proposed instrument, converted back to analog from the DAC of the receiver module and then digitized again by the ADC of the Powerlab hardware.

One of the aims of these experiments was to record alpha wave (7.5–12.5 Hz) activity, which is accepted as the most prominent proof of an instrument's capability to

measure EEG signals. The setup included three electrodes, which were positioned as follows: 1. F3 – Ground Electrode, 2. F4 – Reference Electrode, and 3. O2 – Recording Electrode. In this test, an increased alpha wave activity is expected to appear in the spectrum of the EEG signals recorded when the subject's eyes are closed.

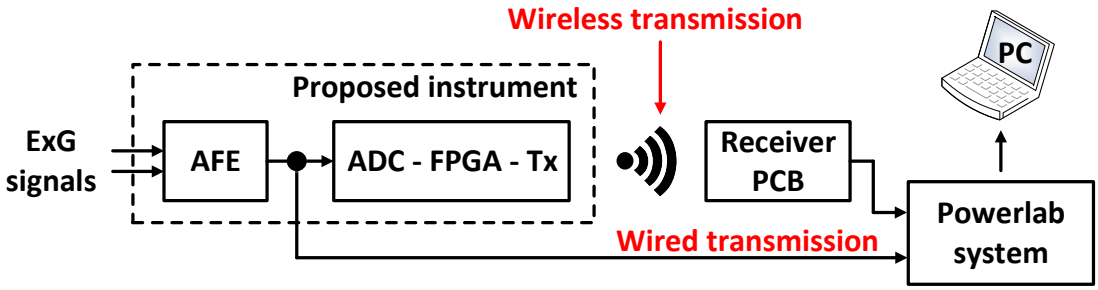

Figure 3.10: Measurement setup for comparing the quality of biosignals recorded using two different methods. In the first method (wired transmission), the signals are recorded by the AFE of the proposed instrument and are directly digitized and depicted on the computer by a commercial instrument (Powerlab 16/35). In the second method (wireless transmission), the signals are recorded by the proposed instrument, are wirelessly transmitted to a receiver module and are depicted on the computer by the Powerlab 16/35 hardware.

In principle, EMG signals are recorded using either minimally invasive or skin surface electrodes. For this study, three skin surface disposable solid gel electrodes (contact size 15x20 mm), produced by Unimed, were placed at the following upper limb positions:

1. Palmaris longus muscle – Recording Electrode
2. Metacarpal bones – Reference Electrode
3. Proximal phalanx – Earth Electrode

Regarding ECG signal acquisition, a simple three electrode monitoring setup was prepared by using two electrodes for active monitoring and a third one as ground electrode [95]. The electrodes were used in lead I (RA-LA) configuration leading to a bipolar signal acquisition. The ground electrode was placed on the right leg ankle. The electrodes used for the signal acquisition are the Max-TAB resting electrodes (contact size 20×24 mm), produced by Unimed.

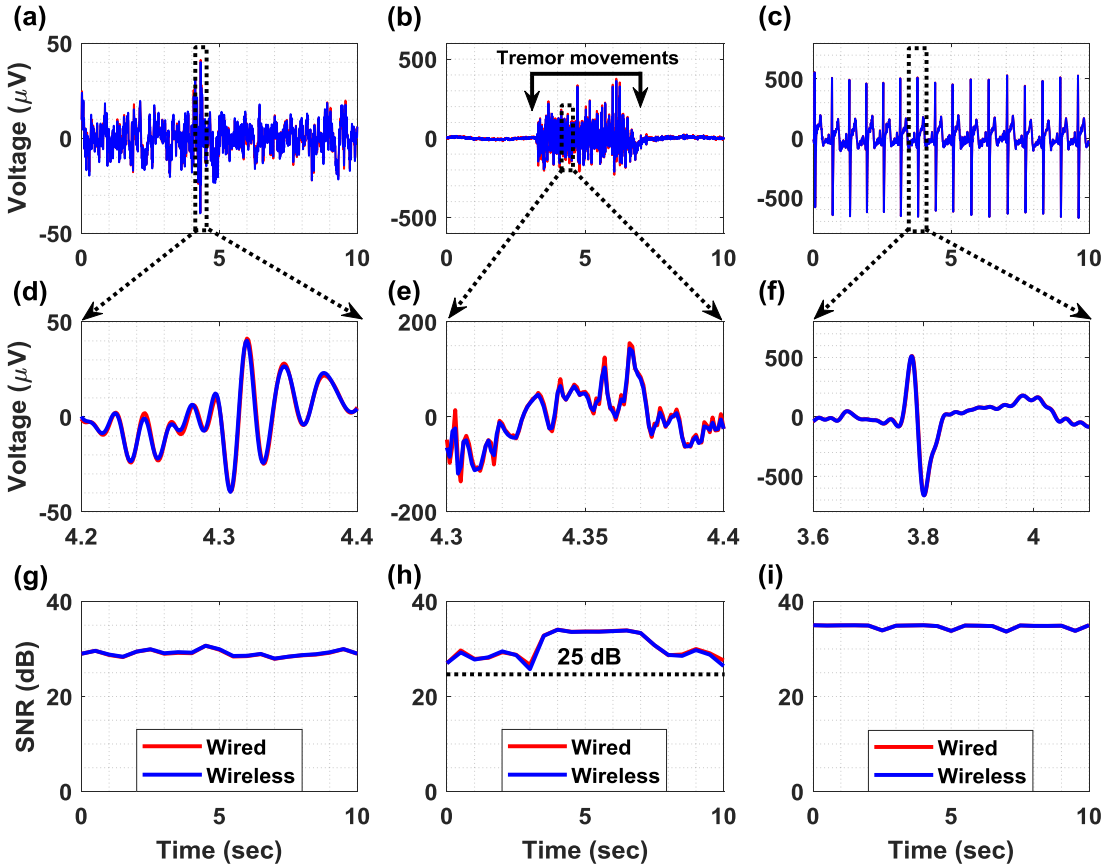

Figure 3.11: Biosignal acquisition using the setup presented in Figure 3.10. The applied gain was 60 dB and the sampling frequency was equal to 1 kSPS. (a) Wired vs wireless EEG acquisition. (b) Wired vs wireless EMG acquisition from the palmaris longus muscle. (c) Wired vs wireless ECG acquisition. (d) Detailed view of the wireless and wired time-domain EEG recordings. (e) Detailed view of the wireless and wired time-domain EMG recordings. (f) Detailed view of the wireless and wired time-domain ECG recordings. (g) The SNR of the EEG signals was measured and found to be continuously higher than 25 dB. (h) The SNR of the EMG signals was measured and found to be continuously higher than 25 dB. (i) The SNR of the ECG signals was measured and found to be continuously higher than 30 dB. SNR, signal-to-noise ratio.

The ExG (EEG, EMG and ECG) signals, which are exhibited in Figure 3.11 after removing the applied gain of 60 dB, were recorded at 1 kSPS. Figure 3.11a illustrates a time-domain EEG recording acquired using both of the previously described methods (wired and wireless). Regarding the EMG measurement (Figure 3.11b), the high amplitude signal was recorded while the subject was producing tremor movements. Moreover, Figure 3.11c shows that ECG signals were successfully

recorded. In order to examine the performance cost introduced by the wireless transmission method, the normalized root mean square error (RMSE) between the time-domain recordings acquired using the two methods (wired and wireless transmission methods) was calculated and found to be equal to 1.7%, 1.1% and 0.39 % for the EEG, EMG and ECG measurement setups, respectively. These errors can be considered tolerable taking into account that this experiment assesses the above-described worst-case scenario.

SNR is defined as the ratio of the signal power to the noise power. The noise recorded from the biopotential recording AFE with both the inputs of the front-end INA grounded (see Figure 3.7b), was used for the calculation of the SNR. Figures 3.11g, 3.11h and 3.11i illustrate the achieved SNR over time during the EEG, EMG and ECG recording sessions, respectively. It is clear that, during all recording sessions, the achieved SNR values were higher than 25 dB.

The alpha waves test, presented in Figure 3.12, shows that in the band 7.5 – 12.5 Hz, the amplitude spectrum of the EEG signals recorded when the eyes are closed is significantly higher than the amplitude spectrum of the signals recorded when the eyes are open (Figure 3.12a). The same conclusion is derived from Figure 3.12b where alpha waves in the band 7.5 – 12.5 Hz, during the eyes closed period, are clearly visible.

Another important observation is that the amplitude spectrums of the EEG signals recorded using the wired and wireless data transmission methods, not only approximate each other, but also they are in perfect agreement with the amplitude spectrum recorded (at 1 kSPS) by a high-performance commercial bioamplifier (Powerlab 26T, ADInstruments) (see Figure 3.12a). This finding suggests that the proposed instrument can provide reliable recordings even when its enhanced recording capabilities are not fully exploited. Indeed, in both methods adopted in this series of experiments (wired and wireless), the biosignals recorded by the proposed instrument were finally digitized by the Powerlab 16/35 system, which provides 16-bit resolution for the analog-to-digital conversion process (whereas the proposed instrument can provide 24-bit resolution, if used independently).

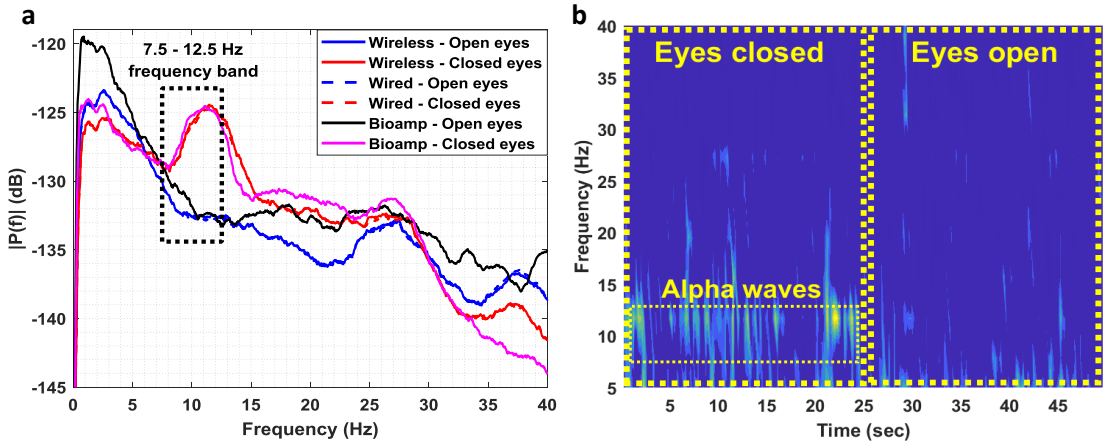

Figure 3.12: (a) Amplitude spectrum (the reference level of amplitudes equals 1 V) of EEG signals recorded by the proposed instrument when the subject's eyes are open and when they are closed. A high-performance commercial bioamplifier (Powerlab 26T, ADInstruments) was also used as a reference instrument in this series of experiments. It is clear that in the 7.5 – 12.5 Hz band the amplitude spectrum of the EEG signals recorded when eyes are closed is significantly higher than the amplitude spectrum of the signals recorded when eyes are open. Furthermore, the results acquired using the wireless transmission method: 1) are in full agreement with the results acquired using the wired transmission method, and 2) are in full agreement with the results acquired using the commercial bioamplifier. (b) EEG spectrogram calculated from the EEG data wirelessly recorded by the proposed instrument. Alpha waves in the 7.5 – 12.5 Hz band during the eyes closed period are clearly visible.

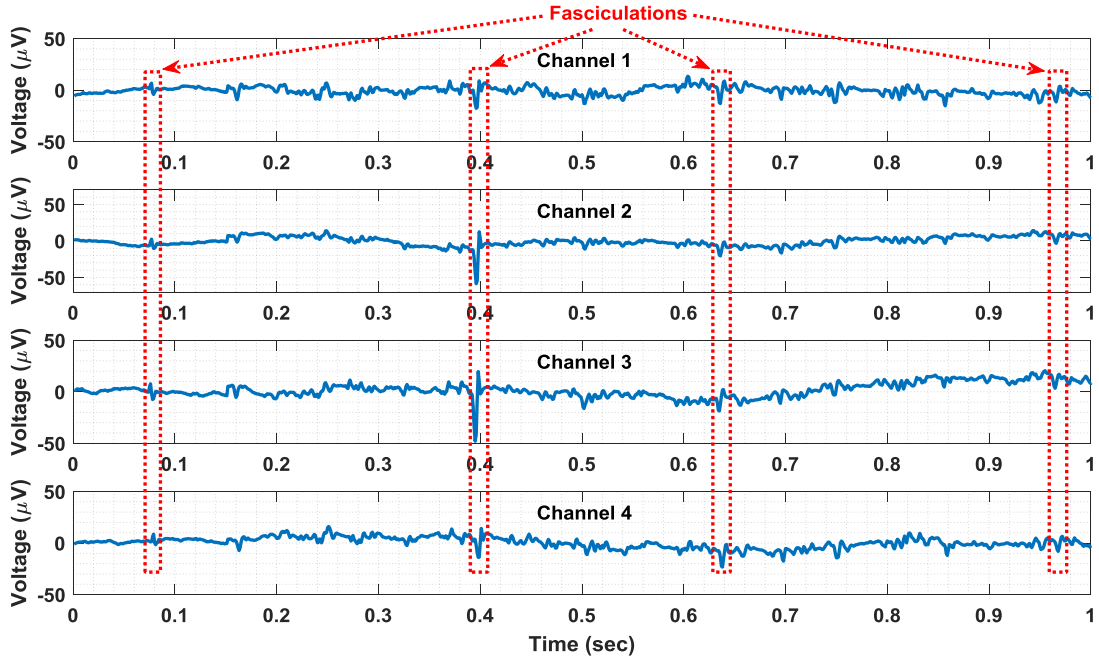

Figure 3.13: Wireless recording of benign fasciculations.

Finally, benign fasciculations have been recorded from a healthy subject using the wireless transmission method. The recorded fasciculations are shown in Figure 3.13. The electrodes that were used for this recording session are the same with the ones used to record EMG signals. Referring to Figure 3.13, it is clear that the proposed instrument can successfully record both weak and strong fasciculations. Hence, it could be used as a research tool to distinguish benign fasciculations and those related to amyotrophic lateral sclerosis (ALS) on the basis of their waveforms or firing characteristics [21]. It could also be used as a wireless, home monitoring device for increasing the biosignal acquisition time and thus enhancing the diagnostics of ALS.

3.3.5 *In vivo* recordings of LFPs

To provide an *in vivo* proof-of-function, LFPs were recorded from the thalamus of a non-human primate, at the end of a non-recovery procedure that was performed for the primary purpose of another ongoing study. A female rhesus macaque was anesthetised with a ketamine/midazolam/alfentanil infusion and a segmented DBS electrode (electrode A, model DB-2201, Boston Scientific Neuromodulation) was implanted into the thalamus as shown in Figure 3.14. The experiments performed on the non-human primate were approved by the local ethics committee at Newcastle University and performed under appropriate UK Home Office licenses in accordance with the Animals (Scientific Procedures) Act 1986.

LFP signals were differentially recorded through contacts 1 and 3 of electrode A (illustrated as A_1 and A_3 in Figure 3.14, respectively). The non-human primate was under anaesthesia during the entire experiment with the head held in a primate stereotactic frame, which was connected to the ground of the recording system. The LFP signals recorded by the wireless instrument were digitized at a sampling frequency of 1 kSPS and were wirelessly transmitted to the receiver module. Then, they were depicted on a computer by the Powerlab data acquisition system (wireless transmission method - described in Figure 3.10). As shown in Figure 3.15, the proposed instrument can wirelessly provide low-noise recordings of weak LFP signals in a noisy animal clinic environment.

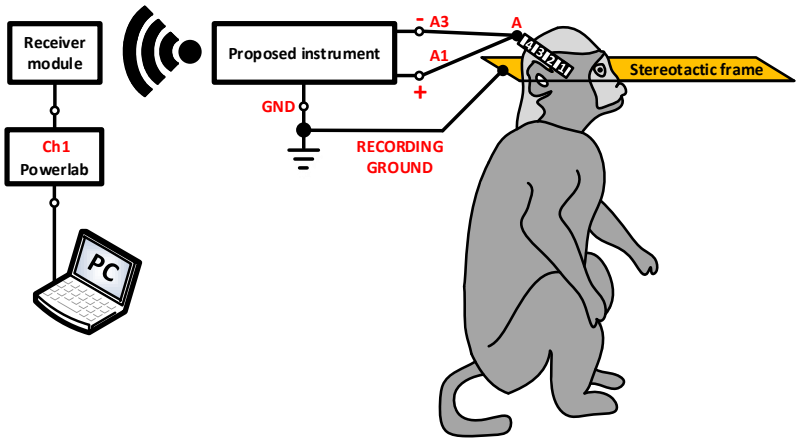

Figure 3.14: Experimental setup for evaluating the recording capabilities of the proposed instrument *in vivo*. A DBS electrode (electrode A, model DB-2201, Boston Scientific Neuromodulation) was implanted into the thalamus of an anaesthetised non-human primate. LFP signals were differentially recorded through contacts 1 and 3 of electrode A. The non-human primate was under anaesthesia with the head held in a primate stereotactic frame, which was connected to the ground of the recording system. The LFP signals were digitized by the wearable/wireless instrument at a sampling frequency of 1 kSPS and were wirelessly transmitted to the receiver module (wireless transmission method – described in Figure 3.10).

3.3.6 Recording of resonant neural response

In this experiment, a signal segment containing ERNA recorded by a dc-coupled commercial instrument from the STN at 2048 SPS, was injected at the instrument's biopotential recording AFE by a commercial waveform generator (Agilent 33220A). The temporal response of the proposed instrument is shown in Figure 3.16a. Since the original signal was recorded at 2048 SPS and the maximum sampling frequency that is allowed by the Zigbee protocol for real-time wireless transmission of raw data is equal to 1 kSPS, the wired transmission method was selected for recording this neural activity (the sampling frequency of the Powerlab 16/35 system was set at 4 kSPS). However, this limitation on the maximum allowable sampling frequency imposed by the employed wireless transmission protocol (Zigbee) for real-time data acquisition does not entail that the instrument is incapable of wirelessly transmitting ERNA because the frequency band that is related to evoked potentials ranges from 300 to 400 Hz, which can normally be recorded at 1 kSPS by the ADS1298 chip and wirelessly transmitted to the receiver module.

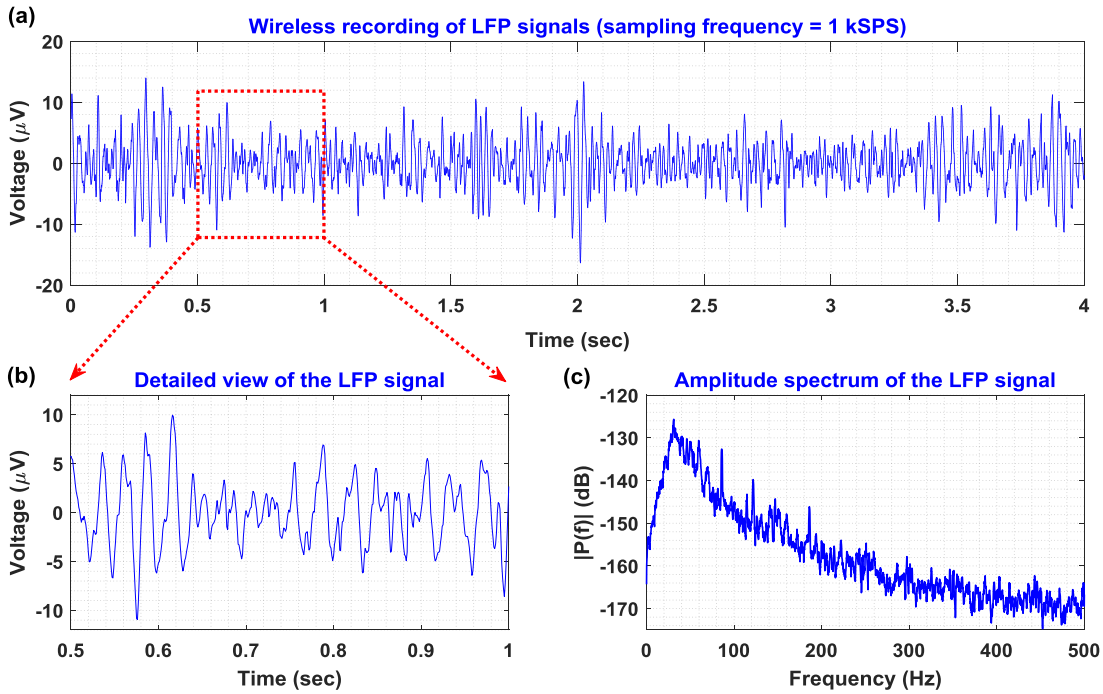

Figure 3.15: (a) Differential LFP recordings acquired from the thalamus of an anaesthetised non-human primate with the experimental setup illustrated in Figure 3.14. (b) A detailed view of the recorded LFPs reveals their small amplitudes (< 20 μV peak). (c) Amplitude spectrum of the recorded LFPs. Clearly, the proposed instrument can wirelessly provide low-noise recordings of weak LFP signals in a noisy clinical environment.

The main aim of this experiment was to ensure that: 1) no overshoot or ringing is produced by the ac-coupled AFE of the instrument as a response to DBS, and 2) the instrument's AFE can reliably record the decaying oscillatory activity that characterizes the evoked potentials recorded from the STN. Indeed, the biopotential recording AFE exhibits a fast and free from any overshoot or ringing effects transient response to the stimulation pulses (see Figure 3.16c). Hence, it can successfully record the ERNA of interest, which is considered to be the signal that appears 4 msec after the last DBS pulse and lasts for 20 msec in total (dotted rectangle in Figure 3.16c) [20].

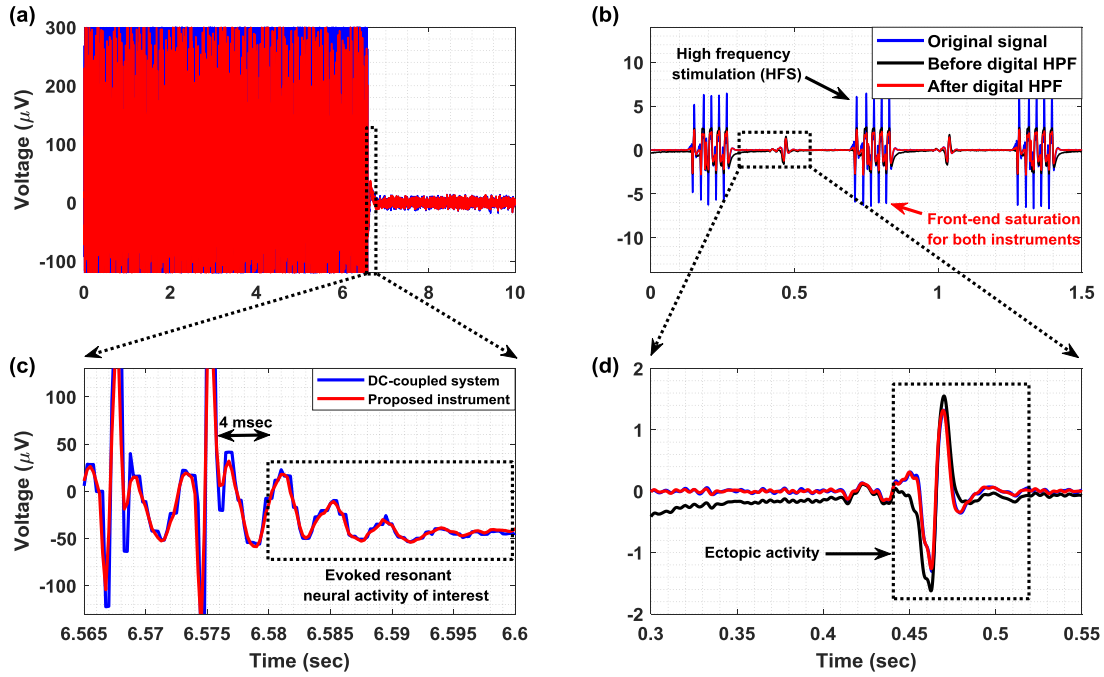

Figure 3.16: (a) Temporal response of the proposed instrument's AFE when a signal segment containing ERNA, recorded by a dc-coupled commercial instrument from the STN at 2048 SPS, is injected to the instrument's AFE. The signal was recorded by the instrument's AFE and was then digitized by the Powerlab hardware at 4 kSPS (wired transmission method). (b) Temporal response recorded by the proposed instrument with and without the application of a real-time digital high-pass filter at 30 Hz when a signal that contains high-frequency stimulation (HFS) pulses and ectopic activity was injected to the biopotential recording AFE's input by a waveform generator (Agilent 33220A). The signal was sampled by means of the wearable/wireless instrument at 1 kSPS, was wirelessly transmitted to the receiver module and was depicted on the computer using the Powerlab 16/35 hardware (wireless transmission method). (c) Detailed view of the successfully recorded ERNA of interest. (d) Detailed view of the successfully recorded ectopic activity. It is clear that the application of a digital high-pass filter enables real-time recording of a high-quality signal, which approximates the signal recorded by the dc-coupled commercial medical device.

3.3.7 Recording of PV ectopic activity

In this experimental procedure, a signal that contains HFS pulses and ectopic activity (represented by a solid blue line in Figure 3.16b) was injected to the input of the proposed instrument by a waveform generator (Agilent 33220A). This signal was previously recorded (in bipolar mode from a catheter placed in the coronary sinus) using a commercially available wired and dc-coupled medical device with the sampling

frequency set at 1 kSPS. The wireless instrument sampled the input signal at 1 kSPS and wirelessly transmitted it to the receiver module (wireless transmission method).

The temporal response of the proposed instrument with (solid red line) and without (solid black line) the application of a real-time digital high-pass filter at 30 Hz is presented in Figure 3.16b. Clearly, the ac-coupled AFE of the proposed instrument exhibits a fast transient response (solid black line), which allows it to recover very quickly from the saturation state (+2.5 mV) it reached due to the high-amplitude HFS pulses and thus record the ectopic activity of interest. Moreover, as shown in Figure 3.16d, a digital high-pass filter applied on the signal recorded by the proposed instrument rejected in real-time the dc offset induced by stimulation, producing an output (solid red line) that approximates the signal recorded by the commercial dc-coupled medical device. This measured result suggests that the application of a digital high-pass filter can significantly enhance the dc offset suppression capabilities of the AFE and increase the quality of the recorded signals. It is important to note here that the AFE of the commercial medical device also saturated during HFS because its maximum dynamic range was set by the clinicians at ± 5 mV so that a sufficiently high gain is ensured.

3.3.8 Recording of acceleration signals

In this experiment, acceleration signals recorded by the accelerometer located on the main PCB of the proposed instrument, were digitized at 1 kSPS and were wirelessly transmitted to the receiver module (wireless transmission method). Figure 3.17 shows the acceleration signals recorded during three separate sessions. During the first session, movements of the proposed instrument's PCB, where the accelerometer is located, were produced on the x-axis for a duration of approximately 9 seconds (Figure 3.17a). During the second session, movements of the proposed instrument's PCB were produced on the y-axis for a duration of approximately 9 seconds (Figure 3.17b). During the third session, movements of the proposed instrument's PCB were produced on the z-axis again for a duration of approximately 9 seconds (Figure 3.17c). In all recording sessions, the instrument started from immobility and at the end of the

produced movements it returned back to immobility. Clearly, under all examined circumstances (tremor movements in X, Y and Z axes), the accelerometer was able to successfully discriminate the state of immobility from the state where tremor occurs.

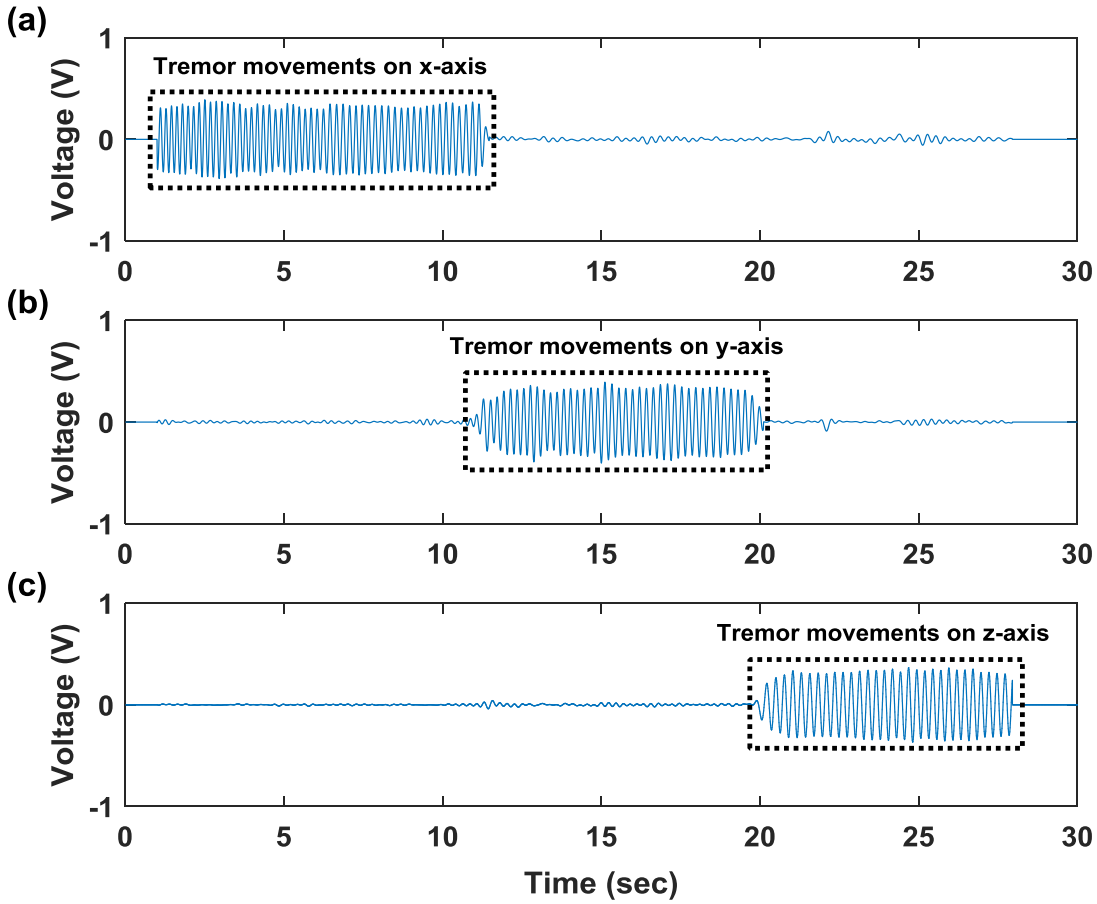

Figure 3.17: Time-domain profiles of acceleration signals recorded during three separate sessions. (a) during the first session, movements of the proposed instrument's PCB, where the accelerometer is located, were produced along the x-axis for a duration of approximately 9 seconds (b) during the second session, movements of the proposed instrument's PCB were produced along the y-axis for a duration of approximately 9 seconds (c) during the third session, movements of the proposed instrument's PCB were produced along the z-axis for a duration of approximately 9 seconds. In all recording sessions, the instrument started from immobility and at the end of the produced movements it returned back to immobility. Clearly, under all examined circumstances (tremor movements in X, Y and Z axes), the accelerometer was able to successfully discriminate the state of immobility from the state where tremor occurs.

3.3.9 Comparison with other biosignal acquisition systems

The aim of the series of tests presented in this section was to compare the performance of the designed biopotential recording AFE with a commercial high-gain differential amplifier (model DP-301, Warner instruments) by injecting extremely weak biosignals to their inputs. More specifically, LFP signals were injected to the inputs of the two AFEs by a waveform generator (Agilent 33220A) and the quality of the output signals was assessed in both time and frequency domains. In the time domain, the normalized RMSE between the output of each AFE and the original LFP signal was used to evaluate the quality of biosignal recording. The normalization for the RMSE calculation was performed over the range of the reference signal, which is the original LFP signal.

In order to compare the two AFEs on an equal footing, their analog outputs were digitized by the same ADC (ADC of the Powerlab 16/35 system, which provides a 16-bit resolution) at 1 kSPS. Next, a third device was introduced in the measurement setup (Bioamplifier/Powerlab 26T) to record the same LFPs at 1 kSPS. The role of this device was to act as an independent reference instrument that is optimized for measuring weak bioelectrical signals such as EEG signals. The analog high-pass filters included in the DP-301 amplifier (cut-off frequency at 1 Hz) and the bioamplifier (cut-off frequency at 0.5 Hz) were activated so that their temporal responses can be compared with the temporal response of the proposed instrument's ac-coupled AFE (cut-off frequency at 0.5 Hz) on an equal footing. Moreover, the gain of the DP-301 amplifier was set at 60 dB so that it is equal with the gain introduced by the biopotential recording AFE. Finally, the resolution of the reference instrument (bioamplifier/Powerlab 26T) was set at ± 100 μV (minimum available) during the LFP signal recording sessions. The measurement setup is shown in Figure 3.18.

Referring to Figures 3.19a and 3.19c, it is clear that the output of the proposed instrument's AFE better tracks the changes occurring in the LFP signal presented at its input in comparison to the other two instruments. This is verified by the fact that the normalized RMSE between the original LFP signal and the signal recorded from the

proposed instrument's AFE is less than the errors characterizing the other two instruments. More specifically, the RMSE values that characterize the proposed instrument, the DP-301 amplifier and the bioamplifier are equal to 4%, 4.1% and 4.9%.

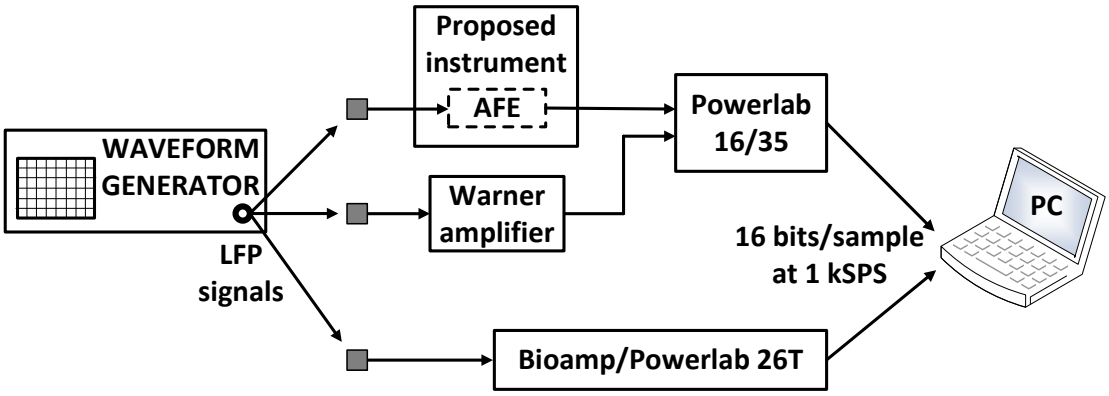

Figure 3.18: Recording of LFPs injected by a waveform generator (Agilent 33220A) to the inputs of: a) the proposed instrument's AFE, b) a commercial high-gain differential amplifier (model DP-301, Warner instruments), and c) a very high-performance commercial bioamplifier (Powerlab 26T, ADInstruments).

According to the amplitude spectrum shown in Figures 3.19b and 3.19d, the AFE of the proposed instrument provides accurate recording of the LFP signal, whereas the other two instruments cannot accurately record the frequencies of the LFP signal that are higher than 120 Hz. It is important to stress here that a significant portion of the calculated RMSE values can be attributed to the fact that four attenuators that provided 70 dB attenuation were used in order to bring the amplitude of the LFP signal injected by the waveform generator down to the level that characterizes the original LFP signal, which is approximately equal to 10 μV peak.

Referring to Figure 3.20, it is clear that the two AFEs and the reference instrument successfully recorded the ECoG signal that was injected to their inputs. This observation is verified by the calculated RMSEs, which are equal to 1.9%, 1.6% and 1.55%, for the proposed instrument, the DP-301 amplifier and the reference bioamplifier, respectively. These errors can be considered tolerable because a significant portion of them can be attributed to the fact that two attenuators that provided 40 dB attenuation were used in order to bring the amplitude of the ECoG

signal injected by the waveform generator down to the level that characterizes the original ECoG signal, which is approximately equal to 100 μV peak (the waveform generator is not able to inject signals that are weaker than 10 mV peak). These attenuators introduce some noise and distortion in the ECoG signal that finally reaches the inputs of the three instruments.

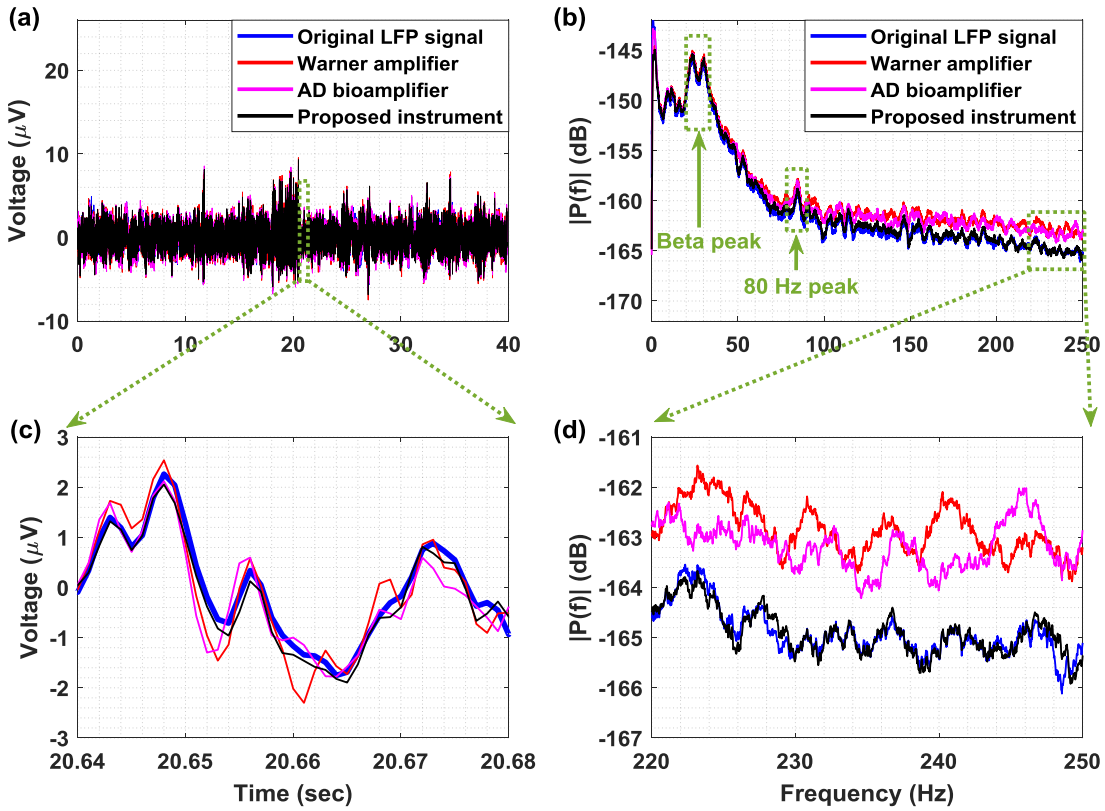

Figure 3.19: (a) Recording of LFPs. The original LFP signal, which was previously recorded from the STN in a patient with PD withdrawn from levodopa, was injected by a waveform generator (Agilent 33220A) to the inputs of the proposed instrument's AFE, the DP-301 differential amplifier and the bioamplifier included in the Powerlab 26T data acquisition system. (b) Amplitude spectrum of the signals presented in Figure 3.19 (a). (c) The output of the proposed instrument's AFE better tracks the changes occurring in the original LFP signal in comparison to the other two instruments. This is verified by the fact that the RMSE between the original LFP signal and the signal recorded by the proposed instrument's AFE is less than the errors characterizing the other two instruments. (d) The detailed amplitude spectrum shows that the AFE of the proposed instrument provides accurate recording of the LFP signal, whereas the other two instruments cannot accurately record the frequencies of the LFP signal that are higher than 120 Hz.

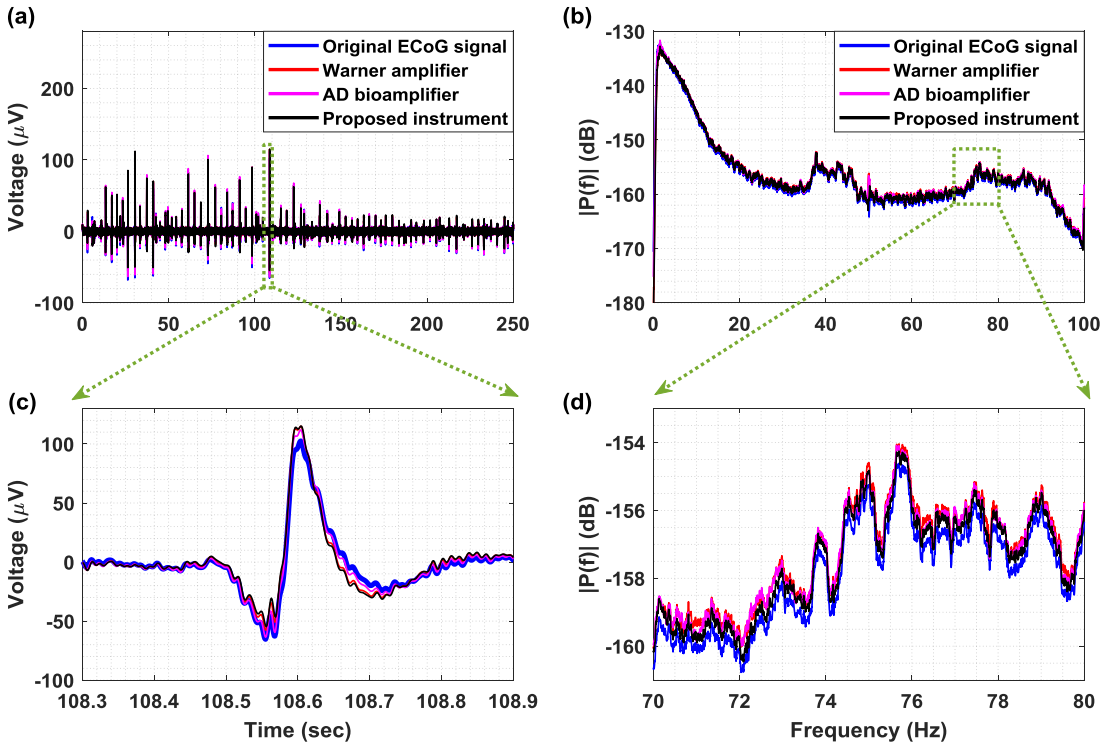

Figure 3.20: (a) Recording of ECoG signals (original signal is shown in blue) injected by a waveform generator (Agilent 33220A) to the inputs of the proposed instrument's AFE (black line), the DP-301 differential amplifier (red line) and the very high-performance bioamplifier included in the Powerlab 26T data acquisition system (pink line). (b) Amplitude spectrum of the signals presented in Figure 3.20 (a). (c) It is clear that the three instruments are able to accurately record the injected ECoG signal. (d) The detailed amplitude spectrum verifies the conclusion that the recorded ECoG signals are of high quality. ECoG, electrocorticography.

Furthermore, Figure 3.21a exhibits the amplitude spectrum of the output voltage recorded from the AFE of the proposed instrument (black line), the DP-301 differential amplifier (red line) and the bioamplifier included in the Powerlab 26T data acquisition system (pink line) when two sinusoidal single tones (5 Hz and 25 Hz, amplitude 100 nV peak) were injected sequentially to the inputs of the instruments and were sampled at 1 kSPS. To push the limits of the recording capabilities of the three instruments towards their noise floors, two weak sinusoidal single tones (5 Hz and 25 Hz, amplitude 30 nV peak) were injected sequentially to the inputs of the instruments and were also sampled at 1 kSPS (Figure 3.21b).

Referring to Figures 3.21c and 3.21d, it is clear that the AFE of the proposed instrument and the bioamplifier can accurately record both of the weak sinusoidal tones presented at their inputs, whereas the DP-301 differential amplifier detected the tones but it did not provide an accurate recording. Furthermore, Figure 3.21 clearly shows that the noise floor of the proposed instrument is lower than the noise floors of the other two instruments. A comparison of the proposed instrument's capabilities against the ones provided by the other two devices (DP-301 amplifier and Powerlab 26T) is drawn in Table 3.2.

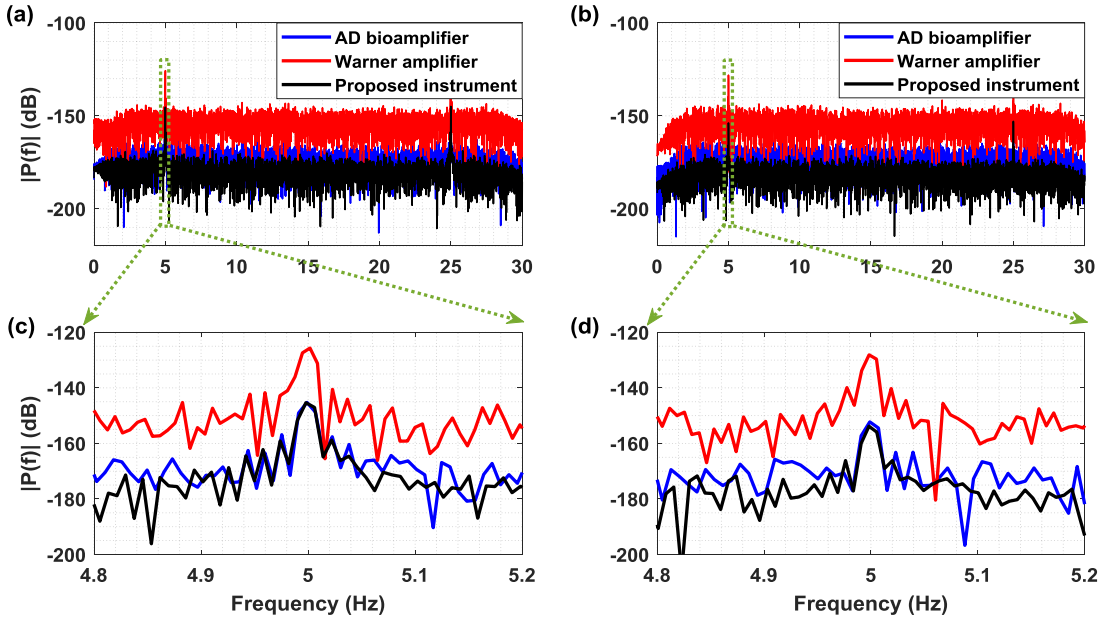

Figure 3.21: (a) Amplitude spectrum of the output voltage recorded from the AFE of the proposed instrument, the DP-301 Warner differential amplifier and the bioamplifier included in the Powerlab 26T data acquisition system when two sinusoidal single tones (5 Hz and 25 Hz, amplitude 100 nV peak) were injected sequentially to the inputs of the instruments. The outputs of the three instruments were sampled at 1 kSPS. (b) Amplitude spectrum of the output voltage recorded from the thee instruments when two sinusoidal single tones (5 Hz and 25 Hz, amplitude 30 nV peak) were injected sequentially to the inputs of the instruments. The outputs of the three instruments were sampled at 1 kSPS. (c) It is clear that the AFE of the proposed instrument and the bioamplifier can accurately record the weak sinusoidal tone, whereas the DP-301 differential amplifier detects the tone but it cannot provide an accurate recording. (d) As in the case of the 100 nV peak sinusoidal tone, only the AFE of the proposed instrument and the bioamplifier can precisely record the 30 nV peak sinusoidal tone. It is important to note here that the noise floor of the proposed instrument is lower than the noise floors of the other two instruments.

Table 3.2: Comparison of the proposed instrument with the Warner amplifier and the bioamplifier included in Powerlab 26T.

Parameters	Warner amplifier	Bioamplifier in Powerlab 26T	**This work**
Number of channels	1	2	5 (+3)
Type of biosignals	EEG, ECG, extracellular spikes	ECG, EMG, EEG	ExG, ECoG, LFP, ERNA, body position and movement, PV ectopic activity (+ amperometric/ potentiometric)
Supply of the ADC	-	±10 V	±2.5 V
Voltage gain	40-80 dB	54-100 dB	60 dB
Input voltage range	±1 mV to ±100 mV	±100 µV to ±20 mV	±2.3 mV
Maximum available bandwidth	DC to 10 kHz	Full bandwidth	0.5 – 500 Hz
Input impedance	1000 GΩ	100 MΩ	200 GΩ
Input referred noise	1.52 µV rms (1 Hz-10 kHz)	< 1 µV rms (0.5-2 kHz)	0.169 µV rms (0.5-500 Hz)
DC tolerance	±3 V	±300 mV	±85 mV
CMRR	100 dB	110 dB	134 dB
Maximum resolution of the ADC	Purely analog output	16 bits	24 bits
Maximum sampling frequency	Purely analog output	100 kSPS	1 kSPS (32 kSPS for wired)
Hours of continuous operation	200 (4 batteries 9V)	Mains powered	8 (1 Ah lithium battery)
Wireless capability	No	No	Yes (Zigbee)
Area (length × width)	350 cm^2	500 cm^2	44 cm^2 (PCB area)

Another important factor that needed to be examined was the latency added by the wireless transmission method for the wireless transmission of eight channels of data. This latency was measured and found to be approximately equal to 1 msec. It is attributed to the time required for the wireless transmission (= 512 μsec) and the time needed for the serial peripheral interface (SPI) communication between the other blocks of the instrument's design. More specifically, 36 μsec are needed for the ADS1298-FPGA communication, 107 μsec for the FPGA-Tx communication, 36 μsec for the Rx-FPGA communication and finally another 32 μsec for the FPGA-DAC communication (in total 723 μsec). Moreover, the integrity and reliability of the wireless biosignal recordings have been confirmed for a distance between the proposed instrument and the receiver module up to 5 m. Finally, it should be noted here that no difficulties were observed in normal operation of the proposed system when the wearable/wireless device and the receiver module were placed in two different adjacent rooms that were separated by a wall.

A comparison of the proposed instrument with (portable and implantable) wireless commercial biopotential acquisition systems is given in Table 3.3. This work demonstrates the highest CMRR and input impedance, the lowest input referred noise and smallest size among the state-of-the-art instruments presented in this table. Moreover, compared to the TMSI Mobita device, it can provide 8 hours of continuous operation (continuous wireless transmission of all eight channels of the simultaneous-sampling ADC included in the instrument) with a smaller lithium battery. This is attributed to the fact that Mobita uses the Wi-Fi protocol for wireless data transmission, which allows for a higher maximum sampling rate (2000 SPS) at the expense of higher power consumption and shorter battery life. It is important to highlight here that, to the best of our knowledge, there are no commercial, small, battery-powered, wearable and wireless recording-only instruments that claim the capability of recording ECoG signals. As shown in Table 3.3, it is clear that, compared to high-performance bidirectional interface systems (such as the Activa PC+S neurostimulator from Medtronic), which are widely used in applications that include concurrent LFP sensing and closed-loop neurostimulation, the proposed device is better suited for applications

Table 3.3: Comparison of the proposed instrument with commercial (portable and implantable) wireless biopotential acquisition systems.

Parameters	TMSI Mobita	TMSI Mobi	Activa PC+S	**This work**
Number of channels	32	6 (+4)	2	5 (+3)
Type of biosignals	ExG, body position and movement	ExG, (+ temperature, respiration, body position and movement)	LFP/ECoG	ExG, ECoG, LFP, ERNA, body position and movement, PV ectopic activity (+ amperometric/ potentiometric)
Supply of the ADC	±2 V	±2 V	1.7 - 2.2 V	±2.5 V
Voltage gain	20 dB	26 dB	48 - 66 dB	60 dB
Input voltage range	±200 mV	±100 mV	±500 µV to ±4.4 mV (for 2.2V supply)	±2.3 mV
Maximum available bandwidth	DC up to 0.13 × sample frequency	-	0.5 – 260 Hz	0.5 – 500 Hz
Input impedance	> 100 MΩ	> 100 MΩ	-	200 GΩ
Input referred noise	< 0.4 µV rms (0.1 – 10 Hz)	< 1 µV rms	< 1 µV rms	0.169 µV rms (0.5-500 Hz)
DC tolerance	-	-	-	±85 mV
CMRR	> 100 dB	> 90 dB	> 80 dB	134 dB
Maximum resolution of the ADC	24 bits	24 bits	10 bits	24 bits
Maximum sampling frequency	2000 SPS	2048 SPS	422 SPS	1 kSPS (32 kSPS for wired)
Hours of continuous operation	6 to 8 (4.1 Ah lithium battery)	- (2 AA batteries)	-	8 (1 Ah lithium battery)
Wireless capability	Yes (Wi-Fi)	Yes (Bluetooth)	Yes (175 kHz near-field inductive)	Yes (Zigbee)
Area (length × width)	105 cm^2	112 cm^2	39 cm^2	44 cm^2 (PCB area)

where multi-channel (> 4 channels) and high-resolution (> 10 bits) ECoG recording (without stimulation) is required.

Moreover, a comparison of the proposed instrument with other state-of-the-art wearable and wireless biopotential acquisition systems that exist in the literature and also use discrete (commercial) components as building blocks is performed in Table 3.4. These systems can record biopotential signals of a specific type by using either commercial analog front-end chips (e.g. the Intan RHD2132 chip in [96] or the ADS1299 chip in [97]) or commercially available components to build application-specific analog front-ends (e.g. in this work and in [98]). It is clear that the proposed instrument achieves a noise performance that is significantly better than the noise performance provided by the other three devices. It is important to emphasize here that although two of the devices presented in Table 3.4 (in [97] and [98]) offer lower bandwidth than the wireless device presented here, they still provide an integrated noise value that is higher than the one offered by the proposed instrument. The versatility of the biopotential recording AFE analysed in this Chapter and the real-time wireless biosignal transmission that can be offered by the employed wireless protocol (IEEE 802.15.4) at 1 kSPS sampling frequency allow the proposed instrument to record a wider variety of biosignals compared to the other systems, with the lowest wireless transmission latency. In addition, it offers the highest input impedance, which allows it to efficiently interface with high-impedance electrodes (e.g. segmented electrodes in DBS), and the highest CMRR value, which can be very useful in applications where large common-mode disturbances (stemming from the application of strong stimulation pulses in simultaneous biosignal recording and stimulation setups) have to be rejected. The remaining features of the suggested wireless device are equally good or comparable to the features of the other wearable and wireless systems presented in Table 3.4.

Finally, a comparison of the biopotential recording AFE presented in this Chapter with state-of-the-art ASICs for biopotential signal acquisition is given in Table 3.5. As anticipated, a tradeoff exists between ultra-low power consumption (state-of-the-art ASICs) and superior noise performance (proposed instrument's AFE).

Table 3.4: Comparison of the proposed instrument with other state-of-the-art wearable and wireless biopotential acquisition systems existing in the literature.

Parameters	[96]	[97]	[98]	**This work**
Number of channels	32	8	4	5 (+3)
Type of biosignals	EMG	ECG, EMG	EEG, LFP	ExG, ECoG, LFP, ERNA, body position and movement, PV ectopic activity (+ amperometric/ potentiometric)
Voltage gain	46 dB	≈ 28 dB (max)	≈ 54 dB	60 dB
Input voltage range	±5 mV	±100 mV	±1.15 mV	±2.3 mV
Maximum available bandwidth	10 - 500 Hz	0 - 250 Hz	1.5 - 100 Hz	0.5 – 500 Hz
Input impedance	1.3 GΩ (10 Hz)	≈ 620 MΩ (10 Hz)	47 kΩ (10 Hz)	≈ 8 GΩ (10 Hz)
Input referred noise	< 3 μV rms	0.2 μV rms (0-250 Hz)	≈ 0.606 μV rms (1.5-100 Hz)	0.169 μV rms (0.5-500 Hz)
CMRR	82 dB	110 dB	-	134 dB
Maximum resolution of the ADC	16 bits	24 bits	16 bits	24 bits
Maximum sampling frequency	2048 SPS	500 SPS (16 kSPS for wired)	500 SPS	1 kSPS (32 kSPS for wired)
Hours of continuous operation	5 (600 mAh 1-Cell LiPo battery)	13.6 (1700 mAh battery)	6 to 8 (CR1/3N lithium ion button-cell battery)	8 (1 Ah lithium battery)
Wireless capability	Yes (Wi-Fi)	Yes (Bluetooth)	Yes (2.4 GHz MSK)	Yes (Zigbee)
Latency	12 ms	-	-	1 ms
Max. transmission range	22 m	10 m	3 – 5 m	5 m
Area (length × width)	10.2 cm^2	21.7 cm^2 (PCB area)	4.76 cm^2	44 cm^2 (PCB area)

Table 3.5: Comparison of the proposed instrument's AFE with state-of-the-art ASICs for biopotential signal acquisition (note that, as anticipated, a tradeoff exists between ultra-low power consumption (state-of-the-art ASICs) and superior noise performance (proposed instrument's AFE)).

Parameters	[99]	[100]	[101]	[43]	**This work**
Supply	0.2/0.8 V	1.8 V	1.8 V	3 V	±5 V
Technology	0.18 µm CMOS	0.8 µm CMOS	0.18 µm CMOS	0.5 µm CMOS	-
Voltage gain	776 V/V	100 V/V	3-100 V/V	10 V/V	1000 V/V
Input impedance	≈ 100 MΩ	> 7.5 MΩ	> 2 GΩ	> 100 MΩ	200 GΩ
Input referred noise	0.94 µV rms (0.5-670 Hz)	0.95 µV rms (0.05-100 Hz)	0.8 µV rms (0.5-100 Hz)	0.6 µV rms (0.5-100 Hz)	85 nV rms (0.5-100 Hz)
DC tolerance	-	±50 mV	Rail-to-rail	±50 mV	±85 mV
CMRR	85 dB	100 dB	82 dB	120 dB	134 dB
Current	≈ 1 µA	1.1 µA	11 µA	11.1 µA	≈ 2.5 mA

3.4 Discussion/Conclusion

The system architecture validated in this Chapter addresses several of the major challenges to the development of a small, high-performance, battery-powered, wearable and wireless multi-instrument that is intended to be used in the ICU or in a High Dependency Unit, or in patient home monitoring studies. A demanding task when designing a readout circuit that is intended to be used in a clinical ward, is to ensure that it can offer real-time biosignal recordings. This real-time character is particularly important for neuromodulation because the stimulation must be adjusted in real time based on the measured state of the neural network [16].

The strategy of rejecting all of the dc electrode offsets and high-frequency noise components by employing (usually high-order) digital filtering techniques could induce significant delays in data processing and challenge the practicality of a real-time, closed-loop neurostimulation system that would employ a digital only artefact

suppression strategy. In addition, this strategy could lead dc-coupled front-end architectures to saturation because most of the biosignals of interest are very weak (in μV scale) and thus a high gain is required to make them detectable by the front-end electronics and the subsequent ADC blocks. However, this high amplification is applied on both biosignals of interest and dc electrode offsets (in mV scale) increasing the risk of saturation. Thus, this approach was rejected.

Another commonly adopted approach is to apply a relatively small gain (< 20 dB) in the front-end amplifier stage in order to a) reduce the risk of saturation originating from the large dc electrode offset voltages produced at the electrode-tissue interface, and b) prevent the front-end electronics from being saturated during electrical stimulation in bidirectional interfaces. In this methodology, the stimulation artefacts and dc offsets can either be suppressed in subsequent AFE blocks or in the digital domain. However, such a strategy would, typically, deteriorate the CMRR of the front-end amplifier leading to an undesired increase in the input referred noise of the overall system and a subsequent decrease of its sensitivity; hence this strategy was also put aside.

An additional approach of recording ac signals which are affected by large dc electrode contact potentials in biopotential recording applications, is to place a passive low-order (either first- or second- order) high-pass filter in front of a dc-coupled differential amplifier. Passive ac-coupling networks are convenient because of their simplicity and input signal ranges, which are wider than those determined by power supply rails for active components [84]. However, the topology preceding a differential amplifier must provide a high CMRR to avoid compromising the CMRR of the entire system [84]. Front-end passive filters can lead to the degradation of the combined (passive filter plus differential amplifier) apparent CMRR of the front-end electronics due to component mismatches [84]. Hence, this strategy was also rejected.

The final adopted approach was to make use of a high-gain (=100 V/V) front-end INA in order to maintain high CMRR values (=134 dB), and add an active feedback integrator to provide high-pass characteristics at the first stage of the AFE. Next, an active 1st order high-pass filter and a passive 2nd order low-pass filter were placed in

the following stages of the AFE in order to ensure that an adequate suppression of dc electrode offsets and high-frequency noise components is accomplished in real time.

Clearly, the strategy of assigning the task of electrode dc offset and high-frequency noise rejection to the analog domain ensures that the real time character of the system is maintained. Measured experimental results show that this aim has been achieved without significantly increasing the power consumption (at least 8 hours of continuous operation is provided) and size (equal to the size of a business card) of the overall system. The proposed biopotential recording AFE consists of three active components per channel, namely one INA and two operational amplifiers, and its current consumption is approximately equal to 2.5 mA. In addition, all of the imposed requirements on the AFE design, which were presented in Table 3.1, have been satisfied. Further improvements in the dc electrode offset suppression capabilities of the instrument that will enhance its performance in applications where strong stimulation artefacts affect the quality of the recorded signals (e.g. DBS, HFS, etc.) can be achieved in the digital domain by applying real-time high-pass filters (see Figure 3.16d).

The strategy of adding a DAC on the receiver module ensures that the high-quality signals recorded and wirelessly transmitted by the proposed instrument can be successfully recorded and depicted on the computer by commercially available data acquisition systems that are widely used in the clinic. This feature enables the proposed instrument to functionally integrate with existing biosignal recording systems to offer wireless communication, while maintaining signal integrity. Indeed, in this work, the biosignals recorded and wirelessly transmitted by the proposed device were collected by the receiver module and were successfully depicted on the computer using the graphical user interface of a commercial data acquisition system (Powerlab 16/35, ADInstruments) widely used by clinicians. Moreover, the addition of a wired communication capability to the proposed device satisfies the extra need that may exist for high sampling frequency (the maximum sampling frequency offered by the ADS1298 chip is 32 kSPS) at the expense of restricted mobility. In this case, the data

sampled by the ADS1298 chip are directed from the FPGA to the computer using a USB 2.0 Hi-Speed chip located on the stacked PCB of the device.

However, having verified that the proposed instrument can offer real-time and high-quality recordings of a wide variety of bioelectrical signals, the next step towards rendering it a functional instrument that can act independently, aiming at facilitating the process of clinical decision-making, would be to design a user-friendly graphical user interface. Finally, the system in its current embodiment utilizes only a small fraction of the available FPGA resources. It is thus clear that there is still ample room for implementing digital FIR filtering blocks and closed-loop classification algorithms to further improve computational efficiency and deliver neurostimulation platforms that adapt electrical stimulation in real time based on changes occurring in the neural network.

In conclusion, the novel, versatile and state-of-the-art device designed, fabricated and tested both *ex vivo* and *in vivo* allows for real-time, low-noise and wireless recording of a plethora of bioelectrical signals for a bandwidth of 0.5 – 500 Hz. Proof of the proposed instrument's recording capabilities has been provided and its performance has been assessed quantitatively by means of a series of tests and comparisons with other high-performance biopotential readout systems (both commercial devices and academic works were used for this purpose).

Since the proposed instrument is small in size (≈ area of a business card), battery-powered, wearable and wireless, it could be used to alleviate the problem of limited mobility encountered by patients due to the fact that they are connected to bulky and mains-powered instruments. As a result, it could allow for continuous monitoring of patients, thus enhancing the diagnostics of various diseases (such as PD, essential tremor, epilepsy, ALS, AF, TBI, cardiovascular disease, etc.). Moreover, since the spectral content of some types of biosignals (e.g. LFPs) varies among patients [18], the extended passband provided by the proposed device may allow for a more accurate analysis of the spectral content recorded from different patients, facilitating the personalization of treatment for patients suffering from serious diseases.

Furthermore, the enhanced recording capabilities of this instrument, originating from its low input referred noise (8 nV/√Hz), have the potential to reveal biomarkers of various neurological disorders existing in weak neural oscillations, previously masked by the inherent noise of older biopotential acquisition systems. Hence, this tool may allow for a deeper understanding of disease mechanisms, physiology and neural processing. Finally, the proposed device can be used for the determination of features extracted from ECoG/LFP signals that could serve as biomarkers for regulating and optimizing ongoing DBS. As a result, among others, the work presented in this Chapter paves the way for the development of a portable/wearable closed-loop neurostimulation modality that utilizes neurochemical signals, acceleration signals, EMG signals and wide-frequency-range ECoG/LFPs as control signals.

Chapter 4. Design of a low-noise analog front-end for recording of field potentials during deep brain stimulation

4.1 Introduction

As previously explained, the wearable/wireless instrument presented in Chapter 3 can provide high-quality ECoG data in bidirectional BMIs where ECoG signals recorded in real time are used as control signals for the adjustment of the stimulation timing. Moreover, this instrument can precisely record LFP signals directly from the stimulation site when DBS is terminated. In addition, by implementing one of the back-end methods presented in Chapter 2 in the FPGA of the wireless instrument, a certain level of artefact suppression could be achieved during DBS. For instance, the incorporation of the method of linear interpolation for artefact cancellation into the FPGA of the wireless instrument would enable it to provide LFP recordings of a decent quality when used in applications where concurrent LFP sensing and stimulation are required. However, information during the artefact would be completely lost. Moreover, as previously explained in detail (Section 2.5.4), all the back-end artefact suppression techniques proposed so far are characterized by specific weaknesses.

Since the issue of stimulation artefact in the recorded LFP signals has not been fully addressed yet in the existing DBS systems [102], the aim of this design effort was to investigate an alternative artefact suppression strategy that: a) is able to provide wide-bandwidth (>100 Hz) LFP recordings during DBS, and b) loses minimal amount of information during DBS.

It is widely accepted in the scientific community that maintaining sensing during stimulation, rather than eliminating the available neural data by simply blanking the signal chain during stimulation, might be pivotal for closed-loop neuromodulation systems. Simultaneous neural recording and stimulation could help maximising treatment effectiveness for patients suffering from epilepsy. In an episodic disorder,

such as epilepsy, maintaining sensing during stimulation helps minimizing the temporal delay between seizure detection and adaptation of the stimulation to achieve the most effective therapy [16]. Furthermore, observations during stimulation could also reveal novel neural activity patterns that are not present in neural tissue in the absence of stimulation. This could uncover new biomarkers of various neurological disorders previously masked by stimulation.

Indeed, increasing evidence suggests that local field potential (LFP) oscillations in the beta frequency band (13–30 Hz) can be consistently picked up in the STN of patients with PD and that their strength correlates with the severity of the disease and the efficacy of therapy [16, 17]. Moreover, the last decade of LFP analysis also focused on spectral power extraction from higher frequency bands, such as high gamma (60 − 80 Hz) and 300 Hz (270 − 330 Hz) [18]. The power of these oscillations also correlates with PD motor symptoms and clinical conditions, thus being eligible as a biomarker [19].

It is thus clear that activity in the aforementioned frequency bands during stimulation could potentially be used to monitor disease progression, evaluate the effects of therapy and direct patient treatment towards more efficient therapeutical strategies. However, the large difference between the amplitude of the stimulation pulses and the relevant underlying neural activity leads to the emergence of stimulation artefacts, which hinder the accurate recording of neural signals of interest and the processing of potential biomarkers. More specifically, the normal amplitude of LFP signals can range from a few microvolts (e.g., in the basal ganglia) [103] to hundreds of microvolts in the cortex. Therefore, it is clear that the magnitude of LFPs is approximately 100 -120 dB (five to six orders of magnitude) smaller than that of the stimulation pulses. Hence, the design of an AFE that can record weak neural signals (in μV range) in the presence of strong stimulation artefacts (in Volts range) without being saturated, is, perhaps, the most demanding challenge associated with the strategy of concurrent sensing and stimulation.

To address this problem, Rossi *et al.* designed an artefact-free recording system for acquisition of LFPs from the DBS lead positioned in the STN [67]. The stimulation

artefact at 130 Hz and the higher harmonics were separated from the neural signals of interest in the frequency domain using a 10th order analog low-pass filter at 40 Hz. This high-order filter was formed by cascading five 2nd order Sallen-Key low-pass filters, designed using Butterworth coefficients. The main advantages of this system are its high gain of 100 dB and its high CMRR of 130 dB. However, the designed front-end suppresses the stimulation interference by significantly restricting the bandwidth of the recorded LFPs and it requires a ± 15 V supply to operate. Another method that has been proposed to remove stimulation artefacts is post-filtering [78]. In this case, an artefact-free biomarker is offered by subtracting the template of the stimulation signal from the recorded signal. However, this strategy degrades the signal quality [102]. In addition, it may not operate correctly in a closed-loop neurostimulation platform where the stimulation rate may fluctuate [102].

Stanslaski *et al*. designed an implantable, chronic, adaptive DBS device that benefits from an LFP/ECoG sensor [16]. This device, which was successfully validated in an ovine model of epilepsy by recording hippocampus seizure activity during and after stimulation, has been chronically implanted in humans [104]. A support vector machine (SVM) classification algorithm with spectral fluctuation processing capabilities was implemented in order to separate the biomarker from the stimulation artefact. The suggested device fits in a 39 cm^3 volume, employing front-end band-pass filtering which ensures that the front-end amplifier operates within its normal range. However, an analog third-order low-pass filter at 100 Hz is used to filter chopping clock interference and stimulation interference, thus limiting the available bandwidth for LFP recording. In addition, the authors found that interactions of stimulation artefact and sampling clock can give rise to an aliased signal in the measurement band.

Finally, Pinnell *et al.* introduced a miniature wireless system weighing 8.5 g (including battery) for rodent use that combined multichannel DBS and LFP recordings [98]. Its performance was confirmed in a working memory task that involved 4-channel fronto-hippocampal LFP recording and bilateral constant-current fimbria-fornix stimulation. The wireless system was capable of providing simultaneous recording and stimulation for a signal bandwidth between 1.5 and 100 Hz. However, the activation of DBS gave

rise to prominent stimulation artefacts on the raw LFP trace consisting of both harmonic repetitions of the stimulus frequency, and aliasing artefacts [98]. The proposed way to alleviate this problem was to reduce the intensity of stimulation and apply a low-pass filter below 80 Hz on the recorded neural signals [98].

All in all, despite the advances in concurrent neural sensing and stimulation, there is still ample room for improvement of the capabilities of both the front-end and back-end artefact suppression strategies. This Chapter[2] focuses on the interface between the neural tissue and the AFE (which amplifies the neural signals of interest and suppresses stimulation artefacts) prior to digitization and presents the design and testing of a novel AFE architecture, which allows for reliable recording of wide-frequency-range LFP signals during either unipolar or bipolar DBS.

4.2 System overview

4.2.1 System requirements, design and implementation of the AFE

As already stated in the Introduction, the power of the oscillations at physiologically significant bands, such as theta (4 − 7 Hz), alpha (8 − 11), low beta (12 − 20 Hz), high beta (20 − 35 Hz), high gamma (60 − 80 Hz), and 300 Hz (270 − 330 Hz) correlates with PD motor symptoms and clinical conditions [19]. Based on these findings, the aim of the work presented in this Chapter was to design and assess a versatile analog front-end that provides the passband needed to investigate the existence of possible biomarkers in these frequency bands. Moreover, since the LFP spectral content varies

[2] Sections 4.2 to 4.3 were excerpted from the author's open access publication with title "A high-performance 4 nV/$\sqrt{Hz}$ analog front-end architecture for artefact suppression in local field potential recordings during deep brain stimulation" published in Journal of Neural Engineering, 2019 [65]. However, some additional information was added in these Sections in order to fully cover the requirements of this Thesis. Professor Jackson, Professor Degenaar and Dr Guiho supported the non-human primate *in vivo* experiment. The contributions of the co-authors are acknowledged here. At this point, it should be highlighted that the author of this Thesis designed and developed the application specific AFE architecture (with artefact suppression capabilities) presented in this Chapter, performed the data collections and processing, and wrote the manuscript of the (published) open access research article under the supervision of Professors Drakakis, Brown and Denison.

among patients [18], the extended passband offered by the proposed AFE could lead to a more in-depth analysis of the spectral content recorded from each patient, facilitating the personalization of treatment for patients suffering from PD.

The proposed AFE is specifically designed to acquire LFPs from DBS electrodes placed in the STN. Post-operative LFPs are usually differentially recorded from two DBS electrode contacts and referred to an electrode placed on the scalp [67]. Differential LFP recording offers the advantage of limiting volume conduction [105] and leveraging the CMRR of the front-end amplifier to reduce the artefacts originating from DBS. The requirements for signal acquisition are summarized in Table 4.1.

Table 4.1: Key AFE requirements for reliable acquisition of LFPs during deep brain stimulation.

Property	Value	Units/Comments
Gain	≥ 60	dB
Integrated noise	≤ 100	nVrms (0.5 to 500 Hz)
CMRR	≥ 100	dB
DC tolerance	tens of	mV
Hours of continuous operation	≥ 24	hours
Input dynamic range	≥ ± 200	μV
High-pass knee frequency	0.5	Hz
Low-pass knee frequency	500	Hz

It is clear that a high gain, CMRR and dynamic range along with low noise levels [54] were required in order to ensure high-performance LFP recording during or without the presence of stimulation. Furthermore, according to the literature [6], when platinum-iridium (PtIr) DBS electrodes are used for recording LFP signals, adequate rejection of differential dc offset voltages that are in the order of tens of millivolts is required. Regarding stimulation artefact suppression, the requirement was to extend

the available bandwidth for LFP recording during stimulation beyond the limit of 100 Hz, which is the bandwidth offered by the existing DBS devices for recording neural signals during stimulation.

To meet the requirements for data acquisition, an AFE consisting of four main stages was designed and fabricated (Figure 4.1): (i) a differential pre-amplification stage with high-pass characteristics, which suppresses the common mode artefact voltage (CMAV); (ii) an 8th order analog notch filter that suppresses the main frequency of the differential mode artefact voltage (DMAV); (iii) a 2nd order analog low-pass filter that suppresses the high-frequency harmonics of the DMAV and defines the passband of the system; and (iv) a final amplification stage that uses a programmable gain INA to achieve the required gain.

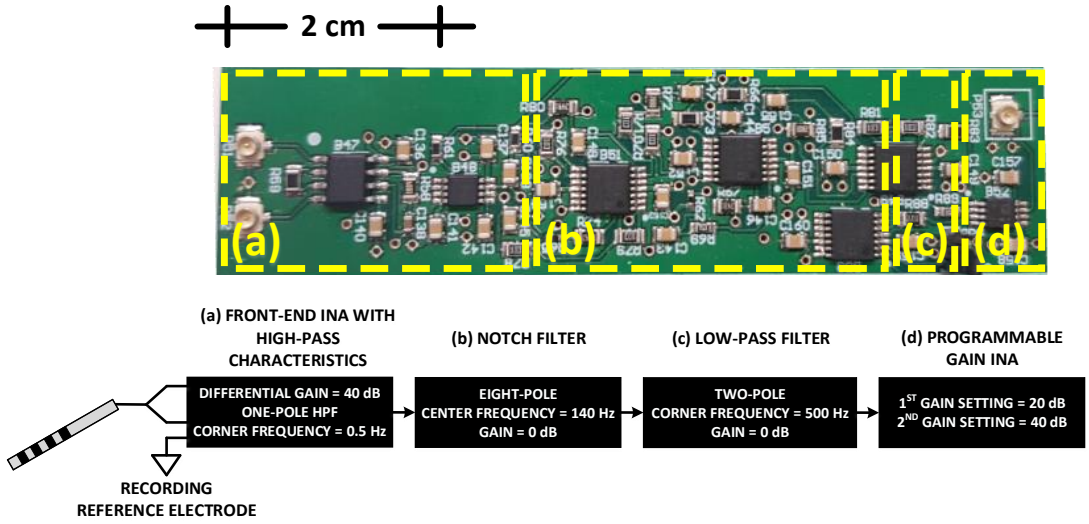

Figure 4.1: Architecture of Analog Front-End (AFE) design for artefact-free local field potential (LFP) recording during deep brain stimulation (DBS). The AFE consists of (a) a differential pre-amplification stage with high-pass characteristics, which suppresses the common mode artefact voltage (CMAV), (b) an 8th order analog notch filter that suppresses the main frequency of the differential mode artefact voltage (DMAV), (c) a 2nd order analog low-pass filter that suppresses the high-frequency harmonics of the DMAV and (d) a final amplification stage that uses a programmable gain instrumentation amplifier to achieve the required gain. Two AFEs, based on the architecture presented above, have been designed. They only differ in their second stage, where the first AFE (Chebyshev notch channel) employs an 8th order Chebyshev notch filter, whereas the second AFE (Bessel notch channel) employs an 8th order Bessel notch filter.

The pre-amplification stage consists of an ultralow noise INA (model AD8429, Analog Devices, USA). Taking into consideration that the high pulse amplitudes of 2 – 3.5 V in a typical stimulation therapy are up to six orders of magnitude larger than the neural signals of interest, which typically are in the order of 1–10 μV when measured from DBS electrodes [16], an artefact suppression strategy has to be employed. The strategy followed in this design was to initially achieve a significant suppression of the CMAV by exploiting the high CMRR offered by the front-end INA and thus avoiding the use of input protective diodes, or passive high-pass filters that would increase the noise and decrease the CMRR of the AFE. Therefore, the gain of the front-end INA was set to 40 dB in order to provide a high CMRR value and thus satisfied the imposed requirement on the CMRR of the system. Moreover, an active feedback integrator (Figure 4.2a), implemented with a single operational amplifier (OPA) (model ADA4522, Analog Devices, USA), was introduced at the first stage of the AFE to remove dc offsets originating from the electrode-tissue interface. The zero introduced by the integrator was set at 0.5 Hz.

The analog filtering stages (notch and low-pass) were introduced between the pre-amplification and the final amplification stages in order to suppress the DMAV. More specifically, an eight-pole Bainter notch filter (Figure 4.2b) was designed and introduced in the signal chain to suppress the main frequency of the DMAV. Since 140 Hz DBS has proven to improve limb bradykinesia [106] and continuous high frequency stimulation (130–180 Hz) of subcortical motor nuclei has proven to be highly effective in suppressing PD motor symptoms, and tremor observed in essential and dystonic tremor [45], the center frequency of the aforedescribed analog notch filter was chosen to be equal to 140 Hz. Moreover, the stopband of the notch filter was tuned between 125 and 155 Hz. It is important to note here that, according to [18], no biomarkers for PD were found in this frequency band though research continues [107, 108].

Two different versions of this notch filter were designed and tested in order to assess which of those two implementations is the most suitable for being placed in the second stage of the final AFE architecture. The first version was a 0.5 dB Chebyshev approximation while the second version was a Bessel approximation. Chebyshev and

Bessel approximations were chosen because the aim of this work was to thoroughly investigate the tradeoff between a steep filter roll-off (Chebyshev filters) and an excellent transient response to a step/pulse input thanks to a linear phase response (Bessel filters) [109]. Both steep roll-off and good transient and phase response are required in neuromodulation. The former is explained by the fact that the proximity of the sensing to the stimulation and the low magnitude of the neural signal relative to the stimulation require the design of filters that can sufficiently suppress the stimulation artefacts, while the latter is required in order to achieve minimally distorted recording of neural signals.

The low-pass filtering stage (Figure 4.2c) includes a two-pole classic Sallen-Key low-pass filter designed using Bessel coefficients to ensure an excellent transient response. The role of this filter is to suppress the high-frequency harmonics of the DMAV and define the passband of the system. The objective of this effort was to reliably extract LFP signals during DBS by applying techniques in the analog domain to avoid saturation. As a result, having ensured that the LFP signals will reach the analog-to-digital-converter (ADC), further a posteriori low-pass filtering in the digital domain can be applied to completely remove higher harmonics coming from stimulation. Taking into account the aforementioned objective and the fact that a higher order low-pass filter would add extra components that would further increase complexity and possibly power consumption of the AFE and would occupy more space on the final printed circuit board (PCB), a low-order filter was introduced at this stage.

The final amplification stage (Figure 4.2d) includes a single-ended amplification with a gain of either 20 dB or 40 dB. An INA (model AD8422, Analog Devices, USA) with its negative input grounded was used to amplify the signals coming from the low-pass filter of the previous stage. The gain is digitally programmable and is determined by a multiplexer (model ADG1404, Analog Devices, USA). The first three stages (differential pre-amplification, notch and low-pass filtering) are supplied with ± 5 V to ensure that an adequate headroom is provided to eliminate the risk of saturation coming from electrode dc offsets and stimulation artefacts. However, the fourth (last)

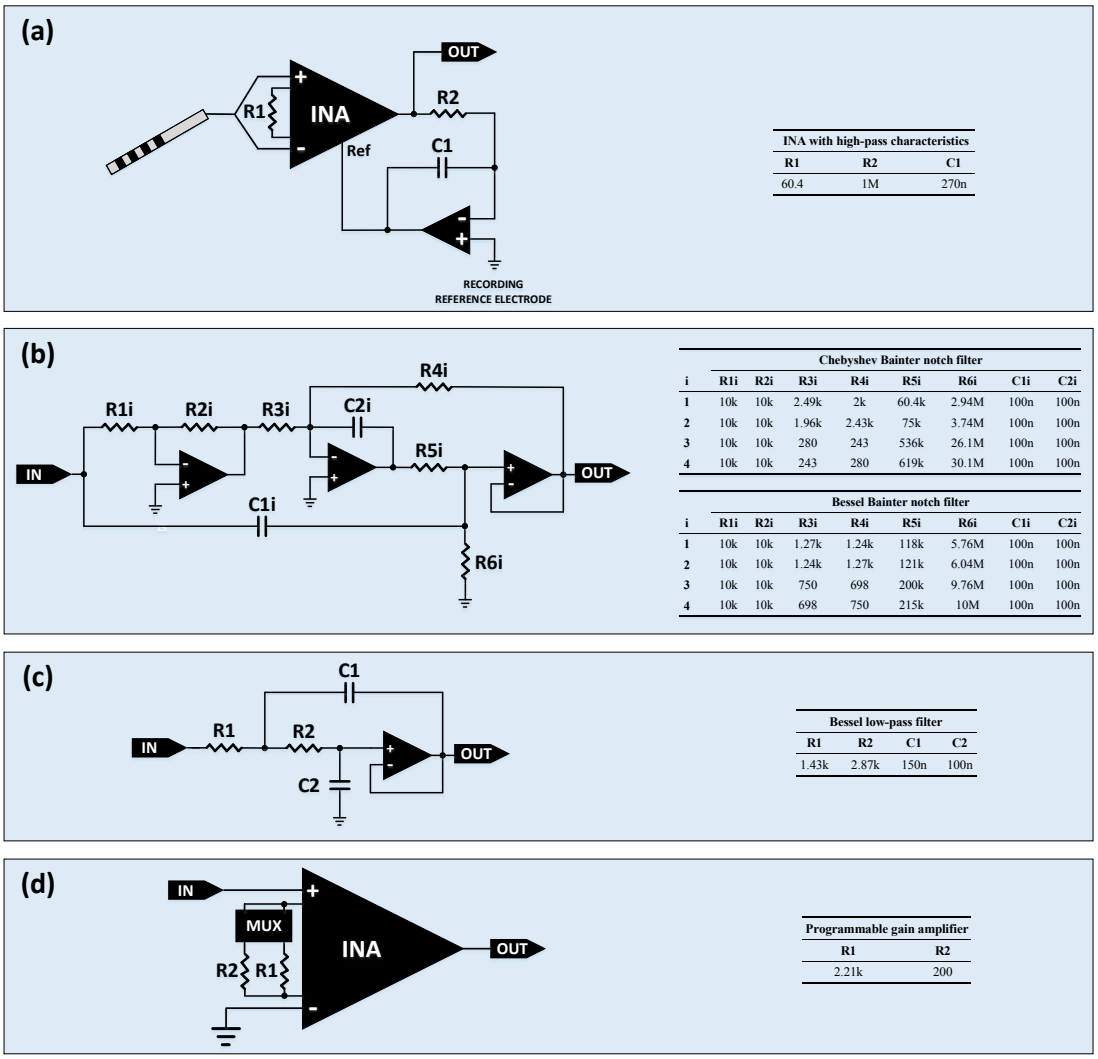

INA with high-pass characteristics		
R1	R2	C1
60.4	1M	270n

Chebyshev Bainter notch filter								
i	R1i	R2i	R3i	R4i	R5i	R6i	C1i	C2i
1	10k	10k	2.49k	2k	60.4k	2.94M	100n	100n
2	10k	10k	1.96k	2.43k	75k	3.74M	100n	100n
3	10k	10k	280	243	536k	26.1M	100n	100n
4	10k	10k	243	280	619k	30.1M	100n	100n

Bessel Bainter notch filter								
i	R1i	R2i	R3i	R4i	R5i	R6i	C1i	C2i
1	10k	10k	1.27k	1.24k	118k	5.76M	100n	100n
2	10k	10k	1.24k	1.27k	121k	6.04M	100n	100n
3	10k	10k	750	698	200k	9.76M	100n	100n
4	10k	10k	698	750	215k	10M	100n	100n

Bessel low-pass filter			
R1	R2	C1	C2
1.43k	2.87k	150n	100n

Programmable gain amplifier	
R1	R2
2.21k	200

Figure 4.2: Graphical representation of the four blocks constituting the AFE architecture. The resistors and capacitors included in these blocks are characterized by a tolerance of 0.1% and 10%, respectively. (a) The signals coming from two contacts of the DBS electrode are subtracted and amplified with a gain of 40 dB by an INA with high-pass characteristics (the high-pass knee frequency was set at 0.5 Hz). (b) An eight-pole Bainter 140 Hz notch filter is used to suppress the main frequency of the stimulation artefacts. (c) A two-pole 500 Hz Sallen-Key low-pass filter is used to suppress the high-frequency harmonics of the stimulation artefacts and define the passband of the system. (d) An INA provides either 20 dB or 40 dB amplification, which is digitally determined via a multiplexer.

stage is supplied with ± 2.5 V to be able to interface with high-performance and low-power commercial ADC chips (e.g. model ADS1298, Texas Instruments, USA). The fundamental building block for the design of the filtering stages is the operational

amplifier ADA4522 by Analog Devices. Finally, the resistors and capacitors included in this four-stage architecture are characterized by a tolerance of 0.1% and 10%, respectively.

The two designed channels (Chebyshev and Bessel notch channel) are powered by a medical DC/DC converter (model THM 10-0521WI by Traco power), which provides a reinforced isolation system for 5000 VACrms isolation and a very low leakage current of less than 2 µA. On the isolated side of the PCB hosting the designed AFEs, a low dropout voltage regulator (model TPS7A7001DDA from Texas Instruments) is used to convert the +5 V originating from the positive (isolated) output of the DC/DC converter into +2.5 V, while a linear voltage regulator (model LM337IMP/NOPB from Texas Instruments) is used to convert the -5 V originating from the negative (isolated) output of the DC/DC converter into -2.5 V.

4.2.2 *In vitro* experimental setup for artefact suppression testing

An *in vitro* experimental setup for unipolar (Figure 4.3a) and bipolar (Figure 4.3b) stimulation was prepared to reproduce the stimulation and recording conditions of a typical post-operative LFP recording session. The DBS electrode used in the experiments (electrode A in Figure 4.3a and 4.3b, model DB-2201, Boston Scientific Neuromodulation) is a directional eight-contact segmented DBS lead. The DBS electrode was placed in a glass container filled with tyrode solution (128.2 mM of NaCl, 1.3 mM of $CaCl_2$, 4.7 mM of KCl, 1.05 mM of $MgCl_2$, 1.19 mM of NaH_2PO_4, 20 mM of $NaHCO_3$ and 11.1 mM of glucose) at room temperature. The segmented DBS electrode has eight contacts in total, two contacts at the two sides of the electrode (which are contacts 0 and 3 of electrode A in Figure 4.3a and 4.3b) and another six contacts (1a, 1b, 1c, 2a, 2b and 2c).

The monophasic stimulation pulses (3 V peak-to-peak amplitude, 140 Hz frequency and 100 µs pulse width) were delivered by a commercial voltage-mode stimulator (Grass, Astromed, Inc., USA) and the LFP signals representing the LPF signals recorded from the neural tissue in a typical post-operative LFP recording session were

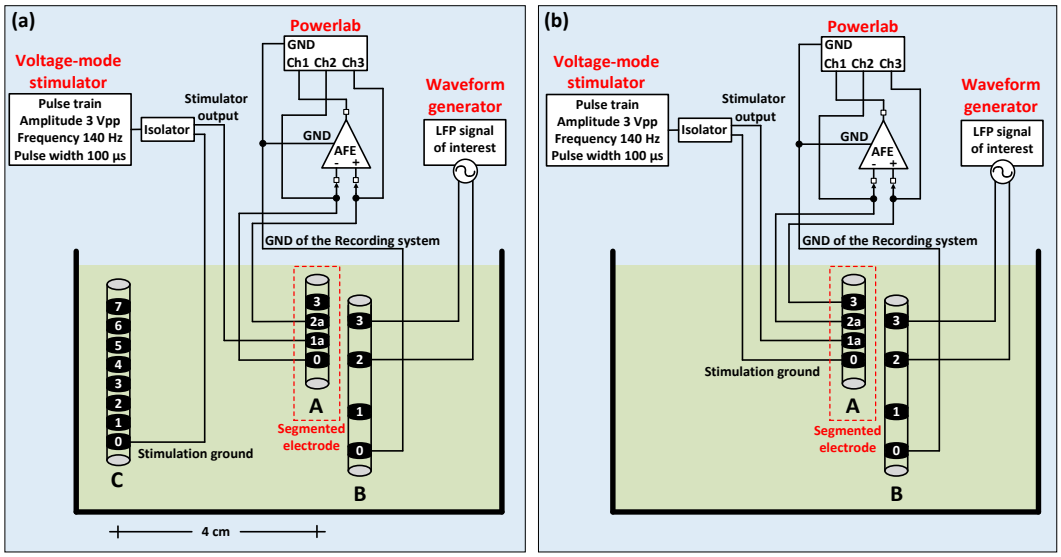

Figure 4.3: The *in vitro* experimental setup for unipolar (a) and bipolar (b) stimulation. A DBS electrode (electrode A in (a) and (b), model DB-2201, Boston Scientific Neuromodulation) was placed in a glass container filled with tyrode solution at room temperature. The monophasic stimulation pulses (3 V peak-to-peak amplitude, 140 Hz frequency and 100 µs pulse width) were delivered by means of a commercial stimulator (Grass, Astromed, Inc., USA) and the LFP signals (representing the LPF signals recorded from the human neural tissue in a typical post-operative LFP recording session) were injected to the solution by an Agilent 33220A waveform generator. The LFP signals were injected to the solution as a differential signal through a second electrode (electrode B in (a) and (b), model 401261, St. Jude Medical). One of the four contacts of electrode B was connected to the ground of the recording system. In both unipolar and bipolar settings the stimulation ground was electrically isolated from the mains by using a commercial isolator (SIU5 stimulus isolation point, Grass, Astromed, Inc., USA). The LFP signals recorded by the proposed AFE were digitized at a sampling frequency of 20 kSPS (samples per second) and depicted on a computer by the Powerlab data acquisition system (ADInstruments). (a) In the unipolar stimulation setting, we sense differentially and symmetrically in space about the unipolar stimulation contact 1a of electrode A by sensing across the two nearest, equi-distant to contact 1a, neighbour contacts (contacts 0 and 2a). However, since the surface areas of contacts 0 and 2a differ, the sensing is not completely symmetrical and thus some differential-mode interference from stimulation is expected to appear and be suppressed by the analog notch filter of the proposed AFE. The anode (ground) of the stimulator was connected to one of the contacts of a third electrode (electrode C), which is the 8-contact Vercise DBS lead (Boston Scientific). Electrode C was placed approximately 4 cm away from the stimulation site and represents the case of the implantable pulse generator, which acts as an anode in the unipolar stimulation setting. (b) In the bipolar stimulation setting, two contacts of electrode A (0 and 1a) were used for stimulation (anode and cathode of the stimulator) and another two for recording (2a and 3).

injected in the solution by an Agilent 33220A waveform generator. The LFP signals were injected in the solution as a differential signal through a second electrode (electrode B in Figure 4.3a and 4.3b, model 401261, St. Jude Medical). One of the

four contacts of electrode B was connected to the ground of the recording system. In both unipolar and bipolar settings the stimulation ground was electrically isolated from the mains using a commercial isolator (SIU5 stimulus isolation point, Grass, Astromed, Inc., USA). The output impedance of the SIU5 isolator equals 1 kΩ. The LFP signals recorded by the proposed AFE were digitized and depicted on a computer by means of the Powerlab data acquisition system (Powerlab 16/35, ADInstruments).

In a unipolar configuration one contact on the electrode is set to cathode and the case of the implantable pulse generator (IPG) acts as an anode. In the unipolar stimulation setting shown in Figure 4.3a, we sense differentially and symmetrically in space about the unipolar stimulation contact 1a of electrode A by sensing across the nearest (bilateral to contact 1a) neighbour contacts, i.e. across contacts 0 and 2a. As a result, a significant part of the interference appears as a common-mode signal at the differential sensing pre-amplifier and is rejected by its high CMRR. However, since the surface areas of contacts 0 and 2a differ, the sensing will not be perfectly symmetrical and thus some differential-mode interference caused by the stimulation is expected to appear and be suppressed by the analog notch filter which follows in the AFE's chain. The anode (ground) of the stimulator was connected to one of the contacts of a third electrode (electrode C), which is the 8-contact Vercise DBS lead (Boston Scientific). Electrode C was placed approximately 4 cm away from the stimulation site and represents the case of the implantable pulse generator, which acts as an anode in the unipolar stimulation setting.

Finally, in a bipolar configuration one electrode contact is used as the anode and another electrode contact as the cathode, while the case of the IPG is neutral. In the bipolar stimulation setting shown in Figure 4.3b, two contacts of electrode A (0 and 1a) were used for stimulation (as the anode and cathode of the stimulator, respectively) and another two for recording (2a and 3). Since contact 2a is closer to the stimulation site in comparison with contact 3, the differential sensing of the contaminating pulses by the front-end INA is asymmetric and thus more differential mode artefacts enter the signal chain. Hence, in the bipolar stimulation setup shown in Figure 4.3b the high CMRR of the front-end INA cannot be fully exploited.

4.3 Measured results

4.3.1 AFE characterization – Measured results

As described in section 4.2.1, two versions of the 8th order Bainter notch filter were designed and introduced in the fundamental AFE architecture shown in Figure 4.1. The aim of this effort was to compare the achieved performance of the two AFE architectures (Chebyshev notch channel versus Bessel notch channel) and decide for the one that is the most suitable for neuromodulation based on the specifications summarized in Table 4.1. In this section, a number of strict tests, which are typically performed on analog electronics to assess their performance in terms of noise, linearity and temporal response are presented and analysed.

4.3.1.1 Impulse/Step response

In Figure 4.4a, the width of the input impulse was set at 100 μsec (which is identical to the DBS pulse duration used in later *in vitro* and *in vivo* experiments) and the amplitude was 2 mV, which is close to the maximum peak amplitude that can be handled by the designed channels (=2.3 mV). Chebyshev and Bessel notch channels exhibit approximately the same settling time (Figure 4.4d). Another important test for evaluating the temporal response of the designed AFEs is to supply them with a biphasic input pulse. The responses of the Chebyshev and Bessel notch channels to a biphasic input pulse are shown in Figure 4.4b. The input pulse was approximately equal to 2 mV for 100 μsec and – 2 mV for another 100 μsec. As anticipated, the responses of both channels to a biphasic input pulse (Figure 4.4e) exhibit a faster settling in comparison to their impulse responses (Figure 4.4d).

The step response of the Chebyshev notch channel shows a slightly bigger overshoot and ringing in comparison to the Bessel notch channel (Figure 4.4f). As in the case of the impulse response, the differences, which are in accordance with the nature of the two notch filters, are not significant. Finally, Figure 4.4c reveals the ac-coupling characteristics of the designed channels. Although the input voltage remains at 2.1

mV, the output voltage returns back to 0 V after a settling time (time needed for the response to reach and stay within 2% of its final value) of:

$$\text{Settling time} = 4\times R\times C \approx 1 \text{ sec} \qquad (4.1)$$

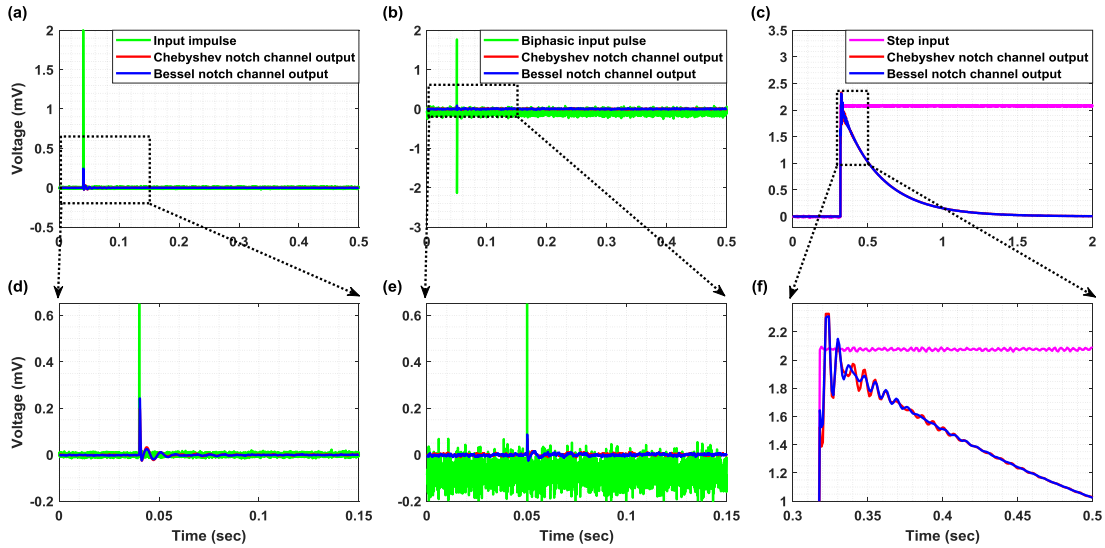

Figure 4.4: (a) Impulse response, (b) response to a biphasic pulse and (c) step response of the Chebyshev (red line) and Bessel (blue line) notch channels. (d) Chebyshev and Bessel notch channels exhibit approximately the same settling time. (e) The response of both channels to a biphasic pulse exhibits a faster settling in comparison to their corresponding impulse responses. (f) The step response of the Chebyshev notch channel shows a slightly bigger overshoot and ringing in comparison to the Bessel notch channel. As in the case of the impulse response, the differences are not significant.

4.3.1.2 Bode magnitude plot/Noise

From the Bode magnitude plot shown in Figure 4.5a, it is clear that both channels provide a passband between 0.5 and 500 Hz and achieve the desired gain of 60 dB. The roll-off of the high- and the low-pass filters equals + 20 dB/decade and - 40 dB/decade, respectively, for both topologies. However, the Chebyshev notch channel achieves a sharper transition between the passband and the stopband at 140 Hz, compared to the transition of the Bessel notch channel. Moreover, the Chebyshev notch channel provides stronger attenuation at the central frequency of the notch, which is equal to 140 Hz, compared to the Bessel notch channel. Although the most serious drawback of the Chebyshev approximation is that it allows ripple in the

frequency response in order to achieve a faster roll-off, the proposed Chebyshev notch channel exhibits a flat magnitude response in the passband and approximates the magnitude response of the Bessel notch channel. This is attributed to the fact that it was designed as a 0.5 dB Chebyshev filter and thus the amount of passband ripple is limited.

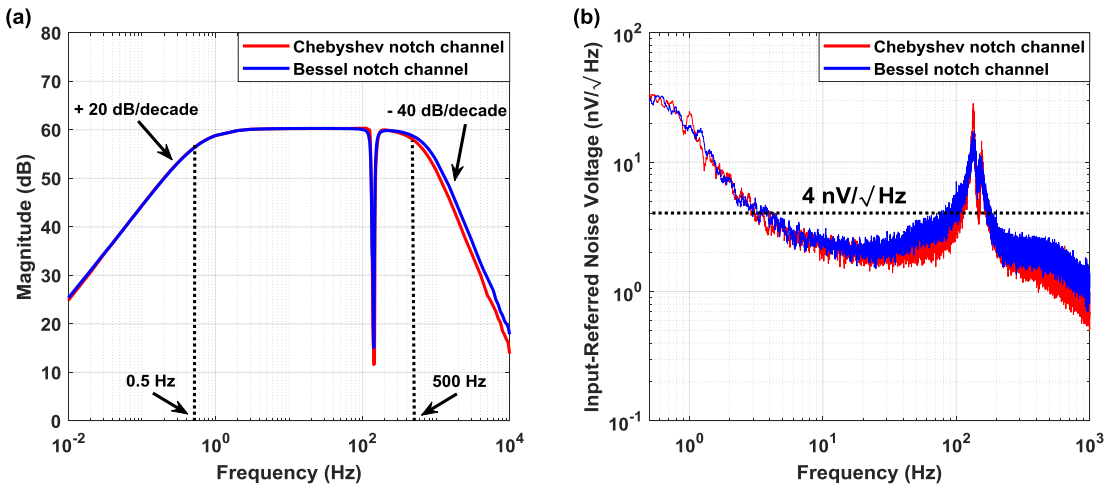

Figure 4.5: Measured Bode magnitude plot with the gain of both channels set at 60 dB (a) and input-referred noise (b) of the Chebyshev notch channel (red line) and the Bessel notch channel (blue line). (a) Both channels provide a passband between 0.5 and 500 Hz. The roll-off of the high- and the low-pass filters equals + 20 dB/decade and -40 dB/decade, respectively, for both topologies. However, the Chebyshev notch channel provides a sharper transition between the passband and the stopband and stronger attenuation at the central frequency of the notch (= 140 Hz), compared to the Bessel notch channel. Besides, the Chebyshev notch channel exhibits a flat magnitude response in the passband and approximates the magnitude response of the Bessel notch channel. (b) Based on the input-referred noise graph, it is concluded that both channels are low-noise with the Chebyshev notch channel presenting a slightly better noise performance. Noise power spectral density estimates in the passband for the Chebyshev and the Bessel notch channels are 4 nV/$\sqrt{\text{Hz}}$ and 4.4 nV/$\sqrt{\text{Hz}}$, respectively, with the residual 1/f corner estimated at roughly 10 Hz for both channels.

The input-referred noise was measured by connecting both inputs of the front-end INA to the ground of the PCB, recording the output voltage of the channel and then dividing it by the gain, which was equal to 60 dB. Since there is no passive filtering network before the front-end AD8429 INA chip and the gain of the first stage is sufficiently high (equal to 40 dB), which allows the effective noise factor to be the noise factor of the first stage without an impact on the subsequent stages, the input-referred noise of the

designed AFEs should approximate the measured input-referred noise reported in the datasheet of the AD8429 chip. The integrated noise of the Chebyshev and Bessel notch channels over the frequency range 0.5 – 500 Hz was measured and found to be equal to 96 nV rms and 121 nV rms, respectively. Figure 4.5b shows that both channels are low-noise with the Chebyshev notch channel characterised by a slightly better noise performance. Noise power spectral density estimates in the passband for the Chebyshev and the Bessel notch channels are 4 nV/$\sqrt{\text{Hz}}$ and 4.4 nV/$\sqrt{\text{Hz}}$, respectively, with the residual 1/f corner estimated at roughly 10 Hz for both channels. Indeed, these measured results are in agreement with the noise measurements reported in the datasheet of the front-end AD8429 INA chip.

4.3.1.3 Measured results versus specifications

Taking into consideration the previously presented Bode amplitude plot and noise performance of the two channels, the recording capabilities of the Chebyshev notch channel satisfy all of the requirements shown in Table 4.1. Regarding the Bessel notch channel, it satisfies all of the requirements except for the one related to the integrated noise of the channel. The integrated noise of the Bessel notch channel over the frequency range 0.5 – 500 Hz was measured and found to be equal to 121 nV rms which is higher than the imposed limit of 100 nV rms (Table 4.1). Since the recording capabilities of the Bessel notch channel have not satisfied all of the imposed specifications, measured results only from the Chebyshev notch channel are presented in sections 4.3.1.4, 4.3.1.5, 4.3.2, 4.3.3, 4.3.4 and 4.3.5.

4.3.1.4 Total harmonic distortion and intermodulation distortion

The THD of the Chebyshev notch channel for a gain of 60 dB is shown in Figure 4.6a. After examining the available dynamic range of the channel (from 1 μV peak to 2.3 mV peak), it is clear that the achieved THD is less than 0.2%. Only input sinusoidal voltages with peak amplitudes approaching the highest input voltage (= 2.5 mV peak)

that can be handled by the rail-to-rail output INA located at the last stage of the AFE present higher THD values.

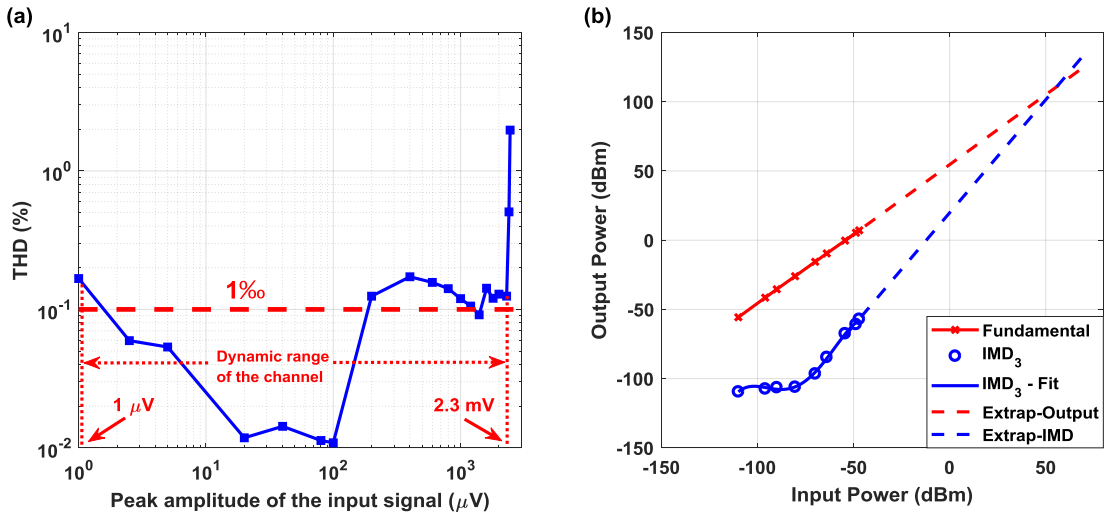

Figure 4.6: THD (a) and IMD_3 (the reference impedance equals 50 Ω) (b) measured with the gain of the Chebyshev notch channel set at 60 dB. (a) After examining the available dynamic range of the channel (from 1 μV peak to 2.3 mV peak), it is clear that the achieved THD is less than 0.2%. (b) The two tones applied to the Chebyshev notch channel were f_1 = 4.9 Hz and f_2 = 5.1 Hz. The output power of a single fundamental tone (in dBm - red line in the graph) and the relative amplitude of the third order IMD_3 products referenced to a single tone (blue circles in Figure 4.6b) are plotted as a function of the applied input power. The third order intercept line (dashed blue line) is extended to intersect the extension of the fundamental output signal line (dashed red line). The calculated IP_3 is characterized by a relatively high value, which is a positive result since the higher the IP_3 values the better the linearity of the amplifier and the weaker the output intermodulation products that will be generated at the amplifier's output. THD, total harmonic distortion; IP_3, third order intercept point; IMD_3, third order intermodulation distortion.

In Figure 4.6b, the output power of a single fundamental tone (in dBm - red line in the graph) and the power of the third order products (blue circles in Figure 4.6b, defined as IMD_3) are plotted as a function of input power. It is clear that the fundamental line is characterized by a slope that is equal to 1. As shown in Figure 4.6b, the IP_3 of the Chebyshev notch AFE is characterized by a high value. It should be stressed that this high IP_3 value of the proposed AFE is a very desirable feature: the non-linearity of the AFE should indeed be very low to avoid artefact coupling into the physiological measurements through intermodulation.

4.3.1.5 Key properties of the Chebyshev notch AFE

Taking into account all the measured results acquired from the Chebyshev notch channel, the key properties of this channel are summarized in Table 4.2.

Table 4.2: Key properties of the Chebyshev notch AFE.

Property	Value	Units/Comments
Supply voltage	± 5, ± 2.5	Volts
Gain	60, 80	dB (programmable)
Integrated noise	26	nVrms (0.5 to 40 Hz)
	33	nVrms (0.5 to 100 Hz)
	96	nVrms (0.5 to 500 Hz)
CMRR	130	dB (dc to 60 Hz)
Maximum tolerable differential DC offset	32/85*	mV
Input dynamic range	± 2.3	mV (peak), gain=1000 V/V
	± 230	μV (peak), gain=10000 V/V
SNR	30	dB (minimum)
Nonlinearity	< 0.2%	THD
High-pass corner	0.5	Hz
Low-pass corner	500	Hz
Total current consumption	32	mA
Hours of continuous operation	28	hours (900 mAh battery)

*Measured differential DC offset rejection of 85 mV is achieved when a 1st order analog 0.5 Hz high-pass filter is cascaded after the front-end INA (stage 1 of the current AFE).

4.3.2 Performance evaluation of the AFE based on recordings of physiological signals

In order to examine the ultra-low-noise recording capabilities of the designed AFE, physiological signal recordings that do not require invasive measurement techniques along with SNR measurements were obtained. Another objective of these biosignal recordings was to show that in spite of the high gain (60 dB minimum – 40 dB from the front-end INA and another 20 dB from the final amplification stage, see Figure 4.1) and the relatively small dynamic range (± 2.3 mV) that characterize the Chebyshev notch channel, it is capable of removing the dc offsets stemming from the electrodes and thus avoiding saturation.

The recorded ExG (EMG, EEG and ECG) signals, which are presented in Figure 4.7 after removing the applied gain of 60 dB, were digitized using the ADC of the Powerlab acquisition system at a sampling frequency of 1 kSPS. This ADC has a resolution of 16 bits and an input range of ± 10 V. It uses the Successive Approximation Register (SAR) analog-to-digital conversion method. Regarding the EMG measurement (Figure 4.7a), the signal inside the dotted rectangle was recorded while the subject was producing tremor movements. In Figure 4.7c, the recorded EEG signals were digitally low-pass filtered at 40 Hz because the frequency range of interest for EEG analysis in studies on PD is between 0.5 and 30 Hz. Figure 4.7e shows that ECG signals were successfully recorded.

The noise recorded from the Chebyshev notch channel with both the inputs of the front-end INA grounded (see Figure 4.5b), was used for the calculation of the SNR. Figures 4.7b, 4.7d and 4.7f illustrate the achieved SNR over time during the EMG, EEG and ECG recording sessions, respectively. It is clear that the achieved SNR is always higher than 30 dB.

The alpha waves test, presented in Figure 4.8, shows that in the band 7.5 – 12.5 Hz, the amplitude spectrum of the EEG signals recorded when the eyes are closed is significantly higher than the amplitude spectrum of the signals recorded when the eyes

are open (Figure 4.8a). The same conclusion is derived from Figure 4.8b where alpha waves in the band 7.5 – 12.5 Hz, during the eyes closed period, are clearly visible.

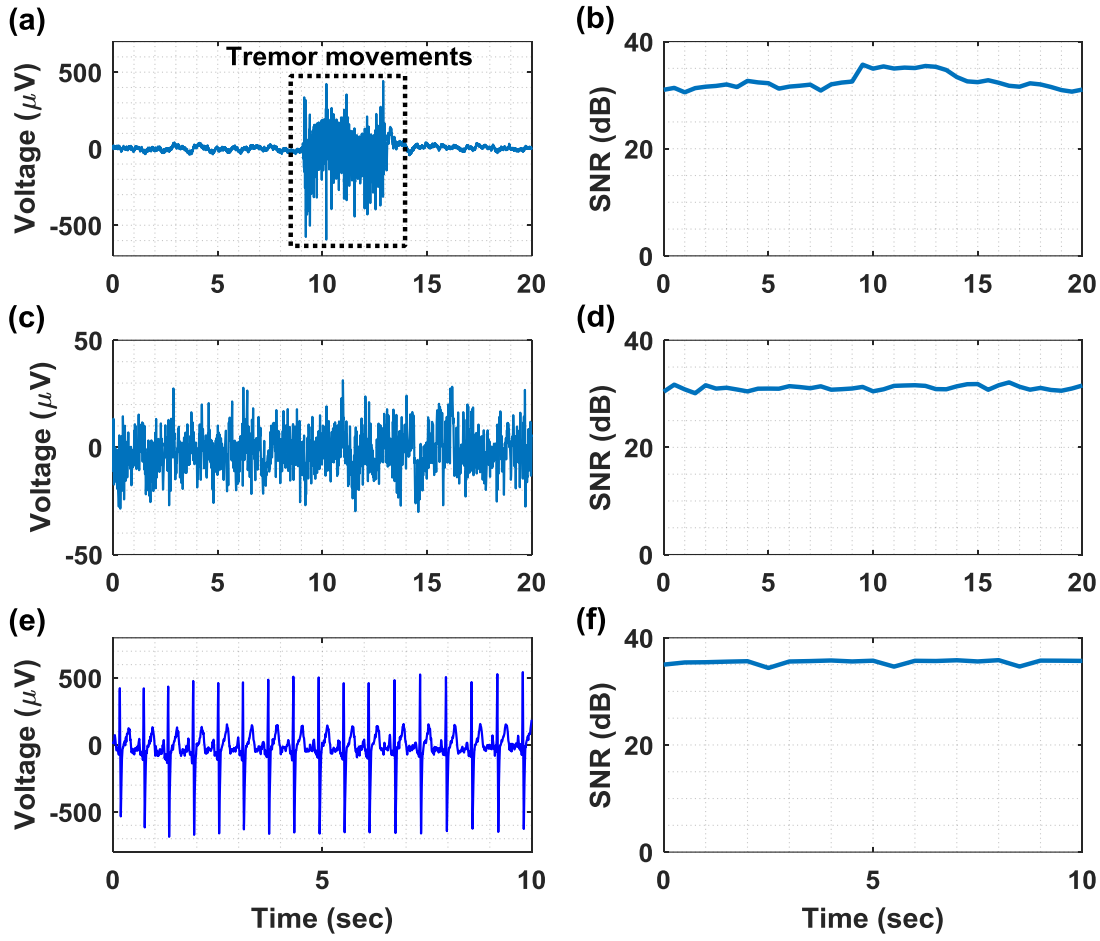

Figure 4.7: Biosignal acquisition using the Chebyshev notch channel. The applied gain was 60 dB and the sampling frequency was equal to 1 kSPS. (a) EMG signal acquisition. The signal inside the dotted rectangle was recorded while the subject was producing tremor movements. (b) The SNR of the EMG signals was measured and found to be continuously higher than 30 dB. (c) EEG signal acquisition. Since the frequency range of interest for EEG analysis in studies on PD is between 0.5 and 30 Hz, a digital low-pass filter at 40 Hz was applied on the recorded EEG signals. (d) The SNR of the EEG signals was measured and found to be continuously higher than 30 dB. (e) ECG signal acquisition. (f) The SNR of the ECG signals was measured and found to be continuously higher than 34 dB.

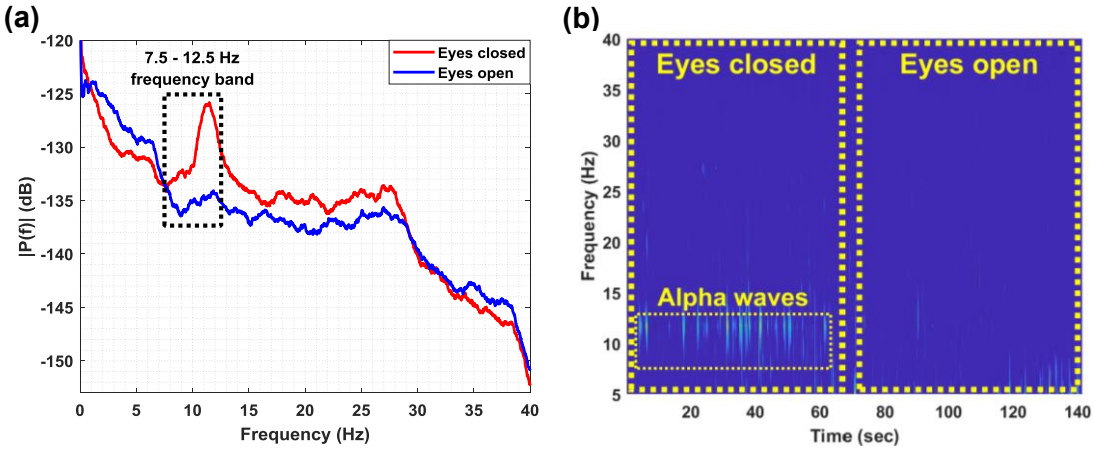

Figure 4.8: (a) Amplitude spectrum (the reference level of amplitudes equals 1 V) of the EEG signals recorded when the subject's eyes are open (blue line) and when they are closed (red line). It is clear that in the 7.5 – 12.5 Hz band the amplitude spectrum of the EEG signals recorded when eyes are closed is significantly higher than the amplitude spectrum of the signals recorded when eyes are open. (b) EEG spectrogram. Alpha waves in the 7.5 – 12.5 Hz band during the eyes closed period are clearly visible.

4.3.3 Performance evaluation of the AFE based on comparisons with commercial biopotential acquisition devices

To compare the proposed system with available devices, identical, extremely weak single tones were introduced to the Chebyshev notch channel and to a state-of-the-art, commercial biological amplifier (Bioamplifier included in Powerlab 26T, ADInstruments), which is optimized for measuring a wide variety of biological signals such as ECG, EMG and EEG. In the first case, the signals were recorded by the AFE of the Chebyshev notch channel and were digitized by the 16-bit ADC of the Powerlab 16/35 system at 1 kSPS, whereas in the second case the signals were recorded and digitized by the Powerlab 26T (bioamplifier and 16-bit ADC) system at 1 kSPS.

More specifically, a weak sinusoidal single tone (100 nV peak, 25 Hz) was presented to the inputs of the two systems. This weak sinusoidal single tone was provided by the Agilent 33220A waveform generator. However, since the weakest signal that can be injected by the specific generator is a 10 mV peak sinewave, ohmic attenuators (Cinch Connectivity Solutions), which provided 100 dB attenuation to the signals injected by

the waveform generator, were used. A digital low-pass filter at 30 Hz was applied on the recordings of both systems in order to ensure that the noise coming from the front-ends of both systems (integrated noise) stays at levels lower than 100 nV peak (so that the 100 nV peak signal dominates the noise), and be able to compare them on an equal footing. Moreover, the mean values of the signals recorded by the two systems were removed in order to facilitate a more direct comparison between the two AFEs in terms of signal quality.

Regarding the first system (Chebyshev notch channel), its gain was set at 80 dB (or 10,000 V/V) and the range of the Powerlab ADC at ± 10 V (maximum available). The reason behind the choice of applying a gain of 80 dB lies with the fact that a gain of 60 dB would not allow for the amplified signals to overcome the smallest input increment the specific ADC can resolve (20/65536= 305 μV). Regarding the second system (Powerlab 26T bioamplifier), its recording range was set at ± 100 μV (lowest available), which means that a gain of 100 dB (or 100,000 V/V) was applied upon the input signals by the bioamplifier's AFE.

Figure 4.9 shows that the Chebyshev notch channel (Figure 4.9a) is less vulnerable to dc offsets that exist in the weak sinusoidal signal and can thus provide more stable signal recordings compared to the commercial bioamplifier (Figure 4.9b). Next, a second sinusoidal single tone with the same amplitude but lower frequency (= 5 Hz) was injected to the inputs of the two AFEs and the amplitude spectrum of the overall recorded signal was calculated (Figure 4.9c). It is clear that the spectrums of both systems include visible spectral peaks at the two test frequencies (5 and 25 Hz). Based on the graph, the amplitude (the reference voltage equals 1 V) of each of these two spectral peaks is approximately equal to – 143 dB, which is in accordance to the expected theoretical value of

$$\text{Amplitude} = 20 \times \log_{10}\left(\frac{100 \times 10^{-9}}{\sqrt{2}}\right) \approx -143 \text{ dB } \{\text{reference voltage} = 1 \text{ V}\} \qquad (4.2)$$

To push the limits of the Chebyshev notch channel's recording capabilities towards the noise floor of the system, an extremely weak sinusoidal single tone (30 nV peak, 25 Hz) was presented to the inputs of the two systems. Again, this sinusoidal single

tone was provided by the Agilent 33220A waveform generator in combination with attenuators that provided 110 dB attenuation to the signals injected by the waveform generator. A digital low-pass filter at 30 Hz was applied on the recordings of both systems. The gain and digitization settings were left the same with the ones used in the experiment where 100 nV peak test tones were applied.

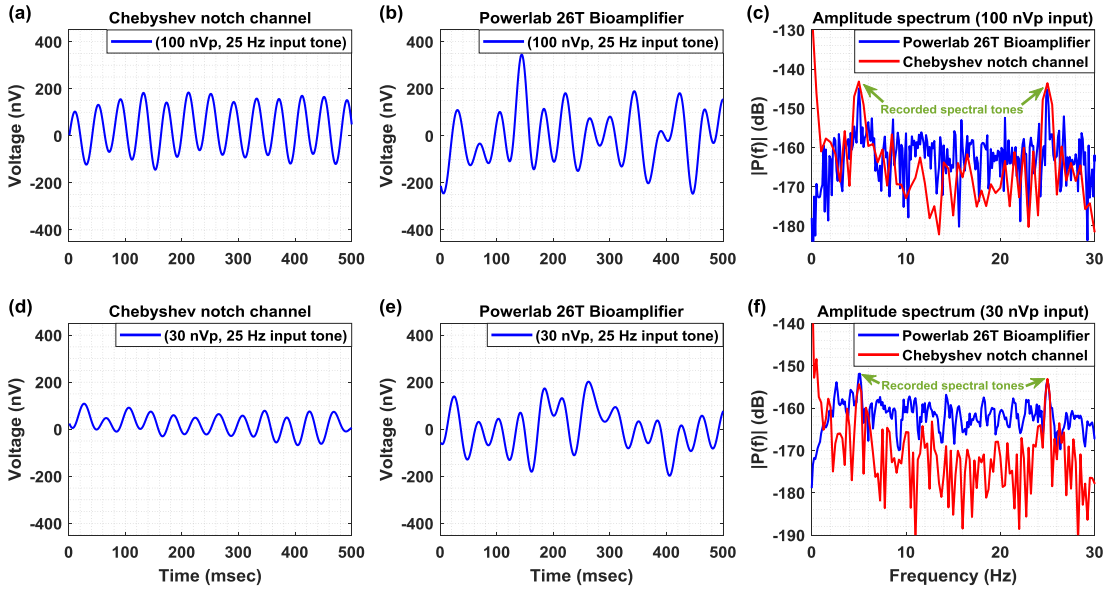

Figure 4.9: (a) Output voltage (after removing the gain of 80 dB) recorded from the Chebyshev notch channel when a sinusoidal single tone (25 Hz, amplitude 100 nV peak) was injected to the input of the channel. (b) Output voltage recorded from the Powerlab 26T bioamplifier when a sinusoidal single tone (25 Hz, amplitude 100 nV peak) was injected to the input of the system. (c) Amplitude spectrum calculated when two sinusoidal tones, one low-frequency (= 5 Hz) and one higher-frequency (= 25 Hz) are sequentially injected to the inputs of the two AFEs. The amplitude spectrums of both systems present two spectral peaks at 5 and 25 Hz, which are characterized by the same amplitude. (d) Output voltage (after removing the gain of 80 dB) recorded from the Chebyshev notch channel when a sinusoidal single tone (25 Hz, amplitude 30 nV peak) was injected to the input of the channel. (e) Output voltage recorded from the Powerlab 26T bioamplifier when a sinusoidal single tone (25 Hz, amplitude 30 nV peak) was injected to the input of the system. (f) Amplitude spectrum calculated when two sinusoidal tones, one low-frequency (= 5 Hz) and one higher-frequency (= 25 Hz), are sequentially injected to the inputs of the two AFEs. The amplitude spectrums of both systems present two spectral peaks at 5 and 25 Hz, which are characterized by the same amplitude.

As anticipated based on the results acquired by the injection of the 100 nV peak test tone, the Chebyshev notch channel (Figure 4.9d) provides more stable signal recordings compared to the commercial bioamplifier (Figure 4.9e). Next, a second

sinusoidal single tone with the same amplitude but lower frequency (= 5 Hz) was injected to the inputs of the two AFEs and the amplitude spectrum of the overall recorded signal was calculated (Figure 4.9f). It is clear that the spectrums of both systems include visible spectral peaks at the two test frequencies (5 and 25 Hz). It is important to note here that the noise floor of the Chebyshev notch channel (spectrum in red) is lower than the noise floor of the biological amplifier (spectrum in blue). Based on the graph, the amplitude (the reference voltage equals 1 V) of each of these two spectral peaks is approximately equal to – 153 dB, which is in accordance to the expected theoretical value of

$$\text{Amplitude} = 20 \times \log_{10}\left(\frac{30 \times 10^{-9}}{\sqrt{2}}\right) \approx -153 \text{ dB } \{\text{reference voltage} = 1 \text{ V}\} \qquad (4.3)$$

Finally, a 50 sec segment of LFP signal recorded (low-pass filtered by a high-order digital low-pass filter at 553 Hz) from the subthalamic nucleus in a patient with PD withdrawn from levodopa was injected by means of a waveform generator to the input of the Chebyshev notch channel. Moreover, in order to ensure that no phase distortion or ringing oscillations are introduced by the analog Chebyshev notch filter when LFP recordings are obtained, the same LFP signal was injected to a commercial high-performance differential amplifier that does not include any analog notch filtering stage in its front-end electronics. The commercial amplifier used in this series of experiments is the DP-301 model (ADInstruments), which has been designed for amplifying weak signals such as extracellular action potentials, and weaker EEG and ECG signals.

However, since the waveform generator is not able to inject signals that are weaker that 10 mV peak, the injected LFP signal at the generator's output (which was in mV range) had to be attenuated before entering the input of the Chebyshev notch channel. More specifically, four attenuators (Cinch Connectivity Solutions) that provided 80 dB attenuation were used in order to bring the amplitude of the LFP signal injected by the waveform generator down to the level that characterizes the original LPF signal, which is approximately equal to 0.32 μV rms. The spectrum of this signal contains a peak in the beta frequency band (13-30 Hz) and another peak at 80 Hz. The gain of the DP-301 amplifier was set at 80 dB (maximum available) in order to ensure that this

instrument will provide a reliable recording of the weak LFP signal. The gain of the Chebyshev notch channel was also set at 80 dB to compare the two systems on an equal footing. Finally, the analog outputs of the two systems were sampled by the ADC of the Powerlab 16/35 system at 1 kSPS (the range was set at ± 2 V so the smallest resolvable input increment of the ADC and the smallest detectable signal by the two systems (Chebyshev notch channel and commercial amplifier) were equal to 61 μV and 6.1 nV, respectively). The analog high-pass filter included in the DP-301 amplifier (cut-off frequency at 1 Hz) was activated so that its temporal response can be compared with the temporal response of the Chebyshev notch channel's ac-coupled AFE (cut-off frequency at 0.5 Hz) on an equal footing.

Figure 4.10a depicts the LFP signal recorded by the high-order Chebyshev notch channel (red line) and the DP-301 amplifier (blue line). The two signals approximate each other which shows that the Chebyshev notch channel is able to record the LFP signal without introducing any phase distortion or ringing oscillations (Figure 4.10c). Moreover, since the amplitude spectrum of the LFP signal recorded by the Chebyshev notch channel (Figure 4.10b) contains both the beta peak and the peak at 80 Hz, it can be concluded that the proposed AFE architecture can record, save for the stopband frequencies, both the low and high frequencies of the original LFP signal. It is important to note here that the peak (red line) existing in the stopband (125 – 155 Hz) is introduced by the notch operation (bear in mind Figure 4.5b). As shown in Figure 4.10b, the noise added by the Chebyshev notch filter does not significantly affect the frequencies below and above the stopband of this filter. However, physiological information should not be sought after in the stopband of the notch (pink region in Figure 4.10b).

On the other hand, as shown in Figure 4.10a, the stopband noise does not seem to significantly affect the time-domain recording of the Chebyshev notch channel. The normalised RMSE between the time-domain LFP signals recorded by the two systems (Chebyshev notch channel and DP-301 amplifier) was measured and found to be equal to 4.6%. This error, which can be considered tolerable taking into account the extremely low amplitude of the specific LFP signal, can be attributed to 1) the fact that

the DP-301 amplifier cannot accurately record frequencies of the LFP signal that are higher than 350 Hz (Figure 4.10d), 2) the fact that small dc offsets existing in the extremely weak LFP signal are not completely rejected by the two systems, and 3) the noise in the stopband coming from the Chebyshev notch operation.

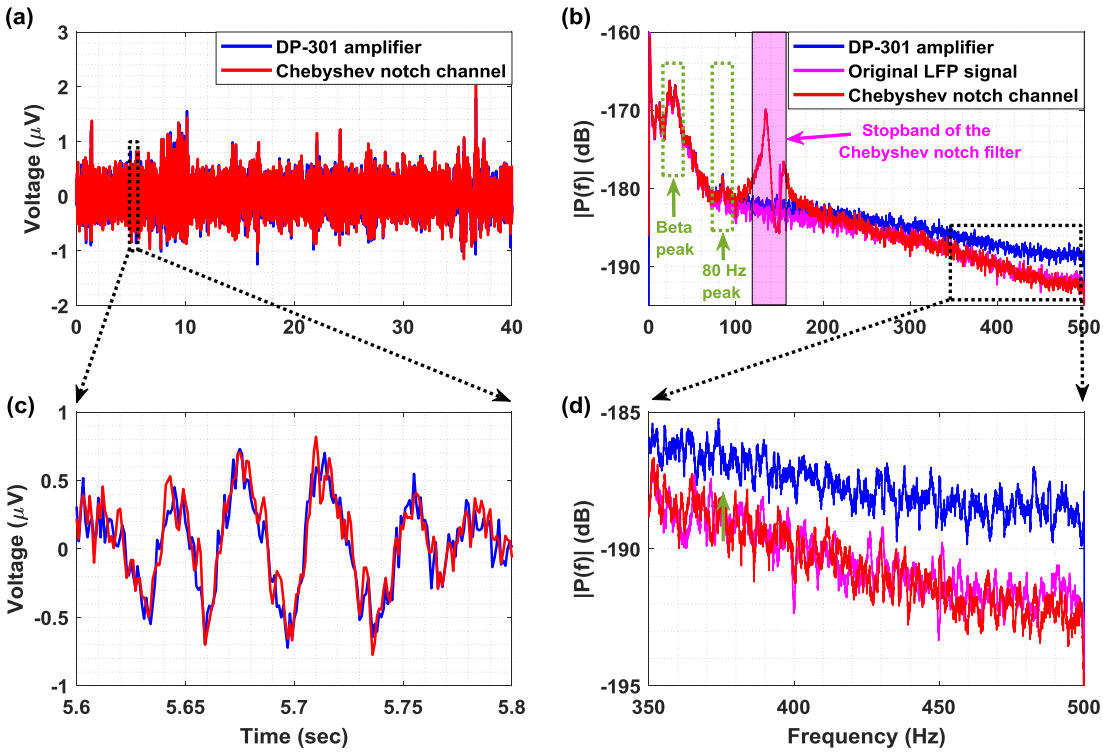

Figure 4.10: A weak LFP signal is injected into the inputs of the Chebyshev notch channel and the DP-301 commercial differential amplifier (ADInstruments). (a) Comparison of the Chebyshev notch channel's output (red line – after removing the gain of 80 dB) with the DP-301 amplifier's output (blue line – after removing the gain of 80 dB) in the time domain. (b) The amplitude spectrum of the Chebyshev notch channel's output (red line) approximates the amplitude spectrum of the original LFP signal (pink line). (c) The LFP recordings acquired by the Chebyshev notch channel and the DP-301 amplifier approximate each other. This shows that the proposed AFE architecture is capable of recording weak LFP signals without introducing any phase distortion or ringing oscillations. (d) The proposed AFE architecture provides more accurate recording of the high frequencies (f>350 Hz) included in the original LFP signal in comparison to the DP-301 amplifier.

4.3.4 Evaluation of the artefact suppression capabilities of the AFE by *in vitro* DBS tests

To examine the capability of the proposed Chebyshev notch channel to suppress stimulation artefacts and thus allow artefact-free LFP recording during stimulation, two *in vitro* setups were prepared, one for testing unipolar DBS and one for testing bipolar DBS. The details of these two setups have been given in Figure 4.3 (Section 4.2.2). More specifically, the aim of these experiments was to investigate whether or not the proposed Chebyshev notch channel could extend the available bandwidth of LFP recording during stimulation, and to further compare its performance with the Bessel notch channel's performance but with the focus to be on their stimulation suppression capabilities rather than their recording capabilities, which have already been tested (Sections 4.3.1.1 and 4.3.1.2).

The strategy followed for the tests was to gradually increase the available bandwidth and thus allow more artefacts to affect the recorded signals. At each bandwidth setting, the quality of the recorded signals was assessed. The shortening of the available bandwidth was achieved by the application of a real-time and high-order digital low-pass filter. The first step towards increasing the available bandwidth for recording during stimulation setups, was to define a passband between 0.5 and 140 Hz, with 140 Hz being the stimulation frequency and the central frequency of the notch filters. The next step was to define a passband between 0.5 and 250 Hz to examine the impact of the artefacts coming from the stimulation harmonic at 280 Hz on the recorded signals.

The first test (for both bandwidths) was to inject a weak sinusoidal single tone (1 μV peak, 15 Hz) into tyrode solution and examine the recording capabilities of the Chebyshev notch channel in and without the presence of bipolar stimulation (140 Hz, 3 V peak, 100 μs). Given 0.5-140 Hz bandwidth, the Chebyshev notch channel was able to record the weak sinusoidal single tone without (Figure 4.11a and 4.11e) and in (Figure 4.11b and 4.11f) the presence of bipolar stimulation. Finally, when the bandwidth was set from 0.5 to 250 Hz, the Chebyshev notch channel was again able

to record the weak sinusoidal single tone without (Figure 4.11c and 4.11g) and in (Figure 4.11d and 4.11h) the presence of bipolar stimulation.

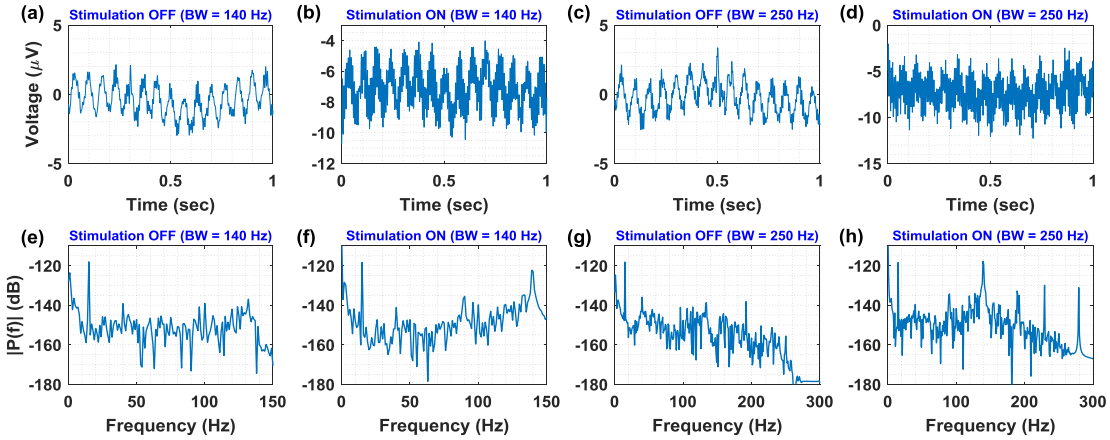

Figure 4.11: Time and frequency responses of the Chebyshev notch channel, in and without the presence of bipolar stimulation (140 Hz, 3 V peak, 100 μs). The test signal was a sinusoidal single tone with an amplitude of approximately 1 μV peak and a frequency of 15 Hz. (a) Time-domain recording without the presence of stimulation for a passband set from 0.5 to 140 Hz. (b) Time-domain recording in the presence of stimulation for a passband set from 0.5 to 140 Hz. (c) Time-domain recording without the presence of stimulation for a passband ranging from 0.5 to 250 Hz. (d) Time-domain recording in the presence of stimulation for a passband ranging from 0.5 to 250 Hz. (e) Amplitude spectrum of the signals presented in Figure 4.11a. (f) Amplitude spectrum of the signals presented in Figure 4.11b. (g) Amplitude spectrum of the signals presented in Figure 4.11c. (h) Amplitude spectrum of the signals presented in Figure 4.11d.

Having ensured that the designed Chebyshev notch channel was able to record a weak sinusoidal single tone during stimulation without facing saturation issues, the next step was to compare its artefact reduction capabilities with the capabilities of the Bessel notch channel. In these tests, “played back” LFP signals (repetitions of an LFP segment lasting for 10 seconds, obtained from [110]) with two visible spectral peaks at approximately 167 Hz and 221 Hz were injected in tyrode solution from a waveform generator, as described in Section 4.2.2 (Figure 4.3). The goal of these experiments was to test all possible circumstances (in/without the presence of bipolar/unipolar stimulation) and prove that 1) the designed Chebyshev AFE can indeed provide a bandwidth that extends beyond the stimulation frequency of 140 Hz and 2) the application of the Chebyshev notch filter does not prevent the successful recording of

frequencies that are close to the stop band (for instance the 167 Hz spectral peak of the LFP signal used in this series of experiments).

In Figure 4.12, the time and frequency responses of the Chebyshev and Bessel notch channels, in and without the presence of bipolar (Figure 4.12a-h) and unipolar (Figure 4.12i-p) stimulation, are represented in two y-axes graphs, where the left (blue) and the right (red) y-axes correspond to the responses of the Chebyshev and the Bessel notch channels, respectively. As shown in Figures 4.12a and 4.12i, “the played back” LFP signals were injected to the solution and were recorded by the Chebyshev (signal in blue) and Bessel (signal in red) notch channels without the presence of stimulation. Figures 4.12e and 4.12m present the amplitude spectrum of the signals shown in Figures 4.12a and 4.12i, respectively. Next, stimulation pulses (140 Hz frequency, 3V pp amplitude and 100 μs pulse width) were injected to the solution and the recorded signals are represented in Figures 4.12b and 4.12j. Figures 4.12f and 4.12n present the amplitude spectrum of the signals shown in Figures 4.12b and 4.12j, respectively.

As shown in Figures 4.12c and 4.12k, “the played back” LFP signals were injected to the solution and were recorded by the Chebyshev (signal in blue) and Bessel (signal in red) notch channels without the presence of stimulation. Figures 4.12g and 4.12o present the amplitude spectrum of the signals shown in Figures 4.12c and 4.12k, respectively. Next, stimulation pulses (140 Hz frequency, 3V pp amplitude and 100 μs pulse width) were injected to the solution and the recorded signals are represented in Figures 4.12d and 4.12l. Figures 4.12h and 4.12p depict the amplitude spectrum of the signals shown in Figures 4.12d and 4.12l, respectively.

A first observation stemming from the time responses shown in Figure 4.12, is that the Bessel notch channel is more vulnerable, in comparison to the Chebyshev one, to dc voltage offsets coming from the electrode-solution interface (in Figures 4.12a and 4.12c the signal in red is more turbulent compared to the signal in blue). Hence, the time-domain signal recorded by the Chebyshev notch channel during stimulation better approximates the signal recorded when no stimulation is applied, compared to the Bessel notch channel. To quantify the differences between the recorded signals during stimulation and the ones recorded without stimulation, the normalised RMSE

calculation was used. The normalisation for the RMSE calculation was performed over the range of the reference signal, which is the signal recorded without the presence of stimulation.

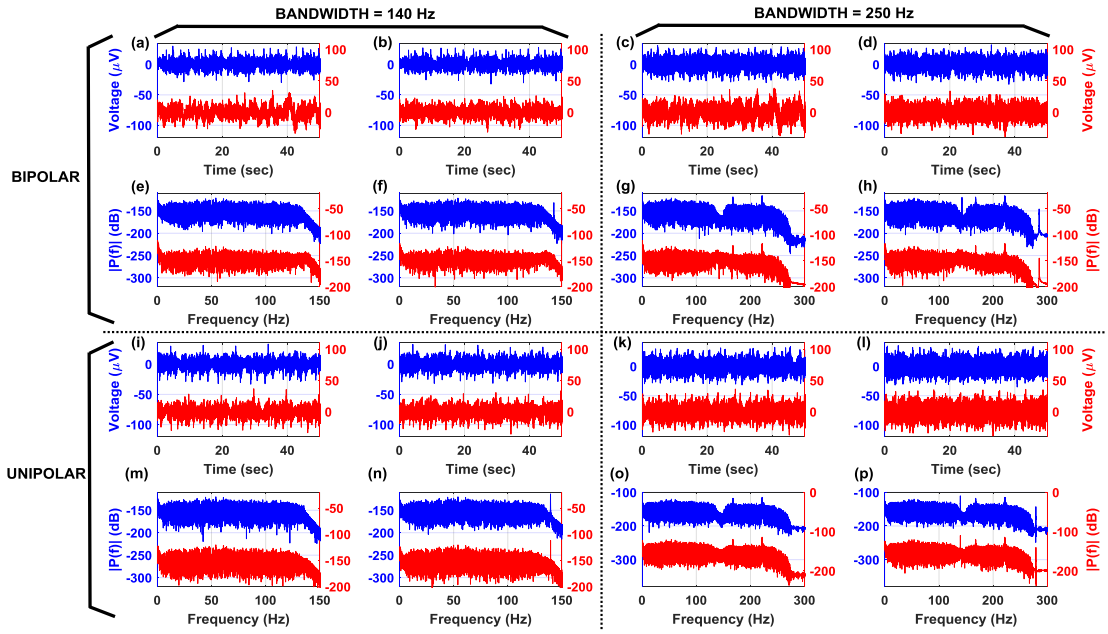

Figure 4.12: Temporal response and spectral profile of the Chebyshev (blue – corresponding to the left y-axis) and Bessel (red – corresponding to the right y-axis) notch channels, in and without the presence of bipolar and unipolar stimulation. (a) Time-domain LFP recording without the presence of bipolar stimulation for a passband of (0.5-140 Hz). (b) Time-domain LFP recording in the presence of bipolar stimulation for a passband of (0.5-140 Hz). (c) Time-domain LFP recording without the presence of bipolar stimulation for a passband of (0.5-250 Hz). (d) Time-domain LFP recording in the presence of bipolar stimulation for a passband of (0.5-250 Hz). (e) Amplitude spectrum of the signals presented in Figure 4.12a. (f) Amplitude spectrum of the signals presented in Figure 4.12b. (g) Amplitude spectrum of the signals presented in Figure 4.12c. (h) Amplitude spectrum of the signals presented in Figure 4.12d. (i) Time-domain LFP recording without the presence of unipolar stimulation for a passband of (0.5-140 Hz). (j) Time-domain LFP recording in the presence of unipolar stimulation for a passband of (0.5-140 Hz). (k) Time-domain LFP recording without the presence of unipolar stimulation for a passband of (0.5-250 Hz). (l) Time-domain LFP recording in the presence of unipolar stimulation for a passband of (0.5-250 Hz). (m) Amplitude spectrum of the signals presented in Figure 4.12i. (n) Amplitude spectrum of the signals presented in Figure 4.12j. (o) Amplitude spectrum of the signals presented in Figure 4.12k. (p) Amplitude spectrum of the signals presented in Figure 4.12l.

Before showing the RMSE values for the two types of stimulation, it is important to present more detailed time-domain recordings where LFP signals, in and without the

presence of stimulation, overlap to each other. In this way, a clearer view on the quality of the recorded signals can be formed. Figures 4.13 and 4.14 illustrate detailed views of the time-domain LFP recordings taken from the Chebyshev (blue line) and the Bessel (red line) notch channels, with (solid line) and without (dash-dot line) unipolar (Figure 4.13) and bipolar (Figure 4.14) stimulation.

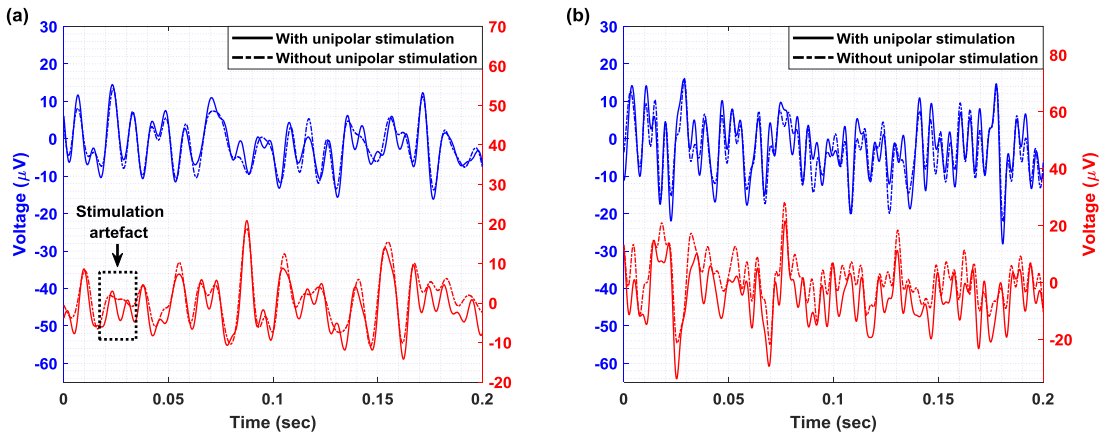

Figure 4.13: Detailed view of the time-domain LFP recordings taken from the Chebyshev (blue line corresponding to the left y-axis) and the Bessel (red line corresponding to the right y-axis) notch channels, with (solid line) and without (dash-dot line) unipolar stimulation. (a) The passband of both channels is between 0.5 Hz and 140 Hz. (b) The passband of both channels is between 0.5 Hz and 250 Hz.

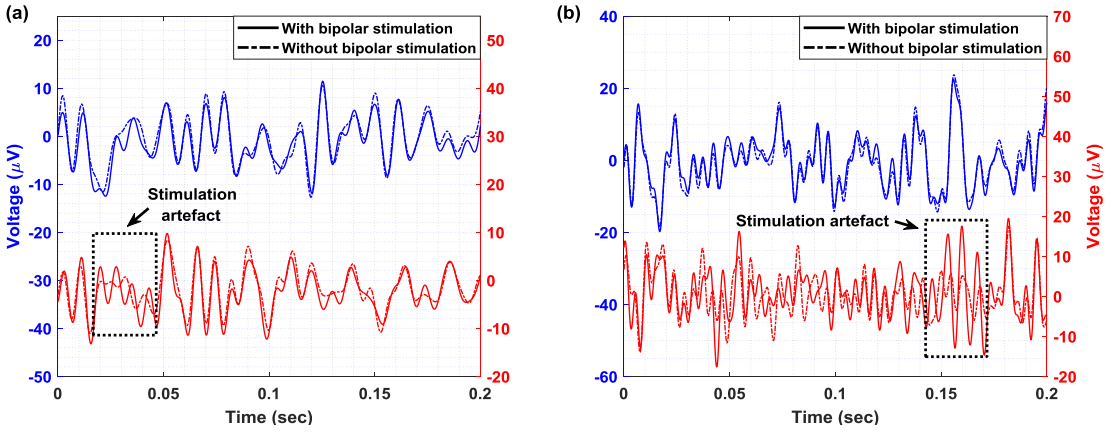

Figure 4.14: Detailed view of the time-domain LFP recordings taken from the Chebyshev (blue line corresponding to the left y-axis) and the Bessel (red line corresponding to the right y-axis) notch channels, with (solid line) and without (dash-dot line) bipolar stimulation. (a) The passband of both channels is between 0.5 Hz and 140 Hz. (b) The passband of both channels is between 0.5 Hz and 250 Hz.

In both figures, some stimulation artefacts appear in the LFP recordings collected by means of the Bessel notch channel. This observation leads to the conclusion that the Chebyshev notch channel provides more stable and reliable recordings of the LFP signals during stimulation in comparison to the Bessel notch channel. This is mainly attributed to the fact that the Chebyshev notch filter provides a stronger attenuation at the notch frequency than the Bessel notch filter (Figure 4.5a).

Furthermore, a graphical representation of the amplitude spectrum of the contaminating signals entering the positive (green colour) and negative (red) input of the front-end INA of the designed Chebyshev notch channel, along with the amplitude spectrum of the channel's output in (black) and without (pink) the presence of stimulation, after digitally removing the 280 Hz harmonic from the recorded LFP signals during stimulation (spectrum in black), is depicted in Figure 4.15. Figure 4.15a and 4.15b correspond to the unipolar and bipolar stimulation setting, respectively. It is clear that aliasing artefacts located at various frequencies that are not harmonic repetitions of the stimulation frequency (=140 Hz) exist in the spectrum of the contaminating signals. This finding is in accordance with results measured from existing DBS devices [16, 98].

However, Figure 4.15 shows that the amplitude spectrum of the channel's output in the presence of either unipolar or bipolar stimulation is free from these artefacts and thus approximates the spectrum of the signals recorded without stimulation. This important finding could be attributed to the fact that the proposed AFE does not include passive filtering before the front-end INA. Front-end passive filters can lead to the degradation of the combined (passive filter plus INA) apparent CMRR of the front-end due to component mismatches [84]. The absence of such a passive filter network enhances the ability of the proposed AFE to reject common-mode disturbances stemming from the electrode-solution interface, thus offering a smooth spectrum at the output of the AFE and an artefact-free LFP recording in both unipolar and bipolar stimulation setups.

Finally, Figure 4.16 presents the normalised RMSE values that quantify the differences between the recorded signals in and without the presence of unipolar (Figure 4.16a)

and bipolar (Figure 4.16b) stimulation for the Chebyshev (dashed blue line) and Bessel (dotted blue line) notch channels. The vertical red lines shown in the graph represent the amplitude Bode plots in each recording case. In other words, they describe the available passband, set by the application of a very steep real-time digital low-pass filter. To examine the benefits gained by the use of an analog notch filter for artefact suppression, a third AFE, which does not include any analog notch filtering circuitry, was introduced in the experimental setup (solid blue line in Figure 4.16). More specifically, this AFE includes a passive, 1st order low-pass filter at 8 kHz, followed by the INA chip AD8420 from Analog Devices set to provide a gain of 20 dB.

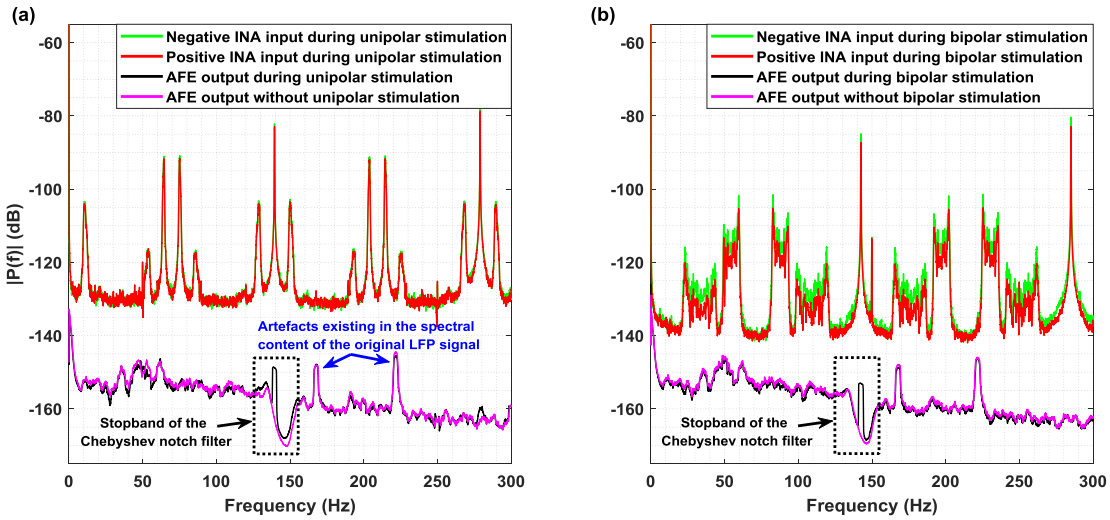

Figure 4.15: Amplitude spectrum (recorded from the Chebyshev notch channel) of the 1) signals entering the negative (green) and positive (red) inputs of the front-end INA during stimulation, 2) the AFE output voltage during stimulation (black), and 3) the AFE output voltage without the presence of stimulation (pink). a) Unipolar stimulation setting, and b) Bipolar stimulation setting. INA, instrumentation amplifier; AFE, analog front-end.

Referring to Figure 4.16a, in the first bandwidth setting (0.5-50 Hz), the Chebyshev and Bessel notch channels present similar RMSE values, whereas the “channel without notch filter” already shows a bigger error. In the next three bandwidth settings (100 Hz, 140 Hz and 250 Hz), the Chebyshev notch channel presents the lowest error, whereas the “channel without notch filter” shows unacceptably high errors, which is attributed to the fact that no artefact suppression strategy exists in that case. The same conclusions are drawn from Figure 4.16b, where the Chebyshev notch channel

presents the lowest error, and the Bessel notch channel shows an error that is higher than the one appeared in the unipolar stimulation. This observation is explained by the Bessel notch channel's vulnerability to offsets noticed in the LFP recordings in and without the presence of bipolar stimulation (Figure 4.12). As in the case of unipolar stimulation, the "channel without notch filter" is characterised by unacceptably high errors at bandwidths greater than 50 Hz.

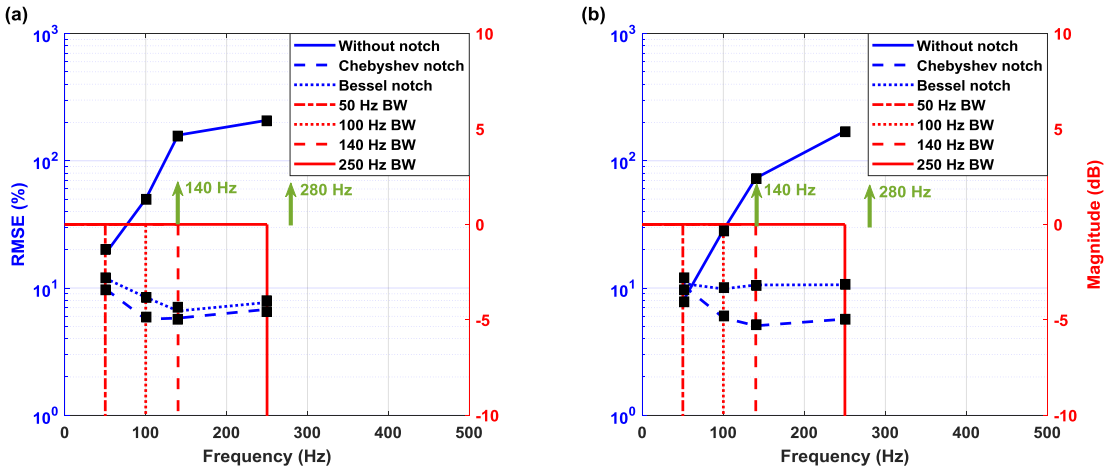

Figure 4.16: Normalised RMSE values between the signals recorded in and without the presence of unipolar (a) and bipolar (b) stimulation. The green vectors show the main stimulation frequency component (=140 Hz) and the stimulation harmonic that is closer to the available passband (=280 Hz). The red lines (correspond to the right y-axis) show the available bandwidth (BW) for each recording trial and the blue lines (correspond to the left y-axis) depict the calculated RMSE values. RMSE, root mean square error; BW, bandwidth.

Another important observation is that the RMSE errors produced by the Chebyshev and Bessel notch channels decrease when the bandwidth increases from 50 Hz to 140 Hz and then slightly increase when the bandwidth is set at 250 Hz. This is attributed to a small intrinsic error that mostly comes from the dc offset voltage which is generated by the electrodes and is not completely rejected by the system. Hence, this small error in voltage is more apparent in smaller bandwidths where the recorded LFP signals are weaker due to filtering (0.5 – 50 Hz), decreases when the available bandwidth (and thus recorded LFP signal strength) increases (0.5 – 140 Hz) and, finally, slightly increases when the available bandwidth increases even more (0.5 –

250 Hz) since more interference leaks into the wide passband (the 280 Hz stimulation harmonic is getting closer to the passband).

4.3.5 Evaluation of the artefact suppression capabilities of the AFE by *in vivo* DBS tests

To provide a proof-of-function *in vivo*, LFPs were recorded from the thalamus of a non-human primate, at the end of a non-recovery procedure that was performed for the primary purpose of another ongoing study. The experiments were approved by the local ethics committee at Newcastle University and performed under appropriate UK Home Office licenses in accordance with the Animals (Scientific Procedures) Act 1986. A female rhesus macaque was anesthetised with a ketamine/midazolam/alfentanil infusion and a segmented DBS electrode (electrode A, model DB-2201, Boston Scientific Neuromodulation) was implanted into the thalamus as shown in Figure 4.17. The monophasic stimulation pulses (6 V peak-to-peak amplitude, 142 Hz frequency and 100 μs pulse width) were delivered by means of a commercial stimulator (Grass, Astromed, Inc., USA). Unipolar stimulation was applied to contact 2 of electrode A (illustrated as A2 in Figure 4.17) and LFP signals were differentially recorded through contacts 1 and 3 of electrode A (illustrated as A1 and A3 in Figure 4.17, respectively). The stimulation ground was introduced into the neural tissue through contact 1 (illustrated as B1 in Figure 4.17) of electrode B (model 401261, St. Jude Medical), which was placed over the frontal cortex. A commercial isolator (SIU5 stimulus isolation point, Grass, Astromed, Inc., USA) was used to electrically isolate the stimulation ground from the mains. The non-human primate was under anaesthesia during the entire experiment with the head held in a primate stereotactic frame, which was connected to the ground of the recording system. The LFP signals recorded by the proposed AFE were digitized at a sampling frequency of 20 kSPS and depicted on a computer by the Powerlab data acquisition system (ADInstruments).

As shown in Figures 4.18a and 4,18b, the Chebyshev notch channel can provide artefact-free LFP recordings during DBS. Moreover, after examining the detailed views of the LFP recordings acquired without and in the presence of DBS (Figures 4.18c-f),

the following conclusions have been drawn: 1) the stimulation artefacts (at 142 Hz and 284 Hz) induced by DBS have been significantly suppressed (blue line in Figure 4.18f), 2) the amplitude spectrum of the LFP signals recorded during DBS (Figure 4.18f) is free from aliasing artefacts, which is in full agreement with the *in vitro* experimental results shown in Figure 4.15, and 3) the contaminating 142 Hz DBS pulses are successfully suppressed by 68 dBs (amplitude spectrums in red and black in Figure 4.18f) thanks to the combined notch filtering action and the front-end INA's (high) CMRR.

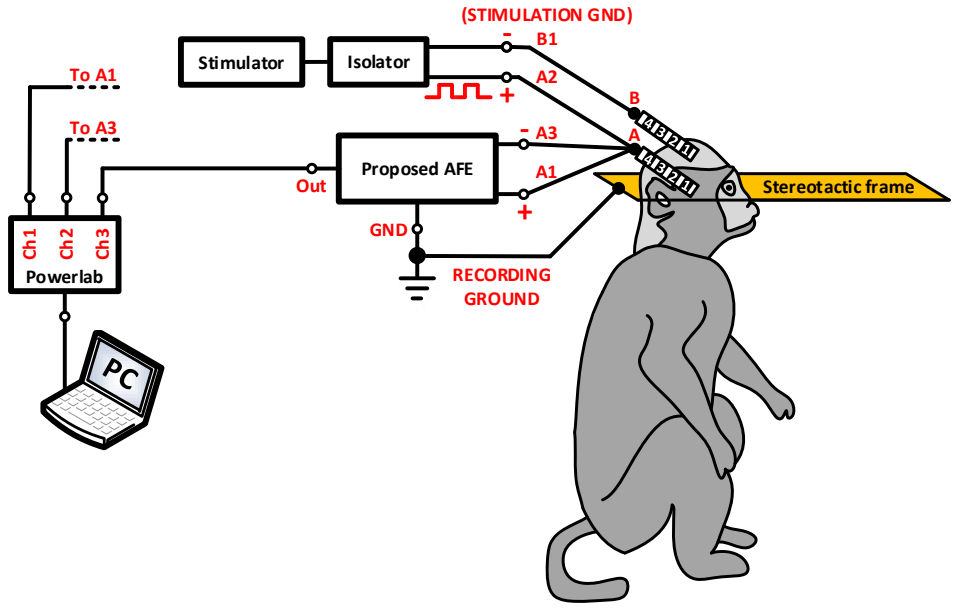

Figure 4.17: Experimental setup for evaluating the artefact suppression capabilities of the proposed Chebyshev AFE channel architecture *in vivo*. A deep brain stimulation electrode (electrode A, model DB-2201, Boston Scientific Neuromodulation) was implanted into the thalamus of an anaesthetised non-human primate. The monophasic stimulation pulses (6 V peak-to-peak amplitude, 142 Hz frequency and 100 µs pulse width) were delivered by means of a commercial stimulator (Grass, Astromed, Inc., USA). Unipolar stimulation was applied to contact A2 and LFP signals were differentially recorded through contacts A1 and A3. The stimulation ground was introduced into the brain tissue through a second electrode (contact B1, model 401261, St. Jude Medical) that was placed over the frontal cortex. The stimulation ground was electrically isolated from the mains using a commercial isolator (SIU5 stimulus isolation point, Grass, Astromed, Inc., USA).The non-human primate was under anaesthesia with the head held in a primate stereotactic frame, which was connected to the ground of the recording system. The LFP signals recorded by the proposed AFE were digitized at a sampling frequency of 20 kSPS (samples per second) and depicted on a computer by the Powerlab data acquisition system (ADInstruments). AFE, analog front-end.

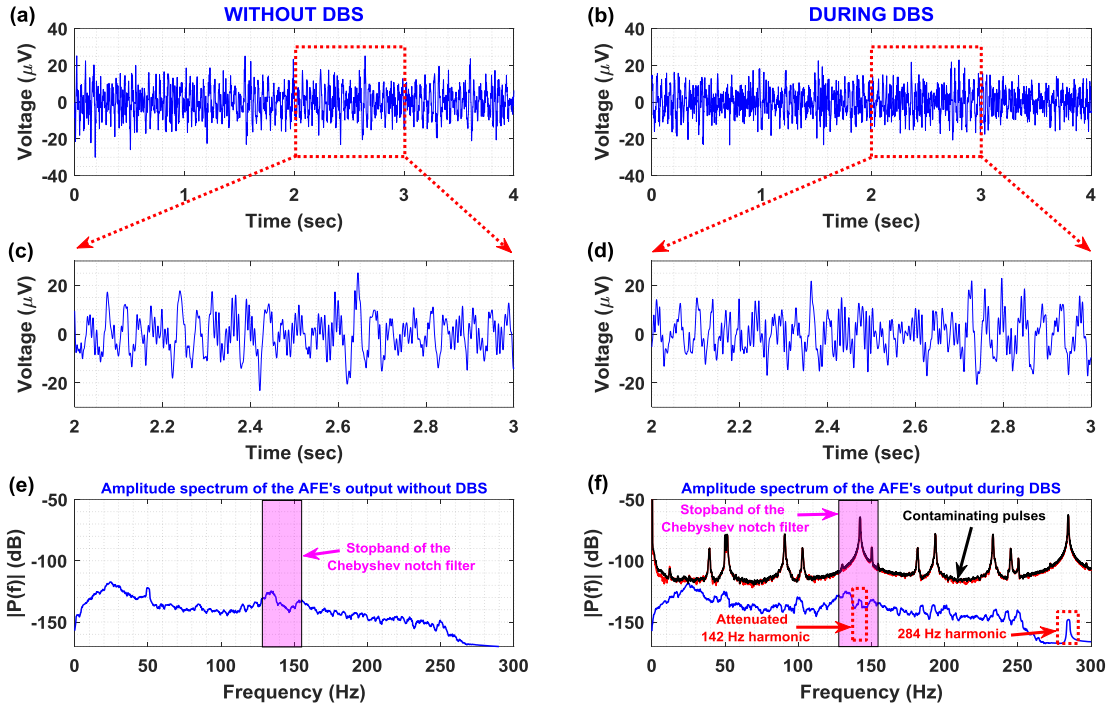

Figure 4.18: The proposed Chebyshev AFE architecture for artefact-free local field potential (LFP) recordings during unipolar deep brain stimulation (DBS) *in vivo*. LFP signals were recorded from the thalamus of an anaesthetised non-human primate in and without the presence of DBS with the experimental setup illustrated in Figure 4.17. (a) Bipolar (differential) LFP recordings without DBS. (b) Bipolar (differential) LFP recordings during DBS. (c) Detailed view of the LFP recordings acquired without DBS. (d) Detailed view of the LFP recordings acquired during DBS. (e) Amplitude spectrum of the LFP signal recorded without DBS. (f) Amplitude spectrum of: 1) the LFP signal recorded during DBS (blue line), and 2) the stimulation pulses presented at the positive (red line) and negative (black line) inputs of the front-end instrumentation amplifier. It is clear that the proposed artefact suppression strategy (analog notch filtering at 140 Hz and digital low-pass filtering at 250 Hz) allows for artefact-free LFP recordings during DBS (observe the 142 Hz stimulation fundamental frequency, which has been strongly attenuated by the high-order notch filtering action).

4.4 Discussion/Conclusion

4.4.1 Methodological significance

The analog filtering strategy proposed in this Chapter is an effective approach to adequately attenuate stimulation artefacts. In our application, the stimulation artefact and the signal of interest are highly overlapping both in the time and frequency domain.

More specifically, the stimulation frequency (=140 Hz) and its first two harmonics (280 and 420 Hz) are located within the system bandwidth (0.5 – 500 Hz). As a result, the stimulation artefact and its harmonics could not be separated from the neural signals of interest using an analog high-order low-pass filter, which was the strategy employed by Rossi *et al*. [67].

An alternative approach that has been extensively adopted is to provide a switching circuit that disconnects the front-end leads of the amplifier during stimulation [67]. This technique is effective for applications, such as transcranial magnetic stimulation [111–114] and evoked potentials [115], because in these bidirectional setups the signal of interest and the stimulation artefact are well separated in the time domain but highly overlapping in the frequency domain [67]. Since the aim of this work was to provide LFP recordings during stimulation, the employment of this method was avoided.

Furthermore, in a typical stimulation therapy (for PD or dystonia) the neural signals of interest, which typically are on the order of 1–10 μV when measured from DBS electrodes, are up to six orders of magnitude weaker than the applied stimulation pulses. Hence, a high gain is required to make the neural signals detectable by the front-end electronics and the subsequent ADC blocks. However, this high amplification is applied on both neural signals and stimulation artefact, which often leads to the saturation of the front-end electronics. As a result, the strategy to completely shift the stimulation suppression to the digital domain by using template subtraction techniques or FIR filtering increases the risk of saturation [67].

It is thus clear that high dynamic range front-ends are required for subtraction and component decomposition techniques, since the artefact waveform has to be recorded without being distorted. Besides that, as previously described (Section 2.5.4), template subtraction techniques usually need high sampling rates to avoid amplitude fluctuation due to aliasing, which leads to variable and incomplete artefact subtraction by a template. In addition, even if a high sampling rate is used, these methods are often prone to error as sampling and stimulation are not perfectly locked. On the other hand, reconstruction techniques lose information during the artefact, degrading the achieved SNR [54].

Taking into account the above discussion of the artefact suppression strategies proposed so far, it can be argued that an alternative strategy for recording in real time artefact-free LFP signals during DBS could be implemented either using an application-specific block of analog filters or an effective combination of analog and digital filters. The preservation of real-time operation is particularly important in closed-loop architectures because the stimulation must change in real time based on the measured state of the neural network [16]. The strategy of removing all of the artefacts by employing (usually high-order) digital filtering techniques could lead to significant delays in data processing and challenge the practicality of a real-time, closed-loop modality that would employ a digital only artefact-reduction strategy; thus this approach was also avoided.

The finally adopted approach was to introduce a Bainter analog notch filter to increase the available bandwidth by attenuating the artefacts originating from the stimulation frequency (=140 Hz) and apply high-order low-pass filtering to suppress the higher-frequency harmonics. For convenience and testing purposes the low-pass filtering was realised in the digital domain to facilitate the experimental study of the suggested methodology. Conceivably, however, a high-order analog low-pass filter could also be used to attenuate high-order harmonics albeit at the expense of size for the externalised device and limited flexibility during the experimental testing of the proposed strategy. The Bainter notch filter topology was selected because its Q factor is dependent on the gain of the amplifiers as opposed to component matching. Therefore, the notch depth is not sensitive to temperature drift or aging [116]. The analog notch filter introduces a negligible delay in the signal processing chain. The digital low-pass filtering block was provided by the Powerlab 16/35 data acquisition system and introduced a processing delay of 75 msec. This delay is in full agreement with the delays introduced by wearable recording systems that apply real-time DSP [117].

Another reason for placing an analog notch filter in the signal chain is to attenuate the stimulation interference produced by the electrode/tissue impedance mismatch. This mismatch exists even in a symmetric sensing and stimulation setup and is hard to be

controlled within a biological environment [16]. Hence, an AFE that includes an 8th order Bainter notch filter with Chebyshev response was designed, fabricated and tested *in vitro* and *in vivo*. In addition, a comparison, in terms of recording quality and artefact suppression capability, between the designed AFE, an identical AFE employing an 8th order Bessel notch filter, and an AFE that does not include any analog band-stop filtering and rejects all the artefacts digitally, was drawn and measured results were provided.

Since the next harmonic after the main stimulation frequency is at 280 Hz, it was decided to gradually increase the available bandwidth from 140 Hz to 250 Hz and calculate the normalised RMSE between the recorded signals in and without the presence of stimulation. In both unipolar and bipolar stimulation, when the bandwidth is restricted between 0.5 and 50 Hz, the RMSE values of the three channels are kept low. However, the channel lacking notch filtering exhibits unacceptably high RMSE values when the bandwidth is extended beyond 50 Hz. This finding, which emphasizes the necessity of using an analog notch filter for artefact removal, is in accordance with results measured from existing DBS devices that offer a passband reaching 100 Hz. Those results indicated that prominent stimulation artefacts existed on the raw LFP trace, consisting of both harmonic repetitions of the stimulation frequency and aliasing artefacts [98]. In respect to the Chebyshev and Bessel notch channels, no significant change in the calculated RMSE was introduced by the extension of the recording bandwidth to 250 Hz, which leads to the conclusion that the artefacts introduced by the 280 Hz harmonic (and higher ones) do not significantly affect the quality of the recorded LFPs when adequately suppressed by a high-order low-pass filter at 250 Hz.

At this point, it would be useful to consider the Fourier representation of the short in duration DBS pulses and how that representation clicks with the experimentally confirmed strong suppression of the stimulation artefact(s). Assuming that the applied periodic DBS pulse-stream is characterised by a pulse amplitude A_{stim}, pulse-stream period T and single pulse duration τ, then it can be shown that:

$$\text{DBS pulse-stream} = (m \cdot A_{stim}) + \sum_{n=1}^{n=+\infty} \left[\frac{2A_{stim}}{n\pi} \times \sin(\mathrm{n}\pi \cdot \mathrm{m}) \times \cos(2\pi \cdot nf \cdot t)\right] \quad (4.4)$$

where $m = (\tau/T)$ = duty cycle of DBS pulses. Given that the DBS pulses are short in duration (in this study $m \sim 1.4/1.5\%$ then for $n\pi m < 0.2\ rad \Leftrightarrow n < \left(\frac{0.2}{0.015\pi}\right) = 4.24$), the amplitudes of the fundamental and the first three harmonics ($n = 1,2,3,4$) can be approximated as

$$\frac{2A_{stim}}{n\pi} \times \sin(\mathrm{n}\pi \cdot \mathrm{m}) \cong \frac{2A_{stim}}{n\pi}(\mathrm{n}\pi \cdot \mathrm{m}) = 2mA_{stim} (= 0.03A_{stim}\ when\ m = 0.015) \qquad (4.5)$$

In other words, thanks to the short duration of DBS pulses, the amplitudes of their constituent harmonics will be much smaller than the applied A_{stim}. Such a low harmonic amplitude both facilitates and demystifies the strong suppression of the fundamental by means of appropriately tuned high-order notch responses and the practical absence of ringing during recording in the presence of DBS (as verified by the multitude of *in vitro* and *in vivo* results). It is this basic analysis which has triggered the investigation of the customised approach for LFP recording during DBS presented in this Chapter. It should be stressed that the response of the Chebyshev notch AFE would be considerably different for pulse-streams characterised by high duty cycle values m.

For instance, for a given n value (i.e. for a given harmonic order) the amplitude of the harmonic varies $\sim \sin(\mathrm{n}\pi \cdot \mathrm{m})$; hence for $\mathrm{n} = 1$ and $\mathrm{m} = 10, 20\ \mathrm{or}\ 30\%$ the amplitude of the fundamental increases to $0.197 \cdot A_{stim}$ (for $\mathrm{m} = 10\%$), to $0.374 \cdot A_{stim}$ (for $\mathrm{m} = 20\%$) and to $0.515 \cdot A_{stim}$ (for $\mathrm{m} = 30\%$). Such amplitudes are 6.6 times (or 16.4 dB) to 17.2 times (or 24.7 dB) stronger than the amplitude $0.03A_{stim}$ corresponding to the DBS duty cycle of $\mathrm{m} = 1.5\%$. In such large m value cases even a high-order notch would not be able to suppress enough the amplitude of the fundamental and the stimulation harmonics would feed through.

A thorough examination of the measured results presented in this Chapter leads to the conclusion that the sensing and stimulation artefact suppression capabilities of the Chebyshev notch channel outperform the capabilities of the Bessel notch channel. Another important finding is that the proposed AFE architecture provides LFP recordings that are not affected by aliasing artefacts located at frequencies that are

not harmonic repetitions of the stimulation frequency. As a result, bearing in mind the desire for wide bandwidth LFP recording with DBS artefacts suppressed, the approach studied here suggests that cascading two analog high-order notch filters at 140 and 280 Hz with a steep, high-order, also analog, low-pass filter of a cut-off frequency ~400 Hz should enable practical, low delay, high-quality and higher bandwidth (~400 Hz) LFP recording with DBS artefacts strongly suppressed; at the expense of somewhat increased size and power consumption of the externalised AFE. The full digital realisation in the Lab (e.g. via Powerlab) of the same architecture (two notch filters and a low-pass one) introduces a total approximate delay higher than 0.6 sec [2×270 msec (notch filters) + 75 msec (low-pass)] which challenges the practicality of a fast, closed-loop neurostimulation system.

One of the important merits of the proposed method is that biosignal blanking during stimulation is avoided. Furthermore, the proposed artefact suppression strategy allows for artefact-free LFP recordings during monophasic DBS, which can be perceived as the worst case scenario, since in biphasic DBS the artefact and the electrochemical DC offsets [54] produced are weaker (Figures 4.4d and 4.4e). Indeed, it should be highlighted that in both *in vitro* and *in vivo* experimental setups, LFP signals were successfully recorded during stimulation even in the presence of inherent asymmetries introduced by the use of segmented DBS electrodes that allowed differential-mode interference to enter the signal chain. Moreover, the design decision to directly connect the front-end amplifier to the DBS electrodes allowed us to avoid the introduction of a passive high-pass filter network at the first stage of the AFE and the subsequent noise deterioration and CMRR reduction this approach would entail. The input bias current of the front-end INA (150 nA maximum) is lower than the limit imposed by the IEC 60601-1 standard (maximum allowable patient auxiliary current for Type B, normally connected applied parts equals 10 μA). Hence, the designed AFE architecture complies with safety requirements.

Finally, when pairs of electrodes are used for recording differential voltages from the human body (invasively or non-invasively), it is recommended to use the same material for each of the electrodes because, in such a case, their half-cell potentials

are approximately equal. According to [39], this strategy: a) ensures that the net DC potential seen at the input of the amplifier connected to the electrodes is relatively small, and b) minimizes possible saturation effects in the case of high-gain direct-coupled amplifiers. Since the high-gain front-end INA (with high-pass characteristics) differentially records LFP signals from two contacts of a DBS electrode that have been formed from the same material (platinum-iridium), the differential DC offset that is produced at the electrode-tissue interface and must be rejected is in the order of tens of millivolts [6], and it is thus removed by the proposed system (the maximum dc offset rejection that can be accomplished by the Chebyshev notch AFE in its current format is ± 32 mV, which is in full agreement with the rejection offered by modern bidirectional neural interface systems [118]), as verified by the *in vitro* and *in vivo* measured experimental results presented in this Chapter. According to the datasheet of the front-end INA (AD8429) chip, the maximum electrochemical DC offset that can be rejected by the proposed system is approximately equal to 2.4 V, as long as it is presented as a common-mode signal at the two inputs of the Chebyshev notch AFE.

4.4.2 Limitations and further improvements

All of the practical merits described above, are achieved at the expense of signal loss in the frequency band ranging from 125 to 155 Hz and the appearance of noise in this frequency band when extremely weak (0.32 μV rms) LFP signals, which are close to the Chebyshev notch channel's noise floor (~0.1 μV rms), are recorded (Figure 4.10b). Crucially, the impulse response of the analog notch filter when stimulated by a DBS pulse is characterized by low-amplitude and short-duration transient ringing (Figures 4.4d and 4.4e), which, as the measured results in Figures 4.10c, 4.13 and 4.14 indicate, does not affect the quality of the recorded LFP signals. However, even this short and weak ringing can be avoided by adding an analog multiplexer which would allow the user to introduce, through software, the analog notch filter in the signal chain just before the onset of DBS and exclude it from the signal chain before the termination of stimulation, e.g. 15 msec before the last stimulation pulse. In this way, the weak ringing effect that may be introduced by the Chebyshev notch filter after the last DBS

pulse it senses, would not appear after the (actual) last stimulation pulse, and thus it would not interfere with evoked resonant neural activity, which is a physiological signal of interest that appears 4 msec after the (actual) last DBS pulse and lasts for ~20 msec [20]. Besides that, in a future version of this architecture (comprised, for example, of two high-order analog notch filters and one high-order analog low-pass filter, as explained above) the introduction of digitally selectable/tunable notch and cut-off frequencies would provide the researchers and clinicians with the ability to reject more than one stimulation rate while preserving wide bandwidth LFP recording.

Finally, the existence of small intrinsic errors produced by the Chebyshev and Bessel notch channels (Figure 4.16) mainly results from the dc offset voltage, which is produced by the electrodes and is not completely rejected by the AFE. However, further rejection (up to 85 mV of differential dc offset voltage, as shown in Table 4.2) of this differential dc offset could be accomplished by introducing a passive 1st order high-pass filter between the front-end INA and notch filtering stages (in other words between stages 1 and 2 of the current AFE design shown in Figure 4.1). The addition of this high-pass filter would introduce a small delay in the transient response of the system [119], however, this delay may be considered tolerable taking into consideration the enhancement this strategy could offer in the recording capabilities of the Chebyshev notch AFE during DBS.

4.4.3 Pathophysiological significance

The key aim for this system is to remove existing constraints for clinical neuroscience discovery with bidirectional neural interfaces. The major attributes of the proposed system are its wide pass band and low noise floor relative to other devices allowing the recording of signals during stimulation at the same site with greater resolution, especially at higher frequencies. An alternative approach is to shift attention from LFPs in subcortical nuclei to electrocorticographic recordings as tractable feedback biomarkers for closed-loop neurostimulation [104, 108, 120]. In some cases, this is necessary as ECoG signals have better SNRs and are spatially separated from deep brain stimulation sites, so they are less corrupted by stimulation-induced artefact.

However, subcortical recordings have their own merits. These include the inherent convergence in basal ganglia targets, so that extensive cortical regions can be modulated, and clearer pathological correlates [121]. Furthermore, the recording of signals from the same electrodes as used for deep brain stimulation limits instrumentation of the brain and thereby the incremental morbidity and expense [65]. The currently described system facilitates consideration of local field potential activity as a source of feedback control. Specifically, it widens the potential feature space beyond the beta band [17, 19, 122] to lower amplitude, higher frequency activities. These include finely tuned gamma activity centred around 70 Hz and associated with dyskinesias [123], and high frequency oscillations of over 200 Hz in frequency, together with related phase amplitude coupling which have both been linked to bradykinesia and rigidity [124]. Moreover, stimulation evoked subcortical potentials have high frequency components that may carry information about targeting and motor impairment in PD [20]. A richer feature space also improves the capability of machine learning approaches to identify control signals [125, 126]. In its current embodiment, the large power dissipation would not allow for placement of the circuit in an implantable system. The intention is to accomplish a more complete sampling of the physiomarker space, and based on what is discovered, define a bespoke application specific integrated circuit (ASIC) that would offer the resolution required within the power constraints of the implant.

To sum up, the *in vivo* experimental results presented in this Chapter show that the proposed recording system: a) does not saturate during DBS, and b) is able to provide wide-frequency-range, artefact-free LFP recordings during DBS. From the pathophysiologic point of view, being able to extend the available bandwidth for LFP recording from the target stimulation site constitutes vital progress for developing novel closed-loop neuromodulation systems that use low and higher-frequency LFPs as control signals.

4.4.4 Conclusion

The novel and versatile Chebyshev notch channel designed, developed and tested *in vitro* and *in vivo*, allows for real-time, low-noise and artefact-free LFP recordings during DBS for a bandwidth of 0.5 – 250 Hz. Proof of the proposed architecture's recording and artefact suppression capabilities has been provided and its performance has been assessed quantitatively by means of a series of *in vitro* and *in vivo* experiments and comparisons with commercial high-performance biopotential acquisition systems. It has been proven that the designed AFE is able to reliably record weak LFP signals (1 - 10 µV peak in Figures 4.13, 4.14 and 4.18), in and without the presence of either unipolar or bipolar DBS. This work is the first step towards developing a closed-loop neuromodulation system which utilizes symptom-related LFPs that are continuously recorded during DBS from the STN of parkinsonian patients as control signals.

Chapter 5. Purely analog and mixed mode (analog & digital) approaches for artefact suppression during electrical stimulation

5.1 Introduction

The artefact suppression strategy presented in Chapter 4 can be characterised as an application specific solution to the problem of artefact coupling into the field potentials of interest in closed-loop neurostimulation systems. However, in its current embodiment, the analog notch filter only offers flexibility on the type of stimulation pulses (both monophasic and biphasic pulses can be attenuated) that can be suppressed and not on the central frequency that can be rejected.

This desired tunability on the value of the filter cut-off frequency could be offered by the incorporation of a tunable analog notch filter into the AFE architecture presented in Chapter 4. This Chapter presents a family of novel continuous-time analog (low-/high-/band-pass and notch) filters that can provide tunability on their cut-off frequency. It is clear that the introduction of a tunable notch filter stemming from this family of filters into the AFE architecture presented in Chapter 4 would: a) preserve the real-time character of the system, which is particularly important in closed-loop neurostimulation, and b) offer flexibility on both the type of stimulation pulses (monophasic/biphasic) and the spectral location of the stimulation harmonics that can be attenuated.

It is important to note here that the artefact suppression methodology presented so far makes use of either fixed or tunable analog notch filter blocks in order to effectively suppress DBS pulses, which are generally characterized by small duty cycles. However, in applications where pulses of higher duty cycles are applied (e.g. up to 20% duty cycle values are used in spinal cord stimulation), ringing oscillations may be induced in the biosignals of interest due to the notch operation. Moreover, in applications where high-bandwidth (>250 Hz) LFP recording is desired, the

introduction of more than one high-order notch filter is required. It is thus clear that the wider the desired bandwidth for LFP recording the more increased the power consumption and the size of the overall system.

This Chapter also presents the design and *in vitro* testing of a novel and robust mixed-mode (analog & digital) artefact suppression strategy, which: a) can provide wide-bandwidth biosignal recordings during electrical stimulation in bidirectional setups where simultaneous sensing and stimulation at the same site are required, without increasing the complexity and size of the overall system, and b) can offer flexibility on the stimulation pulse morphology (monophasic/balanced biphasic pulses of any frequency, amplitude - that stays within the dynamic range of the AFE - and pulse width can be attenuated) it can suppress without introducing any ringing oscillations in the processed bioelectrical signals.

5.2 Tunable analog filters

The key motivation for developing a new family of tunable analog filters was to provide simple analog notch filter blocks that can be introduced in neuromodulation devices to provide tunability in the cut-off frequency along with real-time and artefact-free biosignal recordings during electrical stimulation. One possible implementation of the tunable analog notch filter design introduced in this thesis is shown in Figure 5.1. It consists of two 2nd order tunable analog filters; a 2nd order low-pass filter and a 2nd order high-pass filter, which constitute a 2nd order band-pass filter. Next, an instrumentation amplifier is used to convert the band-pass filter into notch.

Another possible implementation of the tunable analog notch filter design presented in this thesis is shown in Figure 5.2. In this case, a single-operational amplifier 2nd order tunable band-pass filter along with an instrumentation amplifier are used to form the 2nd order tunable notch filter block. It is important to note that the contribution of Dr Georgios Zafeiropoulos towards the development/fabrication of the tunable filter topologies presented in this Section is acknowledged at this point.

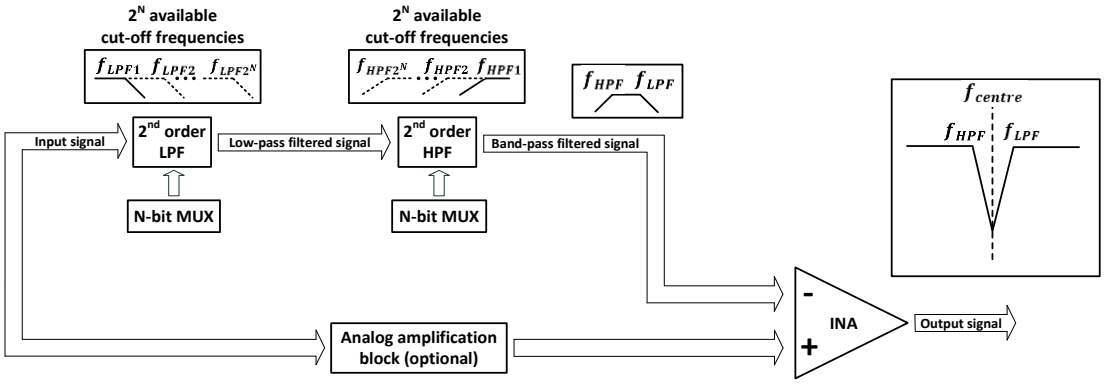

Figure 5.1: Block diagram of a tunable analog notch filter that is implemented by cascading a tunable 2nd order low-pass filter and a tunable 2nd order high-pass filter. An analog amplification block is also added to ensure that the same gain is applied on the signals entering the two inputs of the instrumentation amplifier. LPF, low-pass filter; HPF, high-pass filter; MUX, multiplexer; INA, instrumentation amplifier.

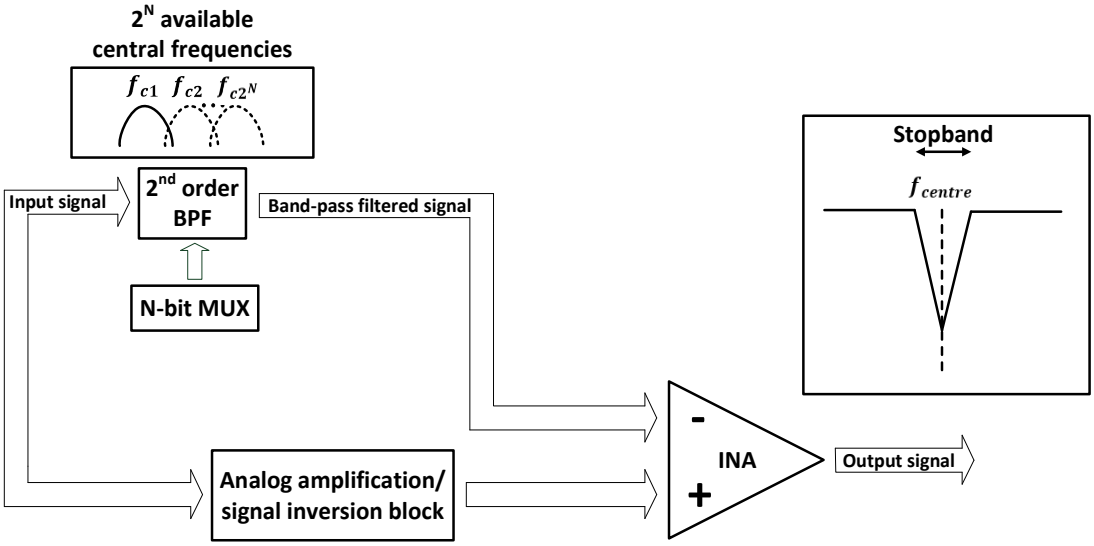

Figure 5.2: Block diagram showing the implementation of a tunable analog notch filter that is based on a single-operational amplifier 2nd order tunable band-pass filter. An analog amplification/signal inversion block is also added to ensure that the signals entering the two inputs of the instrumentation amplifier do not face any gain/phase mismatch. BPF, band-pass filter; MUX, multiplexer; INA, instrumentation amplifier.

The tunable 2nd order (low- and high-pass) filter blocks shown in Figures 5.3 and 5.4 can be placed in the notch filter implementation presented in Figure 5.1. On the other hand, the tunable 2nd order (single-operational amplifier) band-pass filter block shown

in Figure 5.4 can be placed in the notch filter implementation presented in Figure 5.2. The tunable filter topology shown in Figure 5.3 is based on a 2nd order Sallen-Key (SK) filter topology combined with a N:1 multiplexer, where N is the number of available filter cut-off frequencies.

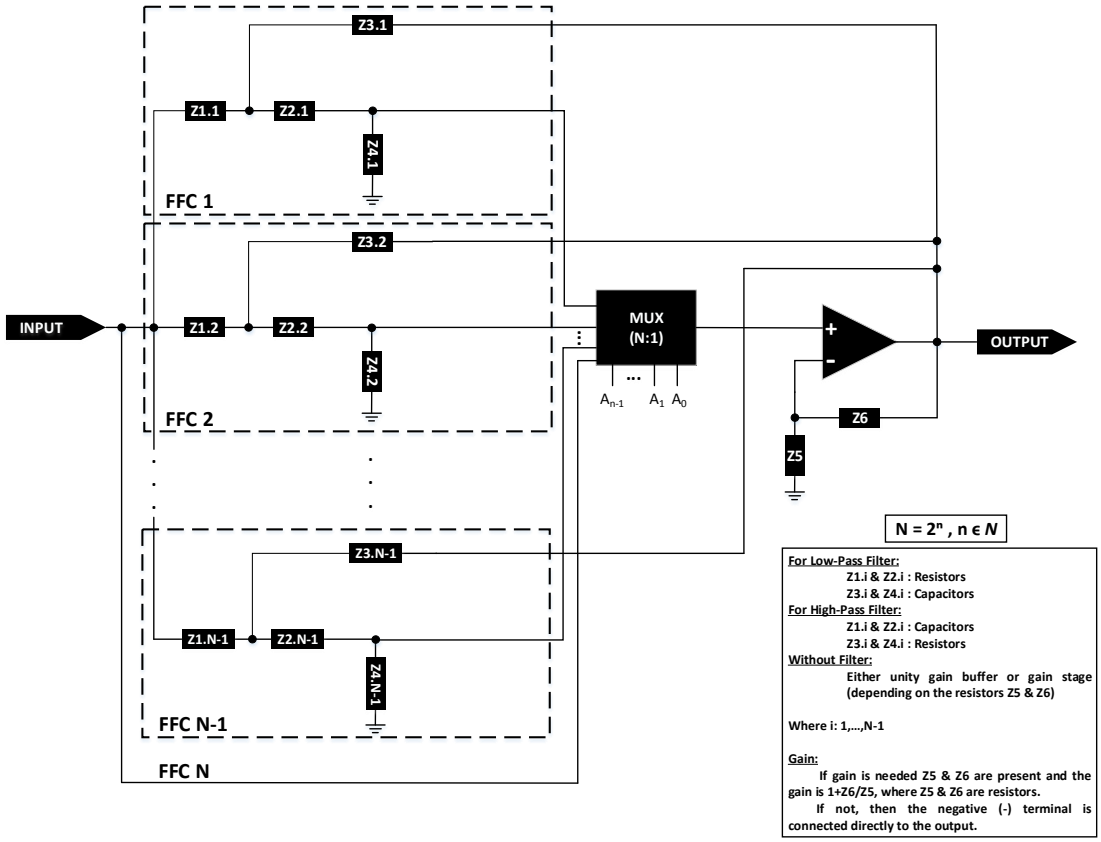

Figure 5.3: Block diagram of a tunable 2nd order (low- or high-pass) filter that is based on the Sallen-Key filter architecture. MUX, multiplexer; FFC, filter forming circuitry.

The fundamental 2nd order SK filter topology (with unity gain) uses one operational amplifier and a filter forming circuitry (FFC) (two resistors and two capacitors) to implement different filter functions (low- or high-pass filters). The proposed topology is also based on one operational amplifier but it adds extra FFCs (every FFC represents a different cut-off frequency), which share the same input signal and they are controlled by a N:1 multiplexer (Figure 5.3). Thus, only one out of the N FFCs is available at the output of the multiplexer. This FFC determines the bandwidth of the

system and its Q factor. The output of the multiplexer is connected to the positive input of the operational amplifier. Additionally, a gain can be introduced by connecting two extra resistors to the negative input of the operational amplifier. However, this gain applies to all the FFCs. It is worth mentioning here that the feedback loops introduced by the additional FFCs are directly connected to the output of the opamp without changing the transfer function of the system. Hence, the response of the proposed system approximates the response of a 2nd order SK topology that uses the same FFC. Measured results of tunable low-pass, high-pass, band-pass (implemented as a cascade of a 2nd order low-pass and a 2nd order high-pass filter), and notch filters based on this architecture are shown in Figures 5.5-5.8.

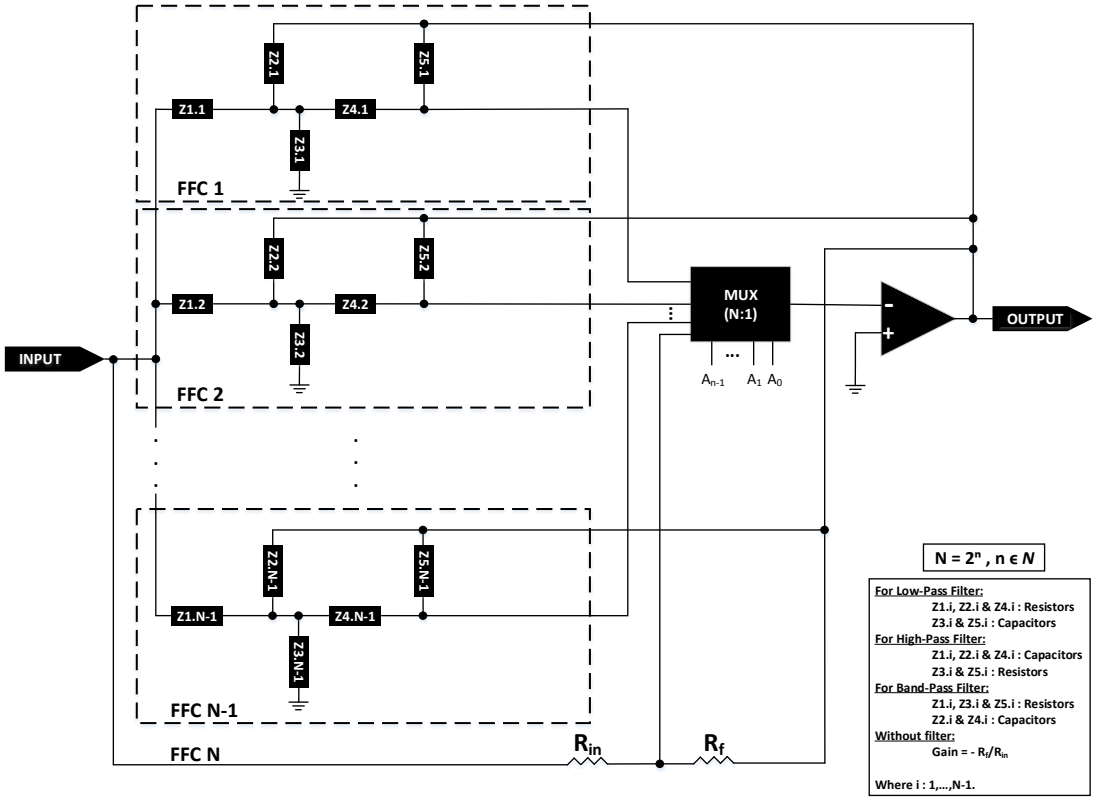

Figure 5.4: Block diagram of a tunable 2nd order (low-, high- or band-pass) filter that is based on the multiple feedback filter architecture. MUX, multiplexer; FFC, filter forming circuitry.

The tunable filter topology shown in Figure 5.4 is based on a 2nd order multiple feedback (MFB) filter topology combined with a N:1 multiplexer, where N is the number

of available filter cut-off frequencies. The fundamental 2nd order MFB filter topology (with unity gain) uses one operational amplifier and a FFC (three resistors and two capacitors) to implement different filter functions (low-, high- or band-pass filters). The proposed topology adds extra FFCs (every FFC represents a different cut-off frequency), which share the same input signal and they are controlled by a N:1 multiplexer (Figure 5.4). Thus, only one out of the N FFCs is available at the output of the multiplexer. This FFC determines the bandwidth of the system and its Q factor. The output of the multiplexer is connected to the negative input of the operational amplifier.

The advantage of this topology is that it doesn't require additional resistors to introduce gain into the system. Each FFC can provide a different gain into the system. It is worth mentioning once more that the feedback loops introduced by the additional FFCs are directly connected to the output of the operational amplifier without changing the transfer function of the system. Thus, the response of the proposed system approximates the response of a 2nd order MFB topology that uses the same FFC.

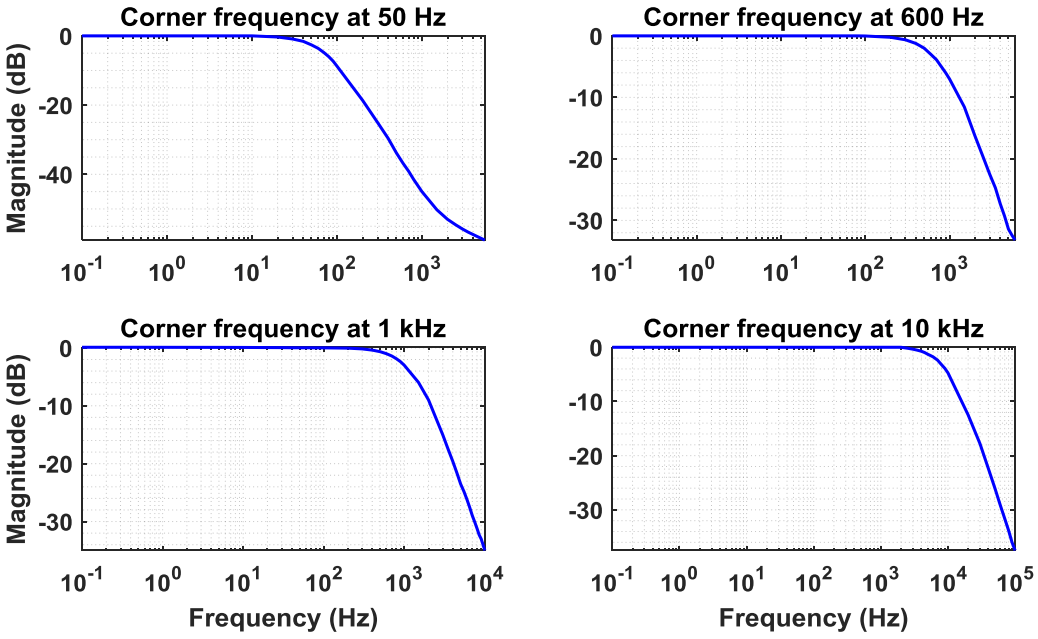

Figure 5.5: Measured system response of a tunable 2nd order low-pass filter that is based on the SK architecture and provides 4 different corner frequencies (50 Hz, 600 Hz, 1 kHz, 10 kHz).

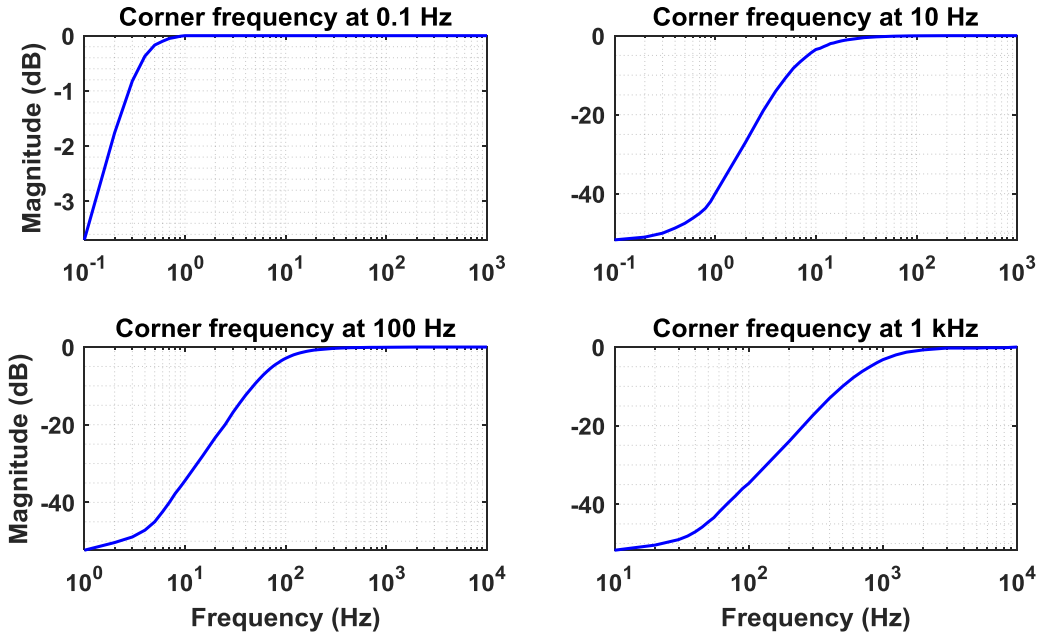

Figure 5.6: Measured system response of a tunable 2nd order high-pass filter that is based on the SK architecture and provides 4 different corner frequencies (0.1 Hz, 10 Hz, 100 Hz, 1 kHz).

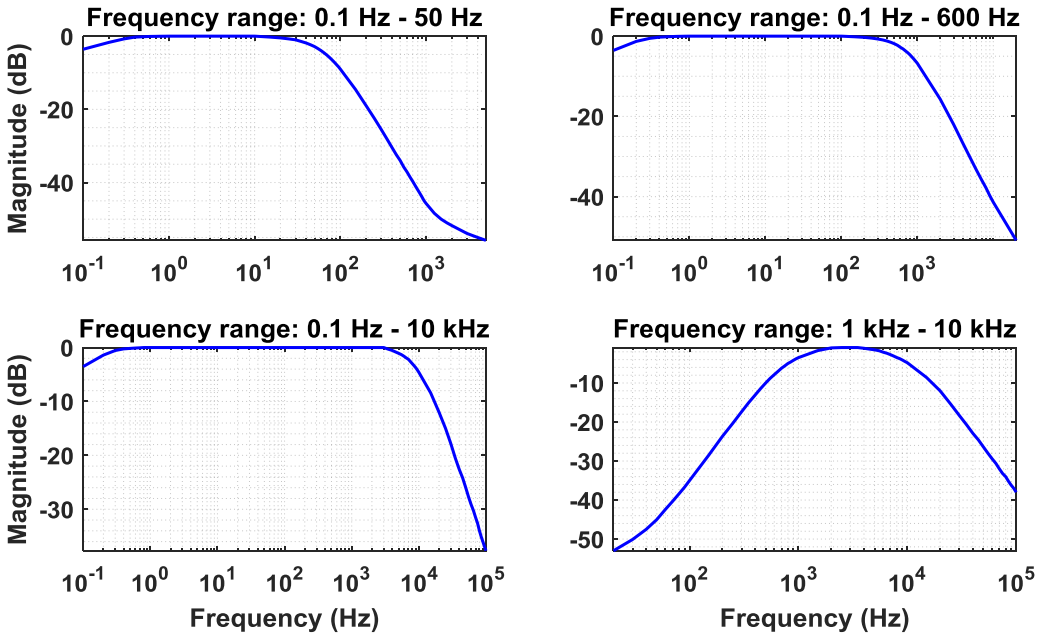

Figure 5.7: Measured system response of a tunable 2nd order band-pass filter that is formed by cascading the tunable low-pass and high-pass filter blocks presented in Figures 5.5 and 5.6, respectively. In order to assess the selectivity of the filter, four different system passbands were selected using the system multiplexers.

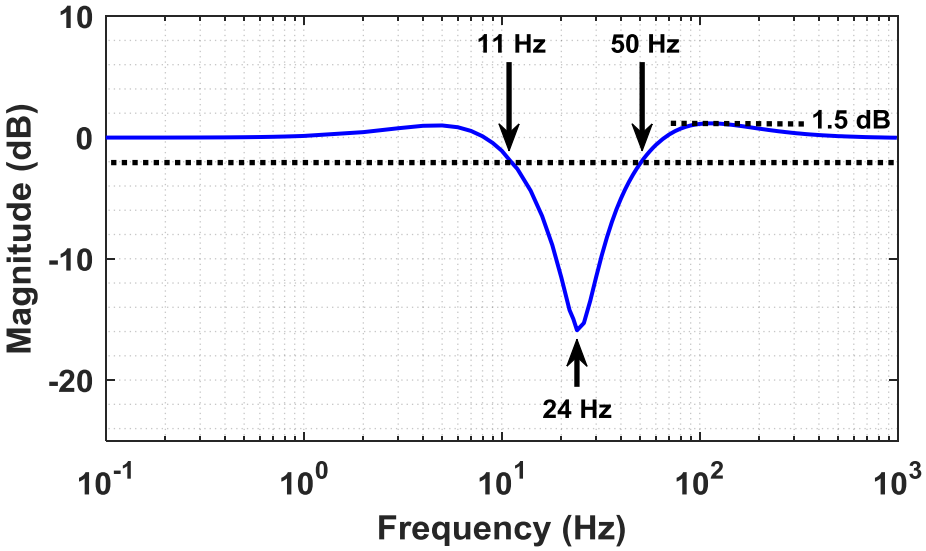

Figure 5.8: Measured system response of a tunable 2nd order notch filter that is based on the architecture shown in Figure 5.1. The passband of the band-pass filter block included in the notch filter architecture was tuned to be between 10 Hz and 50 Hz. Thus, this range of frequencies is anticipated to be cut by the notch filter. The centre frequency of the notch filter is equal to the centre frequency of the band-pass filter, which is $f_C = \sqrt{f_L \times f_H}$, where f_L and f_H are the low- and high- cut-off frequencies of the band-pass filter, respectively. By substituting the values of f_L = 10 Hz and f_H = 50 Hz, the theoretical centre frequency of the notch filter is found to be equal to 22.36 Hz. It is clear that the measured centre frequency (24 Hz) approximates the theoretical one (22.36 Hz), while the measured low- and high- cut-off frequencies are equal to 11 and 50 Hz, respectively. The observed overshoot stays within acceptable levels since it is lower than 1.5 dB.

Moreover, since the same design concept and resulting filter topology characterize the SK and MFB tunable filter topologies, the tunable MFB notch filter (Figure 5.2) can indeed be used for stimulation artefact suppression. The correct operation of the tunable MFB notch filter has been verified by conducting appropriate simulation tests (Figure 5.9) in a widely used SPICE-based analog simulation program (TINA from Texas Instruments). In Figure 5.9 a tunable 2nd order MFB notch filter (which was designed based on the architecture shown in Figure 5.2) is compared with a 2nd order Bainter filter. The two filters were designed to provide approximately the same stopband (ranging from 135 Hz to 145 Hz) and the same central frequency (≈139.6 Hz). It is clear that the tunable 2nd order MFB notch filter does not exhibit any undesired overshoot. Hence, it could be used as a building block in bidirectional systems, where

tunability in the cut-off frequency is required. Finally, the tunable MFB notch filter block could be used to form high-order tunable notch filters in order to achieve stronger attenuation at the central frequency of the notch. The block diagram of such a system is shown in Figure 5.10.

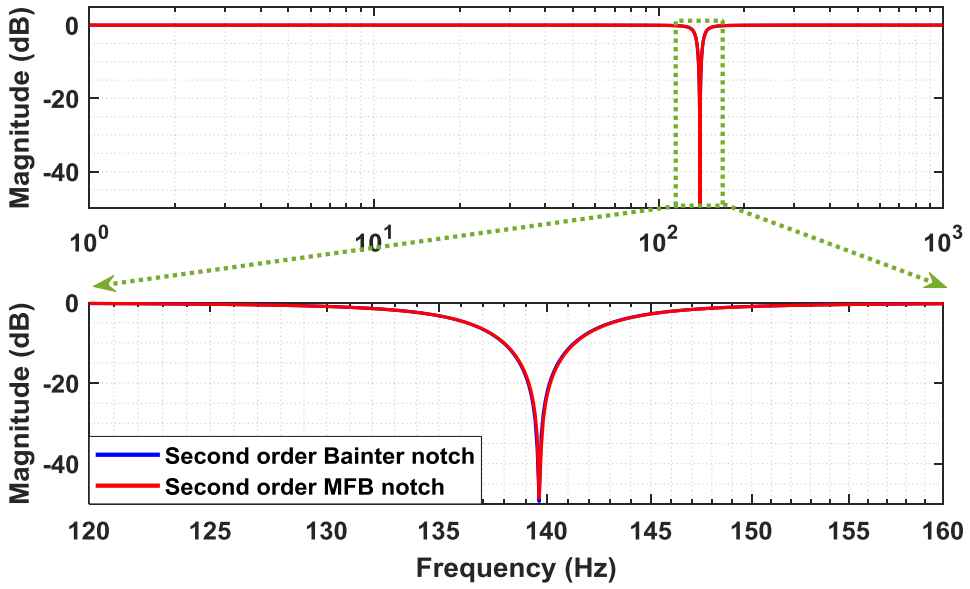

Figure 5.9: Simulated system response of a tunable 2nd order MFB notch filter (solid red line), which is based on the architecture shown in Figure 5.2, and a fixed 2nd order Bainter notch filter (solid blue line). It is clear that the reponse of the MFB notch filter does not exhibit any undesired overshoot.

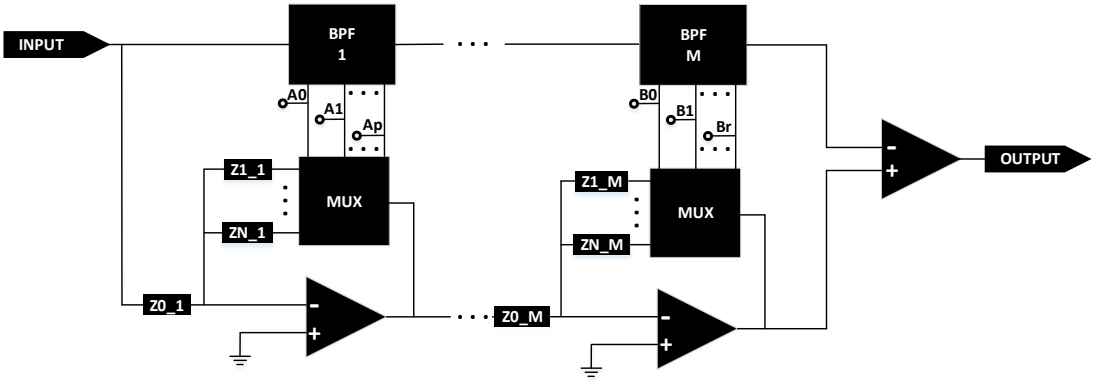

Figure 5.10: Block diagram of a high-order MFB notch filter. In this topology, the multiplexer included in every tunable BPF block shares the same control lines (A0, A1,…, Ap) with the multiplexer of the corresponding inverting amplifier. This approach ensures that the signals at the two paths culminating in the two inputs of the instrumentation amplifier are characterized by the same amplitude and phase.

All in all, based on the measured results presented in Figures 5.5-5.8 and the simulated result shown in Figure 5.9, it is clear that the tunable SK and MFB filter topologies (Figures 5.3 and 5.4) can indeed be used as building blocks for implementing the tunable notch filter architectures shown in Figures 5.1 and 5.2.

5.3 A novel mixed mode (analog & digital) artefact suppression method

5.3.1 Design methodology

The key motivation for developing the novel artefact cancellation strategy presented in this Section was to explore an alternative approach that is not based on notch filtering in order to effectively suppress stimulation artefacts. During the design process, the requirement to provide real-time, artefact-free recordings during stimulation, and tunability in the cut-off frequency led to the development of the artefact suppression method shown in Figure 5.11. It is important to note that the contribution of Mr Simos Koutsoftidis towards the successful implementation of the original concept conceived by the author of this Thesis is acknowledged at this point.

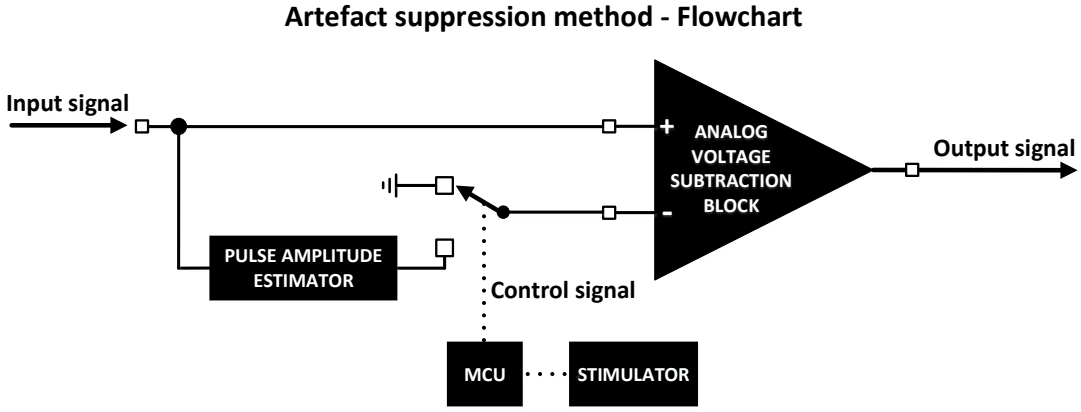

Figure 5.11: Block diagram of the proposed artefact suppression strategy. MCU, microcontroller unit.

The basic operation relies on two signal blocks: a stimulation pulse amplitude estimator and a voltage subtraction block. The estimated amplitude signal is subtracted from the contaminated signal for the duration of every incoming pulse (Figure 5.11). In other words, subtraction takes place only when high-amplitude stimulation pulses enter the signal chain. For the duration between two consecutive pulses, the ground/reference level can be subtracted from the input signal, so that the output tracks the input. An analog switch may be utilized to pass either the ground/reference or the pulse amplitude estimation to the voltage subtraction block (Figure 5.11). Control of this switching action may be performed by the stimulator controller (i.e. the microcontroller unit - MCU) in order to ensure perfect synchronization with stimulus output. It is clear that the proposed method of attenuating, in real time, the amplitude of the strong stimulation pulses does not affect the weak underlying biosignal activity. In this thesis, the aforementioned pulse amplitude estimation is conducted by an analog RMS-to-DC converter block (Figure 5.12). The type of sub-blocks contained in the RMS-to-DC converter block depends on the type of stimulation pulses that need to be suppressed; monophasic or biphasic.

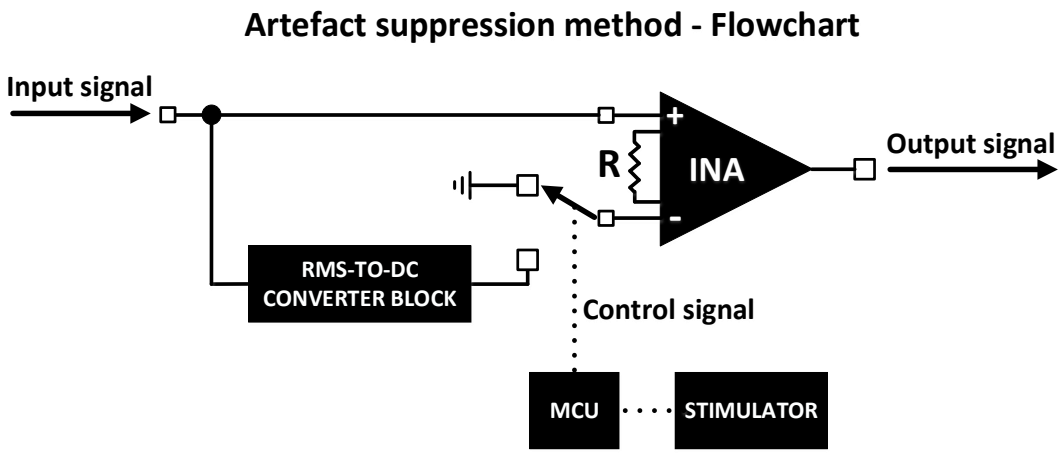

Figure 5.12: Block diagram of the proposed artefact suppression strategy where an RMS-to-DC converter block is used as a pulse amplitude estimator. MCU, microcontroller unit; INA, instrumentation amplifier.

The proposed artefact suppression block can be placed at either the first or at a subsequent signal conditioning stage of a biopotential recording AFE (Figures 5.13 and 5.14, respectively). In applications where both unipolar (against a reference electrode)

and bipolar signal recording capabilities are required, a front-end differential amplifier block (which can be built using an instrumentation or differential amplifier with/without analog filters) must precede the artefact suppression block (Figure 5.14).

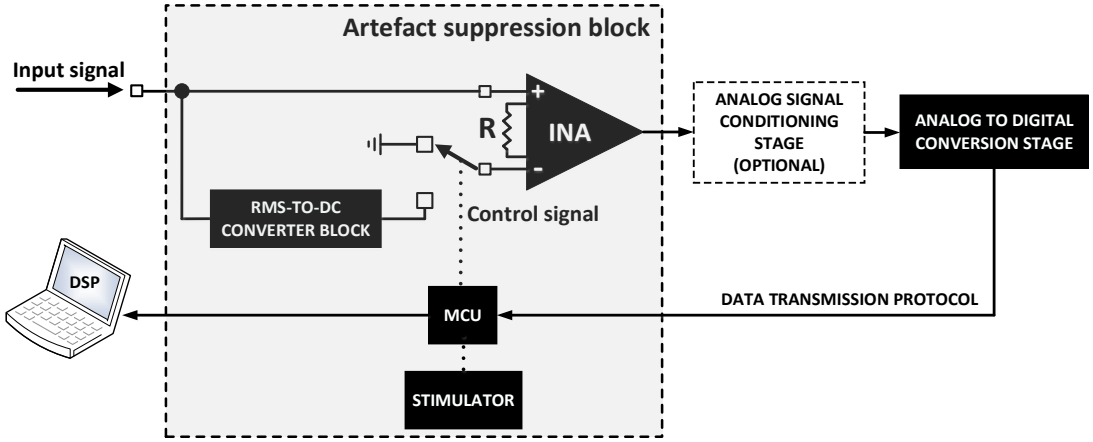

Figure 5.13: Block diagram of an AFE architecture where the proposed artefact suppression block is placed at the first stage of the signal chain. DSP, digital signal processing; MCU, microcontroller unit; INA, instrumentation amplifier.

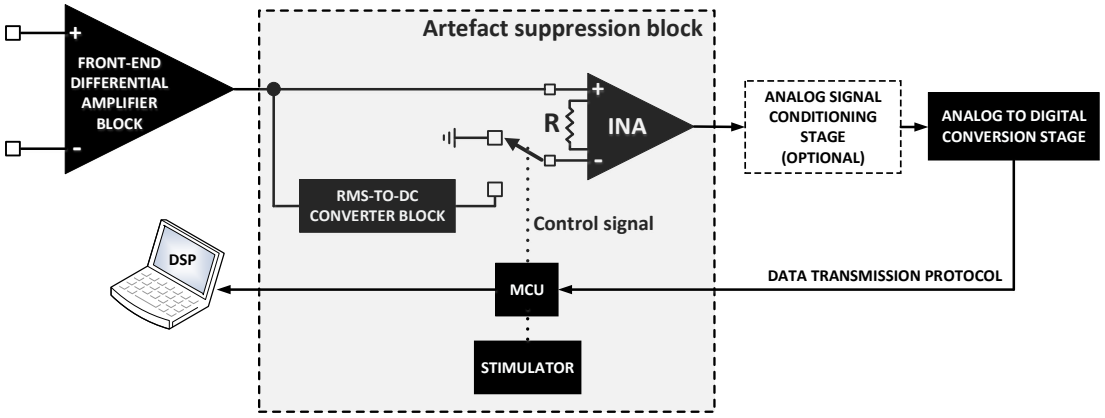

Figure 5.14: Block diagram of an AFE architecture where a front-end differential amplifier block is placed before the proposed artefact suppression block. DSP, digital signal processing; MCU, microcontroller unit; INA, instrumentation amplifier.

As far as the output signal of the proposed artefact suppression block is concerned, it can either be forwarded directly to the ADC that follows in the signal chain or be processed (e.g. an analog low-/high-pass filter could be applied) in the analog domain before being digitized. Finally, the digital signal at the output of the ADC is forwarded to

the MCU and then to a PC in order to be depicted on the computer screen. In this configuration, DSP could either be performed (if needed) in the MCU of the system or on the PC (e.g. a digital low-pass/high-pass/Hampel filter could be applied).

It is important to emphasize here that in the presented topology the control of the stimulation timing and the data processing are performed by the same entity (the MCU shown in Figures 2.13 and 2.14). However, these two tasks (stimulation timing control and data processing) could also be performed by two different processing entities, if required (e.g. two different MCUs or one MCU and one FPGA). In any case though, the processing entity that determines the stimulation timing is the one that controls the switching operation in the proposed artefact suppression block. Finally, in another configuration the analog-to-digital conversion could take place in the MCU of the system.

In the case of monophasic stimulation pulses, the RMS value returned by the RMS-to-DC converter depends on the pulse width and the frequency of the pulses, as shown below:

$$\text{RMS value} = \text{Amplitude} \times \sqrt{\frac{pulse\ width}{stimulation\ period}} \quad \Leftrightarrow$$

$$\text{Amplitude} = \text{RMS value} \times \sqrt{\frac{stimulation\ period}{pulse\ width}}, \quad (5.1)$$

Regarding the architecture of the RMS-to-DC converter block, an analog gain stage should be placed either before or after the RMS-to-DC converter (Figures 5.15 - 5.16, respectively) to convert the pulse RMS value provided by the RMS-to-DC converter to amplitude. A low-order (e.g. 1st) (passive/active) analog low-pass filter could also be added after the RMS-to-DC converter to eliminate any ripple that may exist in the RMS-to-DC converter's output voltage. As long as the pulse width and the stimulation period are kept constant then the gain value ($=\sqrt{\frac{stimulation\ period}{pulse\ width}}$) does not need to change. Hence, the RMS value, calculated in real-time by the RMS-to-DC converter, is directly converted to an accurate estimate of pulse amplitude value even in cases where the applied stimulation amplitude varies over time.

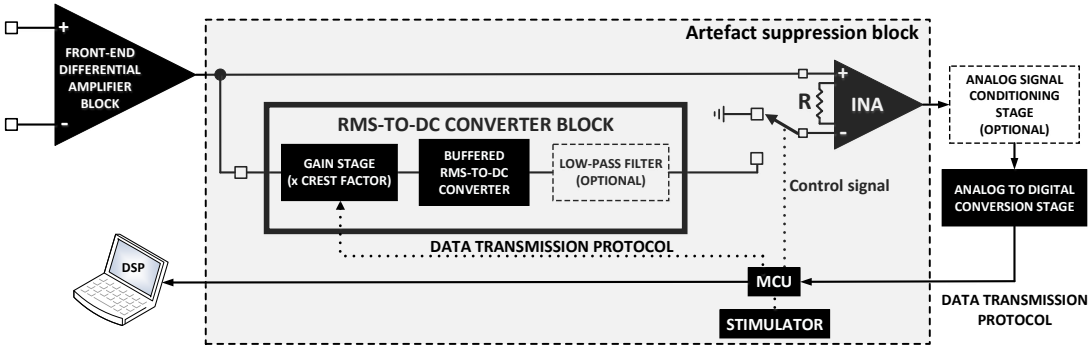

Figure 5.15: Detailed block diagram of the proposed artefact suppression strategy in the case where monophasic pulses have to be suppressed. Regarding the structure of the RMS-to-DC converter block, a gain stage is added before the RMS-to-DC converter to convert the RMS estimate into amplitude estimate and compensate for small errors that may exist in the estimation of the pulse RMS value given by the RMS-to-DC converter. DSP, digital signal processing; MCU, microcontroller unit; INA, instrumentation amplifier.

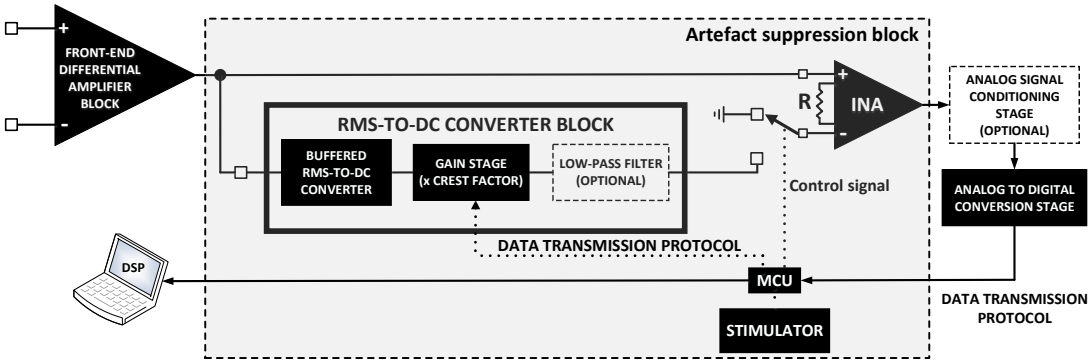

Figure 5.16: Detailed block diagram of the proposed artefact suppression strategy in the case where monophasic pulses have to be suppressed. Regarding the structure of the RMS-to-DC converter block, a gain stage is added after the RMS-to-DC converter to convert the RMS estimate into amplitude estimate and compensate for small errors that may exist in the estimation of the pulse RMS value given by the RMS-to-DC converter. DSP, digital signal processing; MCU, microcontroller unit; INA, instrumentation amplifier.

It should be noted here that if the ratio of period and pulse-width changes (equation 5.1), then the new RMS value estimation stemming from the RMS-to-DC converter has to be multiplied with an updated gain value (= $\sqrt{\frac{stimulation\ period}{pulse\ width}}$) in order to extract the correct amplitude of the input pulses. It is thus clear that in applications where tunability in the pulse width and/or frequency parameters is required, the gain of the analog gain stage should be tunable. This tunability can be achieved by building gain stages with variable

resistors whose resistance can be controlled through software (through the MCU shown in Figures 5.15 and 5.16) using a data transmission protocol (e.g. SPI).

Similarly, **in the case of balanced biphasic pulses**, the RMS value returned by the RMS-to-DC converter depends on the pulse width and the frequency of the pulses, as shown below:

$$\text{RMS value} = \text{Amplitude} \times \sqrt{\frac{total\ pulse\ width}{stimulation\ period}} \quad \Leftrightarrow$$

$$\text{Amplitude} = \text{RMS value} \times \sqrt{\frac{stimulation\ period}{total\ pulse\ width}}, \quad (5.2)$$

The term "total pulse width" in equation (5.2) corresponds to the sum of the widths of the anodic and cathodic phases (total pulse width = width of the anodic phase + width of the cathodic phase) of the biphasic pulse. It is clear that in the case of balanced biphasic pulses the widths of the two phases are equal, so the total pulse width is double the width of each phase. Regarding the architecture of the RMS-to-DC converter block, an analog gain stage should be placed after the RMS-to-DC converter (please see Figure 5.17) to convert the pulse RMS value provided by the RMS-to-DC converter to amplitude. A low-order (e.g. 1st) (passive/active) analog low-pass filter could also be added after the RMS-to-DC converter to eliminate any ripple that may exist in the RMS-to-DC converter's output voltage.

As long as the total pulse width and the stimulation period are kept constant then the gain value (= $\sqrt{\frac{stimulation\ period}{total\ pulse\ width}}$) does not need to change. Hence, the RMS value, calculated in real-time by the RMS-to-DC converter, is directly converted to an accurate estimate of pulse amplitude value even in cases where the applied stimulation amplitude varies over time. It should be noted here that if the ratio of period and total pulse width changes (equation 5.2), then the new RMS value estimation stemming from the RMS-to-DC converter has to be multiplied with an updated gain value (= $\sqrt{\frac{stimulation\ period}{total\ pulse\ width}}$) in order to extract the correct amplitude of the input pulses. It is thus clear that in applications where tunability in the pulse width and/or frequency parameters is required, the gain of

the analog gain stage should be tunable. This tunability can be achieved by building gain stages with variable resistors whose resistance can be controlled through software (through the MCU shown in Figure 5.17) using a data transmission protocol (e.g. SPI).

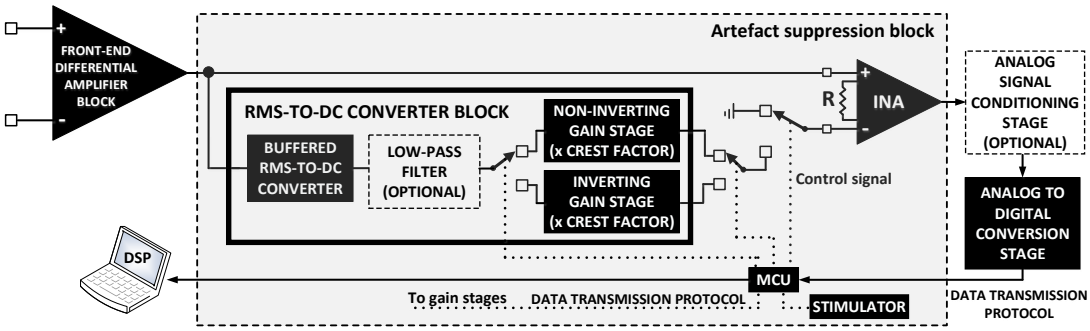

Figure 5.17: Detailed block diagram of the proposed artefact suppression strategy in the case where biphasic pulses have to be suppressed. Regarding the structure of the RMS-to-DC converter block, an inverting stage is added in the signal path (after the RMS-to-DC converter, in parallel to the non-inverting stage) to reject the negative phase of the biphasic pulses. A gain is added in both inverting and non-inverting stages (the same gain value should be used in the case of balanced biphasic pulses, whereas different gain values should be used in the case of non-balanced biphasic pulses) to convert the RMS value returned by the RMS-to-DC converter into amplitude and compensate for small errors that may exist in the estimation of the pulse RMS value given by the RMS-to-DC converter. DSP, digital signal processing; MCU, microcontroller unit; INA, instrumentation amplifier.

It is important to highlight that when the stimulation period equals the total pulse width (in other words when each of the two –anodic and cathodic- phases of the pulse has a duty cycle of 50%), then the RMS value of the balanced biphasic pulse train equals its amplitude. In this case, there is no need for additional gain stages (after the RMS-to-DC converter) since the RMS-to-DC converter returns the (desired) amplitude of the balanced biphasic pulse train.

Furthermore, since the biphasic stimulation pulse has two edges (a positive and a negative) that have to be attenuated, the RMS-to-DC converter block should be able to provide two estimations: 1) a positive estimation when the positive edge of the biphasic pulse enters the signal chain, and 2) a negative estimation (by inverting the positive one) when the negative edge of the biphasic pulse enters the signal chain. This scenario can be easily implemented in hardware by adding two different paths in the RMS-to-DC converter block; one that provides the (positive) output voltage of the

RMS-to-DC converter and another that inverts the positive output voltage of the RMS-to-DC converter (Figure 5.17). In the latter case, the (actual) estimation stemming from the RMS-to-DC converter block is finally added (because the negative estimation is subtracted by the input signal so at the end it is added to the input signal) to the contaminated signal bringing its common mode (which was negative because of the negative edge of the stimulation pulse) back to its normal value.

In another digital implementation (Figure 5.18) of this artefact reduction architecture, the RMS output as well as the input biosignal are simultaneously recorded by the ADC with amplitude extraction and subtraction stages performed in the digital domain (in the MCU shown in Figure 5.18). Control of the subtraction process is again dictated by stimulator control circuitry for synchronization purposes.

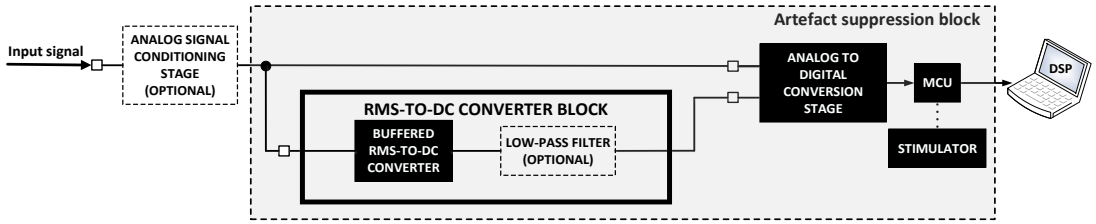

Figure 5.18: Detailed block diagram of the proposed digital artefact suppression implementation. MCU, microcontroller unit.

5.3.2 Measured results

5.3.2.1 Proof of concept using test signals

The first step towards validating the artefact suppression method presented in Section 5.3, was to test the response speed of an RMS-to-DC converter (AD8436 chip from Analog Devices) to sudden changes occurring in the input signal. In this case, the simplest implementation, which is the one shown in Figure 5.13, was used. More specifically, a test signal was injected to the artefact suppression block and was recorded without being processed in the analog domain. The first test was to track the response of the designed system to a sudden change in the dc offset voltage of the stimulation pulse train that enters the signal chain. Since the aim of this series of

experiments was to examine the worst case scenario, strong and low-frequency monophasic pulses were applied (amplitude 200 mV_{pp}, frequency 20 Hz and pulse width 10 msec). It is clear that a change of this type does not affect the estimation returned by the RMS-to-DC converter. Hence, the system (after a short transient response) is able to continue providing reliable recording ("AFE output" in Figure 5.19) of the biosignal of interest during stimulation.

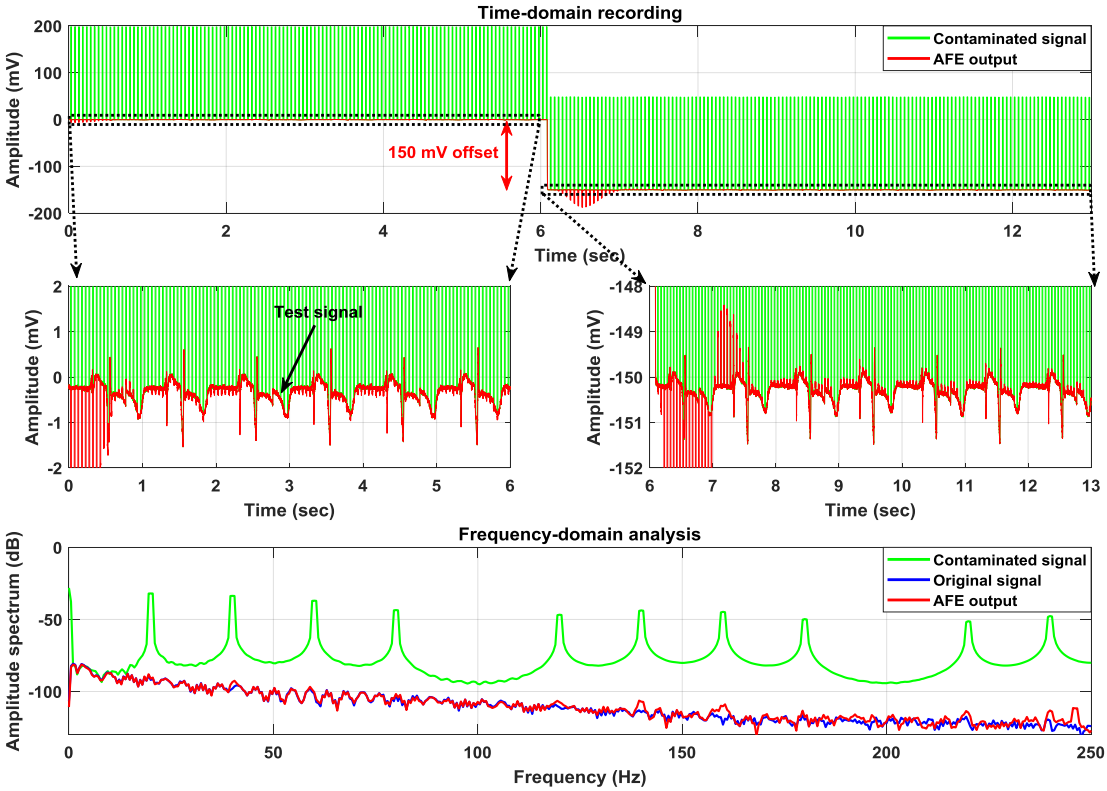

Figure 5.19: Application of stimulation pulses (making use of a commercial waveform generator), which contain a sudden dc offset voltage change, on the designed analog front-end implementing the proposed method. The aim was to examine the real-time capabilities of the proposed artefact suppression method. It is clear that a sudden change in the offset of the pulses does not affect the estimation returned by the RMS-to-DC converter. As a result, the system (after a short transient response) is able to continue providing reliable recording (please see "AFE output") of the biosignal of interest during stimulation. AFE, analog front-end.

Another test (Figure 5.20) was to track the response of the designed system to a sudden change in the amplitude (frequency and pulse width were kept the same) of the stimulation pulse train (monophasic pulses, amplitude 200 mV_{pp}, frequency 20 Hz and

pulse width 10 msec) that enters the signal chain. It is clear that a change of this type is immediately detected by the RMS-to-DC converter and the new amplitude estimate (an analog gain stage which multiplies the RMS estimation with the crest factor - peak value/RMS value - of the monophasic pulses follows the RMS-to-DC converter) is calculated and subtracted from the contaminated signal in the analog domain. Therefore, the system (after a short transient response) is able to continue providing reliable recording ("AFE output" in Figure 5.20) of the biosignal of interest during stimulation.

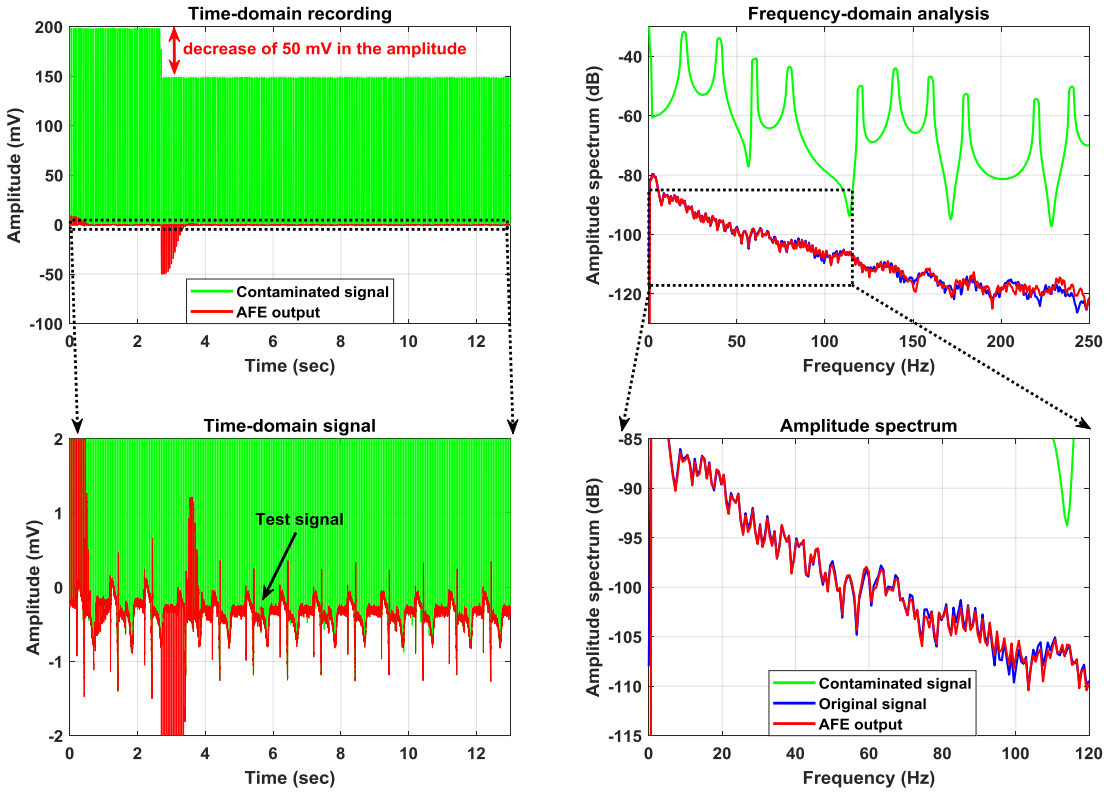

Figure 5.20: Application of stimulation pulses (making use of a commercial waveform generator), which contain a sudden decrease in their amplitude (frequency and pulse width of the pulses are kept the same), on the designed analog front-end (AFE) implementing the proposed method. The aim was to examine the real-time capabilities of the proposed artefact suppression method. It is clear that a sudden change in the amplitude of the pulses is immediately detected by the RMS-to-DC converter and the new amplitude estimate is calculated (an analog gain stage which multiplies the RMS estimation with the crest factor of the monophasic pulses follows the RMS-to-DC converter in this experiment) and subtracted from the contaminated signal in the analog domain. As a result, the system (after a short transient response) is able to continue providing reliable recording (see "AFE output") of the biosignal of interest during stimulation. AFE, analog front-end.

The next step towards validating the artefact suppression capabilities of the proposed approach was to conduct *in vitro* experiments and record LFP signals during DBS. Figure 5.21 exhibits a time-domain recording of LFPs in a saline tank during voltage-mode DBS (monophasic pulses, amplitude 7 V_{pp}, frequency 140 Hz and pulse width 200 μsec). Since post-operative LFPs are usually differentially recorded from two DBS electrodes, the setup in this case was built using the artefact-suppression architecture presented in Figure 5.16. The analog subtraction function, which is required in the system shown in Figure 5.16, was provided by the AD8429 INA (designed with a gain of 20 V/V) chip (Analog Devices, USA). Moreover, a passive 1st order low-pass filter at 1 Hz was placed after the RMS-to-DC converter. An analog 1st order high-pass filter followed by an analog gain stage (gain=200 V/V) were placed after the artefact subtraction block shown in Figure 5.16. As a result, an overall gain of 4000 V/V was applied by the Powerlab acquisition hardware front-end (which is characterized by a dynamic range of ±10 V). Finally, to achieve a more accurate recording of LFP signals during the artefact (the duration of which is very short, usually equal to 60 – 200 μs), the sampling frequency was set at 100 kSPS.

As shown in Figure 5.21, the stimulation artefacts (solid pink line) that pass through the front-end instrumentation amplifier are characterized by an amplitude of approximately 30 mV_{pp} (after removing the gain of 4000 V/V). The application of the proposed method in combination with a real-time digital low-pass filter at 500 Hz (to remove weak switching voltage spikes) leads to the successful retrieval of the neural activity of interest. As shown in the amplitude spectrums, the stimulation harmonics are significantly attenuated at such an extent that allows the time-domain neural recording to be artefact-free. Moreover, the spectrum of the signal recorded during stimulation contains both the peak in the beta frequency band (13-30 Hz) and the peak at 80 Hz, which correspond to physiological activity. Furthermore, the bottom graph indicates that the contaminating 142 Hz harmonic and all the other harmonics within the passband are successfully suppressed by at least 37 dB. Finally, it is clear that the suppression of the stimulation pulses achieved by the suggested method also leads to the suppression of the strong 50 Hz harmonics.

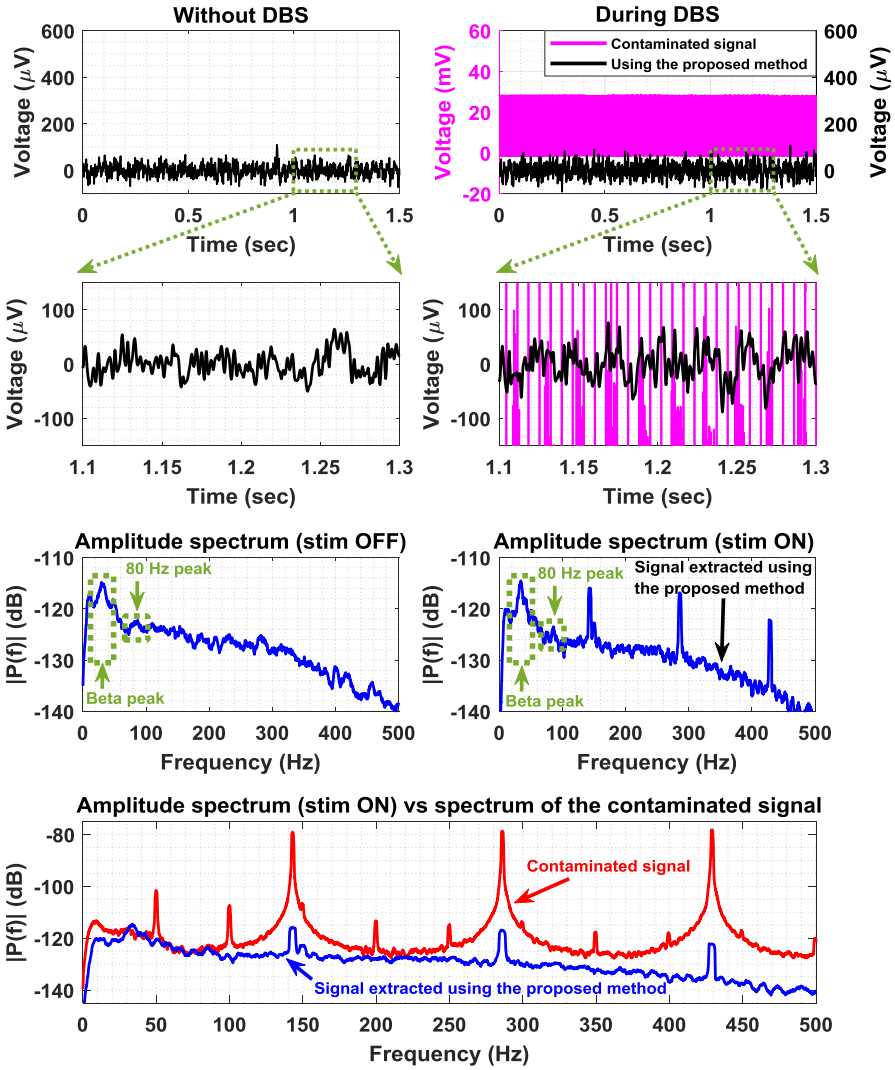

Figure 5.21: Time-domain recording and amplitude spectrum of local field potentials recorded in a saline tank during voltage-mode DBS (monophasic pulses, amplitude 7 V_{pp}, frequency 140 Hz and pulse width 200 μsec). The stimulation artefacts (solid pink line), which pass through the front-end instrumentation amplifier (designed with a gain of 20 V/V), are characterized by an amplitude of approximately 30 mV_{pp} (after removing the gain of 20 V/V). The application of the proposed method in combination with a real-time digital low-pass filter at 500 Hz (to remove weak switching voltage spikes) allows for the successful retrieval of the neural activity of interest. As shown in the amplitude spectrums, the stimulation harmonics are significantly attenuated at such an extent that allows the (time-domain) neural recording to be artefact-free. In addition, the spectrum of the signal recorded during stimulation contains both the peak in the beta frequency band (13-30 Hz) and the peak at 80 Hz, which correspond to physiological activity. As shown in the bottom graph, the contaminating 142 Hz harmonic and all the other harmonics within the passband are successfully suppressed by at least 37 dB. Finally, it is clear that the suppression of the stimulation pulses achieved by the proposed method also leads to the suppression of the strong 50 Hz harmonics. DBS, deep brain stimulation.

5.3.2.2 Application of the proposed method in cardiac sensing & stimulation

At this point, it is important to highlight that the proposed artefact suppression method could also be applied in other bidirectional interfaces to provide biosignal recording during electrical stimulation. Indeed, the assessment of the worst case scenario (Figures 5.19 - 5.20) indicated that the proposed method is able to suppress artefacts stemming from low-frequency and strong stimulation pulses. This finding is important because low-frequency electrical stimulation significantly distorts the biosignal spectrum by introducing a significant number of harmonics into the system passband.

To evaluate the artefact suppression capabilities of the proposed approach, *in vitro* experiments were conducted and cardiac signals were recorded during cardiac stimulation. Since cardiac signals are usually differentially recorded from two contacts of a catheter, the setup was built using the artefact-suppression architecture presented in Figure 5.16. The analog subtraction function, which is required in the system shown in Figure 5.16, was provided by the AD8429 INA (gain=1 V/V) chip (Analog Devices, USA). Furthermore, a passive 1st order low-pass filter at 1 Hz was placed after the RMS-to-DC converter. It is important to note here that an analog 1st order high-pass filter followed by a gain stage (gain=100 V/V) were placed after the artefact subtraction block shown in Figure 5.16. As a result, a gain of 100 V/V was applied by the Powerlab acquisition hardware front-end (which is characterized by a dynamic range of ±10 V). In the digital domain, a Hampel filter was used to remove weak switching voltage spikes. Hampel filter is a robust statistical filter for removing outliers thus it is considered effective and efficient for real-time applications [127, 128]. Finally, all biosignal recordings were acquired at 10 kSPS without applying any (analog or digital) low-pass filtering.

Figure 5.22 illustrates a time-domain recording of cardiac signals in a saline tank during current-mode stimulation (monophasic pulses, amplitude 15 mA, frequency 20 Hz and pulse width 10 msec). A comparison, in terms of signal quality, is drawn between the proposed method and the biosignal blanking during stimulation technique. In contrast to the biosignal blanking during stimulation technique, which eliminates information during the artefact, the proposed method successfully retrieves the signal of interest without

corrupting it. Additionally, the amplitude spectrum of the signal recorded during stimulation using the proposed method approximates the amplitude spectrum of the signal of interest.

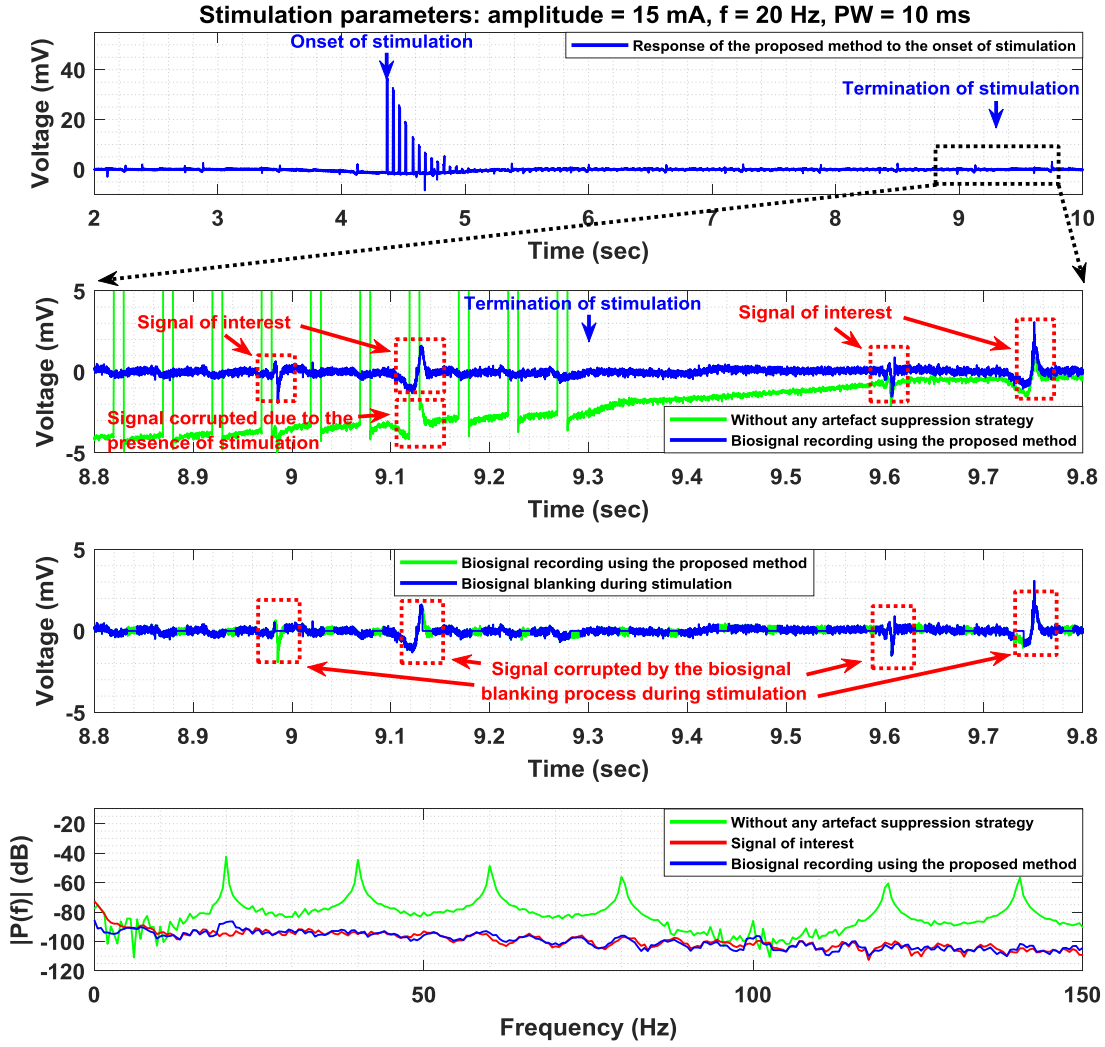

Figure 5.22: Time-domain recording and amplitude spectrum of cardiac signals recorded in a saline tank during current-mode stimulation (monophasic pulses, amplitude 15 mA, frequency 20 Hz and pulse width 10 msec). A comparison, in terms of signal quality, is drawn between the proposed method and the biosignal blanking during stimulation technique. In contrast to the biosignal blanking during stimulation technique, which eliminates information during the artefact, the proposed method successfully retrieves the signal of interest without corrupting it.

5.4 Discussion/Conclusion

The simulated and measured results shown in this Chapter verify the artefact suppression capabilities of the presented tunable filter topologies. It is clear that the incorporation of the multiple feedback notch filter topology presented in this Chapter into the AFE architecture presented in Chapter 4 could provide the desired tunability on the central frequency that has to be rejected.

Furthermore, this Chapter proposes an alternative approach that achieves real-time artefact suppression in bidirectional setups. More specifically, the core of the artefact suppression process takes place in the analog domain. It is well known that analog signal processing techniques introduce a negligible delay in the signal processing chain. Hence, by applying analog signal processing to significantly attenuate the stimulation artefact, delays originating from data processing in the digital domain are avoided. In contrast to other techniques that make use of DACs to subtract the stimulation waveform from the input corrupted signal, the proposed method suppresses the artefacts by using an analog RMS-to-DC converter block. This block continuously estimates in real time the amplitude of the stimulation pulse and then feeds it to a differential subtraction block (e.g. an instrumentation amplifier), which subtracts this estimate from the input contaminated signal. Hence, the artefact suppression takes place in real time and the noise contribution of a DAC to the overall input-referred noise of the recorder is avoided.

Generally speaking, the application of digital filters on the recorded biosignals enhances their quality. However, they often introduce undesired delays in the signal processing chain, which challenge the practicality of a fast bidirectional medical device. Since the proposed method significantly suppresses the artefacts in the analog domain or with minimal additional digital processing, it does not require the introduction of high-order digital filters in the signal path, thus avoiding delays that may undermine the real time character of the system. In cases where weak switching voltage spikes have to be removed (e.g. in deep brain stimulation), low-order analog/digital low-pass filters can be applied.

Moreover, one of the important merits of the proposed approach is that biosignal blanking during stimulation is avoided. Hence, loss of information during the artefact is prevented and the achieved SNR is enhanced. An advantage of all mixed mode (analog & digital) implementations of the method proposed in this Chapter is that the stimulation artefacts are significantly suppressed before reaching the ADC block of the AFE. In this way: a) artefact coupling into the physiological measurements is avoided because the stimulation harmonics are significantly attenuated before the analog signal enters the ADC block, and b) aliasing artefacts (originating from undersampling the artefact shape), which are located at various frequencies that are not harmonic repetitions of the stimulation frequency and often contaminate the biosignal of interest, are prevented.

In addition, by subtracting the pulse amplitude from the input corrupted biosignal in the analog domain (in all implementations of the mixed mode method, except for the one which subtracts the artefacts in the digital domain), this method allows low dynamic range (and thus high-gain) AFEs to quickly recover from saturation and thus provide reliable biosignal recordings during stimulation. Hence, this approach offers the freedom to the circuit designer to increase the gain (so that the full scale voltage range of the ADC is better exploited) of the AFE, rendering it capable of providing more accurate recordings of ultra-weak (e.g. nV-scale LFPs in basal ganglia) biosignals in and without the presence of stimulation. In applications where biosignals are of higher amplitude (e.g. mV in cardiac) and thus high gain is not necessary, the implementation that subtracts the artefact in the digital domain may be utilized to reduce AFE complexity. The use of an analog RMS block reduces computational complexity and time as opposed to a conventional digital calculator.

Another significant factor of the proposed method is the reduction in the power consumption and space needed for its incorporation in an instrument. The proposed approach does not require the introduction of high-order analog filters to suppress the stimulation artefact. Instead, it depends on the function of an RMS-to-DC converter, which is a simple and low-power analog building block. As a result, a significant amount of space in the instrument's PCB is saved and an important decrease in the

power consumption of the overall system is achieved. These two factors (space and power consumption) are particularly important in the design of implantable bidirectional medical devices.

Additionally, an important feature that determines the effectiveness of an artefact suppression strategy is the bandwidth it can offer, the type of stimulation pulses (amplitude, frequency and pulse width) it can suppress and the degree of tunability on the cut-off frequency it can provide. The proposed strategy can in principle provide the whole biosignal bandwidth that is available by the front-end electronics and can suppress stimulation pulses of: a) any frequency, b) any pulse width, c) any amplitude that stays within the input dynamic range of the analog front-end electronics, and d) any type (monophasic or balanced biphasic). Since in all proposed implementations of this method the process of subtracting the artefact from the input contaminated signal is controlled by the MCU of the system, tunability on the stimulation frequency that has to be rejected is easily accomplished. Last but not least, the hardware implementation of the proposed method is based on fundamental building blocks (instrumentation amplifiers, operational amplifiers and RMS-to-DC converters), thus providing a straightforward design process.

In conclusion, the *in vitro* measured results presented in this Chapter show that all the implementations of the mixed mode (analog & digital) artefact suppression method are characterized by significant merits, which render them attractive for a wide range of applications and scenarios. Hence, the next step towards confirming their superiority over the methodologies that base the artefact suppression process on notch filtering is to assess their *in vivo* performance.

Chapter 6. Conclusions – Future work

6.1 Summary

This thesis presented the design, fabrication and testing of high-performance wired and wireless devices that employ either purely analog signal processing techniques or a combination of analog and digital processing techniques in order to provide high-quality bioelectrical signal recordings under a wide range of experimental conditions (in noisy university laboratories and in clinical wards, in and without the presence of various types of electrical stimulation). This thesis unfolded in a series of chapters, as follows:

Chapter 1 was an introduction describing the motivation for this work and questioning the major research topics that were targeted to be answered by this thesis. Followed by an outline of the contents of this presented work.

Chapter 2 introduced the reader to the field of bioelectrical engineering, described the concept and merits of closed-loop neurostimulation and demonstrated the advances in the field of neuromodulation. The challenges associated with the design of ambulatory biopotential acquisition systems which are intended to record extremely weak biosignals from the human body in the presence of various noise sources (ambient noise, inherent noise of the apparatus used, artefacts introduced by the neural stimulation in bidirectional neural interfaces etc) were analysed. Finally, this chapter elaborated on various techniques that have been used so far for achieving artefact suppression in bidirectional neural interfaces.

Chapter 3 introduced a low-noise (8 nV/√Hz), eight-channel, battery-powered, wearable and wireless multi-instrument (55 × 80 mm^2) that can be used in a wide range of applications and scenarios. More specifically, although this instrument has been primarily designed for being part of bidirectional neural interfaces which provide spatial separation between sensing and stimulation sites, it can also precisely record LFP signals from the stimulation site when no DBS is present. Moreover, since its AFE is characterised by a relatively fast transient response, it can also record evoked

resonant neural response (which appears 4 msec after the last DBS pulse) from the stimulation site. The main aim of this design effort was to deliver a high-performance recording modality that is able to provide various symptom-related biosignals (acceleration signals, neurochemical signals, EMG signals and wide-frequency-range LFPs/ECoG) to a closed-loop neurostimulation platform. This portable/wearable device can also alleviate the problem of limited mobility often encountered by patients in the clinic. A number of *ex vivo* and *in vivo* experiments, which were conducted in order to evaluate the instrument's performance in terms of signal quality under different experimental conditions, were presented. Finally, this Chapter demonstrated the instrument's merits and described possible avenues of research that could be further explored using its low-noise capabilities.

Chapter 4 introduced a high-performance (4 nV/√Hz) application specific AFE architecture (70 × 20 mm^2) that provides artefact-free LFP recordings in bidirectional brain-machine interfaces where concurrent sensing and stimulation take place at the same site. In this architecture, artefact suppression is achieved by adequately filtering the stimulation harmonics (using either analog filters or a combination of analog and digital filters). A number of *in vitro* and *in vivo* experiments that prove the instrument's high performance in and without the presence of DBS were presented. Finally, the merits and limitations of the designed AFE architecture were summarized and possible avenues of research that could be explored using the proposed artefact suppression method were highlighted.

Chapter 5 presented a family of novel hardware filter designs which provide tunability on the stimulation frequency that can be rejected. Finally, a novel mixed mode (analog & digital) method for real-time artefact suppression, which provides absolute flexibility on the morphology of stimulation pulses (monophasic/balanced biphasic pulses of any frequency, pulse width and amplitude - that stays within the dynamic range of the AFE - can be suppressed) it can attenuate and enables wide-bandwidth biopotential recordings during electrical stimulation, was described. All the artefact suppression strategies presented in Chapter 5 could be used in bidirectional setups where simultaneous sensing and stimulation at the same site are required.

In respect to the artefact suppression strategies presented in this thesis, it should be clarified that the artefact suppression strategy presented in Chapter 4 can be characterised as an application specific solution to the problem of artefact coupling into the physiological signal of interest in closed-loop DBS systems. The fundamental block of this AFE architecture, which has demonstrated its enhanced artefact suppression capabilities both *in vitro* and *in vivo*, is a high-order (8th) analog notch filter which significantly attenuates the strong artefacts stemming from the stimulation frequency without introducing any ringing oscillations in the recorded LFP signals.

However, in other electrical stimulation types where stimulation pulses of higher duty cycles (e.g. up to 20% duty cycle is used in spinal cord stimulation and cardiac stimulation) are applied, ringing oscillations may appear in the recorded biosignals due to the operation of the high-order analog notch filter. Moreover, in its current embodiment, the notch filter only provides flexibility on the type of stimulation pulses (both monophasic and biphasic pulses can be suppressed) that can be attenuated and not on the central frequency that can be rejected. Besides that, the extension of the available bandwidth for reliable LFP recording during DBS beyond 250 Hz significantly increases the power consumption and size of the overall system (since the incorporation of more than one notch filter into the design is required).

The desired tunability on the value of the filter cut-off frequency could be offered by the incorporation of a tunable analog notch filter into the AFE architecture presented in Chapter 4. This tunable filter could be either a commercial, high-order tunable switched capacitor notch filter or a notch filter (based on the multiple feedback architecture) originating from the family of tunable hardware filters presented in Chapter 5. The significant merit of tunable hardware filter topologies is that: a) they do not put under risk the real time character of the system, which is particularly important in closed-loop neurostimulation, and b) they offer flexibility on both the type of stimulation pulses (monophasic/biphasic) and the spectral location of the stimulation harmonics that can be suppressed. A significant advantage of the tunable filters presented in Chapter 5 is that they are continuous-time (and not switched-capacitor) filters, and thus no clock interference is introduced in the signal chain.

Compared to the above-described artefact suppression strategies, the mixed mode (analog & digital) method presented in Chapter 5 is the simplest and most functional solution for adequately attenuating artefacts in real time during various types of electrical stimulation. Indeed, it does not require the use of high-order analog or digital notch filters to reject artefacts stemming from the stimulation frequency, hence maintaining the complexity of the overall system at low levels. It is clear that this method could be implemented in a microchip since the size and the power consumption of an AFE that applies this strategy can stay within the size and power constraints of an implant. The tunability and flexibility it offers on the stimulation pulse morphology (monophasic/balanced biphasic pulses of any frequency, amplitude - that stays within the dynamic range of the AFE - and pulse width can be suppressed) it can attenuate without introducing any ringing oscillations in the processed biosignals, along with the wide bandwidth it provides for biosignal recording during electrical stimulation, render it as a versatile method to be utilised in a wide range of applications and environments. A performance comparison between the three artefact suppression methods proposed in this thesis is drawn in Table 6.1.

Table 6.1: Provided bandwidth and parameters of the stimulation pulses that can be rejected by the artefact suppression methods proposed in this thesis.

Parameters	Fixed notch	Tunable notch	Mixed mode method
Pulse type	Monophasic/ Biphasic	Monophasic/ Biphasic	Monophasic /Balanced Biphasic
Stimulation amplitude	Any	Any	Any
Stimulation pulse width	Limited range	Limited range	Any
Stimulation frequency	Any	Any	Any
Tunability on cut-off frequency	No	Yes	Yes
Provided Bandwidth	Limited	Limited	Full bandwidth

In conclusion, this work paves the way for the development of miniaturized research tools for closed-loop neuromodulation that could enable the effective monitoring of a greater portion of people suffering from various disorders, such as movement disorders, epilepsy and psychiatric disorders. Importantly however, it should be stressed that the wearable/wireless multi-instrument presented in Chapter 3 could also act as a recording-only device aiming at providing continuous monitoring, thus increasing the biosignal acquisition time and enhancing the diagnostics of various diseases (such as PD, essential tremor, epilepsy, ALS, AF, TBI, cardiovascular disease, etc.).

6.2. Future work

Concerning the future work on the accomplishments of this thesis, it would be important to further investigate the capabilities of the novel circuit topologies presented in this thesis by conducting more *in vivo* experiments. Moreover, further enhancing of the recording capabilities of the presented instruments can be achieved by providing more recording channels (≥16).

More specifically, since the correct operation of the 8-channel wearable and wireless instrument (presented in Chapter 3) has been confirmed, it would be interesting to use this high-performance device in clinical studies in order to achieve a more accurate sampling of the physiomarker space. Moreover, the investigational character of this portable/wearable device led us to maintain the provided number of channels at a relatively moderate level (=8). Since the IEEE 802.15.4 wireless protocol can support much larger data payloads than the one produced and transmitted with the 8-channel architecture, it would be interesting to increase the channel count of the wearable/wireless device without increasing the dimensions of the instrument.

In addition, since the stimulation artefact suppression capabilities of the high-performance AFE architecture presented in Chapter 4 have been confirmed *in vivo*, it would be important to use this device in a clinical study to continuously record LFPs during DBS from the STN of parkinsonian patients and, more specifically, from the

neural tissue surrounding the stimulating electrode. This study would allow the identification of changes in LFP rhythms induced by DBS and the determination of features extracted from the LFP signals that could be used to regulate and optimise ongoing DBS.

Furthermore, the accomplishments of this thesis constitute the foundation of a future implantable medical device that could uncover new biomarkers of serious neurological disorders previously hidden by stimulation. More specifically, the mixed (analog & digital) mode artefact suppression method presented in Chapter 5 could be implemented in a system-on-chip (SoC) to provide reliable sensor data during stimulation. A miniaturised device of this type would provide the ability to chronically sense, process and telemeter biopotential signals and could thus lead to enhanced monitoring of disease progression and increased therapy effectiveness.

The first step towards this direction would be to evaluate this mixed mode artefact suppression method *in vivo.* Next, it would be important to proceed to the design, fabrication and testing (under both *in vitro* and *in vivo* conditions) of a microchip that applies this novel method for achieving artefact rejection in bidirectional neural interfaces.

THESIS CONTRIBUTIONS

The original contributions of this work include:

- Design, fabrication and testing under both *ex vivo* and *in vivo* experimental conditions of a low-noise (8 nV/√Hz), eight-channel, battery-powered, wearable and wireless multi-instrument (55 × 80 mm^2) that can be used as a recording-only device (which can precisely record ExG/ECoG/LFP/ERNA signals, acceleration signals, neurochemical signals and PV ectopic activity) in the clinic to alleviate the problem of limited mobility often encountered by patients, or as a recording modality that provides high-quality sensor data (acceleration signals, neurochemical signals, EMG signals, wide-frequency-range LFPs/ECoG) to a closed-loop neurostimulation platform.

- Design, fabrication and testing under both *in vitro* and *in vivo* experimental conditions of a high-performance (4 nV/√Hz) application specific AFE architecture (70 × 20 mm^2) that provides artefact-free LFP recordings in bidirectional brain-machine interfaces where concurrent sensing and stimulation take place at the same site.

- Design, fabrication and testing of a family of novel analog filter (low/high/band pass and notch) topologies that provide tunability on the stimulation frequency that can be rejected.

- Design, implementation and *in vitro* testing of a novel and robust mixed mode (analog & digital) method that: a) provides flexibility on the morphology of stimulation pulses (monophasic/balanced biphasic pulses of any frequency, pulse width and amplitude - that stays within the dynamic range of the AFE - can be suppressed) it can attenuate, and b) enables real-time and wide-bandwidth biopotential recording during stimulation in bidirectional interfaces where sensing and stimulation take place at the same site.

- Contribution towards the continuous monitoring of patients suffering from various diseases (ALS, TBI, AF, cardiovascular disease) by delivering a high-precision wireless/wearable instrument (presented in Chapter 3) that can increase the biosignal acquisition time, thus enhancing the diagnostics of those diseases.

- Contribution towards the implementation of clinical studies which aim at discovering new biomarkers of serious diseases by delivering a high-performance device (presented in Chapter 4) with increased DBS artefact suppression capabilities. This device can provide a more complete sampling of the physiomarker space, thus enhancing the capability of machine learning approaches to identify control signals.

- Contribution towards the miniaturisation of research tools for closed-loop neuromodulation by proposing a robust mixed mode (analog & digital) artefact suppression method (presented in Chapter 5) that can be implemented at the chip level. Implantable systems implementing this strategy could offer visibility into potentially useful neurological information previously masked by stimulation. In this way, therapy could be successfully delivered in real time (i.e. in a closed-loop mode) to patients suffering from movement disorders, epilepsy and psychiatric disorders.

LIST OF PUBLICATIONS & PATENTS

This is a full list of publications that have been achieved during my Doctoral Research:

- Petkos K, Guiho T, Degenaar P, Jackson A, Brown P, Denison TJ, Drakakis EM (2019) A high-performance 4 nV/√ analog front-end architecture for artefact suppression in local field potential recordings during deep brain stimulation. J Neural Eng 16:066003
- Petkos K, Koutsoftidis S, Guiho T, Degenaar P, Jackson A, Greenwald SE, Brown P, Denison T, Drakakis EM (2019) A high-performance 8 nV/√Hz 8-channel wearable and wireless system for real-time monitoring of bioelectrical signals. J Neuroeng Rehabil 16:156
- Petkos K, Drakakis EM (2020) High-pass pole shifting in bidirectional electrophysiological interfaces using a novel, multi-function and tunable analogue filter block. IEEE Trans Biomed Eng
  [submitted for publication]

This is a full list of patents that have been accomplished during my Doctoral Research:

- Tunable electronic filter, by Petkos K, Zafeiropoulos G, Drakakis EM. (2020, February 13). WO2020030534A1.
- Tunable electronic filter, by Petkos K, Zafeiropoulos G, Drakakis EM. (2020, February 13). WO2020030533A1.
- Method for artefact suppression in bidirectional stimulation and recording applications, by Petkos K, Koutsoftidis S, Drakakis EM. (2020, January 23). Case 10615. Patent Pending.

APPENDICES

A. Permissions

This Agreement between Mr. K. Petkos ("You") and Springer Nature ("Springer Nature") consists of your license details and the terms and conditions provided by Springer Nature and Copyright Clearance Center.

License Number	4670230321036
License date	Sep 15, 2019
Licensed Content Publisher	Springer Nature
Licensed Content Publication	Nature Biotechnology
Licensed Content Title	Emerging technologies for improved deep brain stimulation
Licensed Content Author	Hayriye Cagnan et al
Licensed Content Date	Sep 2, 2019
Type of Use	Thesis/Dissertation
Requestor type	academic/university or research institute
Format	print and electronic
Portion	figures/tables/illustrations
Number of figures/tables/illustrations	4
High-res required	no
Will you be translating?	no
Circulation/distribution	1 - 29
Author of this Springer Nature content	no
Title	Wired, wireless and wearable bioinstrumentation for high-precision recording of bioelectrical signals in bidirectional neural interfaces
Institution name	Imperial College London
Expected presentation date	May 2020
Portions	Table 1 Fig.1 Fig.2 Fig.3
Requestor Location	Mr. K. Petkos Griffon Studios, Winstanley Rd Battersea, London, - SW112DL United Kingdom Attn: Mr. K. Petkos
Total	0.00 GBP

IEEE
Requesting permission to reuse content from an IEEE publication

Title: Models of stimulation artifacts applied to integrated circuit design
Conference Proceedings: The 26th Annual International Conference of the IEEE Engineering in Medicine and Biology Society
Author: R.A. Blum
Publisher: IEEE
Date: 2004
Copyright © 2004, IEEE

LOGIN
If you're a copyright.com user, you can login to RightsLink using your copyright.com credentials.
Already **a RightsLink user** or want to learn more?

Thesis / Dissertation Reuse

The IEEE does not require individuals working on a thesis to obtain a formal reuse license, however, you may print out this statement to be used as a permission grant:

Requirements to be followed when using any portion (e.g., figure, graph, table, or textual material) of an IEEE copyrighted paper in a thesis:

1) In the case of textual material (e.g., using short quotes or referring to the work within these papers) users must give full credit to the original source (author, paper, publication) followed by the IEEE copyright line © 2011 IEEE.
2) In the case of illustrations or tabular material, we require that the copyright line © [Year of original publication] IEEE appear prominently with each reprinted figure and/or table.
3) If a substantial portion of the original paper is to be used, and if you are not the senior author, also obtain the senior author's approval.

Requirements to be followed when using an entire IEEE copyrighted paper in a thesis:

1) The following IEEE copyright/ credit notice should be placed prominently in the references: © [year of original publication] IEEE. Reprinted, with permission, from [author names, paper title, IEEE publication title, and month/year of publication]
2) Only the accepted version of an IEEE copyrighted paper can be used when posting the paper or your thesis on-line.
3) In placing the thesis on the author's university website, please display the following message in a prominent place on the website: In reference to IEEE copyrighted material which is used with permission in this thesis, the IEEE does not endorse any of [university/educational entity's name goes here]'s products or services. Internal or personal use of this material is permitted. If interested in reprinting/republishing IEEE copyrighted material for advertising or promotional purposes or for creating new collective works for resale or redistribution, please go to http://www.ieee.org/publications_standards/publications/rights/rights_link.html to learn how to obtain a License from RightsLink.

If applicable, University Microfilms and/or ProQuest Library, or the Archives of Canada may supply single copies of the dissertation.

IEEE
Requesting permission to reuse content from an IEEE publication

Title: A 60 μW 60 nV/$\surd$Hz Readout Front-End for Portable Biopotential Acquisition Systems
Author: Refet Firat Yazicioglu
Publication: Solid-State Circuits, IEEE Journal of
Publisher: IEEE
Date: May 2007
Copyright © 2007, IEEE

LOGIN
If you're a copyright.com user, you can login to RightsLink using your copyright.com credentials.
Already **a RightsLink user** or want to learn more?

Thesis / Dissertation Reuse

The IEEE does not require individuals working on a thesis to obtain a formal reuse license, however, you may print out this statement to be used as a permission grant:

Requirements to be followed when using any portion (e.g., figure, graph, table, or textual material) of an IEEE copyrighted paper in a thesis:

1) In the case of textual material (e.g., using short quotes or referring to the work within these papers) users must give full credit to the original source (author, paper, publication) followed by the IEEE copyright line © 2011 IEEE.
2) In the case of illustrations or tabular material, we require that the copyright line © [Year of original publication] IEEE appear prominently with each reprinted figure and/or table.
3) If a substantial portion of the original paper is to be used, and if you are not the senior author, also obtain the senior author's approval.

Requirements to be followed when using an entire IEEE copyrighted paper in a thesis:

1) The following IEEE copyright/ credit notice should be placed prominently in the references: © [year of original publication] IEEE. Reprinted, with permission, from [author names, paper title, IEEE publication title, and month/year of publication]
2) Only the accepted version of an IEEE copyrighted paper can be used when posting the paper or your thesis on-line.
3) In placing the thesis on the author's university website, please display the following message in a prominent place on the website: In reference to IEEE copyrighted material which is used with permission in this thesis, the IEEE does not endorse any of [university/educational entity's name goes here]'s products or services. Internal or personal use of this material is permitted. If interested in reprinting/republishing IEEE copyrighted material for advertising or promotional purposes or for creating new collective works for resale or redistribution, please go to http://www.ieee.org/publications_standards/publications/rights/rights_link.html to learn how to obtain a License from RightsLink.

Copyright Clearance Center RightsLink®

Home | Create Account | Help

IEEE Requesting permission to reuse content from an IEEE publication

Title: Design of Ultra-Low Power Biopotential Amplifiers for Biosignal Acquisition Applications
Author: Fan Zhang
Publication: Biomedical Circuits and Systems, IEEE Transactions on
Publisher: IEEE
Date: Aug. 2012
Copyright © 2012, IEEE

LOGIN

If you're a copyright.com user, you can login to RightsLink using your copyright.com credentials.

Already **a RightsLink user** or want to learn more?

Thesis / Dissertation Reuse

The IEEE does not require individuals working on a thesis to obtain a formal reuse license, however, you may print out this statement to be used as a permission grant:

Requirements to be followed when using any portion (e.g., figure, graph, table, or textual material) of an IEEE copyrighted paper in a thesis:

1) In the case of textual material (e.g., using short quotes or referring to the work within these papers) users must give full credit to the original source (author, paper, publication) followed by the IEEE copyright line © 2011 IEEE.
2) In the case of illustrations or tabular material, we require that the copyright line © [Year of original publication] IEEE appear prominently with each reprinted figure and/or table.
3) If a substantial portion of the original paper is to be used, and if you are not the senior author, also obtain the senior author's approval.

Requirements to be followed when using an entire IEEE copyrighted paper in a thesis:

1) The following IEEE copyright/ credit notice should be placed prominently in the references: © [year of original publication] IEEE. Reprinted, with permission, from [author names, paper title, IEEE publication title, and month/year of publication]
2) Only the accepted version of an IEEE copyrighted paper can be used when posting the paper or your thesis on-line.
3) In placing the thesis on the author's university website, please display the following message in a prominent place on the website: In reference to IEEE copyrighted material which is used with permission in this thesis, the IEEE does not endorse any of [university/educational entity's name goes here]'s products or services. Internal or personal use of this material is permitted. If interested in reprinting/republishing IEEE copyrighted material for advertising or promotional purposes or for creating new collective works for resale or redistribution, please go to http://www.ieee.org/publications_standards/publications/rights/rights_link.html to learn how to obtain a License from RightsLink.

Copyright Clearance Center RightsLink®

Home | Account Info | Help | LIVE CHAT

IEEE Requesting permission to reuse content from an IEEE publication

Title: A 32-channel modular bi-directional neural interface system with embedded DSP for closed-loop operation
Conference Proceedings: ESSCIRC 2014 - 40th European Solid State Circuits Conference (ESSCIRC)
Author: Peng Cong
Publisher: IEEE
Date: Sept. 2014
Copyright © 2014, IEEE

Logged in as:
Konstantinos Petkos
Account #:
3001516041
LOGOUT

Thesis / Dissertation Reuse

The IEEE does not require individuals working on a thesis to obtain a formal reuse license, however, you may print out this statement to be used as a permission grant:

Requirements to be followed when using any portion (e.g., figure, graph, table, or textual material) of an IEEE copyrighted paper in a thesis:

1) In the case of textual material (e.g., using short quotes or referring to the work within these papers) users must give full credit to the original source (author, paper, publication) followed by the IEEE copyright line © 2011 IEEE.
2) In the case of illustrations or tabular material, we require that the copyright line © [Year of original publication] IEEE appear prominently with each reprinted figure and/or table.
3) If a substantial portion of the original paper is to be used, and if you are not the senior author, also obtain the senior author's approval.

Requirements to be followed when using an entire IEEE copyrighted paper in a thesis:

1) The following IEEE copyright/ credit notice should be placed prominently in the references: © [year of original publication] IEEE. Reprinted, with permission, from [author names, paper title, IEEE publication title, and month/year of publication]
2) Only the accepted version of an IEEE copyrighted paper can be used when posting the paper or your thesis on-line.
3) In placing the thesis on the author's university website, please display the following message in a prominent place on the website: In reference to IEEE copyrighted material which is used with permission in this thesis, the IEEE does not endorse any of [university/educational entity's name goes here]'s products or services. Internal or personal use of this material is permitted. If interested in reprinting/republishing IEEE copyrighted material for advertising or promotional purposes or for creating new collective works for resale or redistribution, please go to http://www.ieee.org/publications_standards/publications/rights/rights_link.html to learn how to obtain a License from RightsLink.

Order Details

Biopotential Readout Circuits for Portable Acquisition Systems

Billing Status: **N/A**

Order detail ID: 72040300
ISBN: 9789048180707
Publication Type: Book
Publisher: Springer
Author/Editor: Yazicioglu, Refet Firat

Permission Status: Granted
Permission type: Republish or display content
Type of use: Thesis/Dissertation
Order License Id: 4684950885928

Hide details

Requestor type	Academic institution
Format	Print, Electronic
Portion	chart/graph/table/figure
Number of charts/graphs/tables/figures	3
The requesting person/organization	Konstantinos Petkos/Imperial College London
Title or numeric reference of the portion(s)	Figure 2.1, Figure 2.2, Figure 2.3
Title of the article or chapter the portion is from	-
Editor of portion(s)	N/A
Author of portion(s)	N/A
Volume of serial or monograph	N/A
Page range of portion	-
Publication date of portion	-
Rights for	Main product
Duration of use	Life of current edition
Creation of copies for the disabled	no
With minor editing privileges	yes
For distribution to	Worldwide
In the following language(s)	Original language of publication
With incidental promotional use	no
Lifetime unit quantity of new product	Up to 499
Title	Wired, wireless and wearable bioinstrumentation for high-precision recording of bioelectrical signals in bidirectional neural interfaces
Institution name	Imperial College London
Expected presentation date	May 2020

ELSEVIER LICENSE
TERMS AND CONDITIONS

Sep 26, 2019

This Agreement between Mr. K. Petkos ("You") and Elsevier ("Elsevier") consists of your license details and the terms and conditions provided by Elsevier and Copyright Clearance Center.

License Number	4676590332137
License date	Sep 26, 2019
Licensed Content Publisher	Elsevier
Licensed Content Publication	Current Opinion in Neurobiology
Licensed Content Title	Toward true closed-loop neuromodulation: artifact-free recording during stimulation
Licensed Content Author	Andy Zhou,Benjamin C Johnson,Rikky Muller
Licensed Content Date	Jun 1, 2018
Licensed Content Volume	50
Licensed Content Issue	n/a
Licensed Content Pages	9
Start Page	119
End Page	127
Type of Use	reuse in a thesis/dissertation
Intended publisher of new work	other
Portion	figures/tables/illustrations
Number of figures/tables/illustrations	3
Format	both print and electronic
Are you the author of this Elsevier article?	No
Will you be translating?	No
Original figure numbers	Figure 1 Figure 3 Table 1
Title of your thesis/dissertation	Wired, wireless and wearable bioinstrumentation for high-precision recording of bioelectrical signals in bidirectional neural interfaces
Publisher of new work	Imperial College London
Expected completion date	May 2020
Estimated size (number of pages)	1
Requestor Location	Mr. K. Petkos Griffon Studios, Winstanley Rd Battersea, London, - SW112DL United Kingdom Attn: Mr. K. Petkos
Publisher Tax ID	GB 494 6272 12
Total	0.00 GBP
Terms and Conditions	

Journal of Neural Engineering

Order detail ID:	72019104
Order License Id:	4676690813047
ISSN:	1741-2552
Publication Type:	e-Journal
Volume:	
Issue:	
Start page:	
Publisher:	IOP Publishing
Author/Editor:	Institute of Physics (Great Britain)

Permission Status: ✔ **Granted**

Permission type:	Republish or display content
Type of use:	Thesis/Dissertation

Requestor type	Academic institution
Format	Print, Electronic
Portion	chart/graph/table/figure
Number of charts/graphs/tables /figures	1
The requesting person/organization	Konstantinos Petkos
Title or numeric reference of the portion(s)	Figure 3
Title of the article or chapter the portion is from	A chronic generalized bi-directional brain–machine interface
Editor of portion(s)	N/A
Author of portion(s)	N/A
Volume of serial or monograph	N/A
Page range of portion	100-250
Publication date of portion	2020
Rights for	Main product
Duration of use	Life of current edition
Creation of copies for the disabled	no
With minor editing privileges	yes
For distribution to	U.K. and Commonwealth (excluding Canada)
In the following language(s)	Original language of publication
With incidental promotional use	no
Lifetime unit quantity of new product	Up to 499
Title	Wired, wireless and wearable bioinstrumentation for high-precision recording of bioelectrical signals in bidirectional neural interfaces
Institution name	Imperial College London
Expected presentation date	May 2020

BIBLIOGRAPHY

1. Abdelhalim K, Jafari HM, Kokarovtseva L, Velazquez JLP, Genov R (2013) 64-Channel uwb wireless neural vector analyzer soc with a closed-loop phase synchrony-triggered neurostimulator. IEEE J Solid-State Circuits 48:2494–2510
2. Schnitzler A, Gross J (2005) Normal and pathological oscillatory communication in the brain. Nat Rev Neurosci 6:285–296
3. Uhlhaas PJ, Singer W (2006) Neural Synchrony in Brain Disorders: Relevance for Cognitive Dysfunctions and Pathophysiology. Neuron 52:155–168
4. Autism and Developmental Disabilities Monitoring Network Surveillance Year 2008 Principal Investigators, Centers for Disease Control and Prevention (2012) Prevalence of autism spectrum disorders--Autism and Developmental Disabilities Monitoring Network, 14 sites, United States, 2008. MMWR Surveill Summ 61:1–19
5. Wittchen HU, Jacobi F, Rehm J, et al (2011) The size and burden of mental disorders and other disorders of the brain in Europe 2010. Eur Neuropsychopharmacol 21:655–679
6. Denison T, Consoer K, Santa W, Avestruz AT, Cooley J, Kelly A (2007) A 2 μw 100 nV/rtHz Chopper-Stabilized Instrumentation Amplifier for Chronic Measurement of Neural Field Potentials. In: IEEE J. Solid-State Circuits. pp 2934–2945
7. Wessberg J, Stambaugh CR, Kralik JD, Beck PD, Laubach M, Chapin JK, Kim J, Biggs SJ, Srinivasan MA, Nicolelis MAL (2000) Real-time prediction of hand trajectory by ensembles of cortical neurons in primates. Nature 408:361–365
8. Harrison RR, Charles C (2003) A low-power low-noise CMOS amplifier for neural recording applications. IEEE J Solid-State Circuits 38:958–965
9. Schwartz AB, Cui XT, Weber DJJ, Moran DW (2006) Brain-Controlled Interfaces: Movement Restoration with Neural Prosthetics. Neuron 52:205–220
10. Heldman DA, Wang W, Chan SS, Moran DW (2006) Local field potential spectral tuning in motor cortex during reaching. In: IEEE Trans. Neural Syst. Rehabil. Eng. pp 180–183
11. Papadimitriou KI, Wang C, Rogers ML, Gowers SAN, Leong CL, Boutelle MG, Drakakis EM (2016) High-Performance Bioinstrumentation for Real-Time Neuroelectrochemical

Traumatic Brain Injury Monitoring. Front Hum Neurosci 10:212

12. Leuthardt EC, Schalk G, Wolpaw JR, Ojemann JG, Moran DW (2004) A brain-computer interface using electrocorticographic signals in humans. J Neural Eng 1:63–71

13. Litt B, D'Alessandro A, Esteller R, Echauz J, Vachtsevanos G (2003) Translating seizure detection, prediction and brain stimulation into implantable devices for epilepsy. In: Int. IEEE/EMBS Conf. Neural Eng. NER. IEEE, pp 485–488

14. Holleman J, Zhang F, Otis B (2011) Ultra low-power integrated circuit design for wireless neural interfaces. Ultra Low-Power Integr Circuit Des Wirel Neural Interfaces. doi: 10.1007/978-1-4419-6727-5

15. Rouse AG, Stanslaski SR, Cong P, Jensen RM, Afshar P, Ullestad D, Gupta R, Molnar GF, Moran DW, Denison TJ (2011) A chronic generalized bi-directional brain-machine interface. J Neural Eng 8:036018

16. Stanslaski S, Afshar P, Cong P, Giftakis J, Stypulkowski P, Carlson D, Linde D, Ullestad D, Avestruz AT, Denison T (2012) Design and validation of a fully implantable, chronic, closed-loop neuromodulation device with concurrent sensing and stimulation. IEEE Trans Neural Syst Rehabil Eng 20:410–421

17. Little S, Pogosyan A, Neal S, et al (2013) Adaptive deep brain stimulation in advanced Parkinson disease. Ann Neurol 74:449–457

18. Arlotti M, Rossi L, Rosa M, Marceglia S, Priori A (2016) An external portable device for adaptive deep brain stimulation (aDBS) clinical research in advanced Parkinson's Disease. Med Eng Phys 38:498–505

19. Priori A, Foffani G, Rossi L, Marceglia S (2013) Adaptive deep brain stimulation (aDBS) controlled by local field potential oscillations. Exp Neurol 245:77–86

20. Sinclair NC, McDermott HJ, Bulluss KJ, Fallon JB, Perera T, Xu SS, Brown P, Thevathasan W (2018) Subthalamic nucleus deep brain stimulation evokes resonant neural activity. Ann Neurol 83:1027–1031

21. Mills KR (2010) Characteristics of fasciculations in amyotrophic lateral sclerosis and the benign fasciculation syndrome. Brain 133:3458–3469

22. Roth G, Magistris MR (1987) Neuropathies with prolonged conduction block, single and grouped fasciculations, localized limb myokymia. Electroencephalogr Clin Neurophysiol

67:428–438

23. Dumitru D, Diaz CA, King JC (2001) Prevalence of denervation in paraspinal and foot intrinsic musculature. Am J Phys Med Rehabil 80:482–490

24. Newsom-davis J, Mills KR (1993) Immunological associations of acquired neuromyotonia (Isaacs' syndrome): Report of five cases and literature review. Brain 116:453–469

25. Hebb AO, Zhang JJ, Mahoor MH, Tsiokos C, Matlack C, Chizeck HJ, Pouratian N (2014) Creating the Feedback Loop. Closed-Loop Neurostimulation. Neurosurg Clin N Am 25:187–204

26. Rissanen S, Kankaanpää M, Tarvainen MP, Nuutinen J, Tarkka IM, Airaksinen O, Karjalainen PA (2007) Analysis of surface EMG signal morphology in Parkinson's disease. Physiol Meas 28:1507–1521

27. Ruonala V, Meigal A, Rissanen SM, Airaksinen O, Kankaanpaa M, Karjalainen PA (2013) EMG signal morphology in essential tremor and Parkinson's disease. In: Proc. Annu. Int. Conf. IEEE Eng. Med. Biol. Soc. EMBS. IEEE, pp 5765–5768

28. Hilliard JD, Frysinger RC, Elias WJ (2011) Effective subthalamic nucleus deep brain stimulation sites may differ for tremor, bradykinesia and gait disturbances in parkinson's disease. Stereotact Funct Neurosurg 89:357–364

29. Eyuboglu M, Karabag Y, Karakoyun S, Senarslan O, Tanriverdi Z, Akdeniz B (2017) Usefulness of fragmented QRS in hypertensive patients in the absence of left ventricular hypertrophy. J Clin Hypertens 19:861–865

30. Nguyen KT, Vittinghoff E, Dewland TA, et al (2017) Ectopy on a Single 12-Lead ECG, Incident Cardiac Myopathy, and Death in the Community. J Am Heart Assoc. doi: 10.1161/JAHA.117.006028

31. Lim PB, Malcolme-Lawes LC, Stuber T, Wright I, Francis DP, Davies DW, Peters NS, Kanagaratnam P (2011) Intrinsic cardiac autonomic stimulation induces pulmonary vein ectopy and triggers atrial fibrillation in humans. J Cardiovasc Electrophysiol 22:638–646

32. Po SS, Li Y, Tang D, Liu H, Geng N, Jackman WM, Scherlag B, Lazzara R, Patterson E (2005) Rapid and stable re-entry within the pulmonary vein as a mechanism initiating paroxysmal atrial fibrillation. J Am Coll Cardiol 45:1871–1877

33. Schauerte P, Scherlag BJ, Pitha J, Scherlag MA, Reynolds D, Lazzara R, Jackman WM (2000) Catheter ablation of cardiac autonomic nerves for prevention of vagal atrial fibrillation. Circulation 102:2774–2780

34. Schauerte P, Scherlag BJ, Patterson E, Scherlag MA, Matsudaria K, Nakagawa H, Lazzara R, Jackman WM (2001) Focal atrial fibrillation: Experimental evidence for a pathophysiologic role of the autonomic nervous system. J Cardiovasc Electrophysiol 12:592–599

35. Lin J, Scherlag BJ, Zhou J, Lu Z, Patterson E, Jackman WM, Lazzara R, Po SS (2007) Autonomic mechanism to explain complex fractionated atrial electrograms (CFAE). J Cardiovasc Electrophysiol 18:1197–1205

36. Zhou J, Scherlag BJ, Edwards J, Jackman WM, Lazzara R, Po SS (2007) Gradients of atrial refractoriness and inducibility of atrial fibrillation due to stimulation of ganglionated plexi. J Cardiovasc Electrophysiol 18:83–90

37. Yazicioğlu RF, Hoof C van., Puers R (2009) Biopotential Readout Circuits for Portable Acquisition Systems. Springer Sci. doi: 10.1007/978-1-4020-9093-6

38. Bard AJ (1980) Electrochemical methods : fundamentals and applications.

39. Webster JG (2010) Medical Instrumentation Application and Design, Fourth Edition. John Wiley & Sons

40. Nishimura S, Tomita Y, Horiuchi T (1992) Clinical Application of an Active Electrode Using an Operational Amplifier. IEEE Trans Biomed Eng 39:1096–1099

41. Griss P, Tolvanen-Laakso HK, Meriläinen P, Stemme G (2002) Characterization of micromachined spiked biopotential electrodes. IEEE Trans Biomed Eng 49:597–604

42. Zhang F, Holleman J, Otis BP (2012) Design of ultra-low power biopotential amplifiers for biosignal acquisition applications. IEEE Trans Biomed Circuits Syst 6:344–355

43. Yazicioglu RF, Merken P, Puers R, Van Hoof C (2007) A 60 μW 60 nV/√Hz readout front-end for portable biopotential acquisition systems. In: IEEE J. Solid-State Circuits. pp 1100–1110

44. Cagnan H, Denison T, McIntyre C, Brown P (2019) Emerging technologies for improved deep brain stimulation. Nat Biotechnol 37:1024–1033

45. Cagnan H, Pedrosa D, Little S, et al (2017) Stimulating at the right time: Phase-specific

deep brain stimulation. Brain 140:132–145

46. Volkmann J, Albanese A, Kulisevsky J, et al (2009) Long-term effects of pallidal or subthalamic deep brain stimulation on quality of life in Parkinson's disease. Mov Disord 24:1154–1161

47. Kestenbaum M, Ford B, Louis ED (2015) Estimating the Proportion of Essential Tremor and Parkinson's Disease Patients Undergoing Deep Brain Stimulation Surgery: Five-Year Data From Columbia University Medical Center (2009–2014). Mov Disord Clin Pract 2:384–387

48. Yu T, Wang X, Li Y, et al (2018) High-frequency stimulation of anterior nucleus of thalamus desynchronizes epileptic network in humans. Brain 141:2631–2643

49. Okun MS, Tagliati M, Pourfar M, Fernandez HH, Rodriguez RL, Alterman RL, Foote KD (2005) Management of referred deep brain stimulation failures: A retrospective analysis from 2 Movement Disorders Centers. Arch Neurol 62:1250–1255

50. Moro E, Poon Y-YW, Lozano AM, Saint-Cyr JA, Lang AE (2006) Subthalamic Nucleus Stimulation. Arch Neurol 63:1266

51. Rossi PJ, Gunduz A, Judy J, et al (2016) Proceedings of the third annual deep brain stimulation think tank: A review of emerging issues and technologies. Front Neurosci 10:119

52. Ferrer I (2011) Neuropathology and neurochemistry of nonmotor symptoms in Parkinson's disease. Parkinsons Dis 2011:708404

53. Salam MT, Perez Velazquez JL, Genov R (2016) Seizure Suppression Efficacy of Closed-Loop Versus Open-Loop Deep Brain Stimulation in a Rodent Model of Epilepsy. IEEE Trans Neural Syst Rehabil Eng 24:710–719

54. Zhou A, Johnson BC, Muller R (2018) Toward true closed-loop neuromodulation: artifact-free recording during stimulation. Curr Opin Neurobiol 50:119–127

55. Merrill DR, Bikson M, Jefferys JGR (2005) Electrical stimulation of excitable tissue: Design of efficacious and safe protocols. J Neurosci Methods 141:171–198

56. Wang C, Brunton E, Haghgooie S, Cassells K, Lowery A, Rajan R (2013) Characteristics of electrode impedance and stimulation efficacy of a chronic cortical implant using novel annulus electrodes in rat motor cortex. J Neural Eng 10:046010

57. Blum RA, Ross JD, Das SK, Brown EA, DeWeerth SP (2004) Models of stimulation artifacts applied to integrated circuit design. In: Annu. Int. Conf. IEEE Eng. Med. Biol. - Proc. IEEE, pp 4075–4078

58. Brown EA, Ross JD, Blum RA, Nam Y, Wheeler BC, DeWeerth SP (2008) Stimulus-artifact elimination in a multi-electrode system. IEEE Trans Biomed Circuits Syst 2:10–21

59. Noorsal E, Sooksood K, Xu H, Hornig R, Becker J, Ortmanns M (2012) A neural stimulator frontend with high-voltage compliance and programmable pulse shape for epiretinal implants. IEEE J Solid-State Circuits 47:244–256

60. Sit JJ, Sarpeshkar R (2007) A low-power blocking-capacitor-free charge-balanced electrode-stimulator chip with lesst than 6 nA DC error for 1-mA: Full-Scale Stimulation. IEEE Trans Biomed Circuits Syst 1:172–183

61. Greenwald E, Chen C, Thakor N, Maier C, Cauwenberghs G (2013) A CMOS neurostimulator with on-chip DAC calibration and charge balancing. In: 2013 IEEE Biomed. Circuits Syst. Conf. BioCAS 2013. IEEE, pp 89–92

62. Johnson BC, Gambini S, Izyumin I, Moin A, Zhou A, Alexandrov G, Santacruz SR, Rabaey JM, Carmena JM, Muller R (2017) An implantable 700μW 64-channel neuromodulation IC for simultaneous recording and stimulation with rapid artifact recovery. In: IEEE Symp. VLSI Circuits, Dig. Tech. Pap. IEEE, pp C48–C49

63. Bahmer A, Peter O, Baumann U (2010) Recording and analysis of electrically evoked compound action potentials (ECAPs) with MED-EL cochlear implants and different artifact reduction strategies in Matlab. J Neurosci Methods 191:66–74

64. Chu P, Muller R, Koralek A, Carmena JM, Rabaey JM, Gambini S (2013) Equalization for intracortical microstimulation artifact reduction. In: Proc. Annu. Int. Conf. IEEE Eng. Med. Biol. Soc. EMBS. IEEE, pp 245–248

65. Petkos K, Guiho T, Degenaar P, Jackson A, Brown P, Denison TJ, Drakakis EM (2019) A high-performance 4 nV/√ analog front-end architecture for artefact suppression in local field potential recordings during deep brain stimulation. J Neural Eng 16:066003

66. Peterson EJ, Dinsmoor DA, Tyler DJ, Denison TJ (2016) Stimulation artifact rejection in closed-loop, distributed neural interfaces. In: Eur. Solid-State Circuits Conf. IEEE, pp 233–236

67. Rossi L, Foffani G, Marceglia S, Bracchi F, Barbieri S, Priori A (2007) An electronic device for artefact suppression in human local field potential recordings during deep brain stimulation. J Neural Eng 4:96–106

68. Montgomery EB, Gale JT, Huang H (2005) Methods for isolating extracellular action potentials and removing stimulus artifacts from microelectrode recordings of neurons requiring minimal operator intervention. J Neurosci Methods 144:107–125

69. Hartmann C, Došen S, Amsuess S, Farina D (2015) Closed-loop control of myoelectric prostheses with electrotactile feedback: Influence of stimulation artifact and blanking. IEEE Trans Neural Syst Rehabil Eng 23:807–816

70. Heffer LF, Fallon JB (2008) A novel stimulus artifact removal technique for high-rate electrical stimulation. J Neurosci Methods 170:277–284

71. Zhou A, Santacruz SR, Johnson BC, Alexandrov G, Moin A, Burghardt FL, Rabaey JM, Carmena JM, Muller R (2019) A wireless and artefact-free 128-channel neuromodulation device for closed-loop stimulation and recording in non-human primates. Nat Biomed Eng 3:15–26

72. Hoffmann U, Cho W, Ramos-Murguialday A, Keller T (2011) Detection and removal of stimulation artifacts in electroencephalogram recordings. In: Proc. Annu. Int. Conf. IEEE Eng. Med. Biol. Soc. EMBS. IEEE, pp 7159–7162

73. Waddell C, Pratt JA, Porr B, Ewing S (2009) Deep brain stimulation artifact removal through under-sampling and cubic-spline interpolation. In: Proc. 2009 2nd Int. Congr. Image Signal Process. CISP'09. IEEE, pp 1–5

74. Qian X, Chen Y, Feng Y, Ma B, Hao H, Li L (2017) A method for removal of deep brain stimulation artifact from local field potentials. IEEE Trans Neural Syst Rehabil Eng 25:2217–2226

75. Mendrela AE, Cho J, Fredenburg JA, Nagaraj V, Netoff TI, Flynn MP, Yoon E (2016) A Bidirectional Neural Interface Circuit with Active Stimulation Artifact Cancellation and Cross-Channel Common-Mode Noise Suppression. IEEE J Solid-State Circuits 51:955–965

76. Basir-Kazeruni S, Vlaski S, Salami H, Sayed AH, Markovic D (2017) A blind Adaptive Stimulation Artifact Rejection (ASAR) engine for closed-loop implantable neuromodulation systems. In: Int. IEEE/EMBS Conf. Neural Eng. NER. IEEE, pp 186–

189

77. Zeng K, Chen D, Ouyang G, Wang L, Liu X, Li X (2016) An EEMD-ICA Approach to Enhancing Artifact Rejection for Noisy Multivariate Neural Data. IEEE Trans Neural Syst Rehabil Eng 24:630–638

78. Al-ani T, Cazettes F, Palfi S, Lefaucheur JP (2011) Automatic removal of high-amplitude stimulus artefact from neuronal signal recorded in the subthalamic nucleus. J Neurosci Methods 198:135–146

79. Lu Y, Cao P, Sun J, Wang J, Li L, Ren Q, Chen Y, Chai X (2012) Using independent component analysis to remove artifacts in visual cortex responses elicited by electrical stimulation of the optic nerve. J Neural Eng. doi: 10.1088/1741-2560/9/2/026002

80. Cong P, Karande P, Landes J, Corey R, Stanslaski S, Santa W, Jensen R, Pape F, Moran D, Denison T (2014) A 32-channel modular bi-directional neural interface system with embedded DSP for closed-loop operation. In: ESSCIRC 2014 - 40th Eur. Solid State Circuits Conf. IEEE, pp 99–102

81. Buhlmann J, Hofmann L, Tass PA, Hauptmann C (2011) Modeling of a Segmented Electrode for Desynchronizing Deep Brain Stimulation. Front Neuroeng. doi: 10.3389/fneng.2011.00015

82. Wei XF, Grill WM (2005) Current density distributions, field distributions and impedance analysis of segmented deep brain stimulation electrodes. J Neural Eng 2:139–147

83. Spinelli EM, Pallàs-Areny R, Mayosky MA (2003) AC-coupled front-end for biopotential measurements. IEEE Trans Biomed Eng 50:391–395

84. Casas O, Spinelli EM, Pallàs-Areny R (2009) Fully differential AC-coupling networks: A comparative study. In: IEEE Trans. Instrum. Meas. pp 94–98

85. Nikola J, Ratko P, Strahinja D, Dejan PB (2001) A novel AC-amplifier for electrophysiology: Active DC suppression with differential to differential amplifier in the feedback-loop. In: Annu. Reports Res. React. Institute, Kyoto Univ. IEEE, pp 3328–3331

86. Northrop RB (2012) Analysis and application of analog electronic circuits to biomedical instrumentation. CRC Press

87. Poshala P, KK R, Gupta R (2014) Signal Chain Noise Figure Analysis. Texas

Instruments SLAA652:1–14

88. Lee J-S, Su Y-W, Shen C-C (2007) A Comparative Study of Wireless Protocols: Bluetooth, UWB, ZigBee, and Wi-Fi. In: IECON 2007 - 33rd Annu. Conf. IEEE Ind. Electron. Soc. IEEE, pp 46–51

89. Petrova M, Riihijarvi J, Mahonen P, Labella S (2006) Performance study of IEEE 802.15.4 using measurements and simulations. In: IEEE Wirel. Commun. Netw. Conf. 2006. WCNC 2006. IEEE, pp 487–492

90. Zhan Y, Cao Z, Lu J (2005) Spread-spectrum sequence estimation for DSSS signal in non-cooperative communication systems. Commun IEE Proceedings- 152:476–480

91. Wu R, Huijsing JH, Makinwa KAA (2013) Precision instrumentation amplifiers and read-out integrated circuits. Springer

92. Lai Y (2009) MT-053 Op amp distortion: HD, THD, THD+ N, IMD, SFDR, MTPR. In: IMID 2009. pp 1069–1072

93. Zumbahlen H (2008) Analog Filters. Linear Circuit Des Handb 943

94. Ardizzoni BJ (2007) High-Speed Time-Domain Measurements — Practical Tips for Improvement. 2:3–8

95. Francis J (2016) ECG monitoring leads and special leads. Indian Pacing Electrophysiol J 16:92–95

96. Cerone GL, Botter A, Gazzoni M (2019) A Modular, Smart, and Wearable System for High Density sEMG Detection. IEEE Trans Biomed Eng 1–1

97. Sarker VK, Jiang M, Gia TN, Anzanpour A, Rahmani AM, Liljeberg P (2017) Portable multipurpose bio-signal acquisition and wireless streaming device for wearables. In: SAS 2017 - 2017 IEEE Sensors Appl. Symp. Proc. IEEE, pp 1–6

98. Pinnell RC, Dempster J, Pratt J (2015) Miniature wireless recording and stimulation system for rodent behavioural testing. J Neural Eng 12:066015

99. Yaul FM, Chandrakasan AP (2017) A Noise-Efficient 36 nV/√Hz Chopper Amplifier Using an Inverter-Based 0.2-V Supply Input Stage. IEEE J Solid-State Circuits 52:3032–3042

100. Denison T, Consoer K, Kelly A, Hachenburg A, Santa W (2007) A 2.2μW 94nV/√Hz,

chopper-stabilized instrumentation amplifier for EEG detection in chronic implants. In: Dig. Tech. Pap. - IEEE Int. Solid-State Circuits Conf. IEEE, pp 162–594

101. Xu J, Yazicioglu RF, Grundlehner B, Harpe P, Makinwa KAA, Van Hoof C (2011) A 160 μw 8-channel active electrode system for EEG monitoring. In: IEEE Trans. Biomed. Circuits Syst. IEEE, pp 555–567

102. Parastarfeizabadi M, Kouzani AZ (2017) Advances in closed-loop deep brain stimulation devices. J Neuroeng Rehabil 14:79

103. Goldberg JA (2004) Spike Synchronization in the Cortex-Basal Ganglia Networks of Parkinsonian Primates Reflects Global Dynamics of the Local Field Potentials. J Neurosci 24:6003–6010

104. Swann NC, de Hemptinne C, Miocinovic S, Qasim S, Wang SS, Ziman N, Ostrem JL, San Luciano M, Galifianakis NB, Starr PA (2016) Gamma Oscillations in the Hyperkinetic State Detected with Chronic Human Brain Recordings in Parkinson's Disease. J Neurosci 36:6445–6458

105. Gabriel M, Julien C, Salin PA, Jean-Christophe C (2018) Differential recordings of local field potential: A genuine tool to quantify functional connectivity. PLoS One 13:e0209001

106. Blumenfeld Z, Koop MM, Prieto TE, Shreve LA, Velisar A, Quinn EJ, Trager MH, Brontë-Stewart H (2017) Sixty-hertz stimulation improves bradykinesia and amplifies subthalamic low-frequency oscillations. Mov Disord 32:80–88

107. Shimamoto SA, Ryapolova-Webb ES, Ostrem JL, Galifianakis NB, Miller KJ, Starr PA (2013) Subthalamic Nucleus Neurons Are Synchronized to Primary Motor Cortex Local Field Potentials in Parkinson's Disease. J Neurosci 33:7220–7233

108. De Hemptinne C, Swann NC, Ostrem JL, Ryapolova-Webb ES, San Luciano M, Galifianakis NB, Starr PA (2015) Therapeutic deep brain stimulation reduces cortical phase-amplitude coupling in Parkinson's disease. Nat Neurosci 18:779–786

109. Karki J (2002) Active Low-Pass Filter Design.

110. Oostenveld R, Fries P, Maris E, Schoffelen JM (2011) FieldTrip: Open source software for advanced analysis of MEG, EEG, and invasive electrophysiological data. Comput Intell Neurosci 2011:156869

111. Paus T, Sipila PK, Strafella AP (2001) Synchronization of Neuronal Activity in the Human Primary Motor Cortex by Transcranial Magnetic Stimulation: An EEG Study. J Neurophysiol 86:1983–1990

112. Fuggetta G, Fiaschi A, Manganotti P (2005) Modulation of cortical oscillatory activities induced by varying single-pulse transcranial magnetic stimulation intensity over the left primary motor area: A combined EEG and TMS study. Neuroimage 27:896–908

113. Van Der Werf YD, Paus T (2006) The neural response to transcranial magnetic stimulation of the human motor cortex. I. Intracortical and cortico-cortical contributions. Exp brain Res 175:231–45

114. Van Der Werf YD, Sadikot AF, Strafella AP, Paus T (2006) The neural response to transcranial magnetic stimulation of the human motor cortex. II. Thalamocortical contributions. Exp Brain Res 175:246–255

115. Knaflitz M, Knaflitz M, Merletti R, Merletti R (1988) Suppression of Simulation Artifacts from Myoelectric-Evoked Potential Recordings. IEEE Trans Biomed Eng 35:758–763

116. Baker BC (2015) Bandstop filters and the Bainter topology. Analog Appl J 8–10

117. Salehizadeh SMA, Noh Y, Chon KH (2016) Heart Rate Monitoring during Intense Physical Activities Using a Motion Artifact Corrupted Signal Reconstruction Algorithm in Wearable Electrocardiogram Sensor. In: Proc. - 2016 IEEE 1st Int. Conf. Connect. Heal. Appl. Syst. Eng. Technol. CHASE 2016. IEEE, pp 157–162

118. Greenwald E, So E, Wang Q, Mollazadeh M, Maier C, Etienne-Cummings R, Cauwenberghs G, Thakor N (2016) A Bidirectional Neural Interface IC With Chopper Stabilized BioADC Array and Charge Balanced Stimulator. IEEE Trans Biomed Circuits Syst 10:990–1002

119. Henderson KW, Kautz WH (1958) Transient Responses of Conventional Filters. IRE Trans Circuit Theory 5:333–347

120. Herron JA, Thompson MC, Brown T, Chizeck HJ, Ojemann JG, Ko AL (2016) Chronic electrocorticography for sensing movement intention and closed-loop deep brain stimulation with wearable sensors in an essential tremor patient. J Neurosurg 127:580–587

121. Oswal A, Brown P, Litvak V (2013) Synchronized neural oscillations and the pathophysiology of Parkinson's disease. Curr Opin Neurol 26:662–670

122. Arlotti M, Marceglia S, Foffani G, et al (2018) Eight-hours adaptive deep brain stimulation in patients with Parkinson disease. Neurology 90:e971–e976

123. Fogelson N, Pogosyan A, Kühn AA, et al (2005) Reciprocal interactions between oscillatory activities of different frequencies in the subthalamic region of patients with Parkinson's disease. Eur J Neurosci 22:257–266

124. Meidahl AC, Moll CKE, van Wijk BCM, Gulberti A, Tinkhauser G, Westphal M, Engel AK, Hamel W, Brown P, Sharott A (2019) Synchronised spiking activity underlies phase amplitude coupling in the subthalamic nucleus of Parkinson's disease patients. Neurobiol Dis 127:101–113

125. Shah SA, Tinkhauser G, Chen CC, Little S, Brown P (2018) Parkinsonian Tremor Detection from Subthalamic Nucleus Local Field Potentials for Closed-Loop Deep Brain Stimulation. In: Proc. Annu. Int. Conf. IEEE Eng. Med. Biol. Soc. EMBS. IEEE, pp 2320–2324

126. Yao L, Brown P, Shoaran M (2018) Resting Tremor Detection in Parkinson's Disease with Machine Learning and Kalman Filtering. In: 2018 IEEE Biomed. Circuits Syst. Conf. BioCAS 2018 - Proc. IEEE, pp 1–4

127. Liu H, Shah S, Jiang W (2004) On-line outlier detection and data cleaning. Comput Chem Eng 28:1635–1647

128. Ghaleb FA, Kamat MB, Salleh M, Rohani MF, Razak SA (2018) Two-stage motion artefact reduction algorithm for electrocardiogram using weighted adaptive noise cancelling and recursive Hampel filter. PLoS One. doi: 10.1371/journal.pone.0207176

129. Petkos K, Koutsoftidis S, Guiho T, Degenaar P, Jackson A, Greenwald SE, Brown P, Denison T, Drakakis EM (2019) A high-performance 8 nV/√Hz 8-channel wearable and wireless system for real-time monitoring of bioelectrical signals. J Neuroeng Rehabil 16:156